



THE UNIVERSITY OF QUEENSLAND
A U S T R A L I A

Superorbital Re-entry Shock Layers: Flight and Laboratory Comparisons

Elise Joy Fahy

Bachelor of Aerospace Engineering (First Class Honours) &
Bachelor of Science (Theoretical Physics)

A thesis submitted for the degree of Doctor of Philosophy

at the University of Queensland in 2016

School of Mechanical and Mining Engineering

Abstract

Hypervelocity re-entry through the Earth's atmosphere surrounds an aeroshell with a radiating shock layer, which has complex and potentially critical interactions with the thermal protection system, the key component to the vehicle's survival. Aerothermodynamic re-entry flight data is rare, but the available radiation data has potential for replication in ground-based experimental and numerical testing, where flight equivalent conditions can be achieved. A greater understanding and ability to demonstrate the behaviour of re-entry vehicles will allow increased confidence in pre-flight laboratory predictions, design iterations based on testing and simulation, and an overall reduction in the thermal protection system (TPS) mass, therefore increasing the mass available for scientific payload. This thesis aims to replicate flight data from the unmanned Hayabusa and Stardust aeroshell re-entries in expansion tube experiments and numerical simulations, and assess the similarities and differences in the results. The flight data is in the form of infrared (IR) and ultraviolet (UV) spectra emanating from the bow shock, as captured by air- and ground-based observation missions.

The experiments were performed in the X2 expansion tube, a hypervelocity impulse facility capable of producing flight equivalent conditions over a scaled aeroshell model for a brief test time. Prior to optical imaging tests, the conditions were designed through an iterative combination of analytical, experimental and numerical methods, based on binary scaling and enthalpy matching. Emissions from the radiating shock layers were captured by IR and UV spectroscopy, as well as two-dimensional intensity mapping through a narrow wavelength band filter, but the measurements were oriented differently to flight. The axisymmetry of certain imaging planes enabled the transformation of line of sight integrated intensities into radial quantities, which could describe the forebody shock layer and result in an integrated intensity comparable with integrated flight spectra.

Numerical simulations must first model the flowfield before radiation modelling is possible. Compressible flow computational fluid dynamics (CFD) simulations were performed for the Hayabusa and Stardust flight vehicles at the selected trajectory points, and scaled models at idealised and simulated inflow conditions. Radiation spectra calculations were performed along the same lines of sight as imaged in experimental spectra, and over the entire flowfield to be comparable to flight data and experimental 2D imaging.

The flight, experimental and numerical data combined for a series of comparisons to test the hypotheses that under binary scaling, spectral radiance along a line of sight is invariant, and radiative intensity scales with the square of the length scale. Spectra comparisons between experiment and CFD, and CFD and flight, tested the first hypothesis, and integrated intensity comparisons between experiment and CFD, and experiment and flight, tested the second hypothesis. Favourable comparisons were found between experiment and flight, full scale CFD and flight, and full scale CFD and experiment. All comparisons to scaled CFD were poor, and possible causes and areas for investigation were identified. Given the uncertainties inherent in each part of the comparison, including observing at a distance, imperfect scaling, shot-to-shot variation, and assumptions in the CFD and radiation calculations, the favourable comparisons are a significant achievement.

This project is the first work of its kind to directly compare radiation data from re-entry flights with radiation data obtained in expansion tube tests and CFD simulations at matched conditions. The results show that the hypotheses hold, demonstrating the validity and potential of both ground testing methods in re-creating flight environments.

Declaration

This thesis is composed of my original work, and contains no material previously published or written by another person except where due reference has been made in the text. I have clearly stated the contribution by others to jointly-authored works that I have included in my thesis.

I have clearly stated the contribution of others to my thesis as a whole, including statistical assistance, survey design, data analysis, significant technical procedures, professional editorial advice, and any other original research work used or reported in my thesis. The content of my thesis is the result of work I have carried out since the commencement of my research higher degree candidature and does not include a substantial part of work that has been submitted to qualify for the award of any other degree or diploma in any university or other tertiary institution. I have clearly stated which parts of my thesis, if any, have been submitted to qualify for another award.

I acknowledge that an electronic copy of my thesis must be lodged with the University Library and, subject to the policy and procedures of The University of Queensland, the thesis be made available for research and study in accordance with the Copyright Act 1968 unless a period of embargo has been approved by the Dean of the Graduate School.

I acknowledge that copyright of all material contained in my thesis resides with the copyright holder(s) of that material. Where appropriate I have obtained copyright permission from the copyright holder to reproduce material in this thesis.

Publications during candidature

Conference publications (First author only listed)

E.J. Fahy, R.J. Gollan, D.R. Buttsworth, P.A. Jacobs, and R.G. Morgan, Expansion Tube and Computational Fluid Dynamics Studies of Superorbital Earth Re-entry, 46th AIAA Thermophysics Conference, Washington D.C., USA, June 2016.

E.J. Fahy, D.R. Buttsworth and R.G. Morgan, Scaled Earth Re-entry Experiments in the X2 Expansion Tube, 7th Asia-Pacific International Symposium on Aerospace Technology, Cairns, Australia, November 2015.

E.J. Fahy, R.G. Morgan and D.R. Buttsworth, Scaled Hayabusa Experiments in the X2 Expansion Tube, 6th International Workshop on Radiation of High Temperature Gases in Atmospheric Entry, St Andrews, UK, November 2014.

E.J. Fahy, N. Banerji, V. Marguet, Mora-Monteros, J, D. Potter, F. Zander, P. Leyland and R.G. Morgan, Ground to Flight Investigations of Hayabusa with Ablation Effects, ESA Thermal Protection Systems and Hot Structures Workshop, Noordwijk, The Netherlands, April 2013.

E.J. Fahy, F. Zander, D.R. Buttsworth and R.G. Morgan, Fast-Response Pyrometer Development for Expansion Tunnel Testing with Hot Carbon Models, 18th Australasian Fluid Mechanics Conference, Launceston, Australia, December 2012.

Publications included in this thesis

None.

Contributions by others to the thesis

None.

Statement of parts of the thesis submitted to qualify for the award of another degree

None.

Acknowledgments

I am lucky to be surrounded by many wonderful people, in a personal and professional sense, and I am extremely grateful for their part they have played in me reaching this milestone. Thank you...

To my supervisors, for their belief in me and their guidance. To Richard, for his great ideas, love of experiments, stories, banter and leaving a bit of low hanging fruit for those that aren't the man of steel. To David, for his endless enthusiasm in our evolving project and life in general, and being a welcome happy face in the dungeons every week.

To my CFD mentors, Peter and Rowan, for teaching me so much, for their patience when I broke things, and for their reliable advice over many coffees. I may not be able to produce a beard worthy of being your protégée, but I hope my CFD skills are up there!

To everybody in the x-labs who ensured there was never a dull moment and that the tunnels kept running: the old man (Fabs), Waffle (Guerric), Drab/B-rad/the Bard (Brad), Hadas, Han Solo, PP (Pierpaolo), Dougie (Andreas), Umar, Sangdi, Dave, Troy and Jorge. Special mention to my bros, Christoher (Tatts Français) and Steven, for constant craziness and X2 adventures. To Tim for assistance with optics, to Frans, Keith and Barry for assistance in the lab, and to everybody upstairs that came to visit (especially on a Friday afternoon!). To Rowan, Fabs and Jaya for reading my drafts.

To Pénélope for bringing me to EPFL and creating the opportunity for me to live in beautiful Switzerland. To the people that have made working at EPFL/hanging out at Sat and being in Lausanne so enjoyable: Jeremaaaah (Jérémie), Chris, Val, Yannbert (Yann), Oleg, Ermina and Rik. To Hannes Fulge at IRS for use of his Abel inversion code, and Lionel Marraffa for granting permission to use PARADE beyond the ARC project.

To my parents for enabling me to follow my dreams, giving me the best opportunities possible, and inspiring me to lead a life filled with joy. To Sarah, I don't know, do you? But actually for being the best sister one could hope for, and balancing out my exuberance with your quiet brilliance. To my grandparents for their faith and excitement, and to my extended family for the support, the many laughs and wonderful times, and the incredible bonds we all share. To my new family for your

kindness and generosity. To my friends for choosing to share this journey with me and making me a better person for it - you are all stars in my eyes. To all the people that have been mentors and role models, your inspiration has fuelled my enthusiasm.

To Nikhil, *meri jaan*. This thesis is complete due to your unwavering belief and encouragement. You constantly find new ways to inspire me, make me think and wonder, and bring joy and fun to our everyday and our great adventures! Together we will continue to embrace the world, and beyond. I love you.

This project was primarily funded by the Australian Postgraduate Award, and supplementary funding was provided by the Australian Research Council and the European Space Agency ‘Ablation-Radiation Coupling’ project. I also gratefully acknowledge the Zonta Foundation as a recipient of their Amelia Earhart Fellowship in 2015/2016.

Keywords

aerothermodynamics, computational fluid dynamics, emission spectroscopy, expansion tube, hypersonics, radiation, re-entry.

Australian and New Zealand Standard Research Classifications (ANZSRC)

ANZSRC code: 090107, Hypersonic Propulsion and Hypersonic Aerodynamics, 60 %

ANZSRC code: 091501, Computational Fluid Dynamics, 20 %

ANZSRC code: 020503, Nonlinear Optics and Spectroscopy, 20 %

Fields of Research (FoR) Classification

FoR code: 0901, Aerospace Engineering, 100 %

For Pa.

Contents

Abstract	iii
1 Introduction	1
1.1 Motivation	1
1.1.1 The Earth Re-Entry Environment	2
1.1.2 From Flight Data to Ground Testing	5
1.2 Aim	7
1.3 Objectives	7
1.4 Scope	8
1.5 Thesis Outline	8
2 From Re-entry to Experimental and Numerical Ground Testing: A Review	11
2.1 There and back again: A brief history of Earth re-entry	12
2.1.1 Early re-entry missions	12
2.1.2 Genesis re-entry observation mission	13
2.1.3 Stardust re-entry observation mission	14
2.1.4 Hayabusa re-entry observation mission	15
2.1.5 Summary	20
2.2 Experiments in the X2 free-piston driven expansion tube	21
2.2.1 Evolution of the X2 facility	21
2.2.2 X2 condition design	23
2.2.3 Relevant X2 experimental campaigns	25
2.2.4 Summary	27
2.3 Numerical Modelling	28
2.3.1 Importance of numerical modelling	28
2.3.2 Numerical modelling of Stardust	30
2.3.3 Numerical modelling of Hayabusa	32
2.3.4 Scaled model and facility simulations	33
2.3.5 Summary	34
2.4 Summary of Findings	34

3 Condition Establishment	37
3.1 Hayabusa Condition for X2	38
3.1.1 Trajectory point selection	38
3.1.2 Nominal parameters from binary scaling and enthalpy matching	38
3.1.3 Preliminary analysis with <i>Pitot</i>	39
3.1.4 Experimental Condition Testing and Analysis	41
3.1.5 Combined <i>L1d3</i> and <i>eilmer3</i> facility simulation	43
3.2 Stardust Condition	62
3.2.1 Trajectory point selection & condition matching	62
3.2.2 Design Iterations and Analysis	62
3.2.3 Combined <i>L1d3</i> and <i>eilmer3</i> facility simulation	66
3.3 Conclusion	72
4 Scaled Earth Re-entry Experiments in the X2 Expansion Tube	75
4.1 Model Specifications	75
4.2 Optical Systems	77
4.2.1 Emission Spectroscopy	79
4.2.2 2D intensity mapping	81
4.2.3 Calibration	85
4.2.4 Background counts and cosmic ray removal	88
4.2.5 High speed camera	89
4.3 Experimental Methodology	89
4.4 Summary	92
5 Experimental Results and Analysis	93
5.1 Near IR Spectroscopy	94
5.1.1 Hayabusa: vertical orientation	95
5.1.2 Hayabusa: horizontal orientation	97
5.1.3 Stardust: horizontal orientation	99
5.2 Hayabusa UV Spectroscopy	100
5.3 2D Intensity Mapping	103

5.3.1	Hayabusa	104
5.3.2	Stardust	104
5.4	Comparing Integrated Spectra and 2D Results	107
5.4.1	Hayabusa	107
5.5	Summary	109
6	Computational Fluid Dynamics of Aeroshells in <i>eilmer3</i>	111
6.1	Simulation Parameters	112
6.1.1	Grid, Meshing and Block Structure	113
6.1.2	Thermochemistry	117
6.1.3	Diffusion, Turbulence and Non-Continuum Effects	120
6.1.4	Boundary Conditions	121
6.1.5	Summary	123
6.2	Flowfield Results	124
6.2.1	Hayabusa full scale simulation	124
6.2.2	Inclusion of mass flux boundary condition	130
6.2.3	Hayabusa scaled simulations	131
6.2.4	Stardust full scale simulation	139
6.2.5	Stardust scaled simulations	142
6.3	Conclusion	147
7	Experimental and Numerical Flight Rebuilding	149
7.1	Motivation	149
7.2	Flight Rebuilding Objectives	152
7.3	Assumptions	152
7.4	Background	153
7.4.1	Radiation Transport Modelling	154
7.4.2	Radiation Spectra Modelling	156
7.4.3	Abel Inversion	159
7.5	Hypothesis: Scaling Models and Radiation	162
7.6	Methodology	163

7.6.1	Comparing experiment and flight	163
7.6.2	Comparing CFD and flight	165
7.6.3	Comparing CFD and experiment	166
7.7	Results and Analysis	167
7.7.1	Comparing CFD and experiment	167
7.7.2	Comparing CFD and flight	176
7.7.3	Comparing experiment and flight	182
7.8	Summary of Findings	184
8	Conclusions	187
8.1	Addressing the Aim and Objectives	187
8.2	Major Findings	188
8.3	Future Work	190
References		191
A	Facility simulation grid resolution	207
B	Implementation of Ablation Boundary Condition in <i>eilmer3</i>	210
B.1	Surface reactions	210
B.2	Structure of <i>eilmer3</i> boundary condition	211
C	Radiation-Flowfield Coupling for Hayabusa	213
D	Flow visualisation	215
D.1	Facility simulations	215
D.2	Aeroshell simulations	215
D.3	Experimental campaign high speed video	216

List of Figures

1.1 Superorbital re-entry of a small, unmanned, Hayabusa-like capsule through the Earth's atmosphere: an overview.	3
2.1 Stardust entry trajectory schematic with extra annotations from Desai and Qualls [1]. MSL = mean sea level.	15
2.2 Stardust flight spectra from the ECHELLE spectrograph, as reported by Jenniskens [2].	16
2.3 The Hayabusa capsule (lower right) successfully re-entering the Earth's atmosphere as the bus breaks up [3].	17
2.4 Hayabusa IR flight spectra from a ground observation station for the seconds before and after peak heating (13:52:19 UTC). Adapted from data published by McIntyre <i>et al.</i> [4].	19
2.5 Hayabusa flight spectra from the airborne AUS instrument, as reported by Buttsworth, Morgan and Jenniskens [5].	20
2.6 Schematic of the X2 expansion tube and its constituent sections for a typical Earth re-entry experiment (not to scale). Adapted from Gildfind [6].	22
2.7 Comparisons between data sets that will be produced in the thesis work.	36
3.1 Hayabusa 13:52:20 UTC flow condition traces from all available coneheads, to demonstrate test time and core flow, and theoretical and experimental <i>Pitot</i> results. .	42
3.2 X2 facility showing regions simulated with <i>L1d3</i> and <i>eilmer3</i>	45
3.3 sd2 shock tube transducer pressure traces from <i>L1d3</i> , a single shot and the campaign average, from 35 shots. Time base referenced to the <i>L1d3</i> simulation.	46
3.4 Flow properties at the model location, 30 mm downstream of the nozzle exit, nozzle/test section centreline for equilibrium, and Park or Gupta 5 species, 1 temperature schemes.	49
3.5 <i>x</i> -velocity comparison at the nozzle exit centreline for different inflow locations: (a) full profile, (b) zoom to peak and nominal test time.	51
3.6 X2 block layout using SuperBlock constructor, and boundary conditions.	51

3.7	Acceleration tube transducer pressure traces from <i>eilmer3</i> , a single shot and the campaign average, across 34 shots. Time base referenced to the <i>L1d3</i> simulation.	54
3.8	Comparison of campaign average shock speeds with error bars, <i>L1d3</i> and <i>eilmer3</i> shock speeds, and theoretical <i>Pitot</i> shock speeds. Locations are the average distance between the two transducers.	55
3.9	Conehead pressure at the model location, 30 mm downstream of the nozzle exit, nozzle/test section centreline. Time base referenced to facility simulation.	56
3.10	Flow properties at the model location, 30 mm downstream of the nozzle exit, nozzle/test section centreline. Time base referenced to facility simulation.	58
3.11	Radial flow properties at the model location, 30 mm downstream of the nozzle exit, extending from the nozzle/test section centreline to the nozzle exit height (used as reference height). The 0 μ s time refers to the start of the nominal test time.	59
3.12	Stardust 9:57:26 UTC flow condition mapped through conehead pressure data and video stills.	64
3.13	sd2 shock tube transducer pressure trace from <i>L1d3</i> , a single shot and the campaign average, from 15 shots. Time base referenced to the <i>L1d3</i> simulation.	66
3.14	Acceleration tube transducer pressure traces from <i>eilmer3</i> , a single shot and the campaign average, from 15 shots. Time base referenced to the <i>L1d3</i> simulation.	67
3.15	Comparison of Stardust campaign average shock speeds with error bars, <i>L1d3</i> and <i>eilmer3</i> shock speeds, and theoretical <i>Pitot</i> shock speeds. Locations are the average distance between the two transducers.	68
3.16	Conehead pressure at the model location, 30 mm downstream of the nozzle exit, nozzle/test section centreline. Time base referenced to facility simulation.	69
3.17	Flow properties at the Stardust model location, 30 mm downstream of the nozzle exit, nozzle/test section centreline. The 0 μ s time refers to the start of the nominal test time.	70
3.18	Radial flow properties at the model location, 30 mm downstream of the nozzle exit, extending from the nozzle/test section centreline to the nozzle exit height (used as reference height).	71
4.1	Schematics of scaled X2 re-entry capsule models.	76

4.2	Pre-test models (front) and post-test models (back). The two Stardust models are on the left, and two Hayabusa models are on the right.	77
4.3	Schematic demonstrating set-up of optical systems on either side of the X2 test section containing an aeroshell model.	80
4.4	Filter transmissivity curves for each filter used in the 2D imaging experiments.	82
4.5	Calibrated radiance along stagnation line for a nitrogen or air test gas, imaged through the square 780 nm filter.	83
4.6	Calibrated radiance along stagnation line as imaged by 780 nm filters with square and Gaussian transmission curves.	84
4.7	Comparison of calibrated relative intensity along stagnation line for 780 nm (square transmission curve) filter and 600 nm filter.	85
4.8	Calibration curve for the integrating sphere.	87
4.9	Linearity of exposure time for integrating sphere calibration images, and importance of background removal. Circular markers indicate measurement data.	88
5.1	Hayabusa IR spectrum at 0.5 mm upstream of stagnation point, centre wavelength 780 nm.	94
5.2	Hayabusa IR spectrum at 0.5 mm upstream of stagnation point, centre wavelength 840 nm.	95
5.3	Hayabusa IR spectrum at 1 mm upstream of stagnation point, centre wavelength 780 nm.	95
5.4	Hayabusa IR spectrum at 1 mm upstream of stagnation point, centre wavelength 840 nm.	96
5.5	Hayabusa IR spectrum at 1.5 mm upstream of stagnation point, centre wavelength 780 nm.	97
5.6	Hayabusa IR spectrum at 1.5 mm upstream of stagnation point, centre wavelength 840 nm.	98
5.7	Hayabusa IR spectrum from wall, equilibrium and nonequilibrium region on stagnation line, centre wavelength 780 nm.	99
5.8	Hayabusa IR spectrum from equilibrium region on stagnation line, centre wavelength 840 nm.	100
5.9	Stardust IR spectrum from equilibrium region on stagnation line, centre wavelength 780 nm.	101

5.10 Stardust IR spectrum from equilibrium region on stagnation line, centre wavelength 840 nm.	101
5.11 Hayabusa UV spectrum at 0.5 mm upstream of stagnation point, centre wavelength 374 nm.	102
5.12 Hayabusa UV spectrum at 1.0 mm upstream of stagnation point, centre wavelength 374 nm.	102
5.13 Hayabusa UV spectrum at 1.5 mm upstream of stagnation point, centre wavelength 374 nm.	103
5.14 Hayabusa shock layer radiance, imaged through various narrow band filters.	105
5.15 Stardust shock layer radiance, imaged through various narrow band filters.	106
5.16 Convolving the 780 nm filter transmission curve (left y-axis) with the experimental spectrum in the filter wavelength range (right y-axis) to illustrate reduction in intensity.	107
5.17 Convolving the 840 nm filter transmission curve (left y-axis) with the experimental spectrum in the filter wavelength range (right y-axis) to illustrate reduction in intensity.	108
5.18 Comparison between integrated spectra and slices from 2D images for several vertical locations.	109
6.1 Running a simulation in <i>eilmer3</i> : a brief overview.	113
6.2 Aeroshell cell, domain and block layout examples.	114
6.3 Hayabusa grid convergence study using Richardson extrapolation to calculate tem- perature at zero grid spacing.	116
6.4 Stardust grid convergence study using Richardson extrapolation to calculate temper- ature at zero grid spacing.	116
6.5 The trajectories of (1) Space Shuttle and Buran vehicles, and (2) aeroassisted orbital transfer vehicles, mapped by velocity and altitude to indicate important regions for physical and chemical processes. Reproduced from Gollan [7], who redrew the origi- nal figure from Tirsky [8].	119
6.6 Temperatures along stagnation line for Hayabusa scaled simulation, comparing in- flow conditions constructed from equilibrium (eq.) and Park 5 species (sp) 1T facility simulations.	122

6.7 N and O mole fractions along stagnation line for Hayabusa scaled simulation, comparing inflow conditions constructed from equilibrium (eq.) and Park 5 species (sp) 1T facility simulations.	123
6.8 Temperatures along stagnation line for Hayabusa full scale simulation, comparing Park with non-catalytic and super-catalytic wall.	124
6.9 Selected mole fractions along stagnation line for Hayabusa full scale simulation, comparing Park with non-catalytic and super-catalytic wall.	125
6.10 Temperatures along stagnation line for Hayabusa full scale simulation, using Park and Gupta reaction schemes. Super-catalytic wall.	126
6.11 Mole fractions for atomic and molecular N and O, and N_2^+ , along stagnation line for Hayabusa full scale simulation, comparison between Park (solid line) and Gupta (dashed line) reaction schemes.	127
6.12 Mole fractions along stagnation line for Hayabusa full scale simulation, Park reaction scheme.	128
6.13 Temperature and pressure along the vehicle surface from the stagnation point for Hayabusa full scale simulation.	128
6.14 Convective and radiative heat flux along the vehicle surface from the stagnation point for Hayabusa full scale simulation. Radiative heat flux calculated at the end of converged flowfield simulation.	129
6.15 Mole fractions along stagnation line for Hayabusa full scale simulation, using mass flux boundary condition, 20 species and Park's 24 reaction scheme [9].	131
6.16 Temperatures along stagnation line for Hayabusa full scale, 1/5 ideal and 1/5 nozzle inflow simulations.	132
6.17 Mole fractions of atomic species along stagnation line for Hayabusa full scale, 1/5 ideal and 1/5 nozzle inflow simulations.	134
6.18 Mole fractions of atomic ions and electrons along stagnation line for Hayabusa full scale, 1/5 ideal and 1/5 nozzle inflow simulations.	134
6.19 Mole fractions of molecular species along stagnation line for Hayabusa full scale, 1/5 ideal and 1/5 nozzle inflow simulations.	135

6.20 Mole fractions of molecular ions along stagnation line for Hayabusa full scale, 1/5 ideal and 1/5 nozzle inflow simulations.	136
6.21 Pressure over the vehicle surface for Hayabusa full scale, 1/5 ideal and 1/5 nozzle inflow simulations.	136
6.22 Convective heat flux over the vehicle surface from the stagnation point for Hayabusa full scale, 1/5 ideal and 1/5 nozzle inflow simulations.	137
6.23 Mole fractions for atomic and molecular N and O, and N_2^+ , along stagnation line for Hayabusa ideal scaled simulation, comparison between Park (solid line) and Gupta (dashed line) reaction schemes.	138
6.24 Mole fractions for atomic and molecular N and O, and N_2^+ , along stagnation line for Hayabusa X2 scaled simulation, comparison between Park (solid line) and Gupta (dashed line) reaction schemes.	138
6.25 Temperatures along stagnation line for Stardust full scale simulation, Park reaction scheme, super-catalytic wall.	139
6.26 Mole fractions along stagnation line for Stardust full scale simulation, Park reaction scheme, super-catalytic wall.	140
6.27 Temperature and pressure along the vehicle surface from the stagnation point for Stardust full scale simulation.	141
6.28 Convective and radiative heat flux along the vehicle surface from the stagnation point for Stardust full scale simulation.	142
6.29 Temperatures along stagnation line for Stardust full scale, 1/10 ideal and 1/10 nozzle inflow simulations.	143
6.30 Mole fractions of atomic species along stagnation line for Stardust full scale, 1/10 ideal and 1/10 nozzle inflow simulations.	144
6.31 Mole fractions of atomic ions and electrons along stagnation line for Stardust full scale, 1/10 ideal and 1/10 nozzle inflow simulations.	145
6.32 Mole fractions of molecular species along stagnation line for Stardust full scale, 1/10 ideal and 1/10 nozzle inflow simulations.	145
6.33 Mole fractions of molecular ions along stagnation line for Stardust full scale, 1/10 ideal and 1/10 nozzle inflow simulations.	146

6.34 Pressure over the vehicle surface for Stardust full scale, 1/10 ideal and 1/10 nozzle inflow simulations.	146
6.35 Convective heat flux over the vehicle surface from the stagnation point for Stardust full scale, 1/10 ideal and 1/10 nozzle inflow simulations.	147
7.1 Imaging the whole radiating shock layer of a vehicle during re-entry, onto a small number of pixels. Not to scale.	150
7.2 2D illustration of imaging the radiating shock layer around an aeroshell model in X2, using a spectrometer along a single line of sight, or taking a 2D image of an entire section.	151
7.3 Radiation transport and flowfield coupling calculations.	156
7.4 T_{ve} along the stagnation line at the beginning and end of the Stardust radiation-flowfield coupled calculation, with a radiation source term update every one body length of flow.	157
7.5 Calculating spectra from an <i>eilmer3</i> solution along a line of sight, or assuming constant properties in a ‘single-cell’ methodology.	159
7.6 Vertical and horizontal slices through the shock layer in front of an axisymmetric model.	161
7.7 Comparison of full scale simulated Hayabusa numerical spectra, sliced vertically, compared to the same scaled location for the vertical experimental spectra.	168
7.8 Comparison of full scale simulated Hayabusa numerical spectra in the UV, sliced vertically, compared to the same location for the vertical experimental spectra.	169
7.9 Comparison of ideal and nozzle inflow scaled simulated Hayabusa numerical spectra, sliced vertically, compared to the same location for the vertical experimental spectra.	171
7.10 Comparison of ideal and nozzle inflow scaled simulated Hayabusa numerical spectra in the UV, sliced vertically, compared to the same location for the vertical experimental spectra.	172
7.11 Plasma emissivity of Hayabusa simulated shock layers, 773 to 790 nm using <i>eilmer3</i> and <i>Photaura</i> , compared to the Abel-inverted experimental image (2D intensity mapping). Please note the differences in axes scales between each image, to account for the orders of magnitude.	173

7.12	Plasma emissivity of Stardust simulated shock layers, 773 to 790 nm using <i>eilmer3</i> and <i>Photaura</i> , compared to the Abel-inverted experimental image (2D intensity mapping with filter). Please note the differences in axes scales between each image, to account for the orders of magnitude.	175
7.13	Hayabusa IR flight spectra against CFD spectra calculated and averaged over the whole vehicle.	176
7.14	Hayabusa UV flight spectra against CFD spectra calculated and averaged over the whole vehicle. Flight data and published results using PARADE from Kraetzig, Loehle and Buttsworth [10].	177
7.15	Stardust IR flight spectra against CFD spectra calculated and averaged over the whole vehicle. Flight data and published results using DSMC and the DPLR CFD code from Boyd and Jenniskens [11].	179
A.1	Radial variation of selected flow properties at the model location and at 50 % of the test time, across three different grid spacings.	208
A.2	Comparisons of various flow parameters across three different grid spacings.	209
C.1	T_{ve} along the stagnation line at the beginning and end of the Hayabusa radiation-flowfield coupled calculation, with a radiation source term update every 1 body-length of flow.	214
C.2	Divergence of the radiative heat flux along the stagnation line at the beginning and end of the Hayabusa radiation-flowfield coupled calculation.	214
D.1	Velocity ($\text{m} \cdot \text{s}^{-1}$) of flow through entire <i>eilmer3</i> X2 simulation domain, at 100 μs before middle of test time.	216
D.2	Evolution through the X2 nozzle and test section of the magnitude of the velocity vector ($\text{m} \cdot \text{s}^{-1}$) leading up to, and including, the test time.	217
D.3	Featured flow parameters for converged full scale Hayabusa solution.	218
D.4	Featured flow parameters for converged full scale Stardust solution.	219
D.5	Hayabusa high speed video frames, shot x2s2317.	220
D.6	Stardust high speed video frames, shot x2s2817.	220

List of Tables

3.1	Nominal flight parameters for Hayabusa 13:52:20 UTC trajectory point.	38
3.2	Theoretical fill pressures and shock speeds from <i>Pitot</i>	40
3.3	Ideal scaled (where known), <i>Pitot</i> equilibrium (eq) theoretical and <i>Pitot</i> experimental equilibrium (eq) conditions at the nozzle exit.	43
3.4	Flow properties: Hayabusa condition	61
3.5	Nominal flight parameters for Stardust 9:57:26 UTC trajectory point.	62
3.6	Fill pressures and experimental shock speeds for final Stardust condition (shot x2s2701). .	63
3.7	Theoretical and ideal scaled (where known) conditions at the nozzle exit for final Stardust condition.	65
3.8	Flow properties: Stardust condition	73
4.1	Mirror and window specifications for spectroscopy systems.	81
4.2	Filter specifications for 2D intensity mapping.	82
4.3	Shock speed mean and standard deviation for each condition across the entire campaign. .	90
4.4	Most common spectrometer settings for Earth re-entry experiments.	91
4.5	Spectral and spatial resolution of experiments and flight data (where applicable). . .	91
6.1	Summary of flowfield parameters for CFD aeroshell simulations in <i>eilmer3</i>	124
7.1	Goulard numbers for Hayabusa and Stardust at two scales, calculated from preliminary <i>eilmer3</i> simulations and tangent-slab calculation along the stagnation line. . . .	154
7.2	Summary of radiation spectra and transport parameters for CFD aeroshell simulations in <i>eilmer3</i>	160
7.3	Final intensity values and ratios over selected wavelength ranges for Hayabusa CFD and flight data.	178
7.4	Final intensity values and ratios over selected wavelength ranges for Stardust full scale CFD and flight data. All values are unfiltered (no transmission function applied to replicate experimental filter).	181
7.5	Final intensity values and ratios over selected wavelength ranges for Hayabusa X2 experimental data and flight data.	182

7.6	Final intensity values and ratios over selected wavelength ranges for Stardust X2 experimental data and flight data.	183
7.7	Qualitative and quantitative summary of the comparison quality between pairs of data sets for Hayabusa.	184
7.8	Qualitative and quantitative summary of the comparison quality between pairs of data sets for Stardust.	185

Nomenclature

ϵ_w	Emissivity of the capsule wall
Γ	Goulard number
γ	Heat capacity ratio, non-dimensional
\hat{n}	Normal unit vector
κ	Absorption coefficient, m^{-1}
ν	Frequency, Hz
Ω	Solid angle, sr
ρ	Density, $\text{kg} \cdot \text{m}^{-3}$
σ	Stefan-Boltzmann constant, $5.670367 \times 10^{-8} \text{ W} \cdot \text{m}^{-2} \text{K}^{-4}$
ε	Influence of reflectivity and transmissivity from optical components and air in path
A	Area, m^2
A	Model-specific reaction parameter, Equation 6.3
a	Speed of sound, $\text{m} \cdot \text{s}^{-1}$

C_d	Coefficient of drag, non-dimensional
C_f	Coefficient of friction, non-dimensional
C_i	Integrating sphere calibration factor, $\text{W} \cdot \text{cm}^{-2} \cdot \mu\text{m}^{-1} \cdot \text{sr}^{-1}$
C_p	Heat capacity at constant pressure, $\text{J} \cdot \text{K}^{-1}$
C_t	Tungsten lamp calibration factor, $\text{W} \cdot \text{cm}^{-2} \cdot \mu\text{m}^{-1} \cdot \text{sr}^{-1}$
D_i	Binary diffusion coefficient per collision pair
d_{obs}	Distance to observer, m
E	Energy, J
E_a	Activation energy, J
$E_{cal}(\lambda)$	Lamp spectral irradiance per wavelength, $\text{W} \cdot \text{cm}^{-2} \cdot \mu\text{m}^{-1}$
f	Flight (as a subscript)
$f(r)$	Radial function (Abel inversion)
F_i	Inviscid flux vector
F_v	Viscous flux vector
F_y	Integrated value (Abel inversion)
f_{cal}	Calibration image matrix
f_{exp}	Raw experimental image matrix
g_1	Result from finest grid
g_2	Result from medium resolution grid
G_s	Grid resolution safety factor
GCI	Grid convergence index

h	Specific enthalpy, $\text{MJ} \cdot \text{kg}^{-1}$
H_t	Total (stagnation) enthalpy, $\text{MJ} \cdot \text{kg}^{-1}$
I	Spectral radiance, $\text{W} \cdot \text{m}^{-2} \cdot \text{nm}^{-1} \cdot \text{sr}^{-1}$
j	Emission coefficient, $\text{W} \cdot \text{m}^{-3} \cdot \text{nm}^{-1} \cdot \text{sr}^{-1}$
J_s	Diffusive flux per species
k_B	Boltzmann constant, $1.38064852 \times 10^{-23} \text{J} \cdot \text{K}^{-1}$
k_f	Forward reaction rate coefficient
L	Length, m
$L_{cal}(\lambda)$	Sphere spectral radiance per wavelength, $\text{W} \cdot \text{cm}^{-2} \cdot \mu\text{m}^{-1} \cdot \text{sr}^{-1}$
m	Mass, kg
n	Model-specific reaction parameter, Equation 6.3
p	Calculated order of convergence, Equation 6.2
P	Pressure, Pa
Q	Source term vector
q_{cond}	Conductive heat flux, $\text{W} \cdot \text{m}^{-2}$
q_{diff}	Diffusive heat flux, $\text{W} \cdot \text{m}^{-2}$
q_{rad}	Radiative heat flux, $\text{W} \cdot \text{m}^{-2}$
r	Theoretical order of convergence, Equation 6.2
R_n	Nose radius of capsule spherical forebody section, m
$R_{capsule}$	Radius of entire capsule forebody, m
S	Surface, m^2

<i>s</i>	Distance, m
<i>sc</i>	Scaled (as a subscript)
<i>T</i>	Temperature, K
<i>t</i>	Time, s
<i>T_w</i>	Wall temperature (of the capsule), K
<i>T_{tr}</i>	Translational-rotational temperature, K
<i>T_{ve}</i>	Vibrational-electron-electronic temperature, K
<i>U</i>	Conserved quantities vector
<i>V</i>	Volume, m ³
<i>v</i>	Velocity, m · s ⁻¹
<i>v_s</i>	Shock speed (primary = 1, secondary = 2), m · s ⁻¹
<i>v_∞</i>	Freestream velocity, m · s ⁻¹
<i>v_{eq}</i>	Flight equivalent velocity, m · s ⁻¹
1T	One temperature
at	Later acceleration tube transducer
AUS	Australian Ultraviolet Spectrometer
CEA	Chemical Equilibrium with Applications program
CFD	Computational Fluid Dynamics
DPLR	Direct Parallel Line Relaxation program
DSMC	Direct Simulation Monte Carlo
EAST	Electric Arc Shock Tube

eq	Equilibrium
ESA	European Space Agency
exp	Experiment
FWHM	Full width at half-maximum
ICCD	Intensified charge-coupled device
IR	Infrared
JAXA	Japanese Aerospace Exploration Agency
LOS	Line of sight
M	Magnification
MC	Monte-carlo
n.d.	Non-dimensional
NASA	National Aeronautics and Space Administration
NIST	National Institute of Standards and Technology
PICA	Phenolic impregnated carbon ablator
QSS	Quasi-steady state
RCC	Resistive carbon-carbon
RTE	Radiative transfer equation
sd	Shock tube transducer
sp	Species
st	Early acceleration tube transducer
TPS	Thermal protection system

UQ The University of Queensland

UTC Coordinated universal time

UV Ultraviolet

VUV Vacuum ultraviolet

Chapter 1

Introduction

1.1 Motivation

As the stars are an eternal focus of human philosophy and imagination, space exploration is the realisation of a collective dream, taking both small steps and giant leaps towards understanding the universe. Since the 1950's humankind have sent their own and myriad scientific experiments beyond the atmosphere, to orbit the Earth, step foot on the Moon, investigate the solar system and reach further into outer space. The enormous scientific and technological achievements of these missions should not be understated; they are possibly the greatest achievements of humankind, and with every new discovery comes new advancements and possibilities. The successful progression of exploratory space flight from dreams to reality would not have been achieved without the ability to return humans on board, or the results of a scientific mission, safely to Earth. The vehicles thermal protection system (TPS) is the critical component for enduring and surviving the hypervelocity conditions and aerothermal heating experienced in the radiating shock layer that surrounds the vehicle during re-entry. The majority of manned or unmanned spacecraft return missions have been successful, but incomplete knowledge of the hypervelocity radiating shock layer and TPS behaviour throughout a re-entry trajectory results in large design factors to size the TPS. The major consequence of overestimating the required TPS shape and thickness is a mass penalty that limits the available payload capacity, which results in a cost increase if an increase in payload capacity is required. Complete understanding of re-entry aerothermodynamics is required for confident prediction of shock layer and TPS behaviour, therefore re-entry data is required, but is scarcely recorded or available. Therefore, ground testing

methods are essential for attempting to reproduce the rare sets of flight data on Earth. Looking towards the future of space travel, safe and frequent missions will only be possible through enhancing our knowledge of the re-entry environment and our capabilities for optimised design and predictive analyses.

1.1.1 The Earth Re-Entry Environment

A spacecraft must withstand the harsh re-entry environment to travel from low Earth orbit or a superorbital trajectory to the surface. On a direct entry trajectory from beyond Earth orbit, the atmospheric drag slows the vehicle from over $11.2 \text{ km} \cdot \text{s}^{-1}$ to a velocity at which parachutes can be deployed. For entry from an Earth orbit, the entry velocities are in the range of 8 to $11.2 \text{ km} \cdot \text{s}^{-1}$. This trajectory is ballistic for smaller, unmanned vehicles, but the angle of attack can be controlled for larger vehicles, such as the manned Apollo capsules. Re-entry capsules have a blunt nose in order to reduce the integrated heat load to the vehicle, which depends on the ratio of the coefficient of drag, C_d , to the coefficient of friction, C_f . Blunt bodies have a high C_d and low C_f , therefore deceleration is due to the effects of static pressure, and kinetic energy is processed by compressing and heating the large mass of gas encountering the near-normal shock [12]. Conversely, a sharper, increasingly slender nose has a high C_f and low C_d , and braking through friction leaves the energy inside the boundary layer, inducing large total heating rates to the vehicle surface. Reduction of total heating rates with larger radii noses is a benefit but was not the primary issue when the sphere-cone configuration was developed [12]. The effect of radiative heating upon current superorbital missions involving small, unmanned vehicles calls for reliable TPS design capabilities.

An overview of the direct entry trajectory from beyond Earth orbit for a small unmanned capsule, and the environment encountered by the spacecraft, is presented and accompanied by the illustration in Figure 1.1. The blunt-nosed vehicle begins its descent from space to the Earth's surface, at up to $12 \text{ km} \cdot \text{s}^{-1}$. As it encounters the upper reaches of the atmosphere, the flow over the vehicle is rarified, but a bow shock envelops the windward side of the vehicle and strengthens as the flow becomes continuum. The velocity drops from up to or above $12 \text{ km} \cdot \text{s}^{-1}$ to less than $1 \text{ km} \cdot \text{s}^{-1}$, and the mass flux entrained in the boundary layer is nearly zero at the stagnation point. Such a strong shock has

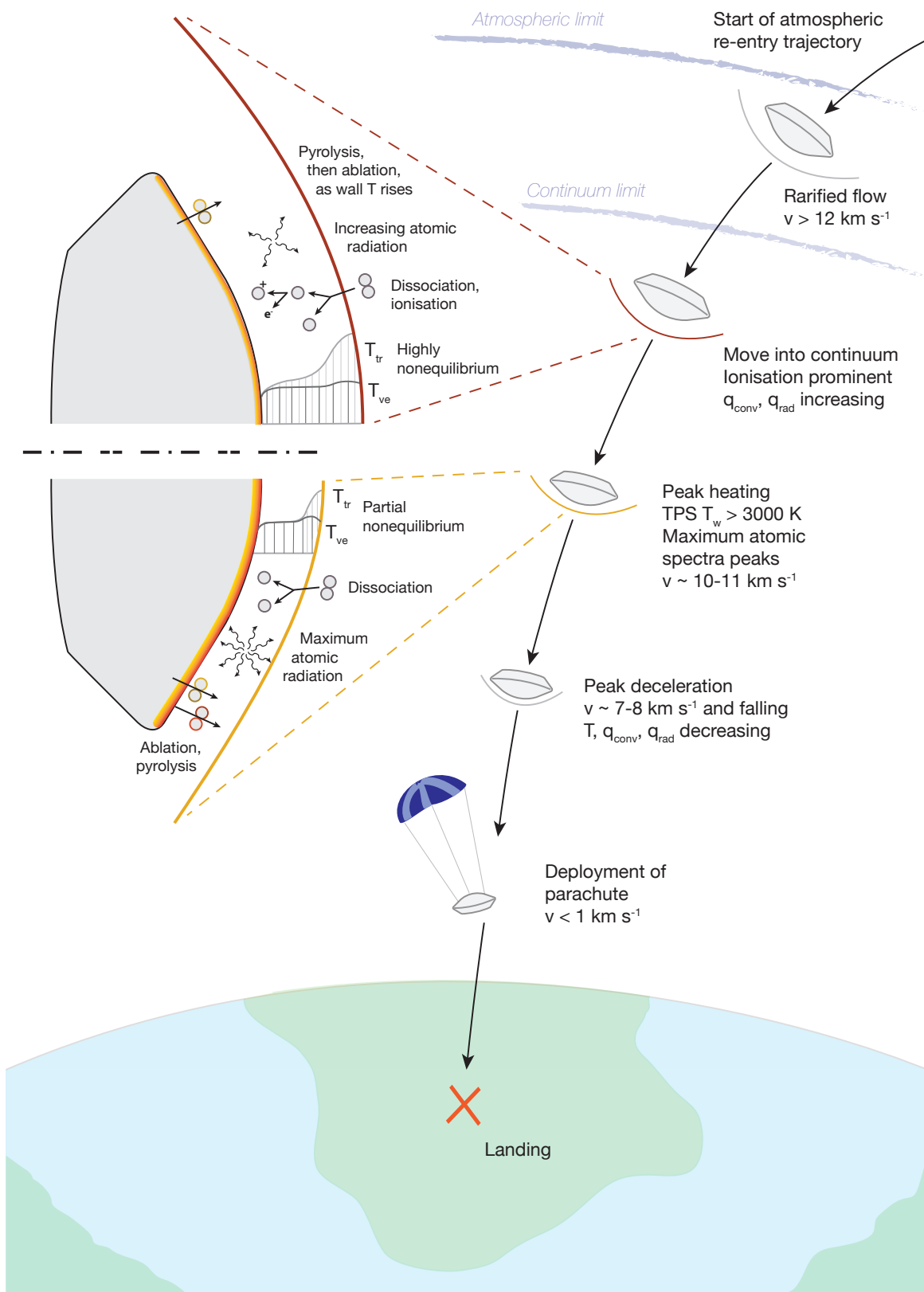


Figure 1.1: Superorbital re-entry of a small, unmanned, Hayabusa-like capsule through the Earth's atmosphere: an overview.

extreme and complex effects on the air passing into the shock layer. There is a large increase in translational energy as the freestream gas encounters the shock, and collisions between particles in the shock layer increase rotational, vibrational and electron-electronic energies [13]. The energy change is reflected in the temperatures, which will stratify according to the energy modes that are excited. Higher in the trajectory, there are not enough collisions and reactions for the processes to relax to equilibrium. The large increase in temperature at the shock front forces dissociation of N₂ and O₂ molecules in the air to atomic N and O, excitation of vibrational and electronic states, as well as ionisation of atoms and molecules. The flow is in chemical nonequilibrium when the forward reaction rates are favoured, and this occurs more commonly at higher velocities. Molecular ions generally form soon after the nonequilibrium shock front but recombine with electrons when the shock layer temperature is low enough. Thermochemical nonequilibrium introduces the need for kinetic modelling of different energy modes, and a method to evaluate electronic level populations and the radiation due to changes in these populations [13]. It is extremely important to understand as part of the re-entry problem but is costly to model comprehensively. Currently, a fair approach to modelling thermochemical nonequilibrium consists of describing the thermodynamic state of the entry plasma by two temperatures, which will be specified later.

Particle collisions and vibrations increase due to density increase throughout the entry, and as a consequence of these excitation processes, excited energy levels contribute to increasing radiative processes. Photons are emitted during spontaneous decay to lower energy levels or a ground state, which are absorbed by the TPS, and the electromagnetic energy is converted to heat [14]. Radiative heating is proportional to the characteristic length of the vehicle for an optically thin medium, so by increasing R_n in an attempt to decrease the convective heat flux, the radiative heat flux will increase. There must be a balance between the two criteria in larger vehicles where radiative heat flux can be a major contributor to the total heat flux. In smaller vehicles, the nose radius is sufficiently small that convective heating is much more prevalent than radiative heat flux.

As the small capsule moves towards peak heating, the TPS temperature may rise to over 3000 K and the radiative emissions increase to a maximum. The shock layer is well defined by a sharper temperature rise and a smaller shock stand-off distance, and thermochemical processes move towards

equilibrium perpendicular to, and ever closer to, the shock. Dissociation reactions produce atomic N and O, which are the dominant species around peak heating as the energy is no longer high enough to sustain a large population of ions in the plasma. The TPS is typically a medium to low density carbon fibre composite with a phenolic resin, which can decompose due to the incoming heat flux and react with the air in the boundary layer. The two main TPS degradation processes are ablation, where surface reactions take place between air and charred fibre species, and pyrolysis, where the matrix phase gasifies and enters the boundary layer. A more dense boundary layer, especially including TPS species, assists in absorbing incoming radiation and cooling the vehicle surface, although some resultant species, like CN, can radiate strongly and return some energy to the TPS.

Moving on from peak heating, the vehicle continues to slow its velocity and reaches a peak deceleration point. By this stage, most of the shock layer is in local thermochemical equilibrium, the shock layer temperatures are lower, and the TPS temperature is lower than around peak heating. The material has continued to release species into the flowfield and recession has occurred. At a sufficiently low speed (less than $1 \text{ km} \cdot \text{s}^{-1}$), parachutes can be deployed to bring the capsule safely to the ground. It is important to have a smooth landing for the safety of the payload.

There are many extreme thermal, chemical and radiative processes that occur in the shock layer, and that involve the TPS, during the hypervelocity phase of re-entry. The complex interactions between all of these processes are beginning to be understood through collection and analysis of flight data. Every new aerothermodynamic data set gives a new opportunity to expand the current knowledge regarding hypervelocity re-entry, but there is still much to improve upon before our understanding is complete.

1.1.2 From Flight Data to Ground Testing

Re-entry flight measurements are imperative for a proper understanding of the conditions a vehicle and its TPS is subjected to. However, taking such measurements is difficult because there are few flights, aerothermodynamic instrumentation is not usually included in the TPS due to size and weight restrictions, and observations are challenging to carry out successfully. Therefore, there is

an obvious need to be able to perform re-entry testing on the ground, and not only for post-flight analysis, but also for pre-flight design optimisation and trajectory predictions. Experimental ground testing facilities are able to focus on particular parts of the re-entry problem, from shock layer relaxation to high enthalpy TPS testing. Expansion tubes are an impulse facility that can recreate the aerothermodynamics of the hypervelocity shock layer over a scaled model for a very short duration. This allows measurement of the radiating shock layer using spectroscopy, 2D intensity mapping, high-speed imaging, and surface gauges such as thermocouples and thin film heat transfer gauges. X2, the smaller expansion tube at The University of Queensland, is able to simulate scaled, flight equivalent Earth re-entry flows over appropriately scaled aeroshell models. Compressible flow computational fluid dynamics enables numerical simulations of particular trajectory points in flight, the transient flow through the expansion tube and the flow over the model. The thermochemistry can be modelled in detail, and numerical spectra can be generated through radiation transport and spectra modelling to compare to flight and experiment. Numerical data can be validated and methods improved using the results of expansion tube measurements, but more importantly, flight data can be used to compare against both methods. Considering these experimental and numerical data sets are able to closely replicate flight data, they can be implemented and developed using flight data to accurately simulate re-entry conditions on Earth for a range of vehicles and trajectory points.

There are two published examples of successful capsule re-entries and observation missions that recorded aerothermodynamic flight data, in the form of shock layer spectral intensity. Those two unmanned spacecraft are Stardust, NASA's explorer of comet dust, and Hayabusa, JAXA's asteroid sample return mission. This project is the first work of its kind to directly compare spectra from those two re-entry flights with spectra obtained in expansion tube tests and computational fluid dynamics (CFD) simulations at matched conditions, in order to demonstrate the validity of both ground-based methods in recreating a flight environment. A greater understanding and ability to demonstrate the behaviour of re-entry vehicles will allow increased confidence in pre-flight laboratory predictions, design iterations based on testing and simulation, and an overall reduction in the TPS mass, therefore increasing the mass available for scientific payload.

1.2 Aim

The main aim of the project is to determine the reproducibility on ground of plasma (re-)entry radiative signatures, through a three point comparison between flight, experimental and numerical data. Flight data were recorded during the Hayabusa and Stardust re-entries, experimental data were produced in scaled, flight equivalent experiments in the X2 expansion tube, and numerical spectra were generated from CFD simulations and radiation modelling of flight and laboratory tests with the in-house compressible flow CFD code, *eilmr3*. The significance of flight spectra replication in the laboratory is in validation and verification of experimental and numerical methods, increasing confidence in pre-flight predictions and post-flight analyses of re-entry shock layer aerothermodynamics. Conversely, differences in results can assist in identifying the areas in which further development or refinement is needed.

1.3 Objectives

The aim was achieved by the realisation of several objectives, as listed below.

- Review of Hayabusa and Stardust flight data in the ultraviolet (UV) and near infrared (IR) spectral regions.
- Selection of a trajectory point from each of the Hayabusa and Stardust re-entries for flight simulations and development of expansion tube test conditions.
- X2 condition development (two conditions) with pitot code, CFD simulations and pitot tube measurements.
- Development, set-up, alignment, calibration and operation of optical imaging systems for expansion tube campaigns.
- X2 testing of scaled Hayabusa model at equivalent flight conditions with IR and UV emission spectroscopy, 2D intensity mapping and high-speed imaging.
- X2 testing of scaled Stardust model at equivalent flight conditions with IR emission spectroscopy and 2D intensity mapping and high-speed imaging.

- Development of features in radiation module; for example, the line of sight calculation of intensity.
- CFD simulations and analysis of expansion tunnel experiments, including radiation analysis and calculation of numerical spectra.
- CFD simulations and analysis of true flight vehicle, including radiation analysis and calculation of numerical spectra, and a first attempt at a gas-surface interaction boundary condition.
- Full comparison between spectra obtained from flight data, expansion tube experimental data and numerical data, including development of methodology for experimental and numerical flight rebuilding.

1.4 Scope

The project was restricted to comparisons concerning the Hayabusa flight data, as this data is readily available from the UQ observation teams and available in publications including Buttsworth *et al.* [5] and McIntyre *et al.* [4], and the Stardust flight data published by Jenniskens [15]. One trajectory point was selected for each vehicle as the basis for experimental and numerical comparisons so that attention can be focused on obtaining good quality data to make the best possible comparisons. Experimental models were initially at room temperature since development of heated resistive carbon-carbon (RCC) aeroshell models beyond proof-of-concept tests could not be conducted while achieving the other objectives. Development of features in the radiation module, for example the line-of-sight intensity calculations, was constrained by the requirements of the author to build simulations that sufficiently represent flight and experimental tests, as well as available time and resources.

1.5 Thesis Outline

Chapter 2 presents a review of the Hayabusa and Stardust flight data in the UV and IR spectral regions, as well as other mission details and re-entry data. The literature review also focuses on the X2 expansion tube facility and relevant past experimental campaigns, modelling hypervelocity flows

and radiating shock layers with compressible flow CFD program *eilmer3*, and relevant published CFD and radiation simulations, especially involving Hayabusa and Stardust.

Chapter 3 discusses the selection of a trajectory point from each of the Hayabusa and Stardust re-entries for flight simulations and development of expansion tube test conditions. Establishment of two conditions through an iterative analytical, experimental and numerical process is demonstrated, and the final parameters resulting from each method are displayed and discussed. Simulations of transient flow through the X2 facility, using a combination of the one-dimensional tool *L1d3* and a two-dimensional axisymmetric *eilmer3* calculation, are presented as part of the condition development.

Chapter 4 provides an overview of the experimental design, set-up and methodology, covering model specifications, IR and UV emission spectroscopy, 2D intensity mapping, calibration and background removal, high-speed imaging, and operation of the facility and optical systems to yield experimental results.

Chapter 5 presents the results from testing scaled Hayabusa and Stardust models at equivalent flight conditions in the X2 expansion tube. The results and discussion include IR spectra at varying locations and centre wavelengths, 2D intensity mapping through five narrow band filters in the IR, comparisons of integrated spectra and 2D intensity mapping measurements, and UV spectra (Hayabusa only).

Chapter 6 details the selections for, and results from, 2D axisymmetric simulations of the hypervelocity radiating shock layer using *eilmer3*. The simulations were performed for full scale Hayabusa and Stardust vehicles at the selected flight trajectory points, and scaled Hayabusa and Stardust aeroshell models at ideal scaled conditions, and with inflow conditions from *Chapter 3*'s facility simulations.

Chapter 7 brings together the experimental results from *Chapter 5* and the numerical results from *Chapter 6* for rebuilding of the flight data. After radiation analysis of the CFD results and calculation of numerical spectra, three comparisons are presented: experiment to flight, CFD to experiment, and CFD to flight.

The aim, objectives and major findings are addressed in *Chapter 8*'s conclusions and ideas for future work are given.

Chapter 2

From Re-entry to Experimental and Numerical Ground Testing: A Review

The aim of the thesis centres upon a comparison between three data sets: flight, experimental and numerical, therefore the review of previous works will be focused around each data set. The flight data will come from the Hayabusa and Stardust re-entries, which are the only superorbital re-entries with successful aerothermodynamic observation missions, and the significance of these measurements is shown by the few aeroshell re-entry missions that have taken place, and fewer that yielded aerothermodynamic data. A summary of the mission findings will identify the most useful data for the proposed experimental and numerical comparisons, which then influence the requirements and outcomes of ground testing. Experiments will be performed in the X2 facility, which has been developed from a concept stage and through several iterations and upgrades to its current expansion tube capabilities. A review of relevant past experimental campaigns will discuss experimental design and data acquisition methods, and highlight possible choices for performing and observing Hayabusa and Stardust experiments that can replicate re-entry. The complexities in simulating hypervelocity flow, including thermochemistry and radiation modelling, are presented but not detailed, as the main points to draw from published results relate specifically to Hayabusa and Stardust aeroshell simulations, and facility simulations involving X2. Comparisons can be made to the present simulations, to assess performance and potential areas for improvement, and inform modelling choices. The discussions centering on each data set will remain narrow, as the aim itself is narrow, and the most important features will be described in greater detail in upcoming chapters.

2.1 There and back again: A brief history of Earth re-entry

2.1.1 Early re-entry missions

Voyaging from our planet Earth into orbit and outer space remains the pinnacle of exploration; a journey that represents humankind's best efforts to understand the universe and ourselves, whilst demonstrating our scientific and technological advancements. Many unmanned missions have been sent to orbit, have traversed the atmosphere or landed on the surface of celestial bodies, and a handful are travelling beyond the reaches of the solar system with no expectation of return. Many missions carrying human or scientific payload into space are designed to venture out and return to Earth, and re-entry through the Earth's atmosphere is one of the most crucial and challenging segments of the mission.

Human spaceflight began in 1959 with Yuri Gagarin's famous flight onboard the Russian Soyuz rocket. The capsule returned safely to Earth, successfully using the atmosphere as a braking mechanism on a ballistic trajectory until reaching an altitude and speed at which parachutes could be deployed. NASA (the National Aeronautics and Space Administration of the USA) followed soon after with their Gemini and Apollo programs, culminating in six moon landings between 1969 and 1972. Aerothermodynamic data was required to increase understanding of re-entry forebody heating, especially radiative heating, and test heat shield designs and TPS materials. The first vehicles to successfully record aerothermodynamic data during re-entry were Fire II, in 1965, and Apollo 4, in 1967 [16]. Fire II was a scaled-down version of the Apollo capsules, and had calorimeters and radiometers embedded in the three-layer beryllium heat shield to measure total and radiative heat transfer, respectively [17]. Apollo 4 had a single ablating heat shield and successfully recorded radiative heat transfer measurements at the stagnation point throughout the re-entry [18]. These two cases are considered pioneering in aerothermodynamic ground testing efforts due to the lack of instrumented flight vehicles, though the heat transfer data has been notoriously difficult to reproduce in CFD or numerical methods [19] and experiment [17].

The space shuttle, NASA's primary vehicle from 1981 to 2011, was designed for short, low Earth

orbit missions and its re-entry trajectory was based on a gliding entry unlike the ballistic entry of the Apollo-era capsules. The entry speeds were much slower and the shock layer exhibited different characteristics, such as a large separation region on the leeward side [20]. The performance of the TPS, a combination of reinforced carbon-carbon and reusable surface insulation, was gauged by thermocouples at ranging depths and radiometers [21] and could be used for scaled comparisons in the T4 shock tube [20], but not for capsule re-entry flight or ground testing comparisons.

2.1.2 Genesis re-entry observation mission

Remote observations of capsule re-entries came to prominence with an attempt to observe the NASA Genesis spacecraft, as this and ensuing unmanned capsules were not equipped with instrumentation to measure aerothermodynamics. Genesis re-entered the atmosphere over the USA on September 8, 2004 after its mission to observe the Sun and collect solar wind ions, and was the first hypervelocity re-entry from beyond low-Earth orbit since Apollo 17 in 1972 [2]. The airborne observation campaign was based upon an earlier campaign targeting meteor showers, and although spectroscopy was attempted, the trajectory track was miscalculated and the scopes were unable to capture the vehicle [2]. It was doubtful that slitless spectroscopy data could be recorded, however, as the re-entry occurred during the day and the capsule may not have been clearly observable in daylight. Photometry was captured from the aircraft as well as from a ground observation station, enabling estimation of surface temperature [2] [22] and comparison to pre-flight predictions.

Spectroscopy was attempted during the Genesis observation mission as it can provide temporal measurements of the species present in the hypervelocity radiating shock layer, either from high-temperature reacting air or ablative products. Calibrated intensities show how strongly a species is radiating, indicating number densities per species for absolute calibration, and temperatures for absolute and relative calibration. The surface temperature of the heat shield can also be estimated by examining the grey-body thermal radiation. Currently, there are two extremely valuable sets of spectroscopic re-entry observation data for two small capsules, Stardust and Hayabusa, that can be investigated for comparison to experimental and numerical ground testing. The combination of a spectroscopic observation campaign with on-board equipment, such as heat

flux gauges or thermocouples, would be ideal for ground comparisons but this falls to future missions.

2.1.3 Stardust re-entry observation mission

The lessons learned from the 2004 Genesis mission were applied to the Stardust re-entry observation mission, which successfully yielded spectroscopic measurements of the fastest atmospheric re-entry. Until this point, only early radiative heat transfer measurements from the heat shield surfaces had provided any flight testing insight into re-entry aerothermodynamics. Stardust was launched on February 7, 1999, journeyed to the comet Wild 2 and collected samples of dust and debris as it traversed its coma, passing as close as 240 km from the icy core [1]. Stardust re-entered the atmosphere on January 15, 2006, descending through various flow regimes until parachute deployment and landing as shown in Figure 2.1. American, Japanese and German teams onboard the NASA DC-8 aircraft collected optical data from 11 experiments, including the ECHELLE spectrograph, that recorded from the ultraviolet (UV) to infrared (IR), the NIRSPEC near-IR spectrometer [23] and the SLIT UV spectrometer [24]. The ECHELLE data was the most useful for this work as it extended into the IR, overlapping with the target wavelength regions of the X2 experiments. NIRSPEC operated between 930 and 1100 nm, wavelengths that are too high to measure with the X2 spectroscopy equipment. The spectrograph setup and calibration procedure is detailed by Jenniskens [2], and 100 frames were recorded between 9:57:15 UTC and 9:57:26 UTC over a wavelength range of 336 nm to 880 nm. The first frames captured the spacecraft at approximately 82 km altitude and its extremely high entry velocity of $12.8 \text{ km} \cdot \text{s}^{-1}$, which is on the edge of the non-continuum regime [25]. Stardust was at approximately 69 km altitude and travelling at $12.2 \text{ km} \cdot \text{s}^{-1}$ when the last spectra were recorded; in comparison, peak heating occurred at 9:57:33 UTC once the vehicle had slowed to about $10.8 \text{ km} \cdot \text{s}^{-1}$, at an altitude of 62 km [25].

The growth of a variety of spectral features is evident in the Stardust flight spectra in Figure 2.2. As the shock layer develops around the vehicle forebody, a paint layer containing Ca^+ , Zn , Na and K ablates away, before air shock layer and conventional ablative species become prominent. The atomic oxygen lines grow exponentially with decreasing altitude [2], and several typical atomic nitrogen features grow nearby in the IR region. Spectral features created by atomic species emission in the

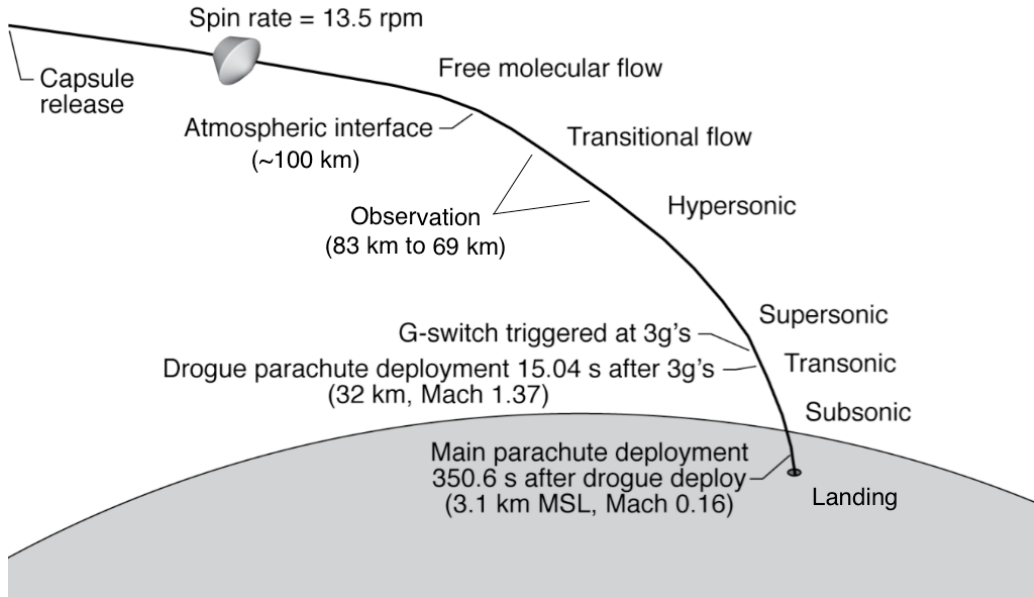


Figure 2.1: Stardust entry trajectory schematic with extra annotations from Desai and Qualls [1]. MSL = mean sea level.

IR are especially useful for examining in the expansion tube, as they are strong signatures of the air shock layer. Radiation modelling of atomic species is the best understood and therefore the most straightforward to simulate. A small amount of CN develops from the ablating phenolic-impregnated carbon ablator (PICA) TPS, and the visible H line is most likely from pyrolysis of the PICA resin, but heat shield species are more difficult to include in ground testing. Key findings of post-flight CFD analysis and radiation modelling for Stardust will be discussed further in Section 2.3.2.

2.1.4 Hayabusa re-entry observation mission

Another small unmanned capsule had ventured into the solar system before Stardust's successful return, and became the perfect candidate for the next observation mission. Hayabusa was launched as the MUSES-C mission on May 9, 2003 and was the third engineering space mission by the Japanese Aerospace Exploration Agency (JAXA) and the Institute of Space and Aeronautical Sciences (ISAS) [26]. Hayabusa, a small vehicle with a nose radius of 200 mm and weight of 16.5 kg, designed

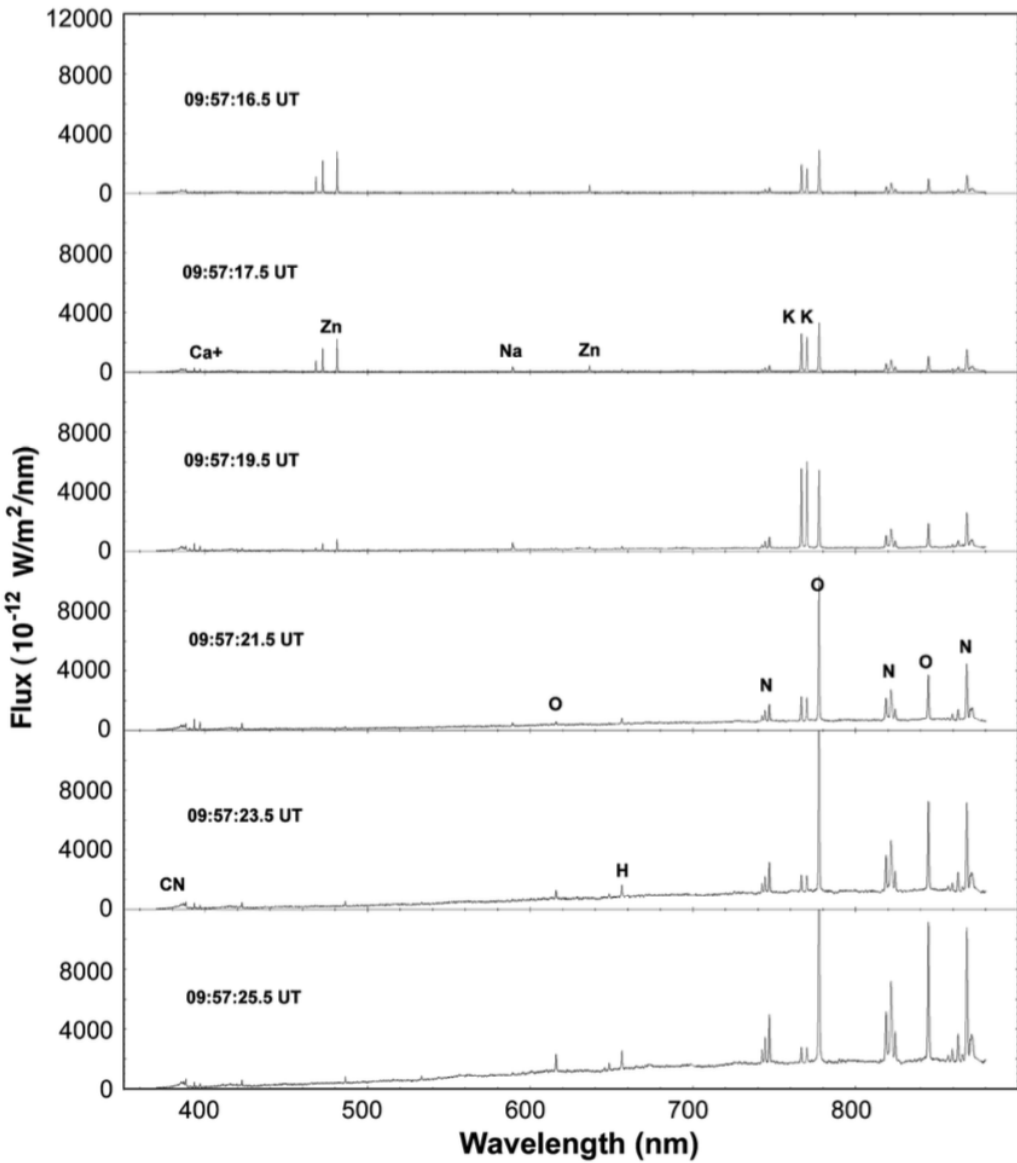


Figure 2.2: Stardust flight spectra from the ECHELLE spectrograph, as reported by Jenniskens [2].

the TPS carefully for the extreme entry conditions and to integrate with the structure [27]. The mission was the first sample return mission to visit an asteroid (25143 Itokawa), return dust samples to Earth for analysis [28], and record high-resolution spectra of the asteroid [29]. Contact with the vehicle was lost after landing on the asteroid in late 2005 and the mission appeared failed until the vehicle re-established contact in early 2007, commencing its return to Earth [26]. The near-ballistic re-entry and landing took place at Woomera, Australia on June 13, 2010, providing a unique opportunity for observation teams to record time-resolved measurements of the radiating shock layer, the capsule surface and the wake including the spacecraft bus, all captured in Figure 2.3.

Through these measurements, the observation teams characterised the re-entry aerothermodynamic environment for the Hayabusa trajectory [30]. The spacecraft was not equipped with any sensors for aerothermodynamic measurements, but the data gathered by ground-based and airborne observation teams continues to reveal information about the conditions experienced by the vehicle upon re-entry. The data includes velocity and trajectory calculations correct to within $\pm 100 \text{ m} \cdot \text{s}^{-1}$ and a few hundred metres, respectively [31], total flux measurements across varying wavelength ranges [32], surface temperature measurements [33] [34] and spectra in the UV [5] [26] [35], visible [26] and different sections of the near infrared, to focus on atomic N and O between 700 and 900 nm [4] [35], and atomic N and C between 980 and 1080 nm [36].



Figure 2.3: The Hayabusa capsule (lower right) successfully re-entering the Earth’s atmosphere as the bus breaks up [3].

The ground-based observation data taken by a team from The University of Queensland was the most important for the current work. Near infrared spectra of the Hayabusa radiating shock layer was recorded using tracking cameras attached to a spectrometer with a 300 lines/mm grating to image between 500 and 900 nm [37]. The 15 s of calibrated spectra reported by McIntyre *et al.* charts the temporal evolution of spectral radiance around peak heating [4], and ten of those seconds are illustrated in Figure 2.4. The 500 and 700 nm region showed no significant emissions and was left out of the calibrated spectra. The main features in the spectra are all air species that are prevalent following

the dissociation of molecular nitrogen and oxygen: two atomic oxygen triplets, at 777 nm and 844 nm, and three groups of atomic nitrogen lines in regions near 740 nm, 820 nm and 870 nm. All features increase to peak heating at the 13:52:19 UTC trajectory point, before gradually diminishing. The spectra have been corrected for atmospheric absorption and the blackbody radiation emanating from the capsule has been removed assuming a temperature that peaks at 3100 K. The blackbody radiation is observed in combination with the shock layer radiation as each image included the whole capsule. Thus, separating the blackbody component is useful for experimental and numerical comparisons that would not include those effects. Winter *et al.* provides IR spectra in the same wavelength region from the NASA IRIS (Intermediate Resolution Infrared Spectrograph) instrument as spectral irradiance at selected trajectory points [35]. The data for the two atomic O triplets and the N line at approximately 745 nm were integrated over the line width to illustrate the temporal change in intensity from each line in $\text{W} \cdot \text{cm}^{-2}$. Loehle, Mezger and Fulge also gave a frame of IR spectra at a single trajectory point from the S2000 spectrometer and camera, which was ground-based [34]. The spectral irradiance plotted from 300 to 800 nm has a blackbody curve fitted at 3200 K, slightly higher than the value fitted by McIntyre *et al.* but within the quoted error of ± 100 K [4]. Access to the UQ data makes it the primary source for comparison to experimental and numerical results obtained in this work, and can be complemented by other published data.

A main focus of airborne spectroscopic measurements was the UV part of the spectrum nearing the visible in order to observe CN, a molecule that forms from the ablating and pyrolysing heat shield reacting with dissociating air and radiates profusely. A joint University of Southern Queensland (USQ)-UQ team onboard the NASA DC-8 airborne laboratory used the AUS (Australian Ultraviolet Spectrometer) instrument to image between 330 and 470 nm [5], and analogous to the IR data, this is the primary source involved in the present work. Buttsworth, Morgan and Jenniskens report the temporal evolution of the calibrated spectral irradiance data over the entire recording time, with frames separated by 0.3 to 0.4 s. An example frame from one second after peak heating is shown in Figure 2.5. The images show a CN band, culminating in a peak at 389 nm, mixed with two N_2^+ bands that cover 365 to 392 nm and 345 to 365 nm [5]. This overlap makes it difficult to distinguish the effects from each species, apart from the N_2^+ bandhead at 391 nm, which stands clear of other bands. Noise across the flight spectra further complicates analyses. N_2^+ will be the easier species to measure in ground

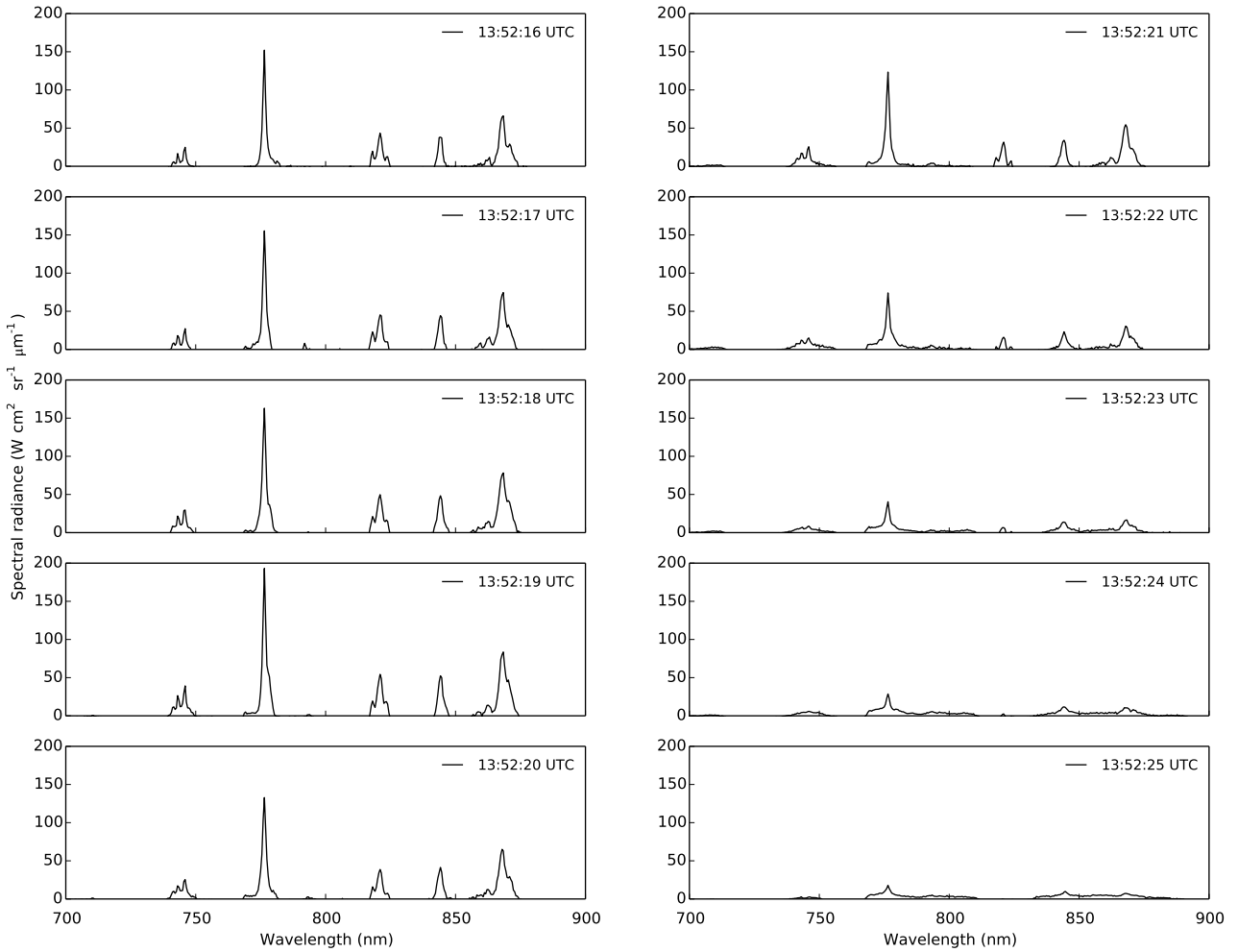


Figure 2.4: Hayabusa IR flight spectra from a ground observation station for the seconds before and after peak heating (13:52:19 UTC). Adapted from data published by McIntyre *et al.* [4].

testing as it is produced in the nonequilibrium part of the air shock layer, rather than requiring surface reactions. The wavelength-integrated intensity was also calculated over two bands and across the trajectory. The apparent temperature of the capsule surface was calculated by fitting blackbody curves to each spectra, and peaks at about 3050 K for an assumed surface emissivity of 0.9, which is similar to results obtained from the ground. The HDVS1 instrument, operating from 410 to 470 nm, shows comparable results to AUS in terms of spectral irradiance and surface temperature. Winter *et al.* also report the AUS data and discusses the HDVS1 data [35], and Loehle, Mezger and Fulge's spectra extends into the UV to overlap with AUS, but the spectra are too noisy below 400 nm to provide any useful information [34]. The spectra from Abe *et al.* that overlapped with AUS was uncalibrated at the time of publication, and the visible spectra are not useful for the present work as it focuses on

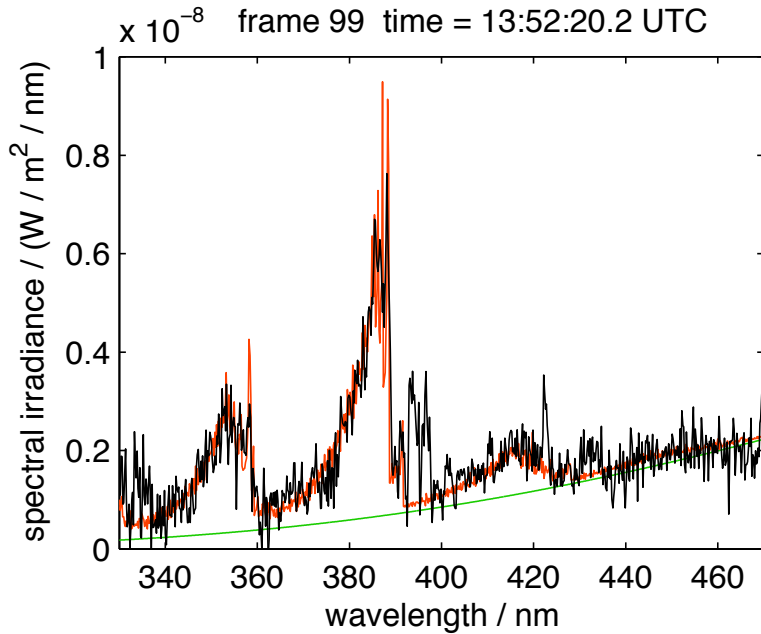


Figure 2.5: Hayabusa flight spectra from the airborne AUS instrument, as reported by Buttsworth, Morgan and Jenniskens [5].

metallic species that come from paint or the spacecraft bus [26]. Higher altitude UV spectra (above 63 km) was predicted numerically to have less CN than N_2^+ in the region between 380 and 400 nm, and an overarching peak from Fe and Al [26]. Buttsworth, Morgan and Jenniskens' data suggests that this will change leading up to and following peak heating, where CN will become dominant and the metallic lines will not feature.

2.1.5 Summary

The scarcity of aerothermodynamic flight data, as evidenced by this synopsis of the data from Earth re-entry missions, raises its value for verifying ground-based simulation capabilities, both experimental and numerical. As the most interesting Hayabusa and Stardust flight observations are in the form of spectra, the comparative data from ground testing must be in the form of spectra or radiance, integrated over a certain wavelength band. The strong, easily identifiable atomic lines in the IR flight spectra are created by air shock layer species, and are therefore the most promising for reproduction in an expansion tube and numerical simulations. The Hayabusa UV flight data can also be used, but the focus would most likely be on N_2^+ as a species that can be produced only from air.

Unlocking the spectra from wavelength dependence, as performed for flight data by Winter *et al.* [35] and Buttsworth, Morgan and Jenniskens [5], introduces potential for more imaging techniques beyond spectroscopy.

As outlined in Chapter 1's Aim and Objectives, ground testing was proposed for the present work and will constitute experimental and numerical analysis. There is a need for post-testing of Hayabusa and Stardust in the unique facility that is the X2 expansion tube, as well as CFD to compare to both flight and experimental data, in order to understand the current capabilities of all methods and identify where the data do not match. The facilities and tools for achieving the experimental and numerical objectives are thus described in the following sections, focusing on findings from relevant previous studies.

2.2 Experiments in the X2 free-piston driven expansion tube

2.2.1 Evolution of the X2 facility

The X2 free piston driven expansion tube is The University of Queensland's primary impulse facility for atmospheric re-entry research, and can produce a hypervelocity shock layer over a model at representative re-entry conditions. James *et al.* present a succinct definition for the need to use expansion tubes to simulate atmospheric re-entry flows: expansion tubes add part of the overall required energy to the test flow through shock waves, and the rest by unsteady expansion [38]. Axial progression of isobaric contours in supersonic flow greatly increase total enthalpy and pressure from a cascade of energy downstream. The negative effects of energy addition in a non-reflected shock tube are reduced as the static temperature never stagnates to its total temperature. However, not all of the test gas can be processed by unsteady expansion, as it relies on moving energy from upstream gas, and the test times are thus significantly reduced [12]. In X2, test times for Earth re-entry are on the order of 100 µs, but this is enough time to accurately construct the aerothermodynamics in the shock layer, maintain it in a quasi-steady state and measure consequent radiative emissions with spectroscopy, intensity mapping and high-speed video.

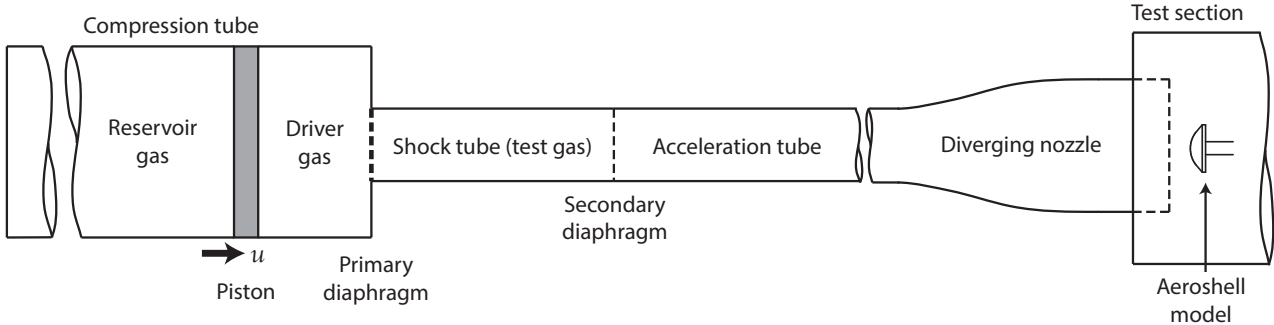


Figure 2.6: Schematic of the X2 expansion tube and its constituent sections for a typical Earth re-entry experiment (not to scale). Adapted from Gildfind [6].

X2 is illustrated in its configuration for the scaled Earth re-entry experiments in Figure 2.6. In brief, the production of a quasi-steady shock layer over scaled Hayabusa and Stardust models in the test section is enabled by the propagation of a series of shocks and expansions through the various tube sections, starting from the reservoir. When the lightweight, tuned piston is released from the launcher, 6.85 MPa of compressed air propels the piston along the driver tube, compressing the driver gas ahead of it. A tuned reservoir and piston configuration also means a defined 100 % He driver gas pressure of 92.8 kPa, and the use of a certain orifice plate, through which the compressed driver gas is forced before bursting the primary diaphragm. The burst creates the primary shock wave that then compresses the air test gas in the shock tube and bursts the thin secondary diaphragm. The faster secondary shock wave is created and accelerates the test gas as it expands into the low pressure acceleration tube air through an unsteady expansion, which increases velocity, and total pressure and temperature. The shock-processed test gas undergoes an unsteady expansion as it passes through the diverging nozzle, marginally increasing the velocity, conserving the total enthalpy and pressure, and increasing the core flow diameter. A bow shock is created when the test gas interface encounters the scaled aeroshell model, steadies with the passing of the test gas, and becomes unsteady with noise propagating from the interface between the driver gas and test gas. Optical measurements are taken when the bow shock is quasi-steady, at flow conditions specified by flight scaling and matching, and the unique combination of fill pressures in each section.

The realisation of X2 as a unique, world-class facility has progressed through many stages, and this is

well-documented by current and past members of the Centre for Hypersonics, which the readers are encouraged to view (including [39], [6], [40], [41]). From a theoretical concept by Resler and Bloxom [42], early performance predictions by Trimpi [43] and discouraging test results from facilities including the NASA Langley expansion tube (see [44], for example), Stalker combined his free-piston driver with the expansion tube idea to create X1 at The University of Queensland [45]. Promising tests and discoveries about the small X1 tube's operation led to the construction of X2 and its larger sibling X3, measuring approximately 25 m and 65 m, respectively [46]. X2 was commissioned in 1995 [39], and has undergone several significant changes to reach its current format. It moved from a compound two-stage free piston driver [47] to a lightweight single free piston driver [48] [6], and the ability to change the driver conditions using different gases and orifice plates was added. A diverging nozzle was introduced between the acceleration tube and the test section to develop a test flow capable of creating bow shocks in front of scaled models [49]. Diaphragms have developed to be 2 mm steel as the primary diaphragm and thin aluminium foil as the secondary for most (re-)entry flow conditions, including the two conditions in this work. Optical imaging techniques have greatly evolved to enable spectroscopy of radiating shock layers from the vacuum ultraviolet (VUV) [50] and UV [33] to the IR, high-speed video imaging at up to one million frames per second [51], intensity mapping of the flowfield through narrow band filters [52], and pyrometry [53]. X2 is able to simulate (re-)entry for Earth [54], Mars [33], Venus [55], Titan [56] and gas giant atmospheres [38] in expansion tube mode or non-reflected shock tube mode (straight acceleration tube into test section, no nozzle, no model) [57] as well as high-pressure scramjet conditions (straight acceleration tube into test section, no nozzle) [6] [58].

2.2.2 X2 condition design

To achieve this diverse range of planetary entry and scramjet conditions, and the specific focus of each experimental campaign, defined operating conditions are required. Conditions are developed through an iterative series of analytical, experimental and numerical processes of varying detail, based on target test section flow parameters. James *et al.* have developed and used the analytical tool *Pitot* to design and analyse a range of X2 conditions [38], as it provides the first step for generating nominal fill pressures from target flow parameters, and provides analysis of the test section flow

parameters with experimentally measured shock speeds. Experimental condition testing is a major step for all X2 campaigns, and measurements of pressure over conehead probes in the test section, as well as shock speeds in the shock and acceleration tubes, can be obtained (examples for air condition testing include [54] [59] [52]). Numerical simulations of the X2 facility add to the prediction of test section conditions and provide a comparison for the analytical and experimental methods. Facility simulations have generally been performed using a combination of 1D solver *L1d3* to model piston movement, diaphragm burst and primary shock processes, and the compressible flow CFD program *eilmer3* to model the more complex expanding flow through the acceleration tube, nozzle and test section [6] [57]. However, the complexity of transient, hypervelocity flows in expansion tubes has made it difficult to produce results that are directly comparable to experimental data [6]. As part of the research into obtaining experimental data, the analytical, experimental and numerical processes will be attempted in order to obtain as much information about the predicted flow conditions as possible, and provide more data for improving facility simulations.

Conditions can be designed with a target velocity in mind, to approximately replicate a point on an entry trajectory without any particular vehicle or mission constraints. This is useful for studying spectral profiles or heat fluxes for possible trajectories, especially for planetary or lunar atmospheres other than Earth where flight observations are not possible and few, if any, missions have been completed. Recreating known trajectory points of two particular vehicles requires scaling of the models, due to constraints from the X2 nozzle exit diameter, and appropriate scaling of the flow to maintain representative flight conditions. Binary scaling maintains the product of freestream density and length for hypersonic blunt body flows, such as flows around aeroshells, by maintaining the relaxation distance, two-body reactions and therefore mass fractions along a stagnation line, and Reynolds number [60]. The desired experimental freestream density of the flow exiting the nozzle can be calculated via Equation 2.1, using the selected trajectory point density, and the flight and experimental scale nose radii as the characteristic length.

$$[\rho L]_{flight} = [\rho L]_{experiment} \quad (2.1)$$

As binary scaling applies to two-body reactions, which are mostly dissociation reactions, the trajectory point and scaled condition must have a sufficiently large thermochemical nonequilibrium region that three-body reactions, such as recombination reactions, do not dominate [61]. Binary scaling can break down in the case of radiation-flowfield coupling, as radiation changes the flowfield properties [17].

Total, or stagnation, enthalpy (H_t) is an important quantity to match because it describes the energy within a gas due to its gas state and velocity, as shown in Equation 2.2. Matching H_t maintains the flight equivalent velocity v_{eq} , which is a convenient way to compare the speed of the tube flow at scaled conditions to the actual flight speed in low density atmospheric air. In the flight case, the freestream flow is sufficiently cold that the specific static enthalpy, h , is negligible, and the flight equivalent speed is the freestream speed of the vehicle, to a very good approximation. In contrast, the shock-heated nozzle flow in the X2 case has a temperature of several thousand Kelvin and may be partially dissociated, hence the static enthalpy contributes to H_t and v_{eq} .

$$H_t = h + \frac{v_\infty^2}{2} = \frac{v_{eq}^2}{2} \quad (2.2)$$

When binary scaling is applied in X2 hypervelocity re-entry experiments, the model sizing and condition design must be complementary to ensure proper reproduction of the flight trajectory point and enable the best possible comparisons with flight data.

2.2.3 Relevant X2 experimental campaigns

Many experimental campaigns have been completed in X2 and several in X1 and X3, and those that had similar aspects to the current campaign were most instrumental in planning the experiments. Capra investigated binary scaling and heat flux measurements on the surface of the FIRE II vehicle in X1, prior to the acquisition of optical imaging systems in the laboratory [17]. The binary scaling of the flight vehicle and trajectory point to a suitable model size and test condition, especially

maintaining the aeroshell geometry, is a good precursor to the scaled Hayabusa and Stardust experiments. The application of binary scaling to surface heat transfer, in particular radiative heat flux to the surface, resulted in the hypothesis that radiative heat flux is invariant under binary scaling. Hence, if binary scaling holds and if the medium is non-absorbing and not coupled to the flow, the radiative heat transfer is the same in both the flight case and the scaled experimental case [17].

Spectroscopy has become a prominent and powerful tool for observing the shock layer around an expansion tube model non-invasively, and for several years has been a standard inclusion in experimental campaigns. The spectral lines give information about the species present and differences in concentration through the shock layer, and can compare to radiation calculations, in some cases resulting from CFD, to find temperatures and examine differences between numerical and experimental data. Experiments in a Mars atmosphere were conducted by Eichmann, using a cylinder, sphere and a 60° Stardust-like aeroshell [33]. Observations focused on the UV, dominated by CN in the carbon-rich test gas but also extended through to the visible and near IR, and detailed identification of lines mapped the species in the spectra. Numerical spectra from several radiation databases, including NIST, Specair and LIFBASE, were fitted iteratively to the experimental data and temperatures and densities were estimated, to compare with CFD. Jacobs tested several Titan entry conditions but using X2 in non-reflected shock tube (NRST) mode instead of expansion tube mode, meaning there is no model, and instead the spectra measurements are recorded from a moving shock wave [57]. These measurements are similar to those produced in the NASA Electric Arc Shock Tube (EAST) facility, from which the behaviour of spectra from Earth experiments can be compared to the Hayabusa and Stardust experiments [62]. Eichmann's [33] and Jacobs' [57] works provide detailed information about the spectroscopy systems, optical theory, the use of geometric optics to set up the elements, alignment, background levels, calibration, and image processing. Porat [56] continued the use of Titan conditions, but X2 was operated in expansion tube mode and the UV spectra were recorded in the radiating shock layer of hemispherical and cylindrical models. Zander [59] used three Earth conditions and UV spectroscopy, but unfortunately it was not calibrated and cannot be compared to current experiments or CFD, and the IR spectrometer was used to measure temperature and not the N and O atomic lines that are prominent between 700 and 900 nm.

The most relevant overall campaign to the aim and objectives of this project was the campaign performed by Buttsworth *et al.* on a scaled Hayabusa model prior to the re-entry [63]. A one-tenth scale aeroshell model that maintained the geometry of the Hayabusa flight vehicle was tested with an approximate effective flight speed of $9.7 \text{ km} \cdot \text{s}^{-1}$ [63]. The UV spectra was made more interesting by the addition of an epoxy layer over the steel model, in an attempt to replicate ablation and pyrolysis from the vehicle surface and produce CN. The calibrated comparison between the standard air shock layer and the shock layer with added species shows that the bands and bandheads between 350 and 400 nm do increase for the epoxy coated models, but only by at most double the height, and the N_2^+ bandhead at 391 nm has not been clearly resolved to show a distinct species from the air shock layer [63]. An attempt was also made to measure the luminosity of the shock layer from visible emissions captured by the high-speed camera, but these are uncalibrated and only show the relative emission strength across the shock layer [64]. Calibrating this data would be difficult as the exact wavelength range is unknown, but a new imaging method was recently developed to capture the intensity radiating shock layer across two distance dimensions using the ICCD [52]. The light passes through a narrow band filter to give a wavelength-integrated value, similar to the plots of Winter *et al.* [35] and Buttsworth, Morgan and Jenniskens [5] that were mentioned earlier, and can be calibrated to give quantitative radiance data. The preliminary results use only one filter to look at the O 777 nm triplet, but this could be expanded to other wavelength bands depending upon the availability of filters. VUV spectroscopy was developed for the laboratory to examine wavelengths between 120 and 200 nm [50] but was not measured in flight due to complete absorption by air, water and other molecules across hundreds of kilometres, and thus will not be considered for scaled flight experiments.

2.2.4 Summary

The developments made in previous X2 experimental campaigns provide a strong foundation for performing scaled Hayabusa and Stardust re-entry experiments. The current standard configuration of X2 is sufficient for a series of Earth re-entry conditions, and involves the lightweight piston and corresponding driver fill conditions, a single 2 mm steel primary diaphragm, a single thin Al diaphragm, air as the test gas in the shock tube, and the acceleration tube and test section at low pressure. The aeroshell models and test conditions will be developed with binary scaling and

enthalpy matching to produce a shock layer as close to the flight trajectory points as possible, and the binary-scaled parameters will serve as constraints for the iterative condition design process. IR and UV spectroscopy, and 2D imaging, were the optical methods identified for studying the radiating shock layer over the aeroshell model, and producing spectra and radiation measurements that could be used in flight and numerical comparisons.

2.3 Numerical Modelling

2.3.1 Importance of numerical modelling

Though hypervelocity experiments and flight observations are exciting because there is still much to discover and understand, a main aim of re-entry research is to develop numerical methods and associated numerical modelling to the point where experiments will no longer be necessary for fundamental studies, and the exact impact of a radiating shock layer on re-entry will be predicted with enough confidence for engineering design purposes. Presently, the verification and validation of compressible flow computational fluid dynamics and radiation modelling programs with experimental and flight data is crucial to continued development of numerical modelling, and confidence in the accuracy of results [7]. The difficulties in achieving high levels of modelling accuracy are explained in the following paragraph by Morgan [46]:

'A feature of hypervelocity flows is the strong influence real gas effects will have on the thermodynamics and fluid dynamics of the flow field surrounding the entry body. The energy transfer from kinetic to chemical, thermal and radiative forms as the flow passes around the body is so high that dramatic changes to the gas properties occur. This includes non-equilibrium chemistry, non-equilibrium thermal storage modes, non-equilibrium radiation and severe ionisation.'

Each of those flow features must be considered in hypervelocity compressible flow CFD, on top of viscous effects, diffusion, turbulence and ablation and pyrolysis, in order to replicate re-entry or experimental flows, and produce results that are comparable to flight spectra. The CFD program that

will be used for the simulations in this work is *eilmer3*, a compressible flow computational fluid dynamics simulation program developed in-house at The University of Queensland [65]. The current iteration has built upon previous 2D and 3D compressible flow solvers, such as *mb_cns2* and *elmer2* [66], and has been applied to a range of applications, including steady-state aeroshell calculations at a certain trajectory point, and transient flow through expansion tubes. As the goal is to generate radiation data to compare to flight data, and to fully model the complex shock layer described by Morgan [46], radiation modelling is necessary, and comes from the in-built solver and database *Photaura* [13].

In aeroshell calculations, a singular trajectory point is simulated to resolve the entire shock layer in great detail and capture the complex physico-chemical processes, including nonequilibrium thermochemistry. Good quality simulations begin with a properly verified and validated compressible flow solver, as shown to be the case for *eilmer3*'s previous versions [7]. The thermochemistry model must include the full set of atomic, molecular and ionised species and appropriately model the chemical reactions and kinetics, thermal modes and energy exchange, and diffusion of mass, momentum and energy through transport properties [14]. CFD simulations are the basis of radiation calculations, which generate spectra by solving the radiative transfer equation along specified lines of sight, or determine radiation transport and its influence on the flowfield. Radiation calculations are fraught with challenges, and require vast databases for modelling excited state populations, energy levels and transitions, equations and models for determining equilibrium and nonequilibrium radiation. Ray tracing methods are often required to compute transport over an entire flowfield. As Gnoffo stated, '*The accurate modeling of radiation and radiation coupling is one of the great remaining challenges in computational aerothermodynamic design*' [14], and this is evidenced by the continued attempts, including in this research, to model radiation and compare to experimental results. Many of the thermochemical and radiation simulation parameters require assumptions to simplify the problem based on the extent of current knowledge or implementation in the software, and this can lead to uncertainties in the results [67]. Continuing simulations with current knowledge and tools and comparing with other data sources, especially experimental sources, is therefore extremely valuable in advancing the numerical modelling of aeroshell re-entry hypersonics and aerothermodynamics.

Since aeroshell simulations of Hayabusa and Stardust are a goal of this work, useful comparisons

can be made to other simulation results in order to gain perspective on the performance of *eilmer3* and *Photaura* for two different re-entry problems. Hence, the theory behind compressible flow simulations, thermochemistry and radiation modelling will not be explored in more detail here, nor will the methodology behind the Stardust and Hayabusa simulations, as the focus is on the results and their relevance for the present numerical studies. Gnoffo's review on significant aspects of planetary entry, including thermochemistry and radiation as part of the re-entry heating problem [14], and Gollan and Potter's works on thermochemistry and radiation modelling related to *eilmer3* [7] [13], provide a good knowledge base for those aiming to perform aeroshell simulations. Numerical modelling featuring the Stardust and Hayabusa aeroshells have been performed with a variety of flowfield and radiation solvers, and results from literature with potential for comparisons to the present work are summarised in the following sections.

2.3.2 Numerical modelling of Stardust

As Stardust observations occurred early in the re-entry trajectory, at high altitudes, Boyd, Trumble and Wright took two approaches in modelling the flowfield: CFD with the NASA DPLR program, assuming continuum flow held, and Direct Simulation Monte Carlo (DSMC), assuming non-continuum flow effects were dominant [68]. The simulations were performed at 81 km and 71 km, and the differences are illustrated by parameters such as stagnation line temperatures. Boyd and Jenniskens' resulting radiation calculations in NEQAIR, a NASA line-by-line radiation tool, were compared to the flight data at the two trajectory points and the spectra are much closer at 81 km for both flowfield methods than at 71 km [11]. Numerical spectra in the UV was calculated from a Stardust simulation at 71 km by Martin, Farbar and Boyd [69], which included ablative species generated by material response modelling of PICA, and overestimated the CN radiation by about a factor of 2. The N_2^+ bandhead was not identifiable in numerical calculations. Martin, Farbar and Boyd predicted a heavily nonequilibrium shock layer at 71 km and a peak in T_{tr} reaching towards 60 000 K [69], which is similar to Boyd, Trumble and Wright's modified chemistry case in DPLR, but the baseline chemistry case has a T_{tr} peak of less than 35 000 K [68]. Liu *et al.* also used DPLR and NEQAIR for their Stardust CFD flowfield and numerical spectra simulations, and at an altitude of 71 km, the atomic N lines came close to the IR flight data, while the atomic O lines in the same region were underpredicted by

numerical methods [70]. The flowfield did not equilibrate thermally or chemically, but T_{tr} flattens for about half of the shock layer, between the shock front and the wall boundary layer. The peak in T_{tr} for the 11 species air model is only 28 000 K and T_{ve} barely reaches 10 000 K at 5 mm from the wall, which is lower than Martin, Farbar and Boyd [69] and Boyd, Trumble and Wright [68] but at a similar location.

Trumble *et al.* performed similar post-flight flowfield CFD modelling with DPLR to Boyd, Trumble and Wright, and Liu *et al.*, and reported on a larger range of Stardust trajectory points, but only radiative equilibrium wall blackbody curves were calculated to compare to the flight radiation data. The surface heat flux at 41 s after the 120 km re-entry start with the radiative equilibrium wall peaked at about $550 \text{ W} \cdot \text{cm}^{-2}$, and surface temperature was predicted to peak at close to 3400 K, at an altitude of approximately 62 km. Gupta [71] and Olynick, Chen and Tauber [72] performed Stardust simulations at several theoretical trajectory points during early stages of the mission, to understand the behaviour of the capsule years prior to completion of its scientific objectives and return to Earth. Both simulations were run with ablating and non-ablating walls to predict the effect of the PICA TPS on the hypervelocity shock layer, which included reduced surface heat flux and temperature [71] [72], and a change in shock stand-off distance [72]. Park also conducted Stardust simulations to compare to Gupta and Olynick, Chen and Tauber using the post-flight trajectory data and updated thermochemical models, and the total heat flux for the laminar case at 42 s was $782 \text{ W} \cdot \text{cm}^{-2}$ [73]. Olynick, Chen and Tauber's total heat flux at 42 s is estimated to be about $700 \text{ W} \cdot \text{cm}^{-2}$ without ablation, and about $500 \text{ W} \cdot \text{cm}^{-2}$ with ablation [72], whereas Gupta found close to $700 \text{ W} \cdot \text{cm}^{-2}$ for a fully or equilibrium catalytic wall, and about $400 \text{ W} \cdot \text{cm}^{-2}$ for a non-catalytic wall [71]. Martin, Farbar and Boyd's super-catalytic wall heat flux was also around $700 \text{ W} \cdot \text{cm}^{-2}$ at the stagnation point, which reduced to below $300 \text{ W} \cdot \text{cm}^{-2}$ when ablation was considered [69]. The difference between the results show the impact of catalycity, radiative equilibrium or ablation can have on the surface heat flux. Radiative heat flux was generally less than 10 % of the total heat flux.

2.3.3 Numerical modelling of Hayabusa

Hayabusa simulations also show results pertaining to the flowfield, radiation and ablation. Winter *et al.* reports on the Hayabusa re-entry and covers several aspects of numerical modelling and comparison to flight data [35]. The temperature and number density plots through the observation period illustrate the thermochemical equilibrium regions that are present, and the numerical spectra in the IR show the resulting N and O peaks. At 58 km, which is around peak heating, NEQAIR overpredicts the flight spectra between 700 and 900 nm by up to a factor of 2 [35]. The numerical spectral irradiance integrated over atomic lines in the IR, which could be useful for 2D imaging comparisons, is higher than flight for atomic O and the 745 nm N line [35]. Simulations of Hayabusa by Suzuki *et al.* [74] and Kihara *et al.* [75] both examine several trajectory points and include ablation effects from a charred material ablation (CMA) code, and the loosely coupled method and simulation structure is outlined by Suzuki *et al.* in earlier work [76]. The two temperatures plotted along the stagnation line at 13:52:21 UTC (52 km altitude) show a shock stand-off of about 12 mm, a thermal equilibrium region that extends for about 4 mm inside the shock layer, and very little difference caused by the inclusion of ablation in both sets of results [74] [75]. Kihara *et al.* appear to have a better resolved grid than Suzuki *et al.*, as the T_{ve} curve is smooth and the T_{tr} peak is resolved up to about 40 000 K, whereas the straight sections of Suzuki *et al.*'s T_{tr} and T_{ve} plots indicate that the nonequilibrium region has not been entirely resolved. Winter *et al.* do not have the same trajectory point, but at 54 km, the equilibrium temperature is slightly higher than Suzuki *et al.* and Kihara *et al.*, both of whom had a value of approximately 10 000 K. Winter *et al.*'s T_{tr} peak is similar to Suzuki *et al.*, but also has an equilibrium region that extends for about 8 mm, indicating a difference in models and grid resolution issues could explain the similarities.

Loehle *et al* [77] simulated several points on the Hayabusa trajectory using the URANUS CFD code and FABL material response code, and showed a comparison of surface temperatures from the various CFD and material response calculations against the temperature determined from flight data. Around peak heating, the CFD, material response and flight values are within a few hundred K. The surface temperature peaks at just above 3000 K, which is very similar to the findings by Kihara *et al.*, and the CFD results and flight data plotted by Suzuki *et al.* The similarities in surface temperatures

across the observable part of the trajectory are maintained through the comparisons of surface heat fluxes, as simulated by Suzuki *et al* and Kihara *et al*. The heat fluxes predicted by empirical methods overestimate the CFD results by about a factor of 2, where the non-ablative cases peak at near $5.5 \text{ MW} \cdot \text{m}^{-2}$ and the ablative cases are up to $2 \text{ MW} \cdot \text{m}^{-2}$ lower.

2.3.4 Scaled model and facility simulations

Experiments of a 1/10 scale Hayabusa model were previously performed in X2 [63] and the corresponding simulations were completed with *eilmer3* and the in-house radiation database *Photaura* [13]. The numerical simulations are a good illustration of the methodology in *eilmer3* and *Photaura*, however, the trajectory point is quite low altitude and not on the final Hayabusa trajectory. Comparisons between experimental and numerical data show large discrepancies, including numerical overprediction of the scaled nonequilibrium N_2^+ radiation in the UV [63] [13], overprediction of the scaled N and O atomic radiation in the IR, and a disparity between scaled and equivalent full scale spectra [13]. The scaled spectra are noticeably larger than the full scale spectra across the entire simulated spectrum, from 50 to 1200 nm [13]. Scaled experiments will be necessary due to the size constraints of the X2 nozzle and test section, and therefore scaled CFD simulations attempting to replicate the current experiments will provide another interesting comparison to the experimental data and results from full scale simulations. Potter was critical of the manner in which the experiments were performed, the somewhat inescapable nature of shot-to-shot variation (the shock speeds, among other properties, varying between each shot) and the data obtained and processed [13], and so the comparisons in this work will investigate if the indicated differences to numerical data still exist against new experimental and flight data.

The previous scaled Hayabusa simulations required definition of the inflow conditions from simulations of flow through the X2 expansion tube [13]. Facility simulations have been performed in conjunction with several past experimental campaigns, in order to model the transient nature of the test flow and the flow properties as the ‘steady’ flow passes the model location in the test section. The simulations are generally a combination of the one-dimensional *L1d3* program to capture the reservoir, piston motion, driver, shock tube and diaphragm behaviour, and two-dimensional flow

modelled in *eilmer3*, using the *L1d3* results as the transient inflow condition. Previous X2 facility simulations include those by Gildfind for high pressure scramjet flows [6], Jacobs for non-reflected shock tube Titan flows [57], and Potter for Earth re-entry flows [13] and Mars entry flows [78]. A simplified full facility simulation is proposed, following the methods of Gildfind [6], in an attempt to improve on analytical results for condition design but be straightforward to run. As mentioned, the facility simulations at each of the Hayabusa and Stardust X2 conditions will become inputs to the scaled model simulations, and they will also provide a point of comparison to the analytical and numerical condition development processes discussed earlier.

2.3.5 Summary

Accurate numerical modelling of hypervelocity flows over aeroshells with complex thermochemistry and radiation is a large challenge in the prediction of re-entry environments, and comparison to experimental data for verification and validation. Previous simulations of the full scale Hayabusa and Stardust vehicles at flight trajectory points have provided a solid base for expected results and comparisons with the current simulations, to assess the performance of the selected software and databases. Results include UV and IR spectra, of direct importance to each part of the three point comparison, and flowfield data such as temperature and heat flux. The X2 experimental results, and data from flight, can be compared to full scale simulations of the Hayabusa and Stardust vehicles in flight, following examples in literature. The experimental data can also be compared to scaled simulations of the X2 aeroshell models at estimated inflow conditions from transient facility simulations, to provide more information on simulation performance and identify areas for future development.

2.4 Summary of Findings

This review investigated previous Earth re-entry missions with a focus on Hayabusa and Stardust, and the possibilities of replicating flight data through experimental and numerical ground testing methods. Spectral signatures of the Hayabusa and Stardust radiating shock layers are the only two

re-entry observation data sets of their kind that exist in the literature. The atomic N and O features in the Hayabusa and Stardust IR spectra are from the radiating air shock layer, which is the most straightforward to reproduce in experimental and numerical modelling as there is negligible influence from the TPS. The UV spectra from Hayabusa has contributions from the air shock layer species N_2^+ and the ablating TPS species CN, and both are possible to simulate numerically, but only the air species appear in experiment due to the lack of an ablating wall. The published UV spectra for Stardust are weak in magnitude compared to the IR, and therefore the focus will be on replicating the IR spectra only. The selected trajectory points from each re-entry will determine the parameters and constraints for designing experiments and numerical simulations. The features identified in observed re-entry spectra will be the focus of ground spectroscopic measurements and radiation calculations.

Experiments will be performed in the X2 expansion tube at The University of Queensland, and in its current configuration, X2 is capable of producing a range of scaled Earth re-entry conditions. Binary scaling and enthalpy matching have not previously been applied to Earth experiments in X2, but are the most appropriate constraints for hypervelocity re-entry conditions featuring an aeroshell model. Condition development will follow the identified analytical, experimental and numerical processes to produce and attempt to quantify a condition for each capsule. Small Hayabusa aeroshell models and larger hemispheres and cylinders were tested in previous X2 campaigns, therefore larger, binary scaled aeroshell models are possible. Spectroscopy in the IR and UV has also been performed in previous campaigns and will be used to record comparable data to flight. 2D imaging will be developed further for narrow band radiation measurements of several flight features across two spatial dimensions, as wavelength-integrated flight and simulations values were reported along with wavelength-resolved data.

Numerical simulations of Hayabusa and Stardust have been performed with a variety of flowfield and radiation solvers at a range of trajectory points. These results provide useful comparisons to the proposed simulations in *eilmer3* and *Photaura*, to investigate performance against other solvers as well as against flight and experimental results. Every comparison can assist in further development of the numerical tools, increasing confidence in the accuracy of the results. Discrepancies between numerical and experimental spectra have been identified previously, and can be further examined with

new experimental and flight data. Scaled simulations of the X2 aeroshell models will be performed following the facility simulations that are part of the condition establishment process, as this has been performed only once before, for a small Hayabusa model at a condition away from the true trajectory.

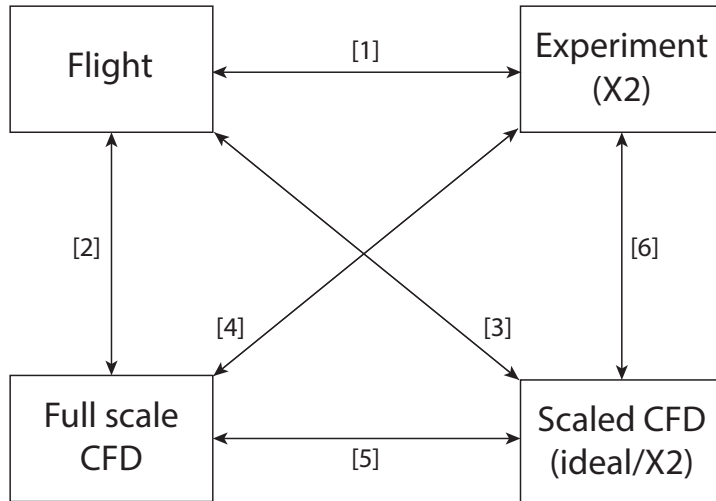


Figure 2.7: Comparisons between data sets that will be produced in the thesis work.

The eventual comparisons forming the results of each data set introduced in the aim and objectives, for each vehicle, are therefore:

1. Flight spectra \leftrightarrow scaled X2 expansion tube spectra, and 2D imaging
2. Flight spectra \leftrightarrow full scale CFD and numerical spectra
3. Flight spectra \leftrightarrow scaled model CFD and numerical spectra, following facility simulations
4. Full scale CFD and numerical spectra \leftrightarrow scaled X2 expansion tube spectra, and 2D imaging
5. full scale CFD and numerical spectra \leftrightarrow scaled model CFD and numerical spectra, following facility simulations
6. Scaled X2 expansion tube spectra, and 2D imaging \leftrightarrow scaled model CFD and numerical spectra, following facility simulations

The comparisons are illustrated in Figure 2.7, corresponding to the numbers in listed form. The Hayabusa comparison will consider IR and UV data, and Stardust comparisons will consider IR only.

Chapter 3

Condition Establishment

The hypervelocity experiments proposed for X2 were to investigate the radiative shock layers produced over scaled aeroshell models, at conditions replicating two selected re-entry conditions. Two new flow conditions were designed for the X2 expansion tube to match a point on each of the Hayabusa and Stardust flight trajectories using analytical, numerical and experimental methods. Condition design in a high-enthalpy facility such as X2 requires some understanding of how each section of the tube affects the test flow exiting the nozzle, the operating envelope and restrictions on certain sections (for example, keeping the driver fill pressure and composition consistent with the reservoir fill pressure, the orifice and the primary diaphragm), the aim of the condition being designed, and how the measurements taken can compare to numerical results and prove the condition is working, within reasonable error. The methodology for condition design and analysis begins with selecting a trajectory point, and matching or scaling design parameters such as density and total enthalpy. Calculating theoretical flow states, selecting fill pressures with a calculation tool called *Pitot*, and testing these conditions in X2 then leads to design iterations where necessary. Using the simulation tools *L1d3* and *eilmer3* to simulate the entire facility in a combined 1D and 2D axisymmetric calculation produces numerical results for comparison to theoretical and experimental data. The chapter steps through the process of creating and testing a condition for Hayabusa, followed by Stardust, through to the collection of pressure traces and shock speeds across the experimental campaign for comparison with detailed condition simulations. In this way, choices, methods and results will be presented to the reader as if they are working through the process, so that more data becomes available in each stage for analysis and comparison. Identifying and attempting to understand any differences between

the analytical, experimental and numerical condition development methods is important for developing these methods further. This could include improving the measurement techniques on X2, finding current limitations of *Pitot* and updating components of the facility simulations.

3.1 Hayabusa Condition for X2

A condition was designed to simulate the flow over a one-fifth scale Hayabusa model in the X2 expansion tube at near-peak heating conditions.

3.1.1 Trajectory point selection

USQ and UQ had observation teams that were collecting spectra remotely during the Hayabusa re-entry. IR spectra were collected by a ground-based tracking camera [4] and UV spectra were recorded by the AUS spectrometer that flew on a NASA DC-8 aircraft [64]. The trajectory point required good quality data in both spectral regions, and due to optical interference from the spacecraft bus break-up in the UV data until 13:52:19.5 UTC [79], the selected trajectory point was 13:52:20 UTC, slightly after the peak heating point evident in the IR spectra at 13:52:19 UTC [4]. The nominal flight parameters for the 13:52:20 UTC trajectory point are provided in Table 3.1 [35].

Altitude (m)	Velocity (m/s)	Density ($\text{kg} \cdot \text{m}^{-3}$)	Total Enthalpy ($\text{MJ} \cdot \text{kg}^{-1}$)
55 000	10 440	5.2×10^{-4}	55

Table 3.1: Nominal flight parameters for Hayabusa 13:52:20 UTC trajectory point.

3.1.2 Nominal parameters from binary scaling and enthalpy matching

Binary scaling and enthalpy matching were used to design the nominal freestream density and flight equivalent velocity, based on the model size. For imaging the shock layer over a scaled experimental model, the shock stand-off had to be as large as possible, hence the model was designed as large as possible. The upper limit on model size is the diameter of the assumed axisymmetric core flow out of the X2 nozzle, which has a physical exit diameter of 201.68 mm [49]. A nominal safe upper limit on the Hayabusa model diameter was selected as 80 mm, based on past experiments [33]

[59] [56] and confirmed by subsequent experimental and numerical analysis, presented later in this chapter. Thus, the characteristic lengths in Equation 2.1 were the Hayabusa vehicle nose radius of 200 mm and the X2 model nose radius of 40 mm, and the required test flow density was calculated as $0.0026 \text{ kg} \cdot \text{m}^{-3}$. Maintaining the product of characteristic length and density causes the mass fractions along a certain streamline to be largely invariant for binary reactions. Binary scaling is only applicable to dissociation reactions that occur through two-body collisions and not to recombination or other tertiary reactions, so the relation can break down as the gas progresses back to equilibrium [60]. Decisions regarding the flight trajectory point took place when only the preliminary results of full scale CFD simulations were available, and the simulation of Hayabusa at the conditions provided in Table 3.1 showed a reasonable region of nonequilibrium in the shock layer. The equilibrium region along the stagnation line was no more than 4 mm in width for the 11 mm wide shock layer, and this was deemed sufficient for the binary scaling principle to hold. The reader can refer to Figures 6.8 and 6.12 in Chapter 6 for the results used to make this decision. The flight equivalent velocity was previously quoted in Table 3.1 as $10.44 \text{ km} \cdot \text{s}^{-1}$, and the aim is to produce this velocity at the X2 nozzle exit.

3.1.3 Preliminary analysis with *Pitot*

Preliminary analysis of the target X2 condition was conducted using the *Pitot* code in ‘theoretical mode’. *Pitot* is an equilibrium expansion tube and shock tunnel analysis code that performs quick parametric calculations to design X2 conditions that are as close as possible to meeting scaled or matched parameters whilst staying within the X2 operating envelope [41]. Fill conditions for each section of X2 (reservoir, driver, shock tube and acceleration tube) are selected as inputs to *Pitot*, and the calculation produces nominal primary and secondary shock speeds, as well as the gas state at different locations in the expansion tube using analytical equations (see, for example, [60] or [43]) and equilibrium gas dynamics. The initial design process involves iterating through a series of shock and acceleration tube fill pressure combinations until the desired nozzle outlet density, flight equivalent speed and total enthalpy are reached. The Hayabusa 13:52:20 UTC condition for X2 had standard operating conditions for the reservoir and driver, including the standard lightweight piston [6] and 2 mm thick steel primary diaphragm. As this is an Earth entry condition, the shock tube

contains air as the test gas, and a single thin aluminium diaphragm was specified as the secondary diaphragm for ease of operation and reasonable fill pressure limits (c.f. [33] and [59]). Also, Al lines are discrete and easy to identify in spectra, without a detrimental impact on air measurements. Table 3.2 provides the fill pressures and shock speeds in different tube sections, and Table 3.3 lists the nozzle exit conditions from *Pitot* alongside ideal scaled or matched values, where applicable. The nozzle exit Mach number was estimated to be 12.4, which means that this condition operates above the design Mach number of 10. Only one nozzle is currently available for X2, and prior experiments were successful over a range of operating conditions, thus it was expected that the nozzle would perform adequately.

At this point, the condition was tested in X2 and the experimentally measured shock speeds, as well as the known fill pressures, become inputs to the ‘Experimental’ mode of *Pitot*. Condition testing is presented in Section 3.1.4. The code now calculates flow parameters through an unsteady expansion using experimental shock speeds, and the nozzle exit parameters can be checked by comparing the experimental conehead pressure against the result from *Pitot*. The expansion through the nozzle is difficult to account for in simple inviscid analyses because the expansion of the core flow does not follow the geometric area ratio, and so the area ratio used can be tailored until the numerical and experimental conehead pressures match. This methodology has proven effective for many previous flow conditions, including those designed by Zander [59] and James *et al.* [41], but it may mask important flow effects. Hence, simulations of the full X2 facility were performed using a one-dimensional code combined with CFD to remove the area ratio assumption, calculate parameters that *Pitot* cannot, investigate nonequilibrium effects and improve understanding of numerical methods applied to simulate such a system. This is discussed in detail in Section 3.1.5.

The main benefits of the *Pitot* tool are the ability to obtain information about possible conditions

Reservoir	Driver	Shock tube	Acceleration tube	Primary shock speed	Secondary shock speed
6.85 MPa air	928 kPa, 100% He	13 500 Pa air	17 Pa air	4505 m · s ⁻¹	10 145 m · s ⁻¹

Table 3.2: Theoretical fill pressures and shock speeds from *Pitot*.

easily and in a vastly shorter time than any other numerical facility simulation. The main downside is that it is an approximate code using simple analytical methods, modelling only the primary physical processes involved in flow development, and its best solution may not always match the behaviour seen in the experimental facility. For the Hayabusa condition, the difference between theory and experiment is small as the following section explains, resulting in straightforward development of the experimental condition.

3.1.4 Experimental Condition Testing and Analysis

Conditions are tested in X2 by measurements from a series of pressure transducers along the shock and acceleration tubes, and pressure transducers inside 15° coneheads mounted linearly in a rake, positioned slightly downstream of the nozzle exit. The tube transducer responses provide the time at which the shock front passes, hence the shock speed can be calculated from time of flight between two transducers with a known spacing. Experimental shock speeds will be presented and discussed further alongside numerically determined shock speeds in Section 3.1.5. The conehead transducers measure the static pressure behind conical shocks in the test flow, and in the process of establishing a new condition, there are usually multiple shots performed at that condition to gather shock speed and pitot rake data. The reader is directed to Gildfind's work on the design and implementation of 15° coneheads for X2 [6]. Figure 3.1 shows the evolution of the flow through conehead pressure data for shot x2s2315. The conehead pressure traces provide indications about the steady flow time by identifying the shock arrival (1), where the flow settles (2) and where unsteadiness in the flow caused by noise begins (3) and increases (4). The measured test time for optical experiments could be selected for any period between points 2 and 3, as the flow is sufficiently steady. In Appendix D the high-speed video stills from shot x2s2800 provide a visual representation of the Hayabusa model at these critical moments in the flow. The response of each transducer, at fixed distances from the nozzle centreline, also gives an estimation of the width of the core flow. This condition shows uniformity through all of the traces except conehead 5, which had no response in these tests and was not plotted. Hence, it was assumed that the core flow covered at least 144 mm, equivalent to the distance from coneheads 1 to 9 on the far ends of the rake. The core flow will therefore surround the 80 mm diameter model with a minimum of 30 mm of reasonably uniform flow around the periphery.

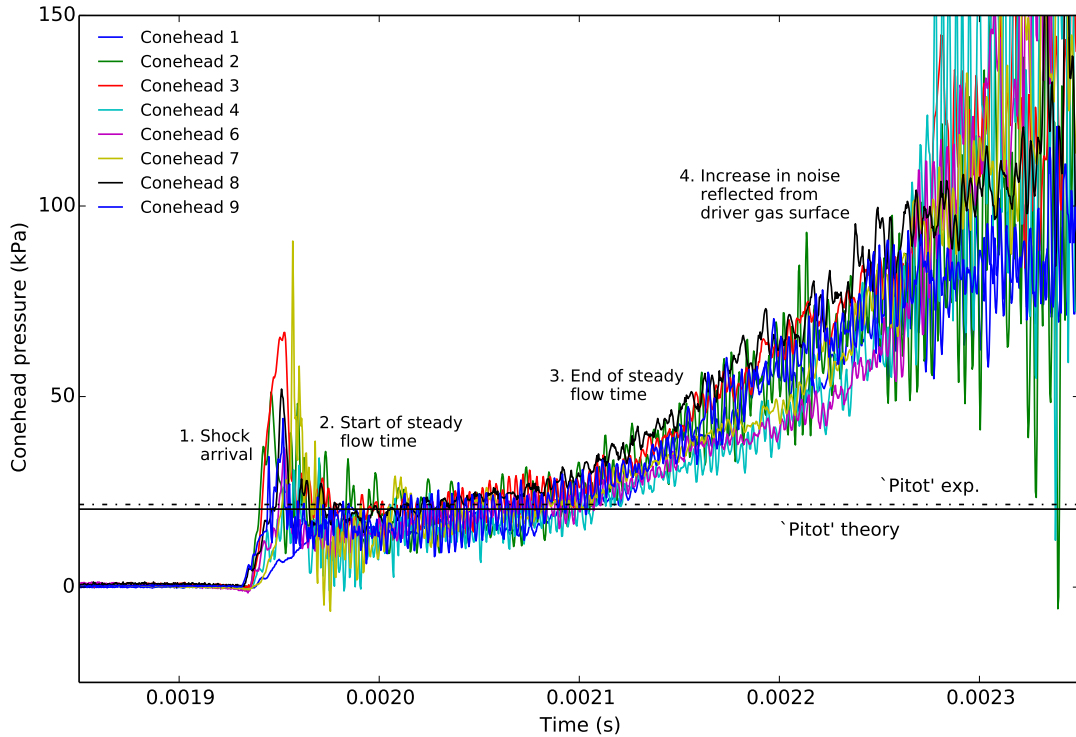


Figure 3.1: Hayabusa 13:52:20 UTC flow condition traces from all available coneheads, to demonstrate test time and core flow, and theoretical and experimental *Pitot* results.

Table 3.3 shows that there are small differences between experimental conehead pressure results, which include three successful condition test shots with average shock speeds (x2s2311, x2s2312 and x2s2315), earlier theoretical results using equilibrium gas dynamics, and the ideal scaled flight values. The experimental nozzle exit density is slightly higher and the flight equivalent speed is slightly lower in experiment than predicted. The conehead pressure is higher in experiment than theory (both values were calculated using the geometric nozzle area ratio of 5.64) but the experimental *Pitot* value approximates the measured experimental traces, with average uncertainties of -6 kPa and $+3\text{ kPa}$. The area ratio can be reduced in the *Pitot* experimental calculations if there is a significant difference to experiment, but the match between the geometric area ratio conehead pressure and the experimental value appears sufficient for this condition. This is also demonstrated in Figure 3.1, where the aforementioned transducer traces are plotted alongside theoretical and experimental *Pitot* results, denoted by horizontal lines. Both the theoretical and experimental *Pitot* values are within the range of the experimental traces during the steady flow time. The parameters are close enough

	Density (kg · m ⁻³)	Eq. velocity (m · s ⁻¹)	Total enthalpy (MJ · kg ⁻¹)	Temperature (K)	Pressure (Pa)	Conehead pressure (Pa)
Ideal (scaled flight)	0.0026	10440	55	—	—	...
<i>Pitot</i> (theory, eq)	0.0026	10414	54.2	1860	1378	20464
<i>Pitot</i> (experiment, eq)	0.0027	10382	53.9	2224	1755	21683

Table 3.3: Ideal scaled (where known), *Pitot* equilibrium (eq) theoretical and *Pitot* experimental equilibrium (eq) conditions at the nozzle exit.

to move forward with the condition and employ it for optical imaging experiments, but it is still valuable to model the facility at higher fidelity.

3.1.5 Combined *L1d3* and *eilmer3* facility simulation

Detailed numerical simulations of the entire X2 facility model many of the intricate and complex processes that occur from the moment of piston launch to beyond the end of the steady test time, marked by the driver gas passing into the test section. Simulation results are more robust than those from the analytical approach of *Pitot*, and at the same time, experimental results contribute to developing and improving the numerical methodology. Certain conditions may require detailed calculations to match to experimental data since the approximations in *Pitot* may not be sufficient. Attempting to produce a reasonable, time-optimal approach to expansion tube simulations enables straightforward comparisons between facility simulations and experiment, to understand where more detailed calculations are required.

The numerical simulations were performed using two different solvers: *L1d3*, a one-dimensional shock tube analysis code [80] and *eilmer3*, a 2D or 3D compressible flow CFD code [65]. *L1d3* simulated the piston movement, driver gas, area change through the orifice plate, bursting of the primary diaphragm, movement of the primary shock, bursting of the secondary diaphragm and initial movement of the shock beyond the secondary diaphragm. The solver can handle these effects well in 1D, and the constant area sections are accurately represented in 1D. The primary shock speeds produced by *L1d3* are generally very similar to those calculated by *Pitot* or measured in experiment for the current conditions. 2D axisymmetric simulations in *eilmer3* are possible through the nozzle

because *eilmer3* is capable of modelling the interactions of viscous effects, flow compressibility, and thermochemistry and coupling them to the nozzle geometry. These features influence the spatial and temporal variation of the flow state, especially as the test gas reaches the test section. The secondary shock speeds tend to diverge from the experimentally measured values in the acceleration tube as multidimensional effects become important, and the hypervelocity flows in question can no longer be treated as one-dimensional gas slugs in *L1d3*. These effects have also been observed for scramjet conditions in X2 [6]. The trade-off between a time-optimal approach and an accurate solution influences the amount of the simulation performed with each program: *L1d3* is much faster, but *eilmer3* simulates multidimensional effects that become significant as the test section is reached. Therefore, a break point between the two solvers at a location just beyond the secondary diaphragm seemed a reasonable compromise that proved sufficiently robust in practice. Justification of this methodology was initially presented by Wheatley *et al.*, where it was argued that 1D simulations were sufficient for the lower velocity, higher density shock tube flow and 2D simulations were only necessary once the boundary layer began to develop in the acceleration tube [81]. Figure 3.2 illustrates this breakpoint between the two numerical methods by showing the sections of the tube that each solver will simulate, and also shows the progression from *L1d3* into the *eilmer3* tube and nozzle simulation, followed by a separate simulation of flow over the model where the test section flow results become the inflow conditions.

The following sections will step through the methodology, findings, analysis and choices made with each of the codes, leading to the results that become inflow conditions to CFD simulations over the test models in Chapter 6.

3.1.5.1 *L1d3* one-dimensional calculation

The *L1d3* modelling of X2 follows previous work by Gildfind [6], Sheikh [50] and James *et al.* [41], where the geometry, gas slugs, diaphragms and piston were set to a standard X2 configuration. Immediately prior to the primary diaphragm, there is an area change determined by an orifice plate, which has a diameter specified by the driver gas composition and pressure. The loss factor at the end of the driver tube modelled the area contraction for the orifice plate and was selected as 0.7 based on

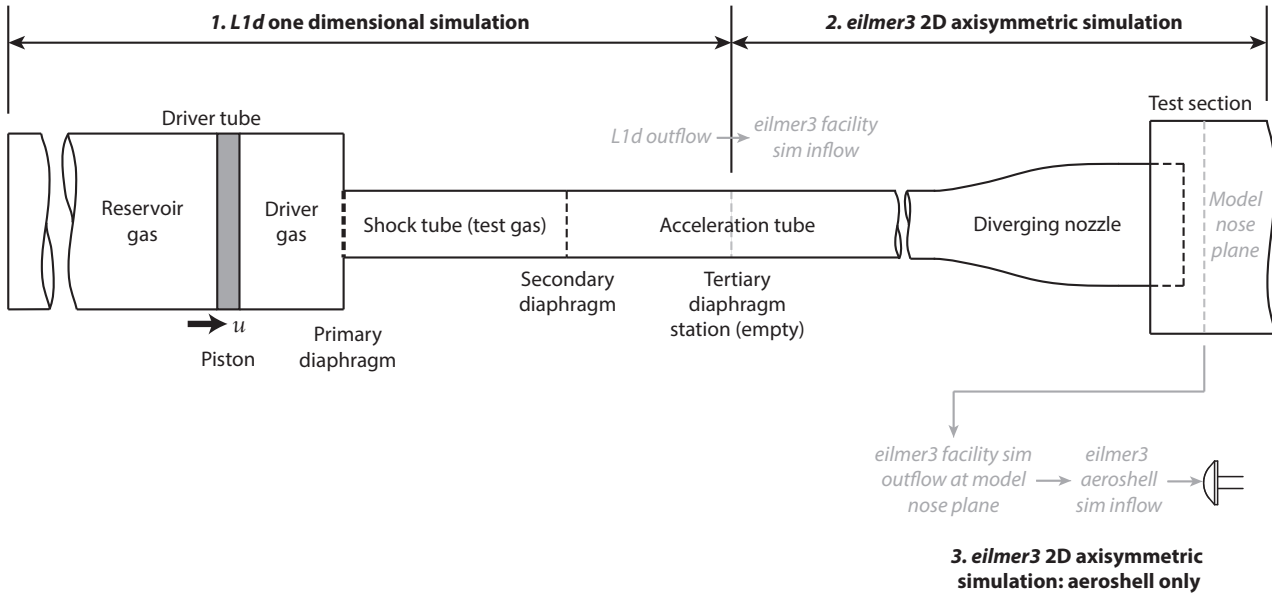


Figure 3.2: X2 facility showing regions simulated with *L1d3* and *eilmer3*.

Gildfind's analyses for 100 % He at 928 mbar [6]. The mesh also followed previous simulations by applying a mesh factor to adjust the number of cells and coarsen or refine the mesh in each section. A mesh factor of 2.0 was appropriate for the Hayabusa condition, resulting in 200 cells each for the reservoir gas and driver gas, and 600 cells each for the test gas and acceleration tube gas. The acceleration tube gas slug had an adaptive grid, meaning the number of cells was dynamic and could change as the shock moved through the tube. Modelling the full piston dynamics and diaphragm bursts as standard in *L1d3* was suitable for the Hayabusa condition, and fill pressures of the driver, shock tube and acceleration tube were set as specified in Section 3.1.3. The flow was assumed to be in thermochemical equilibrium and modelled by a look-up table generated by NASA's Chemical Equilibrium with Applications (CEA) program [82].

The most important results from the *L1d3* simulation are the primary shock speeds, and these were calculated using the known spacing between transducer locations and the time of pressure rise, as for experiment. The primary shock speeds averaged across 35 shots in the campaign, and associated uncertainties, are summarised in Table 3.4. An example of the measured and simulated pressure trace features, from which the shock speeds are calculated, is shown for shock tube transducer sd2 in Figure 3.3. Time is referenced to the *L1d3* simulation, which is relative to the piston launch and therefore

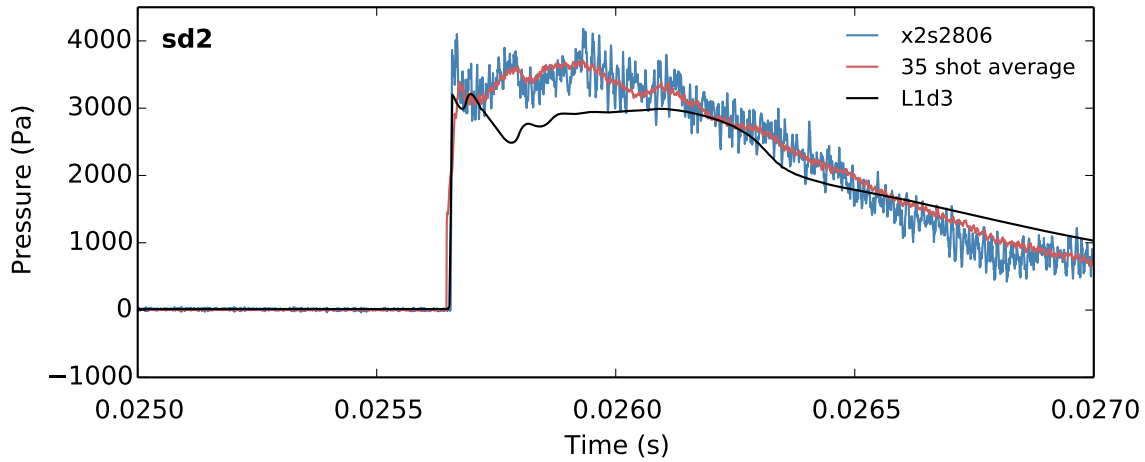


Figure 3.3: sd2 shock tube transducer pressure traces from *L1d3*, a single shot and the campaign average, from 35 shots. Time base referenced to the *L1d3* simulation.

has an offset to the time base of the experimental measurement. The simulated traces are procured by placing history points at the location of the pressure transducers and recording the transient data. Each trace used in the campaign average was adjusted temporally if there were slight offsets in the data, and a single shot with near-average shock speeds is also plotted to show similarity in the overall shape. Comparing the campaign average trace to the single experimental trace indicates very good repeatability as the trace features are almost identical, except for the smaller amplitudes of noise in the campaign average due to the averaging process. The experimental and *L1d3* pressures are very similar immediately following the rise in sd2, but the profiles differ from there and this could be due to calibration of the transducers or underestimation by the *L1d3* solution. The primary shock speeds from experiment and *L1d3* are within the experimental error bounds, maximum $77 \text{ m} \cdot \text{s}^{-1}$ as given in Table 3.4, therefore the differences post-rise are not a major concern. Results downstream of the shock tube are presented in Section 3.1.5.5.

3.1.5.2 *eilmer3* modelling parameters

The transient flow through the X2 acceleration tube, nozzle and test section was modelled using the 2D axisymmetric implementation of the *eilmer3* compressible flow CFD program. Chapter 2 introduced CFD modelling and applications of *eilmer3*, and Chapter 6 will expand on the modelling procedure for aeroshells, with a focus on thermochemistry and radiation. The reader is directed to Figure 6.1 for a pictorial summary of the *eilmer3* simulation process, and Section 6.1 for the

detailed discussion of aeroshell CFD simulation parameters. The thermodynamic, chemistry and flow modelling is simpler for the X2 conditions than for the aeroshell conditions as the moving shock does not produce conditions as complex as the bow shock around a model, which stagnates the hypervelocity flow. The X2 flow is compressible and viscous, and the boundary layer along the tube and nozzle wall is captured by refining the grid towards the wall. The same transport models are applied here as in Section 6.1.2. Tube boundary layers were simulated as laminar rather than turbulent based on the assumption that density is low enough and viscosity is high enough that turbulence can be neglected. This assumption was confirmed by calculating the cell Reynold's number at the wall in the acceleration tube, following the methodology of McGilvray [83]. The cell Reynold's number of the test gas at the at6 transducer location was calculated to be about 6, which is less than the turbulent threshold of 10 quoted by McGilvray [83]. This indicated that laminar boundary layers are an appropriate assumption for the test flow.

The use of different thermal and chemical kinetics models could influence the flow properties exiting the nozzle and over the aeroshell model, as well as the simulation time. Equilibrium thermochemistry is satisfactory when the focus is shock speed, Mach number and pressure; for example, in Gildfind's [6] development of scramjet conditions. However, it was suggested that thermochemical nonequilibrium simulations using two temperatures and finite-rate chemistry in *eilmer3* are necessary for producing the correct inflow over a model [13]. Three thermochemical models were initially tested to investigate flow properties at the model location (30 mm downstream of the nozzle exit): thermochemical equilibrium air with a CEA look-up table, single temperature and five species finite-rate air chemistry with the Park scheme, and single temperature and five species finite-rate air chemistry with the Gupta scheme. The five species to be considered are the molecular and atomic species only: N₂, O₂, N, O and NO. The *x* dimension in these simulations refers to the axial flow direction through the tube, and *y* is the radial dimension. Pressure, temperature, *x*-velocity and density are plotted against time for each set-up in Figure 3.4, and although the simulations are not referenced to one time base, the similarity across the initial rise and into the test time can be recognised. The use of Park or Gupta finite-rate reaction schemes makes a negligible difference to the results, due to near-identical reactions when considering atomic and molecular species only. Pressure and *x*-velocity traces are similar with equilibrium or finite-rate chemistry. The decrease in temperature

in the finite-rate reacting cases is due to dispersing energy through chemical reactions, but this has also introduced a rise in density compared to the equilibrium case. As the density is a target scaling parameter, it was considered to be the more important result. Post-rise temperature magnitudes of 2000 to 3000 K seem to indicate that splitting into two temperature modes and including ionised species is unnecessary, therefore further simulations with two temperatures and 11 air species were not performed. Simulation time approximately doubles between equilibrium and single temperature, 5 species finite-rate chemistry simulations, and it is expected that a more complex thermochemistry model would more than double the simulation time again.

Fundamental studies by Macrossan [84] on nitrogen dissociation in the T4 shock tube showed that there is little difference in shock layer properties over a model between a finite-rate and equilibrium chemistry inflow, despite having about 40 % dissociation in the finite-rate chemistry freestream. The degree of shock layer dissociation was also shown to be virtually identical. A higher freestream density for ‘real’ as opposed to equilibrium inflows was found for a condition employing binary scaling [84]. Considering Macrossan’s findings, the differences in flow properties, including density and temperature, in Figure 3.4 should not have a significant influence on the shock layer properties over the aeroshell model. It is assumed that since the flow through the nozzle is at very high speeds, with high temperatures compared to flight or upstream tube sections, then equilibrium is adequate [12]. Therefore, equilibrium thermochemistry was selected for the X2 facility simulations in this work, as there should be a negligible difference to shock layer properties over a model caused by chemistry, as well as ease of calculation and reduced simulation time. This is investigated further in Section 6.1.4.

3.1.5.3 Domain creation and boundary conditions

The X2 dimensions were obtained from Scott [49], Jacobs [57] and Gildfind [6]. The acceleration tube, nozzle and test section centrelines form the symmetry axis for the 2D axisymmetric simulation, to which a slip wall boundary is applied (no shear stress, no viscous effects). The nozzle protrudes into the dump tank and the section extending upstream of and surrounding the nozzle exit is included in a slightly simplified manner for ease of computational block definition. The tube and test section walls are fixed at the ambient temperature, and the outflow boundary is fixed at the initial test

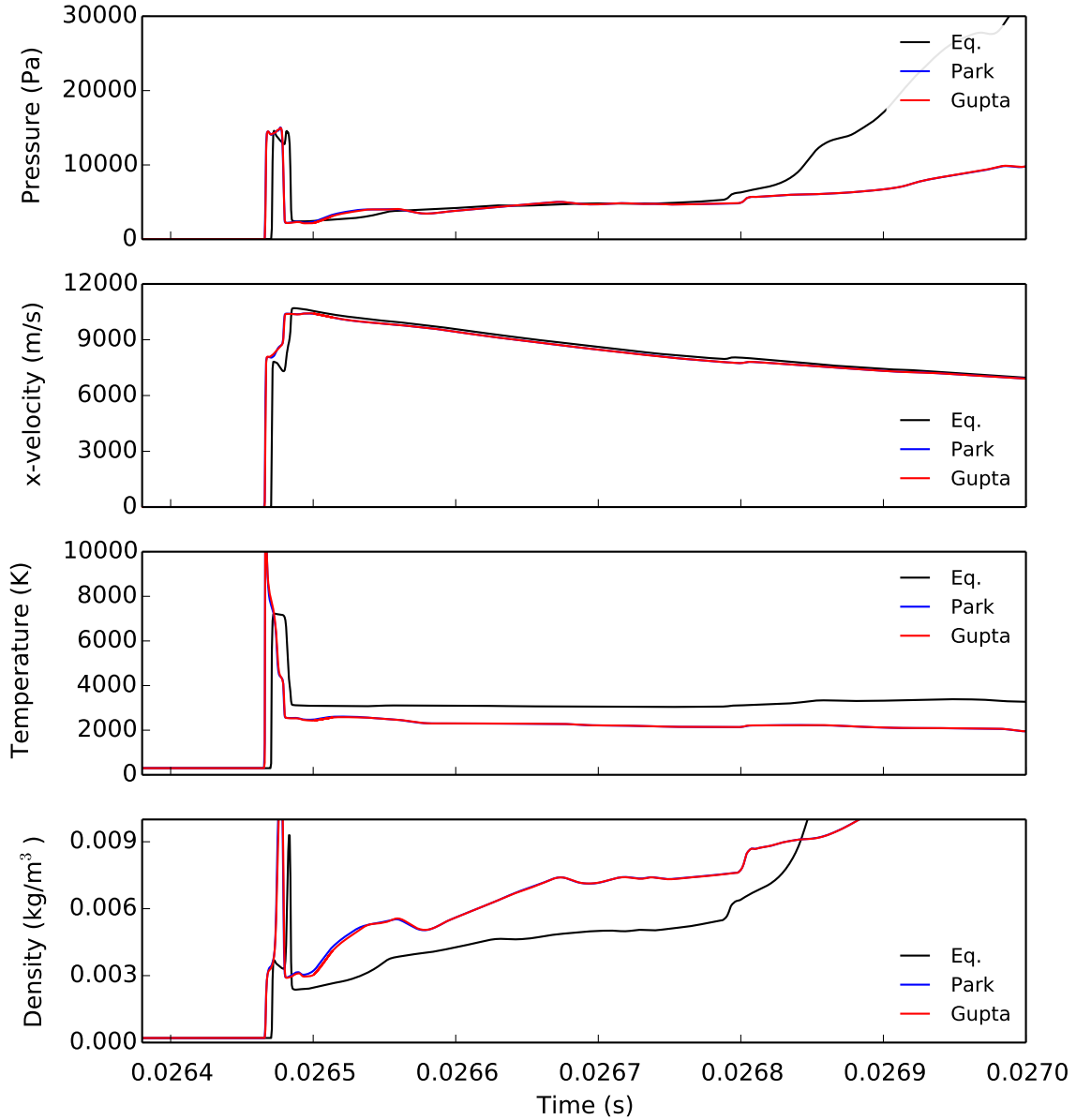


Figure 3.4: Flow properties at the model location, 30 mm downstream of the nozzle exit, nozzle/test section centreline for equilibrium, and Park or Gupta 5 species, 1 temperature schemes.

section pressure. This approach was sufficient for Gildfind's scramjet conditions [6] and Jacobs' Titan entry conditions [57], as the reflected shocks from the test section walls did not return in time to interfere with the test flow. The same approach should hold for Earth (re-)entry flows. The outflow boundary was placed 150 mm downstream of the nozzle exit to enable the test section flow to easily accommodate the model at any suitable location, including the eventual position at 30 mm downstream of the nozzle exit.

The acceleration tube inflow condition was created from results of the *L1d3* simulations, following the methodology of Gildfind [6]. The *L1d3* history file recorded at the inflow location was processed into a simply formatted file with the desired parameters to define the transient inflow, then read in through a user-defined boundary condition. If the *eilmer3* simulation involves chemical nonequilibrium, the processing script determines species mass fractions from CEA at each timestep and includes them in the file. The inflow location was originally selected as the tertiary diaphragm station, which did not contain a diaphragm for the Hayabusa or Stardust conditions, but was a well-defined breakpoint. Diaphragm rupture mechanics are notoriously difficult to simulate in CFD [6] [57] [40] but can be simulated at high enough fidelity in *L1d3*, therefore it was decided that the breakpoint would be downstream of the secondary diaphragm. The early acceleration tube (st) transducers that are located between the secondary and tertiary diaphragm stations recorded poor quality pressure traces in experiments due to the high pressure differential between the shock tube and acceleration tube gas, as well as the establishing secondary shock. The transducers were checked for calibration or measurement errors, but the poor traces were condition-based. The tertiary diaphragm station was the next major breakpoint and was selected on the assumption that the post-secondary diaphragm flow would have stabilised, and the inflow was far enough upstream of the later acceleration tube (at) transducers that good comparative results could be recorded through that section of the tube.

A study was performed to check that moving the inflow location upstream or downstream of the tertiary diaphragm station had sufficiently small impact on the nozzle exit flow conditions. Simulations maintained the same *L1d3* inflow, geometry and grid, and all were in thermal and chemical equilibrium as defined by a look-up table from CEA. The upstream inflow was at the st3 transducer location and the downstream inflow at the at1 transducer location. The x -component of velocity was compared at the centreline of the nozzle exit location in Figure 3.5. The unsteadiness of the x -velocity following the rise is evident in all traces, and appears to be a feature of the simulation's flow structure. The difference in location caused the time bases to differ by several microseconds, and so a time offset was applied to match the tertiary diaphragm trace and compare their magnitudes relative to the rise. The velocity is almost identical throughout Figure 3.5 (a), and it is only when the nominal test time section is enlarged in Figure 3.5 (b) that the variations are visible. The shock tube inflow results in a

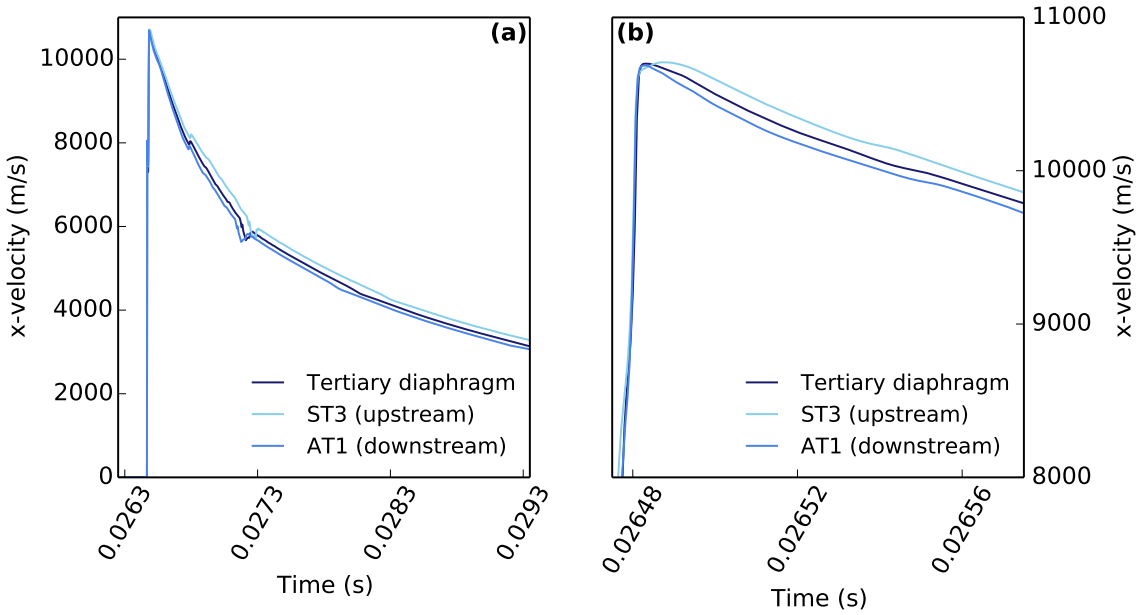


Figure 3.5: x -velocity comparison at the nozzle exit centreline for different inflow locations: (a) full profile, (b) zoom to peak and nominal test time.

velocity about $50 \text{ m} \cdot \text{s}^{-1}$ higher than the tertiary diaphragm inflow, which is about $50 \text{ m} \cdot \text{s}^{-1}$ higher than the acceleration tube inflow at a given time. Temperature and density were not plotted because the difference is negligible, and therefore it is unlikely that slight variation in the x -velocity due to inflow location will significantly affect post-shock conditions beyond uncertainty limits.

3.1.5.4 Grid, meshing and block structure

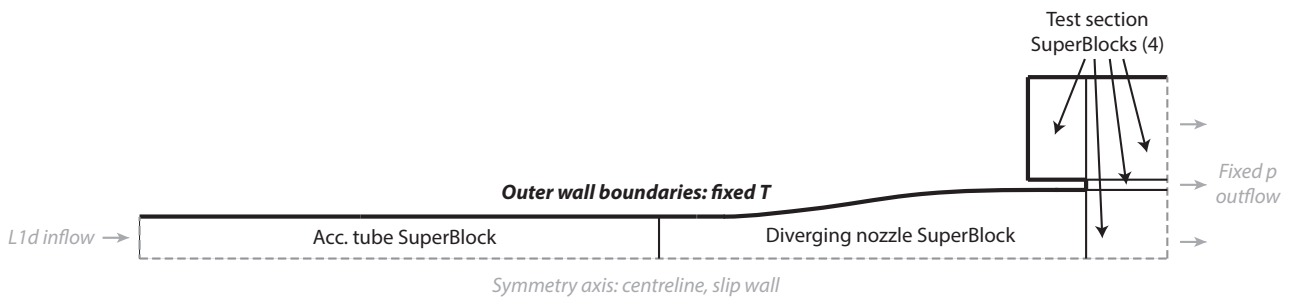


Figure 3.6: X2 block layout using SuperBlock constructor, and boundary conditions.

The general layout of the simulation domain is illustrated in Figure 3.6, showing the inflow at the tertiary diaphragm station, the acceleration tube, the diverging nozzle protruding into the test section, and the outflow boundary that slices through the test section. The dimensions around the nozzle exit

are simplified, since the hypervelocity conditions should mean that the test time is complete before reflected shocks impinge on the core flow. Once the defining nodes and boundaries are created, the structured, quadrilateral cells create the grid. The cells are clustered towards the walls to resolve the boundary layer, and towards the inflow and outflow boundaries. A coarse grid was initially applied to test the equilibrium and finite-rate simulations, as well as changing the inflow condition, before refining substantially for the final results. Blocks are overlaid on the grid in SuperBlock structures, which each hold a specified number of blocks in the x and y direction. These overarching structures are shown in Figure 3.6, and the numbers of blocks allocated, balance critical points in the simulation with the number of processors for efficient simulations. Generally, 64 blocks were assigned to 64 processors and equilibrium simulations would complete in around 48 hours.

The grid convergence was examined through a range of parameters, for three grid spacings: the most refined case, used for the final simulations, a less refined grid with 50 % of the cells and the coarsest grid with 25 % of the cells. The plots are provided in Appendix A. The radial flow parameters at 50 % of the nominal test time are shown in Figure A.1 and are nearly identical for v_x and T . A slight deviation in pressure and density for the most refined grid indicates a flow feature that may not be distinguishable on the coarser grids, but in general, the results are similar enough to suggest the most refined grid is reasonable for the final simulations. The pressure histories for the three grids were plotted for the at6 transducer location in Figure A.2a, and for the nozzle exit in Figure A.2b. Both cases show adequately similar traces, despite the unsteady expansion causing larger differences in the nozzle exit traces.

In Figures A.2c through A.2f, the nominal test time averaged properties are presented just above the nozzle centreline in y (0.15 m) and at the model location in x for the three grids. A Richardson extrapolation process has been applied to estimate the value at zero grid spacing [85], and the fits are most favourable for v_x and T , showing little deviation between the grids. The middle grid, with 50 % of the cells, is defying the trend in terms of pressure and density, and the larger unsteadiness is evident in the deviation between these parameters and the estimated zero grid spacing value. It is difficult to assess the grid convergence of a simulation with a transient, hypervelocity flow, and Gildfind [6] saw similar effects and difficulties when trying to compare three facility simulation

grids. The radial comparisons, pressure histories and model location parameter comparisons show enough similarities to consider the grid converged to a level sufficient for this study, where a main aim is simplifying facility simulations. Future work could investigate improving methods to assess grid convergence of these transient and complex simulations.

3.1.5.5 Final simulation

The numerical facility simulation was continued in *eilmer3* from the *L1d3* results obtained to the tertiary diaphragm station and the grid and parameters outlined in the previous sections. Results of interest include secondary shock speeds and pressure traces in the acceleration tube, and conehead pressure at the model location, as they can be compared to experimental measurements. Flow parameters in the test section are useful for attempting to characterise the flow, especially when contrasted against *Pitot* estimations and true flight values in the results table.

The acceleration tube traces from a single shot, the campaign average and the *eilmer3* facility simulation are plotted for at4, at5 and at6 in Figure 3.7. Traces from at1, at2 and at3 have been omitted as the latter transducers provided more trustworthy results. The campaign average is over 34 shots and the time base is continued from the *L1d3* simulation through the *eilmer3* simulation. The experimental pressures again show good consistency across the campaign for each transducer, as the campaign average is very similar to the single example shot, even maintaining the highly repeatable noise in the signals. The post-rise experimental pressures remain steady and very similar in magnitude for approximately 40 μs before the CFD trace begins to increase, and the discrepancy could be due to transducer response lag or higher compression in the CFD case. As expressed in Figure 3.8 and Table 3.4, the secondary shock speeds from the *eilmer3* simulation are slower than the experimental averages, which could be a consequence of the difference in pressure. The secondary shock speed builds through the acceleration tube and the velocity at the model location in Table 3.4 shows significant growth as the flow expands through the nozzle. The numerical and experimental primary shock speeds have minimal difference in magnitude indicating reliability in the *L1d3* simulation for this condition, but the *Pitot* theoretical value is about $200 \text{ m} \cdot \text{s}^{-1}$ lower. The issues with relying upon the *Pitot* theoretical values are further revealed in the overestimate

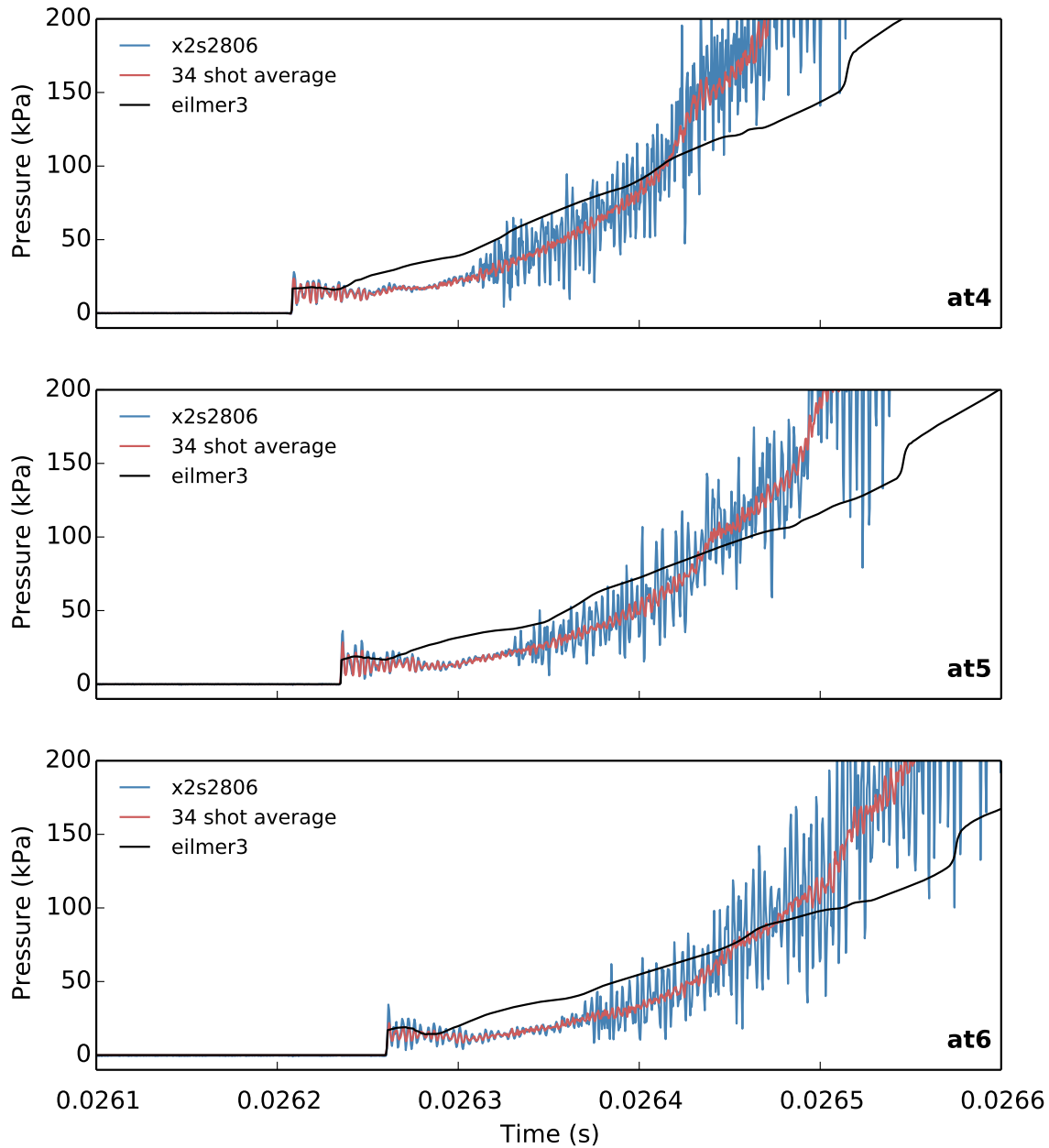


Figure 3.7: Acceleration tube transducer pressure traces from *eilmer3*, a single shot and the campaign average, across 34 shots. Time base referenced to the *L1d3* simulation.

of the secondary shock speed, underlining the importance of adjusting the *Pitot* calculation with experimentally measured shock speeds. Error bars on the campaign average shock speeds are an average on the uncertainties in selecting the initial rise in post-processing, and were cross-checked with the standard deviation to ensure the rise uncertainty was appropriate. Shock tube transducers acquired pressure rises that were better defined than the acceleration tube transducers, potentially

due to the lower speed, and also because at lower speeds and longer times of flight, the same Δt error produces a smaller error in v . Therefore the primary shock speeds carry less uncertainty than the secondary shock speeds, and this is also evident in the shape of the traces, shown in Figures 3.3 and 3.7.

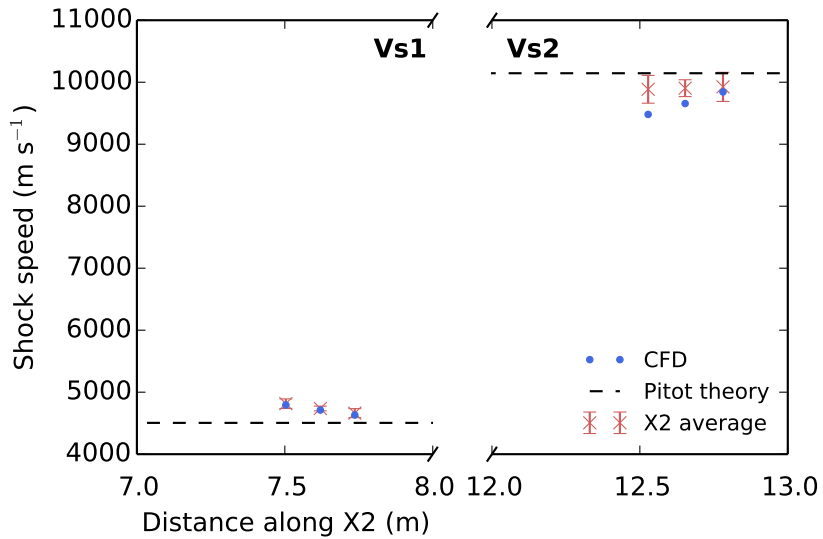


Figure 3.8: Comparison of campaign average shock speeds with error bars, *L1d3* and *eilmer3* shock speeds, and theoretical *Pitot* shock speeds. Locations are the average distance between the two transducers.

The numerical conehead pressure was calculated by performing an *eilmer3* simulation of the transient flow over a single 15° conehead located at approximately 30 mm downstream of the nozzle exit, as in the experiments. The history data recorded during the facility simulation became the transient inflow to the calculation, which used the same simulation parameters as the facility simulation, and a grid clustered to the conehead surface. Several history locations were recorded along the cone surface and returned similar traces, hence the trace quoted in the results is from a location close to the holes on the experimental coneheads [6]. Traces from coneheads 6 and 8 (the central conehead, 5, was not functional in the Hayabusa condition tests) were plotted alongside the numerical conehead pressure in Figure 3.9 with a shifted time base to match the facility simulation. Following the preliminary condition test shots and post-test analysis with *Pitot*, and based upon previous experiments, it was decided that the photodiode trigger delay time would be $50\ \mu\text{s}$ and the nominal test time for recording spectra would be $10\ \mu\text{s}$. This will be explained in greater detail in Chapter 4. However, as the numerical simulations were not completed before the beginning of the experimental campaign, these are the

constraints that must be applied to test time selection in the numerical results, based on the assumption that the photodiode triggers at the initial peak in pressure around 0.02648 s. The percentage change of, or uncertainty in, the conehead pressures over the test time from the average value are provided in Table 3.4.

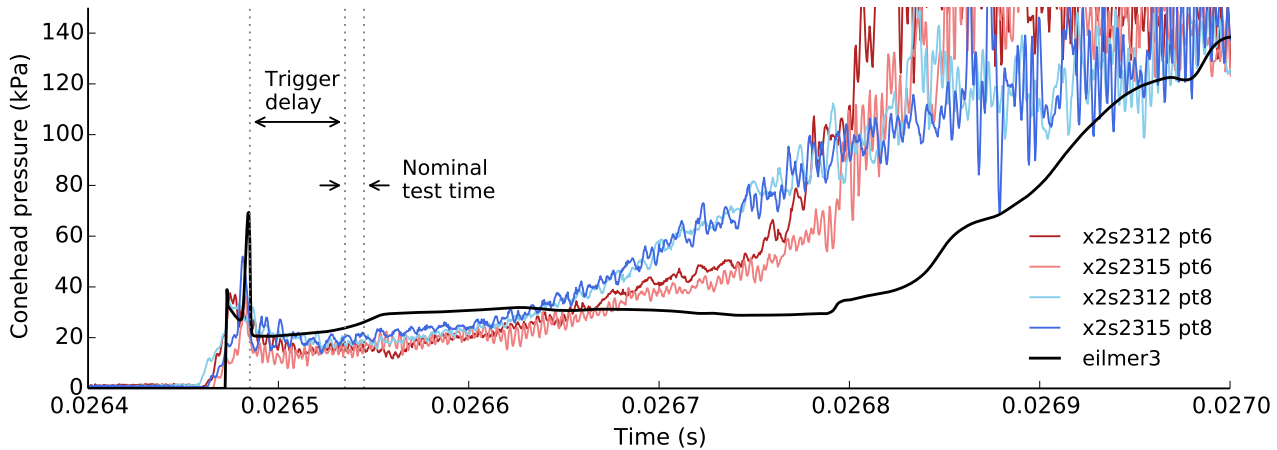


Figure 3.9: Conehead pressure at the model location, 30 mm downstream of the nozzle exit, nozzle/test section centreline. Time base referenced to facility simulation.

The experimental conehead pressures follow a similar rise to the numerical conehead pressure and have similar values through the first half of the trigger delay. From this time, the numerical conehead pressure grows slightly faster than the experimental traces, and maintains a fairly constant value while the experimental values continue to grow. At about 0.0268 s, where the experimental flow becomes exceedingly noisy, the numerical pressure also begins to rise more rapidly, indicating some consistency between the numerical and experimental test flow. The shift in the numerical trace during the experimentally determined test time is also seen in the static pressure (Figure 3.10) but could be a consequence of the simulation rather than a realistic flow feature. The greatest error in the conehead could be coming from the x -velocity, as this dominates the calculation of Mach number and is therefore present in every step of the shock relations. There is a small possibility that a systematic offset was present in the calibration rig, as all the transducers were calibrated immediately prior to the condition tests, and that all the experimental traces are shifted. The conehead pressure appears to have a weaker variation than the static pressure profile in Figure 3.10, and so the identification of a steady flow region and presuming its application to all flow parameters may be flawed. As the pitot, and thus

conehead, pressures will vary with ρv^2 , the *eilmer3* simulated decrease in velocity is compensating for the simulated increase in density, producing an overall variation in simulated conehead pressure that is more constant in time than ρ or v individually. The conehead pressure hovers between the static and pitot pressure, and affected by the ρv^2 combination, will have a weaker variation than static pressure.

Static pressure, x -velocity, temperature and density at the model location are plotted in Figure 3.10. The standout feature is the lack of steadiness after the rise in the pressure, x -velocity and density plots, despite the hypothesis of ‘steady flow’ to produce the scaled flight conditions. If the real flow does follow the trends of the numerical flow, the freestream conditions incident on the model will be transient, with the high likelihood of producing a shock layer with changing conditions. The trigger delay and nominal test time are plotted as identified in Figure 3.9. The temperature, although much higher than flight freestream and approximately 1000 K higher than in the finite-rate flows, is steady across the plot and static pressure has a slow rise, following the same trend as the simulated conehead pressure. Despite the transient qualities of numerical flow properties, the average x -velocity and density presented in Table 3.4 are close to the desired values (flight, or scaled flight). The lower simulated x -velocity is acceptable because part of the total enthalpy will be provided by specific enthalpy terms, based on the shock-heated X2 freestream temperature. A simple estimation of the total enthalpy using *eilmer3* thermodynamic curve fits [65], and a C_p of $1297 \text{ J} \cdot \text{K}^{-1}$ calculated by assuming air at $T = 3100 \text{ K}$ (as in Figure 3.10), shows that the incoming x -velocity may need to be 100 to $200 \text{ m} \cdot \text{s}^{-1}$ lower to maintain the flight target total enthalpy. The higher density is an unfortunate outcome of attempting binary scaling in X2 conditions, where there are uncertainties in experimental measurements and differences to the analytical design tools.

In tandem with the axial profiles shown in Figure 3.10, the radial properties at the model location are plotted in Figure 3.11. Slices are based around the start of the nominal test time identified in Figures 3.9 and 3.10, which is set as the $0 \mu\text{s}$ reference time, and the end of the nominal test time is at $10 \mu\text{s}$. The other plotted times are to show the development of the flow before the nominal test time, and the deviation away from the $0 \mu\text{s}$ and $10 \mu\text{s}$ values following the nominal test time. The temporal steadiness in temperature is seen radially as well as axially, and the radial profiles of

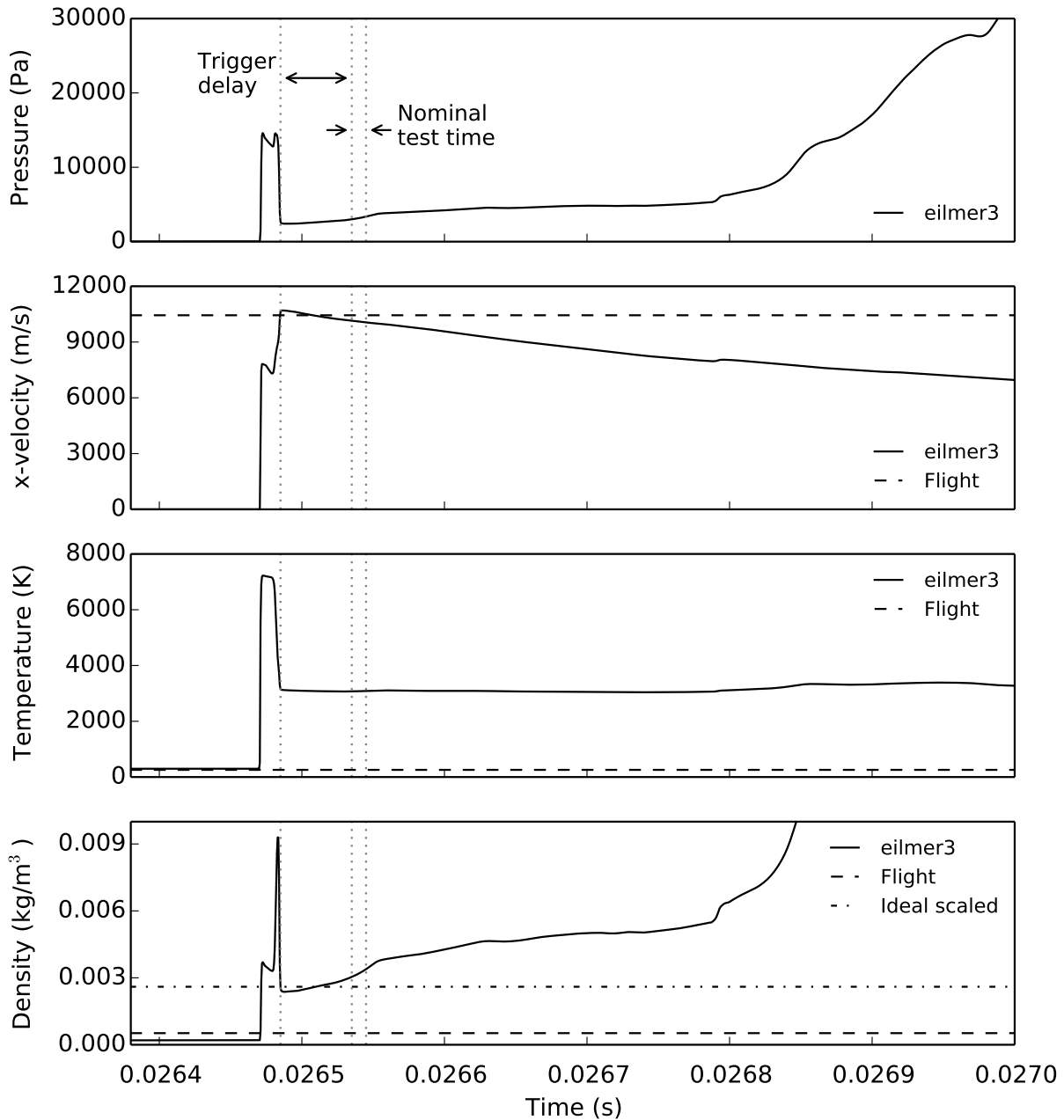


Figure 3.10: Flow properties at the model location, 30 mm downstream of the nozzle exit, nozzle/test section centreline. Time base referenced to facility simulation.

temperature and x -velocity are extremely uniform until the boundary layer slows and heats the flow. There are small radial variations in pressure and density, as well as the temporal variations already identified in Figure 3.10. The steadiest radial flow across each plotted variable can be seen in the $10\ \mu\text{s}$ slice, which corresponds to the end of the nominal test time, and the difference to parameters at the start of the test time ($0\ \mu\text{s}$) is adequately small considering the inherent unsteadiness of the flow.

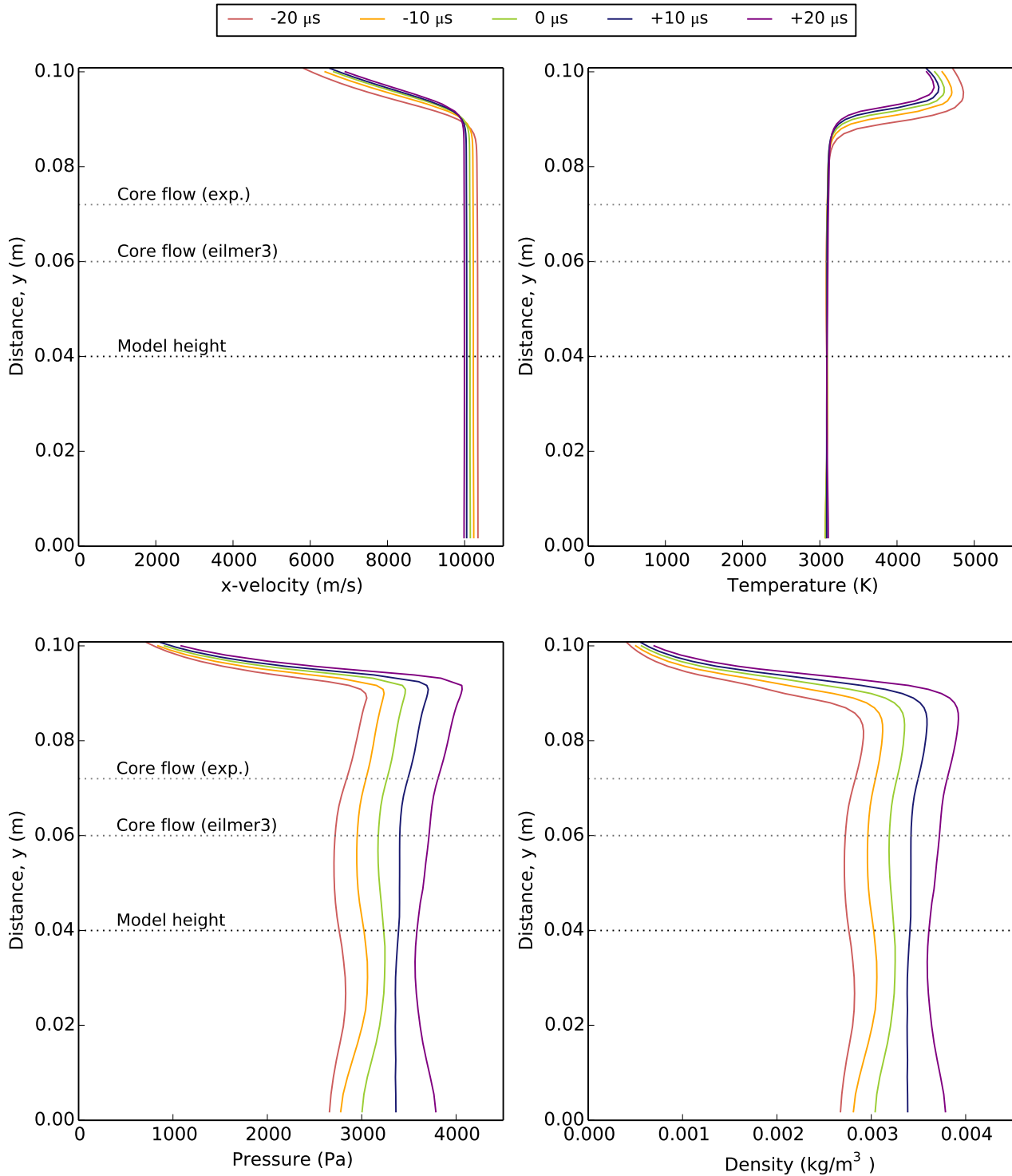


Figure 3.11: Radial flow properties at the model location, 30 mm downstream of the nozzle exit, extending from the nozzle/test section centreline to the nozzle exit height (used as reference height). The 0 μs time refers to the start of the nominal test time.

All significant radial variation occurs beyond the nominal *eilm3* core flow mark at 60 mm from the centreline, comfortably fitting the model height at 40 mm. There is increased pressure and density variation near the nominal experimental core flow mark as identified by the conehead traces, but this is far enough above the model edge that there should be no impact on the flow around the model.

A selection of the Hayabusa flow properties measured in X2 and calculated by *Pitot*, *L1d3* and *eilm3* are presented in Table 3.8. The *Pitot* properties in the last section of the table are referenced to the nozzle exit rather than the model location due to the nature of the calculation, but from analysis of the *eilm3* simulation, there are negligible differences between the two locations during the test time. The campaign average shock speeds were implemented in the referenced *Pitot* calculation, and parameters such as conehead pressure, density and velocity compare well with experimental or CFD, meaning *Pitot* in experimental mode provides a reasonable estimation of the flow properties for this condition.

The numerical primary shock speeds all fall within the experimental uncertainties, but two of the three *eilm3* secondary shock speeds are beyond the range of the experimentally measured values. This affects the velocity at the model location as compared to *Pitot*, but the real comparison should be to the flight equivalent speed, which has a component influenced by temperature. The heated freestream raises the stagnation enthalpy to beyond the flight value, and the CFD calculated density (in equilibrium) is higher than the desired scaled value and just beyond the uncertainty range. Hence, the shock layer properties over the model will be affected, and most likely overestimated. With nonequilibrium chemistry, however, the freestream density would likely be even higher, as indicated in Figure 3.4. If the Mach number of the *eilm3* calculation is correct, the nozzle is operating within its design capabilities for this condition [49]. The test time in CFD and *Pitot* is within a few μs but is enough to accommodate the trigger delay and recording time. Further simulations of this condition should investigate if the total enthalpy can be reduced through more detailed modelling of thermochemistry, including analysis of the applicability of current models to scaled expansion tube flows.

Flow property	Flight (freestream)	Pitot (theory)	Pitot (exp)	Experiment (X2)	L1d3	eilmer3
<i>Shock tube</i>						
Primary v_s (sd1-sd2) ($\text{m} \cdot \text{s}^{-1}$)	-	4505	4738	4815 ± 77	4794	-
Primary v_s (sd2-sd3) ($\text{m} \cdot \text{s}^{-1}$)	-	4505	4738	4662 ± 73	4632	-
Primary v_s (sd1-sd3) ($\text{m} \cdot \text{s}^{-1}$)	-	4505	4738	4737 ± 38	4712	-
<i>Acceleration tube</i>						
Secondary v_s (at4-at5) ($\text{m} \cdot \text{s}^{-1}$)	-	10145	9905	9886 ± 224	-	9481
Secondary v_s (at5-at6) ($\text{m} \cdot \text{s}^{-1}$)	-	10145	9905	9925 ± 235	-	9843
Secondary v_s (at4-at6) ($\text{m} \cdot \text{s}^{-1}$)	-	10145	9905	9904 ± 136	-	9656
<i>Model location plane ($x=3\text{mm}$ downstream of nozzle exit)</i>						
<i>/ Nozzle exit (Pitot results)</i>						
Static pressure (Pa)	38	1378	1755	-	-	$3044 \pm 16\%$
Conehead pressure (kPa)	-	20.5	21.7	$20 \pm 10\%$	-	$24.5 \pm 6\%$
Pitot pressure (kPa)	-	-	-	-	-	$308.0 \pm 12\%$
Density ($\text{kg} \cdot \text{m}^{-3}$)	5.2×10^{-4}	2.6×10^{-3}	2.7×10^{-3}	-	-	$3.1 \times 10^{-3} \pm 16\%$
(scaled)		2.6×10^{-3}				
Velocity ($\text{m} \cdot \text{s}^{-1}$)	10440	10414	10382	-	-	$10216 \pm 2\%$
Static temperature (K)	258	1860	2224	-	-	$3087 \pm 0.4\%$
Stagnation enthalpy ($\text{MJ} \cdot \text{kg}^{-1}$)	54.5	54.2	53.9	-	-	$58.1 \pm 4\%$
Mach number	32.4	12.4	11.5	-	-	$9.6 \pm 2\%$
Core flow diameter (mm)	-	-	-	144	-	120
Test time (μs)	-	58	57	100	-	60

Table 3.4: Flow properties: Hayabusa condition

Altitude (m)	Velocity ($\text{m} \cdot \text{s}^{-1}$)	Density ($\text{kg} \cdot \text{m}^{-3}$)	Total Enthalpy ($\text{MJ} \cdot \text{kg}^{-1}$)
68900	11900 - 12200	8×10^{-5}	72 - 74

Table 3.5: Nominal flight parameters for Stardust 9:57:26 UTC trajectory point.

3.2 Stardust Condition

3.2.1 Trajectory point selection & condition matching

The ECHELLE spectra observation window for the Stardust flight differed from Hayabusa, running from the border between rarified and continuum regions at approximately 81 km altitude and $12.8 \text{ km} \cdot \text{s}^{-1}$ speed, down to 68.9 km altitude and $12 \text{ km} \cdot \text{s}^{-1}$ speed. Peak heating followed about six seconds after the end of the observation. At the lowest altitude observation point (9:57:26 UTC), the density was still very low, at about $8.0 \times 10^{-5} \text{ kg} \cdot \text{m}^{-3}$ [15], and such a low density even when scaled presents large condition design challenges for reproduction in X2. Low test flow densities require reasonable pressures in the shock tube but low pressures in the acceleration tube and test section, as well as an extremely high flight equivalent speed for an air flow, push the edge of the X2 operating envelope. The 9:57:26 UTC trajectory point was therefore selected due to having the highest density of the observed spectral data, and the flight parameters are quoted in Table 3.5 [25]. There is some discrepancy between the shock speeds in Jenniskens ($12.2 \text{ km} \cdot \text{s}^{-1}$) [15] and Trumble *et al.* ($11.9 \text{ km} \cdot \text{s}^{-1}$) [25] so both are quoted here.

Following the binary scaling principle and upper core flow constraint from Section 3.1.2, the maximum possible Stardust model scale is one-tenth, since the flight vehicle diameter was approximately twice that of Hayabusa. The characteristic model length is the 22.86 mm nose radius, which results in a target test density of $8 \times 10^{-4} \text{ kg} \cdot \text{m}^{-3}$ from Equation 2.1.

3.2.2 Design Iterations and Analysis

The design of the Stardust condition followed the same procedure as for Hayabusa in Section 3.1.3, except more iterations between *Pitot* calculations and experimental testing were required. Aiming for such a high flight equivalent speed meant required high primary and secondary shock speeds, but

Reservoir	Driver	Shock tube	Acceleration tube	Primary shock speed	Secondary shock speed
6.85 MPa air	928 kPa, 98 % He, 2 % Ar	6000 Pa air	3 Pa air	5444 m · s ⁻¹	11 609 m · s ⁻¹

Table 3.6: Fill pressures and experimental shock speeds for final Stardust condition (shot x2s2701).

this objective could not come at the expense of increased density through the nozzle exit and into the test section. Several possible conditions were created by selecting fill pressures as input to *Pitot* in theoretical mode, but there were large variations in some variables upon testing. The primary shock speed was underpredicted in *Pitot* by about 400 m · s⁻¹, and the gas was over-expanded through the acceleration tube, making the nozzle entry pressure four times smaller in the theoretical calculation.

Changes to the conditions were tested experimentally and iteratively until the desired outcome was achieved. To combat the higher than expected primary shock speed, a small amount of argon was added to the driver, which was originally operating with 100 % helium. The driver would operate off-design as the change in contraction ratio provided by an orifice plate for a 100 % He condition would be marginally different to a new orifice plate specifically created for this 98 % He, 2 % Ar condition. This lowered the primary shock speed as desired; however, it also reduced the secondary shock speed and the density was not lowered enough as a result. The acceleration tube fill pressure was dropped to 3 Pa in order for a sufficiently fast secondary shock to hold the test nozzle exit density around the desired value. Table 3.6 provides the final fill pressures and approximate experimental shock speeds for the Stardust condition.

Experimental results from shots x2s2700 and x2s2701 show that the condition was adequate for simulating the 9:57:26 UTC trajectory point with a 1/10 scale model. Several conehead pressure traces, the trigger recording (qualitative rise shown, but recorded during the pitot shots) and video stills illustrate the steady flow time and other flow features in Figure 3.12. There is a small discrepancy in the conehead pressure readings between the transducers within the steady flow time, but the uniformity of the flow during this time is evident in the high-speed video, as shown in Figures 3.122 and 3.123. The negative dip on two of the transducers, as well as the test time discrepancy, could be caused by sensitivity to vibrations transmitted into the test section. Coneheads 5 and 7

may have been more sensitive to vibrations due to different mounting or clamping forces, or higher sensitivity of the transducer itself to fluctuations, and thus it is difficult to draw conclusions from such traces. Coneheads 1 and 3 exemplify the expected transducer responses, potentially because of better mounting or clamping inside the rake, and will be called upon for further analysis. The conehead traces and video show uniformity in the axial direction out to conehead 1 at the top of the rake, indicating the core flow is at least as wide as the pitot rake. It should be large enough to comfortably fit the 1/10 scale Stardust model.

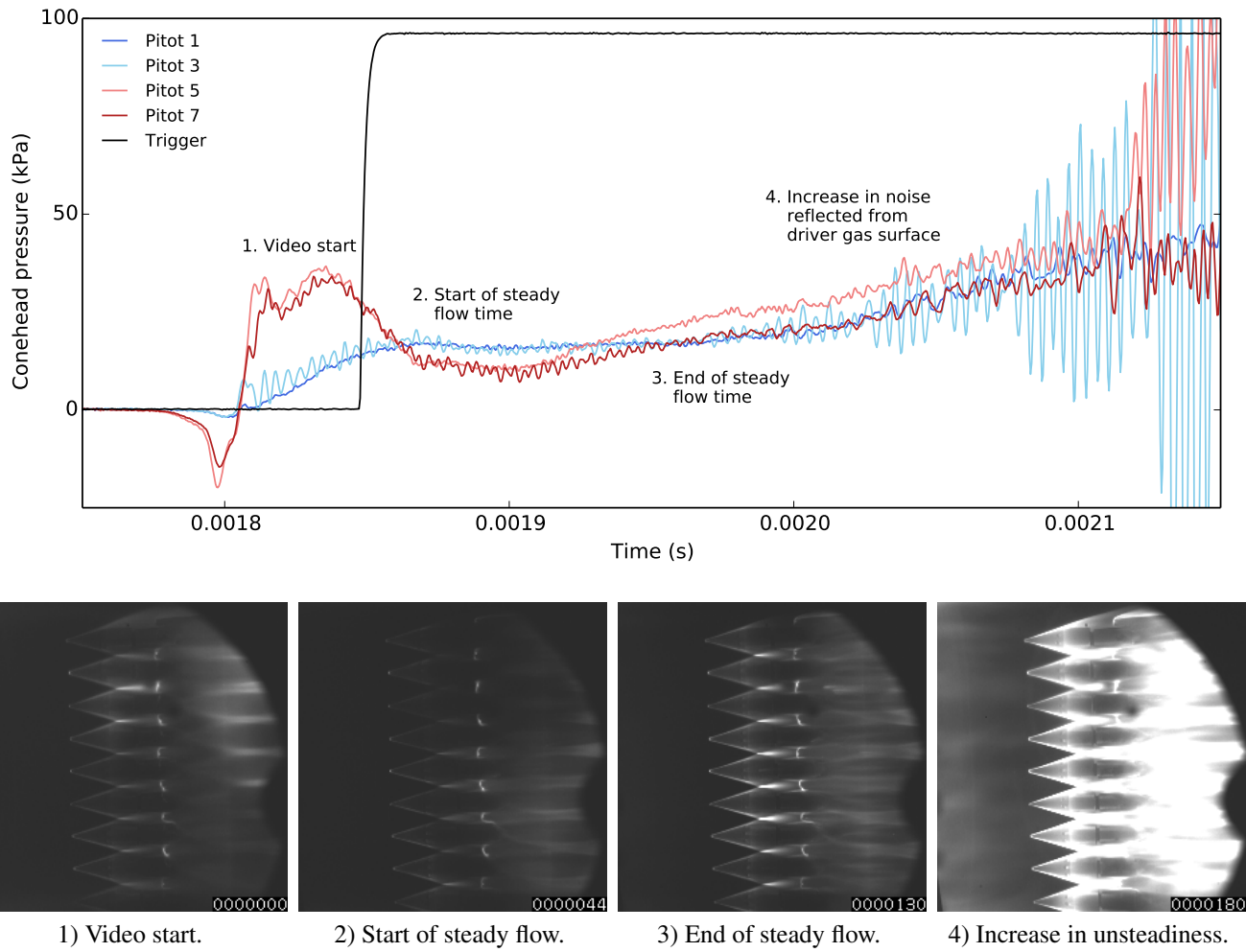


Figure 3.12: Stardust 9:57:26 UTC flow condition mapped through conehead pressure data and video stills.

The inconsistencies between *Pitot's* equilibrium theoretical mode, and experimental equilibrium results determined from measured shock speeds are evident in Table 3.7. Although the total enthalpy

	Density (kg · m ⁻³)	Eq. velocity (m · s ⁻¹)	Total enthalpy (MJ · kg ⁻¹)	Temperature (K)	Pressure (Pa)	Conehead pressure (Pa)
Ideal (scaled flight)	0.0008	12 000	72	–	–	–
Pitot (experiment)	0.0008	12 200	74.4	2477	570	10847
Pitot (theory, eq)	0.00025	12 118	73.4	1763	129	2804

Table 3.7: Theoretical and ideal scaled (where known) conditions at the nozzle exit for final Stardust condition.

and flight equivalent speed are similar, there is a difference of almost four times between the densities and pressures at the nozzle exit. The conehead pressure calculated from measured shock speeds is close to the plotted conehead pressure in Figure 3.12, and the scaled or matched parameters are close to the ideal values.

There were concerns that lowering the acceleration tube pressure, in combination with a low-density test gas and high-speed shock would cause the flow to move beyond the continuum regime. The Knudsen number, a non-dimensional ratio of the molecular mean free path to a physical length scale, should be below the threshold of 0.01 to indicate that the flow is continuum. Using the flow parameters from experimental data and equilibrium analysis of x2s2701, and the model radius as the worst-case characteristic length scale, the Knudsen number was 0.0035, therefore the Stardust condition appears to be in the continuum regime. This finding is consistent with Boyd *et al.*'s Stardust simulation work [68].

This condition was designed with a 1/10 scale model in mind. A smaller scale model would require a higher nozzle exit density through binary scaling, but for these experiments, the largest possible model was desired to make the shock stand-off as large as possible for imaging and rebuilding of the shock layer. Had the final condition (6000 Pa shock tube, 3 Pa acceleration tube) not been achievable, moving to a smaller scale would have been unavoidable. Future works for similar experiments could consider a slightly smaller model so that X2 is more capable of providing the required density, and this would be necessary if looking at other observed trajectory points, which all have lower densities than the Stardust trajectory point considered here.

3.2.3 Combined *L1d3* and *eilmer3* facility simulation

The combined facility simulations for Stardust followed the procedures and lessons learned from the Hayabusa condition simulations in Section 3.1.5. The *L1d3* simulation set-up was the same, except for a mesh scale of 3.0 to adequately capture the higher primary and secondary shock speeds. Shock tube pressure traces and primary shock speeds were obtained from the *L1d3* calculation. The sd2 trace in Figure 3.13, and the acceleration tube traces in 3.14, show good consistency between the single shot and campaign average. In the shock tube, the experimental traces overpredict the numerical trace beyond the initial few microseconds post-rise, but this reverses in the acceleration tube traces, where there is a near systematic offset between CFD and experiment after the rise and first period of steadiness. However, the shock speeds are the most important property calculated from the consistent rises, and the post-rise effects of vibrations or electrical noise in the transducers do not affect the shock speeds. The noise in the initial 15 μ s of flow is minimal in the single shot and campaign average traces, and the pressure is very small due to the attempted low-density condition.

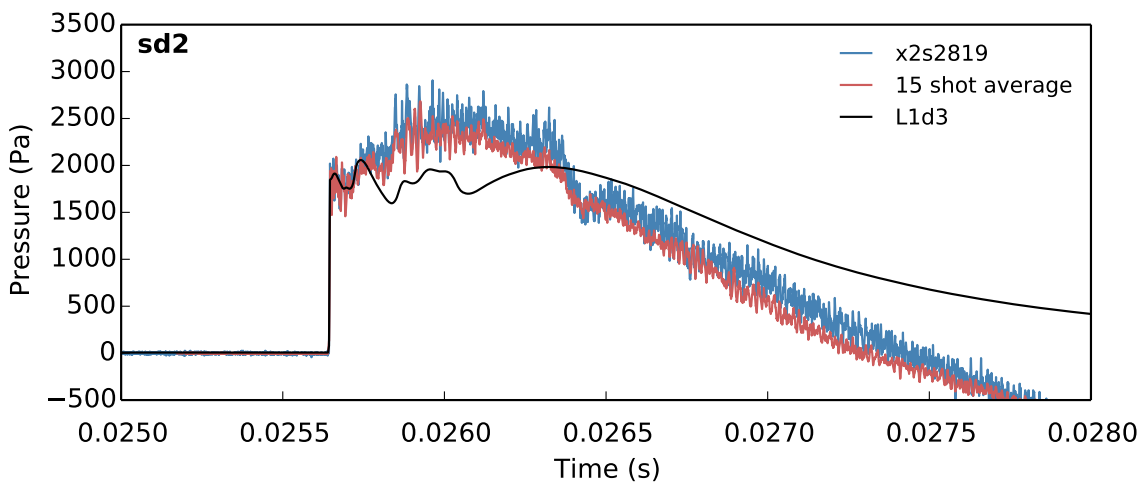


Figure 3.13: sd2 shock tube transducer pressure trace from *L1d3*, a single shot and the campaign average, from 15 shots. Time base referenced to the *L1d3* simulation.

The main concern that arises from the primary shock speed comparison in Figure 3.15 is the disparity between the numerical and experimental primary shock speeds. There was a loss in driver performance across the latter part of the campaign, which is particularly reflected in the Stardust results as these shots were generally performed later than the majority of the Hayabusa shots. The

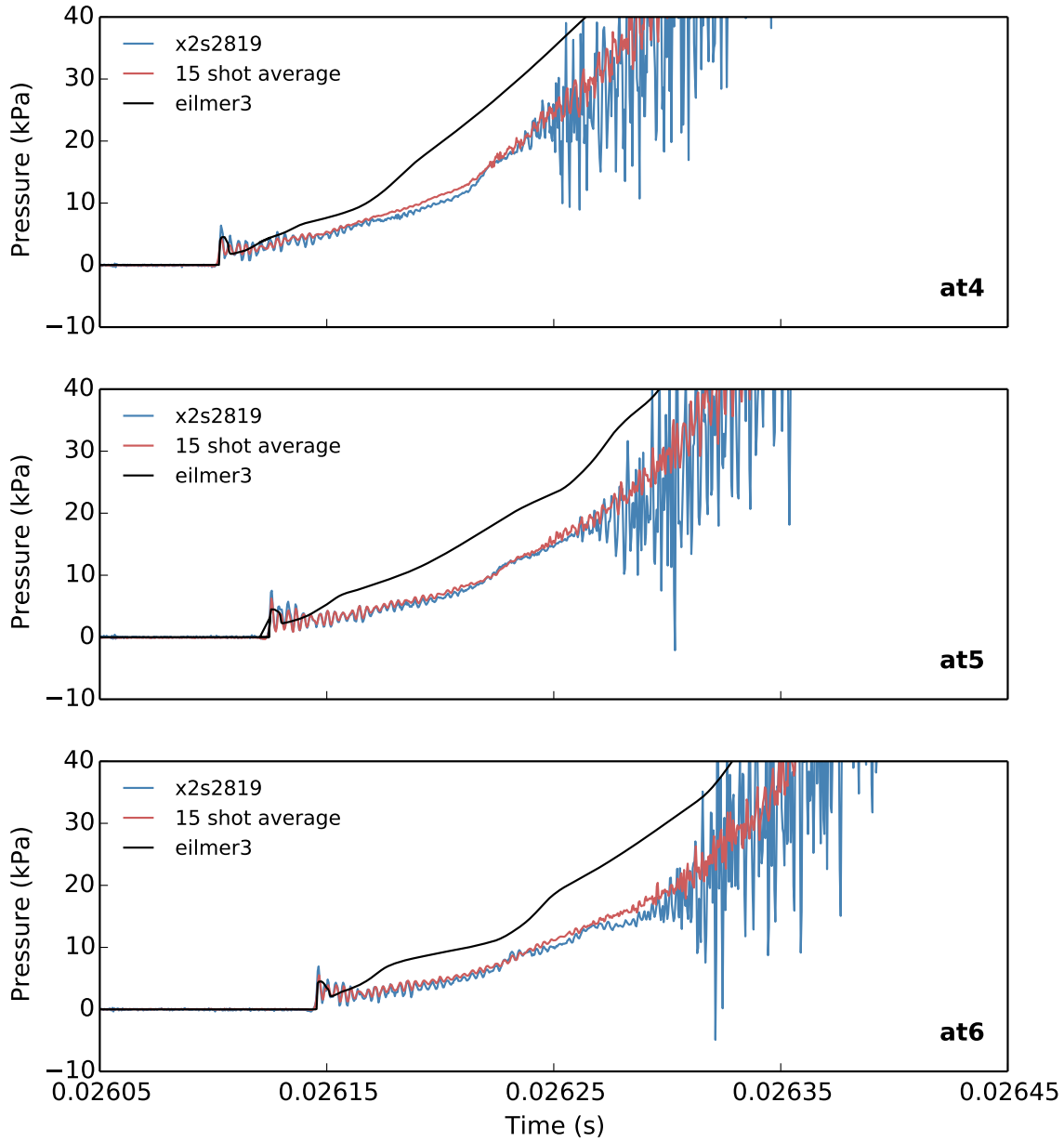


Figure 3.14: Acceleration tube transducer pressure traces from *eilmer3*, a single shot and the campaign average, from 15 shots. Time base referenced to the *L1d3* simulation.

cause is unknown, but there were problems with the piston seals and wear on the buffers that stop the piston, due to off-design driver operation, as well as a series of leaks in the shock tube section. Despite the difference in v_{s1} , the performance seems to improve with the massive increase in speed past the secondary diaphragm, as the CFD and experimental v_{s2} match within the experimental uncertainty. The *Pitot* theoretical shock speeds are significantly different due to the previously mentioned issues with this calculation mode, especially for the tedious Stardust condition.

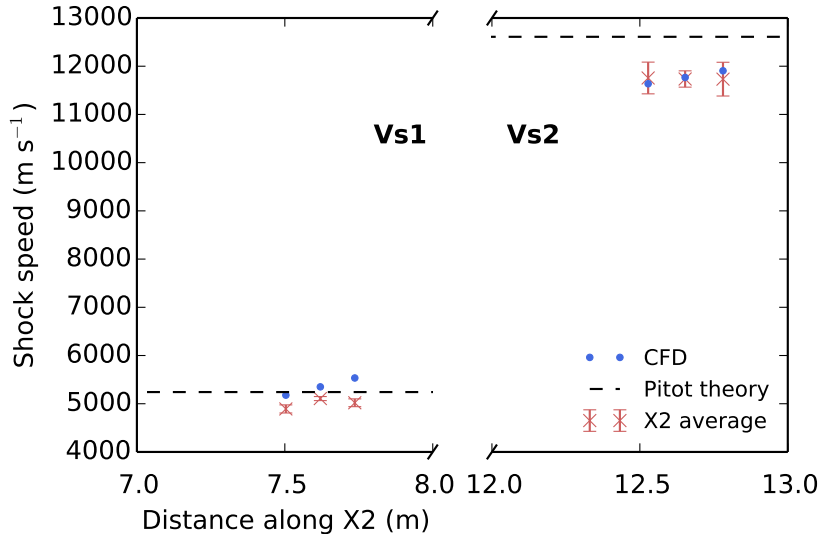


Figure 3.15: Comparison of Stardust campaign average shock speeds with error bars, *L1d3* and *eilmer3* shock speeds, and theoretical *Pitot* shock speeds. Locations are the average distance between the two transducers.

Observing the experimental traces and trigger only, in Figure 3.12, it appeared that the steady test time started at about 0.0264 s as referenced to the time base in Figure 3.16. The selection of nominal trigger and measured test times, as for Hayabusa, are constrained by the known settings for the experimental campaign. In the Stardust case, knowledge of the experimental trigger time against the experimental conehead pressure traces is critical to interpretation of the numerical results, again calculated by simulating the transient flow over one conehead. Unfortunately, this trigger was not recorded when the Hayabusa condition test shots were conducted. The position of the experimental trigger is not obvious in the experimental traces, and the slow, small rise could be a consequence of the extremely high speed, low density and low pressure flow, as seen in the small rises of the acceleration tube transducers. However, the numerical trigger needs to occur at the same time as measured in experiment, and therefore the experimental trigger and conehead traces are shifted to meet the sharp rise in the numerical results that would cause a trigger to occur. The trigger delay and nominal test time then follow in Figure 3.16. Through the trigger delay time, the numerical conehead pressure is rising towards the experimental values, and during the nominal test time, the numerical conehead pressure is almost identical to the *Pitot* experimental value. Similar to the Hayabusa results, the conehead pressures appear steadier in the experimental results than the numerical results. The conehead pressure and its percentage change over the test time is quoted in Table 3.8.

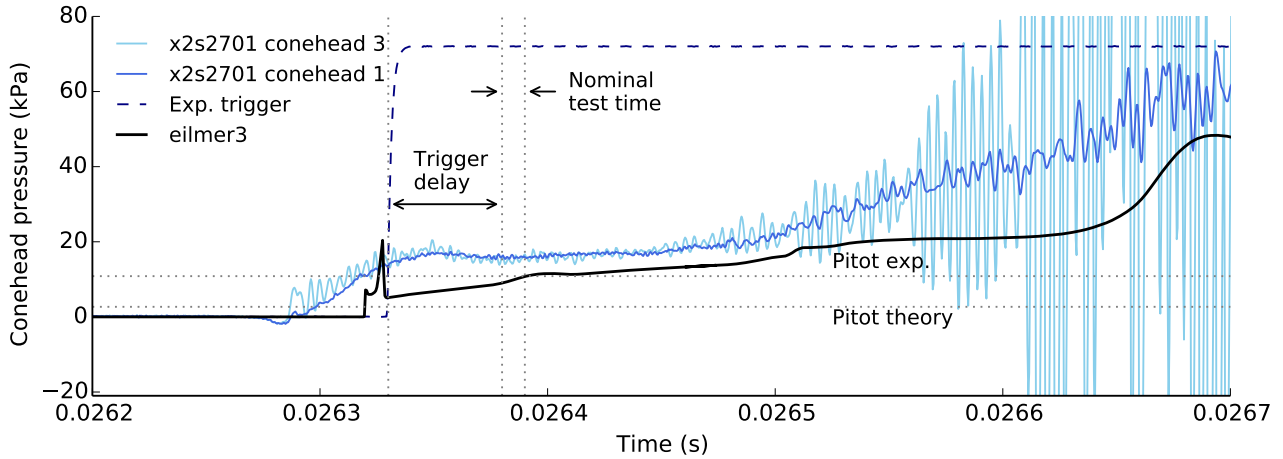


Figure 3.16: Conehead pressure at the model location, 30 mm downstream of the nozzle exit, nozzle/test section centreline. Time base referenced to facility simulation.

Axial properties at the nozzle and test section centreline and model location are plotted in Figure 3.17. The Stardust condition, like the Hayabusa condition, shows unsteadiness in the pressure, density and x -velocity, with no identifiable ‘steady flow’. The temperature remains steady after the initial rise but is very high at around 4000 K; this could decrease if finite-rate reactions were allowed and the dissociated products become frozen through the nozzle expansion. The nominal test time selected on the plot was based around the time at which measurements would be recorded during the experiment: 50 μ s after the rise triggers the photodiode, for 10 μ s. Fortunately, this coincides with the period around the targeted density, so the experiments should feature flow that has, on average, satisfactorily scaled conditions. However, since the x -velocity is equivalent, on average, to the target velocity, the flight equivalent velocity will be too high when the contribution of specific enthalpy is included. This is likely to cause overestimations of shock layer parameters, and therefore spectra, in scaled Stardust simulations.

Radial properties are presented from the test section centreline to the nozzle height, and at the model location, centred upon the start of the test time at 0 μ s and showing two 10 μ s increments before and after the 0 μ s point. The pressure and density variations are persistent across the core flow and in each temporal slice. The steadiest radial slice across the plotted flow parameters is the 0 μ s slice at the start of the test time, but by the end of the test time, there is a reasonable bulge in the centre of

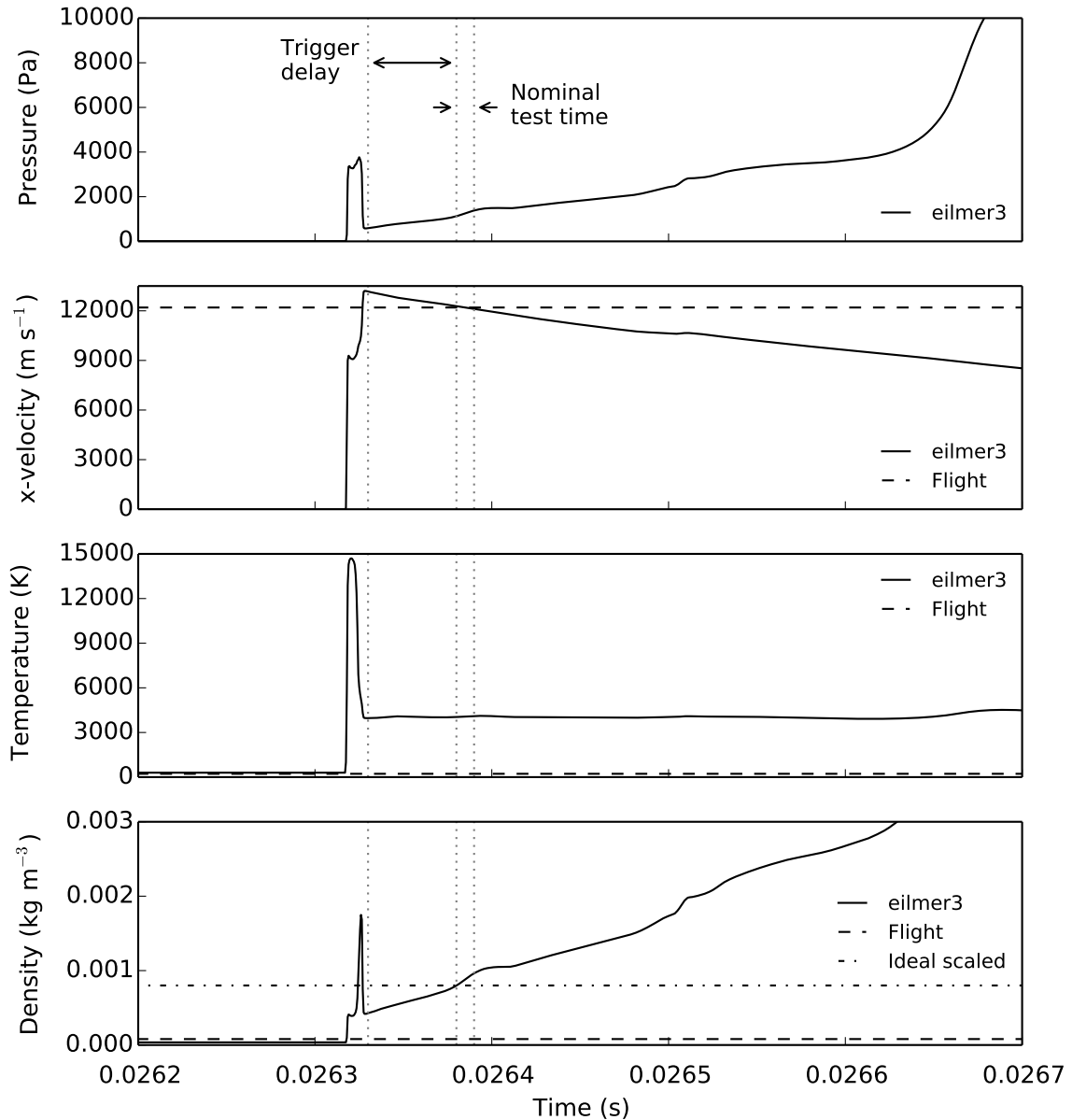


Figure 3.17: Flow properties at the Stardust model location, 30 mm downstream of the nozzle exit, nozzle/test section centreline. The 0 μ s time refers to the start of the nominal test time.

the flow. Although decreasing, the x -velocity and temperature are highly uniform throughout the core flow. The nominal *eilmer3* core flow height is less than the experimental value due to the increase in variations, especially in temperature, above the 60 mm point. Most importantly, the core flow is wider than the model, resulting in properties that are fairly uniform in space at a given time, and show small variations in time.

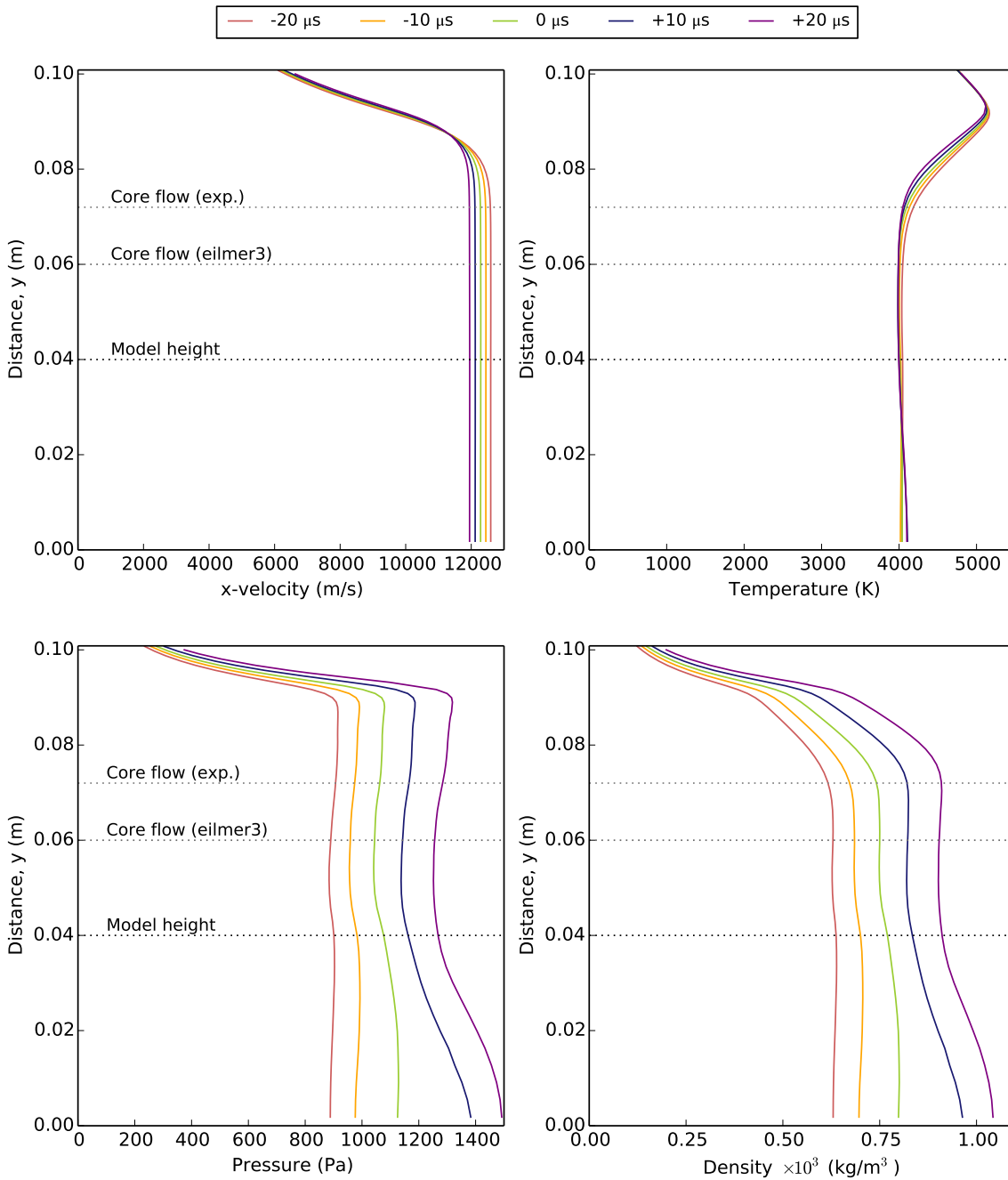


Figure 3.18: Radial flow properties at the model location, 30 mm downstream of the nozzle exit, extending from the nozzle/test section centreline to the nozzle exit height (used as reference height).

Table 3.8 summarises the flow properties calculated by *Pitot*, *L1d3* and *eilmer3*, and measured in X2 experiments, alongside the ideal flight parameters. The *Pitot* properties are again referenced to the nozzle exit rather than the model location. The experimental *Pitot* calculation was re-run with the campaign average shock speeds, and the results changed quite significantly due to v_{s1} falling by

approximately $250 \text{ m} \cdot \text{s}^{-1}$ between the condition test shots and experimental campaign. The area ratio had to be reduced to 2.5 in order for the conehead pressure and nozzle exit density to retain similar values to Table 3.7.

As illustrated in Figure 3.15, v_{s1} does not compare well, probably due to driver performance issues. v_{s2} is comparable within the experimental uncertainty but x -velocity at the model location is too high in CFD, as it seems the flow gains too much pace through the nozzle expansion. The conehead pressure and density are similar across experiment, CFD and experimental *Pitot*, and density compares well with the scaled flight value. Pressure and temperature differ between flight and experiment or CFD due to the heated freestream in X2, but also because equilibrium in CFD causes higher T and p than for a finite-rate reacting flow. This is also the reason for the higher than desired stagnation enthalpy in CFD. Mach number is overestimated in both *Pitot* modes, and if the CFD value is correct, the condition is just below the Mach 10 design point of the nozzle. Mach number is not a scaling parameter for X2 re-entry flows, therefore it cannot be compared to flight. Conservative estimates show an adequate core flow diameter and test time, during which the $10 \mu\text{s}$ should capture reasonable flow conditions. Considering the extremely high shock speeds and low acceleration tube pressure with a slight driver adjustment, the performance of the condition has been satisfactory. Future work on CFD and experimental comparisons for this condition should focus on reducing the x -velocity and temperature (if possible with the thermochemistry) at the model location, as these provide the largest discrepancies with measured data.

3.3 Conclusion

Two X2 expansion tube conditions were established for one trajectory point from each of the Hayabusa and Stardust trajectories, using a range of available methods. Initial fill pressures were estimated using *Pitot* in theoretical mode, tested in X2, and checked in *Pitot*'s experimental mode against measured shock speeds and pressures. Once the fill conditions were decided, facility simulations were run in *L1d3* and *eilmer3* to examine the performance of the numerical simulations against the simple *Pitot* analyses and experiments, and to prepare the inflow conditions for scaled aeroshell

Flow property	Flight (freestream)	Pitot (theory)	Pitot (exp)	Experiment (X2)	L1d3	eilmer3
<i>Shock tube</i>						
Primary v_s (sd1-sd2) ($\text{m} \cdot \text{s}^{-1}$)	-	5242	5108	4892 ± 84	5178	-
Primary v_s (sd2-sd3) ($\text{m} \cdot \text{s}^{-1}$)	-	5242	5108	5020 ± 81	5534	-
Primary v_s (sd1-sd3) ($\text{m} \cdot \text{s}^{-1}$)	-	5242	5108	5107 ± 42	5350	-
<i>Acceleration tube</i>						
Secondary v_s (at4-at5) ($\text{m} \cdot \text{s}^{-1}$)	-	12610	11744	11756 ± 329	-	11636
Secondary v_s (at5-at6) ($\text{m} \cdot \text{s}^{-1}$)	-	12610	11744	11732 ± 350	-	11905
Secondary v_s (at4-at6) ($\text{m} \cdot \text{s}^{-1}$)	-	12610	11744	11735 ± 169	-	11767
<i>Model location plane ($x=3\text{mm}$ downstream of nozzle exit)</i>						
Static pressure (Pa)	5	136	683	-	-	$1037 \pm 19\%$
Conehead pressure (kPa)	-	2.8	10.2	$13 \pm 7\%$	-	$11.5 \pm 6\%$
Pitot pressure (kPa)	-	-	-	-	-	$108 \pm 15\%$
Density ($\text{kg} \cdot \text{m}^{-3}$)	8.0×10^{-5}	2.3×10^{-4}	9.0×10^{-4}	-	-	$7.3 \times 10^{-4} \pm 19\%$
(scaled)		8×10^{-4}				
Velocity ($\text{m} \cdot \text{s}^{-1}$)	12200	12879	12055	-	-	$12437 \pm 2\%$
Static temperature (K)	224	2015	2403	-	-	$4056 \pm 1\%$
Stagnation enthalpy ($\text{MJ} \cdot \text{kg}^{-1}$)	74.4	82.9	72.7	-	-	$86.3 \pm 3\%$
Mach number	39.6	15.2	13.1	-	-	$9.5 \pm 2\%$
Core flow diameter (mm)	-	-	-	144	-	120
Test time (μs)	-	-	-	60	-	40

Table 3.8: Flow properties: Stardust condition

model calculations. Where flight trajectories are available, it is important to design conditions with binary scaling and enthalpy matching so that the results will be comparable to flight, and flight scale CFD. Both conditions had adequate shock speeds, conehead pressures, core flow and test time in experiment and were implemented for the final experimental campaigns, which focused on optical measurements of the forebody radiating shock layer. Variations in the flow parameters between experimental, numerical and analytical methods were shown in Tables 3.4 and 3.8 for Hayabusa and Stardust, respectively, and the facility simulations were useful for verifying the *Pitot* experimental results. Although there are some differences, knowing where they occur and attempting to identify why will allow updating of measurement and simulations techniques for better analysis and understanding of the condition. Many of the numerical pressure traces were similar to experiment, but more investigation is necessary to perfect the tube flow simulation. The most interesting result from the facility simulations was the lack of steadiness in fundamental flow parameters, which is much less evident in numerical and experimental conehead pressure traces and could threaten the notion of ‘steady test time’. The ability to measure any of the fundamental flow parameters at the nozzle exit or model location would be extremely useful in more detailed experimental characterisation of the flow, even though it may be difficult to achieve under such extreme flow conditions.

Chapter 4

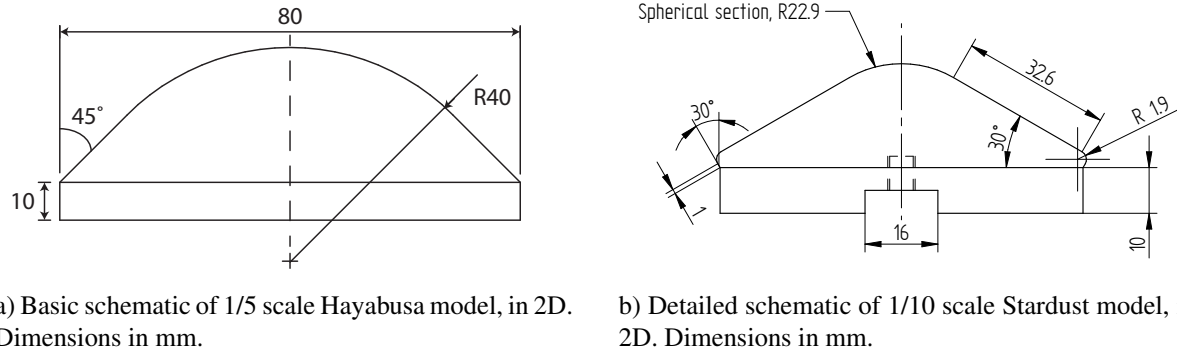
Scaled Earth Re-entry Experiments in the X2 Expansion Tube

Scaled models of the Hayabusa and Stardust Earth re-entry capsules were created, installed and tested in the X2 expansion tube at the conditions developed in the previous chapter. Several optical techniques, employing distinct optical systems and their associated components, captured specific aspects of the hypervelocity radiating shock layers surrounding the models. The design, set-up, focusing, alignment, imaging and calibration procedures are discussed, as well as validation and verification tests for the relatively new 2D imaging technique. The experimental methodology continues from the optical system set-up to the operation of the X2 facility including firing, timing and recording data, and checking the consistency of the conditions by calculating shock speeds in the tube. All experimental results and analysis will be presented in following chapters.

4.1 Model Specifications

The size of the scaled Hayabusa and Stardust models were the starting points for the experimental design processes presented in Section 3.1.2 and 3.2.1. The models are scaled, three-dimensional representations of the flight vehicles' aeroshell forebodies, as the main concern is the radiation that occurs in the bow shock, especially the region surrounding the stagnation line. The one-fifth scale Hayabusa model has a nose radius of 40 mm, and Figure 4.1a is a two-dimensional illustration of the dimensioned scale model, preserving the 45° sphere-cone geometry of the Hayabusa aeroshell. The

one-tenth scale Stardust model maintained the original vehicle's 60° sphere-cone geometry with a nose radius of 22.86 mm and shoulder radius of 1.9 mm, as illustrated in two dimensions in Figure 4.1b.



a) Basic schematic of 1/5 scale Hayabusa model, in 2D.
Dimensions in mm.

b) Detailed schematic of 1/10 scale Stardust model, in
2D. Dimensions in mm.

Figure 4.1: Schematics of scaled X2 re-entry capsule models.

The models were designed to fit an existing mount that previously supported cylindrical and spherical models of 75 mm diameter. There were small cutaways at the top and bottom of the Hayabusa model for placement of an aligning tool, which fitted to the body over the nose. The tool contained rows and columns of 0.5 mm diameter holes, in order to align a spectrometer slit either horizontally or vertically. CFD simulations demonstrated that the flow over the model would not be critically disrupted by the cutaways, as the sonic line reattaches to the body at around 30° , and there are no irregular effects on the flow from the shoulder region. The cutaways and aligning tools were not used for Stardust as vertical spectra were not taken, and the horizontal spectra and 2D imaging systems could be aligned by a digital level and the shape of the magnified nose image on the spectrometer slit. The models were manufactured from stainless steel because the experiments are cold wall, and corrosion and potential contamination of spectra could be minimised during and between tests, as compared to mild steel.

The completed, pre-test Stardust and Hayabusa models are shown in the foreground of Figure 4.2, alongside some tested models in the background. The mounting procedure in X2 is fairly straightforward: an L-shaped steel bracket attaches to a rail in the bottom of the test section and the mounting block attaches to the vertical part of the bracket at the desired height. A solid steel rod

slots into the mounting block and can be bolted in place, and the model mount slides onto the front of the rod and held in place with small screws. The models fit onto the front of the model mount and two screws pass through from the back of the mount into the model. This configuration and has been positioned to centre on the nozzle centreline, approximately 3 cm downstream of the nozzle exit. This was the same location as the upstream edge of the pitot coneheads in condition testing.

4.2 Optical Systems

The main experimental aims of this work are to perform emission spectroscopy and filtered intensity measurements on the hypervelocity radiating shock layer for flight comparison, and these measurements were conducted using several optical systems. Generally, emission spectra in X2 are oriented horizontally along the stagnation line, perpendicular to the stagnation line from a side window, to identify the intensities of selected species through different regions of the shock layer (see, for example, previous expansion tube studies [33] [56] [86]). This, alone, gives important data on the complex physical and chemical processes occurring inside the radiating shock layer. Calibrated quantitative measurements along rays intersecting the stagnation line can be useful in comparing to



Figure 4.2: Pre-test models (front) and post-test models (back). The two Stardust models are on the left, and two Hayabusa models are on the right.

CFD or numerical radiation calculations along the same line of sight. However, the non-axisymmetric profile of a horizontal measurement is unsuitable for direct flight rebuilding. Local properties are obtained through the Abel inversion, which requires an axisymmetric flowfield and line of sight integrated data from the outer radius down to the centre line, or minimum radius of interest. This data is not available from the horizontal spectra without some significant assumptions. A more detailed discussion of the need for vertical measurements to perform the mathematical deconvolution, create a radiation field and trace lines of sight in any direction, and description of the entire flight rebuilding process, is presented in Chapter 7.

Vertical slices through the shock layer over the Hayabusa model were imaged using a spectrometer with a vertical slit, and the shock layer was imaged using 2D intensity mapping. The Stardust shock layer was imaged using the 2D intensity mapping method only, as it was a secondary objective for the project to explore another vehicle and condition. The vertically oriented spectrometer slit can image a single narrow slice at any discrete streamwise location, recording a wavelength-resolved spectrum along a vertical spatial dimension. In this work, three locations upstream of the stagnation point were selected to capture the strong atomic emissions around the stagnation line. Alternatively, the recently developed 2D intensity mapping method used the ICCD camera and narrow band filters to record a snapshot of the radiation in the prescribed wavelength band, and intensity was recorded across two spatial dimensions. There are advantages and disadvantages of both methods, depending on the desired result [52]. Using a spectrometer produces wavelength-resolved data, whereas imaging through a narrow band filter means that the data is integrated across the filter band. The filter transmissivity must also be taken into account as it greatly affects the peak intensities. Imaging the entire shock layer and taking a known distance measurement, for example, the width of the calibration source, maps length dimensions correctly. Each column of pixels, corresponding to a vertical slice, has a defined width and location. On the other hand, the location of the vertically oriented spectra is harder to know definitely. Alignment is conducted using the aligning tools with the test section at a pressure below 100 Pa, because the tube sections will pull together under vacuum and may shift from their location at atmospheric pressure. The tube then needs to be vented for removal of the aligning tool and pumped down again to test conditions (17 Pa for Hayabusa; 3 Pa for Stardust), and this will almost certainly cause a sub-millimetre shift in the imaging location. The shift was tested by pumping

and venting the tube several times and taking measurements each time with the aligning tool in place. Since the adjacent 0.5 mm diameter hole never became visible, the shift would be on the order of ± 0.25 mm. The comparison between vertical spectra and 2D images can assist in assessing the location of the vertical spectra, and it is of benefit to the eventual results that these two methods are used in tandem to check against each other. Stardust was imaged only with the 2D mapping system, as the comparison between 1D and 2D methods for Hayabusa was sufficient to suggest the desired information could be obtained. Comparison with CFD is also possible for both 1D and 2D cases.

4.2.1 Emission Spectroscopy

Air shock layer radiation is the focus of emission spectroscopy measurements for Hayabusa and Stardust, as spectroscopy of axisymmetric, ablating models was beyond the scope of this work, though it is the subject of ongoing efforts [87] [88]. Hypervelocity Earth re-entry produces shock layer radiation from dissociation and ionisation of atomic and molecular nitrogen and oxygen, and the subsequent excitation processes experienced by these species. Radiation can also emanate from trace elements in the atmosphere and products of heat shield ablation and pyrolysis. Remote measurements from the Hayabusa and Stardust re-entries investigated the UV, visible and IR regions of the electromagnetic spectrum. The IR is the most appropriate to recreate in an expansion tube environment because there are a range of atomic N and O features that are dependent on the shock layer properties and on which the cold, non-ablating model wall has a negligible effect beyond the boundary layer. Heated wall models are a focus of recent and current research in the Centre for Hypersonics [59] [87] [88]; however, an aeroshell shape heated to the desired wall temperature, in excess of 3000 K, is not yet possible. The material properties of carbon phenolic ablators used for Hayabusa and Stardust are not available and would have to be approximated, and though CN is evident in flight spectra, most of the features in the IR radiate more strongly. Without carbonaceous species produced by ablation and pyrolysis, and with the potential for carbon contamination from CO₂ in the air or C in the facility, there is only one reproducible feature in the UV: the bandhead of the N₂⁺ band ending at 391 nm. The near IR region is investigated for both Hayabusa and Stardust to compare with data from McIntyre *et al.* [4] and Jenniskens [15], respectively, and the UV region with air only was investigated for Hayabusa to compare with Buttsworth *et al.*'s [64] measurements.

A schematic demonstrating the placement of the model inside the test section, and the location of windows, mirrors, spectrometers and cameras for recording spectra and 2D images is provided in Figure 4.3.

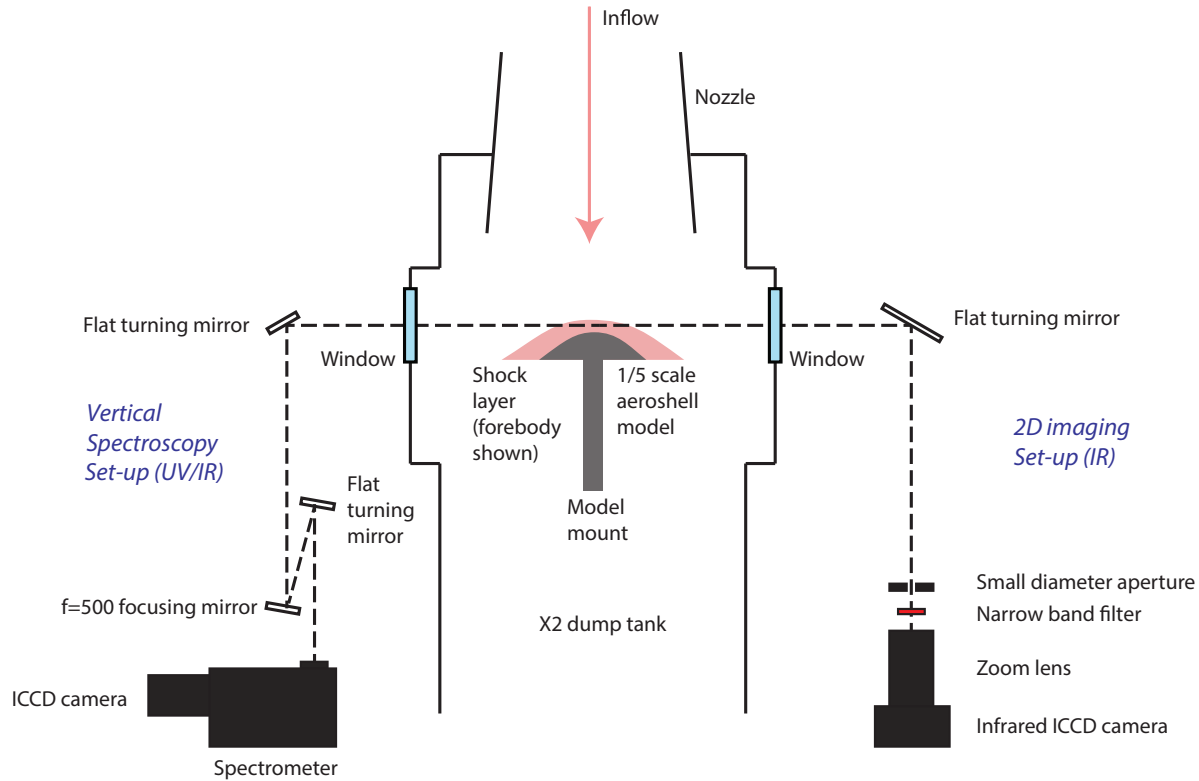


Figure 4.3: Schematic demonstrating set-up of optical systems on either side of the X2 test section containing an aeroshell model.

The laboratory is equipped with two Princeton Instruments PI-MAX2 ICCD cameras, which can be used alone for 2D intensity mapping or combined with one of two Acton Research SpectraPro SP2300i Czerny-Turner spectrometers to record spectra. Vertical spectra measurements had a magnification of 1:4 to reduce the image size onto the slit. The model centreline, mirrors and slit were all placed at the same height as no rotation of the image was necessary. Horizontal spectra measurements along the stagnation line had a 1:1 magnification and the optical system was required to turn image by 90° as the spectrometer slit orientation could not be altered. A schematic by Jacobs [57] shows how this is achieved with a series of flat mirrors, a focusing mirror and a periscope. Information about the mirrors and windows that formed the UV and IR spectroscopy systems are

provided in Table 4.1.

Optical component	Radius	Material	Supplier/code
IR flat mirror	25.4 mm	Protected silver coating	Thorlabs PF20-03-P01
IR focusing (concave) mirror	25.4 mm	Protected silver coating	Newport 20DC1000ER.2
UV flat mirror	25.4 mm	Enhanced aluminium coating	Thorlabs PF20-03-F01
UV focusing (concave) mirror	25.4 mm	Enhanced aluminium coating	Newport 20DC1000AL.2
IR side window	97 mm	Perspex	—
UV side window	97 mm	Fused silica	—

Table 4.1: Mirror and window specifications for spectroscopy systems.

4.2.2 2D intensity mapping

The 2D intensity mapping technique, as introduced previously, takes an image of the radiating flowfield across two spatial dimensions, and the intensity is defined by a wavelength band prescribed by a narrow band filter. The concept and set-up is simple in nature: a two-dimensional projection of the radiating shock layer is captured by the PI-MAX2 camera, in the same way that a standard photograph is taken. In the optical path is a Zoom Nikkor 100-300 mm f/5.6 lens, to magnify and focus the image; an aperture, to reduce the amount of light incident on the ICCD inside the camera; a narrow band filter, to allow radiation from a specific band; and a flat mirror, to turn the image by 90° and make the optical path as large as possible within the constraint of the optical bench size. The optical system layout can be seen in Figure 4.3. This method could be applied in the UV to near IR operating range of the available PI-MAX2 cameras, but as the most interesting features for radiating air species in the Hayabusa and Stardust shock layers occur in the near IR, several filters were selected in this region. Information about the filters is given in Table 4.2, including the wavelengths where light is allowed through, which were confirmed by imaging broadband sources through the filter and the IR spectrometer. The filter transmissivities are plotted over their respective wavelength ranges in Figure 4.4, and referenced by their centre wavelength and, in the case of the 780 nm filters, their curve shape.

Filter centre λ	Species feature(s)	Transmission curve shape	λ band	Band width	Supplier/code
600 \pm 2 nm	none	Gaussian	580-620 nm	40 nm	Thorlabs FB600-10
740 \pm 2 nm	N	Gaussian	720-760 nm	40 nm	Thorlabs FB600-10
780 \pm 2 nm	O (triplet)	Gaussian	760-800 nm	40 nm	Thorlabs FB740-10
780 \pm 2 nm	O (triplet)	Square	773-790 nm	17 nm	Thorlabs FBH780-10
820 \pm 2 nm	N	Gaussian	800-840 nm	40 nm	Thorlabs FB780-10
840 \pm 2 nm	O (triplet)	Gaussian	820-860 nm	40 nm	Thorlabs FB840-10
870 \pm 2 nm	N	Gaussian	850-890 nm	40 nm	Thorlabs FB870-10

Table 4.2: Filter specifications for 2D intensity mapping.

As the 2D method had not matured past the proof-of-concept stage before this campaign, validation and verification experiments were necessary. The ‘validation’ measurements ensure that the system is imaging what it is supposed to. The filter transmissivities were checked against manufacturers’ data by taking the ratio of calibration light source images with and without the filter in the optical path, using the IR spectrometer and ICCD camera at the filter centre wavelength. There were negligible differences as the filters were new.

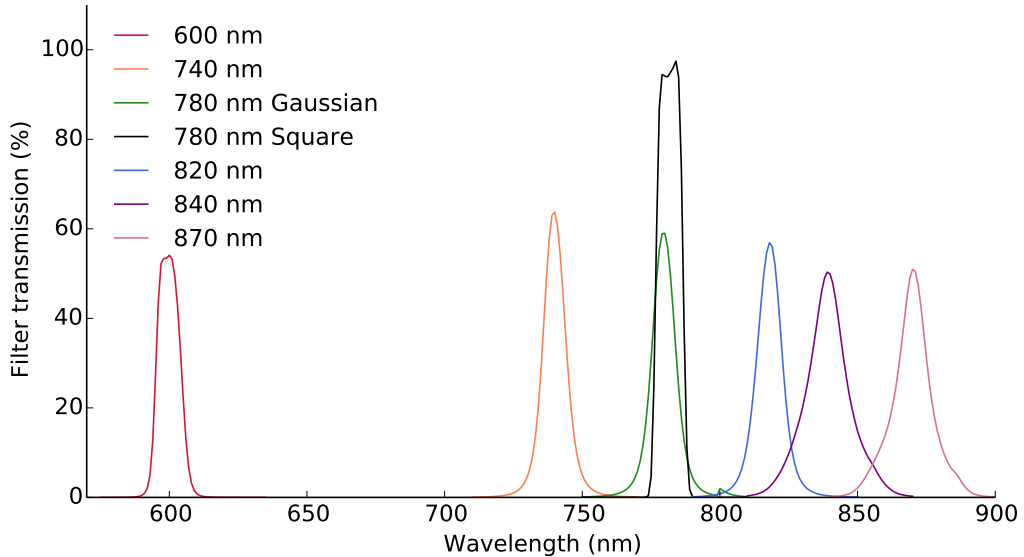


Figure 4.4: Filter transmissivity curves for each filter used in the 2D imaging experiments.

The 780 nm filter should only capture the atomic oxygen triplet at approximately 777 nm, and to test this, an experiment was performed with the square 780 nm filter in the 2D imaging system but

with N_2 as the test gas. The calibrated intensity of N_2 test gas shot (x2s2829) to a regular air shot (x2s2824) at Hayabusa test conditions is shown in Figure 4.5 as a slice along the stagnation line, and as expected, the air shot has a much higher intensity due to the atomic oxygen in the flow. The shock tube was twice flushed with N_2 in an attempt to reduce the oxygen concentration that remained in the 100 Pa of air for the nitrogen test gas shot, but radiation was recorded from the oxygen that was still present.

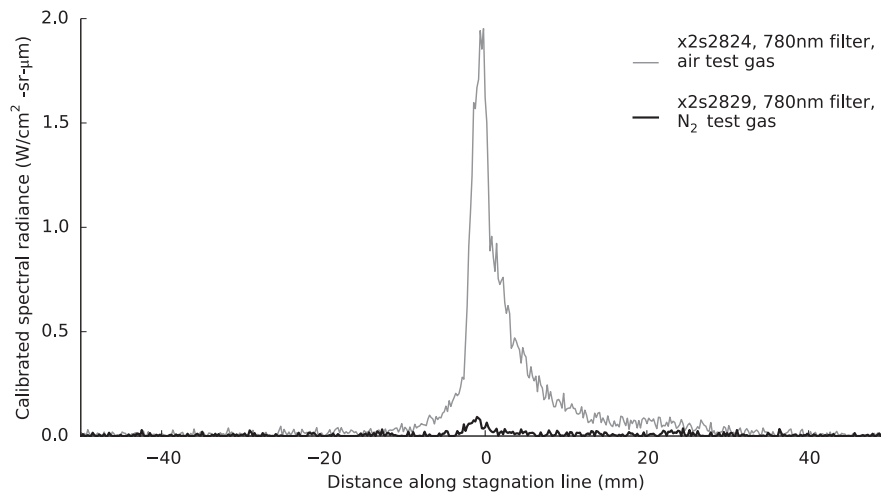


Figure 4.5: Calibrated radiance along stagnation line for a nitrogen or air test gas, imaged through the square 780 nm filter.

The transmission curve shapes of the filter impact the light incident on the ICCD by not only limiting the wavelength range, but only allowing a particular percentage of the incident light at the allowed wavelengths to pass through. As shown in Figure 4.4, the square-shaped premium filter centred at 780 nm has a maximum transmissivity of 97 % and very steep cut-offs near the edge wavelengths of 773 nm and 790 nm. The corresponding Gaussian filter has a maximum transmissivity of 59 % and covers a wavelength range of approximately 40 nm with gradual decreases in transmissivity either side of the maximum. However, the sharp rise of the square filter to its maximum transmissivity cuts across the 777 nm O triplet, interfering with the spectral peak height. The Gaussian filter has a lower maximum transmissivity but its rise has a more gradual effect on the atomic line, and this will be demonstrated in more detail in Chapter 5. The comparison of calibrated radiance between a shot with the 780 nm square filter and 780 nm Gaussian filter, in Figure 4.6, shows a difference in maximum intensity of about $0.6 \text{ W} \cdot \text{cm}^{-2} \cdot \text{sr}^{-1}$ and a greater area under the curve using the square

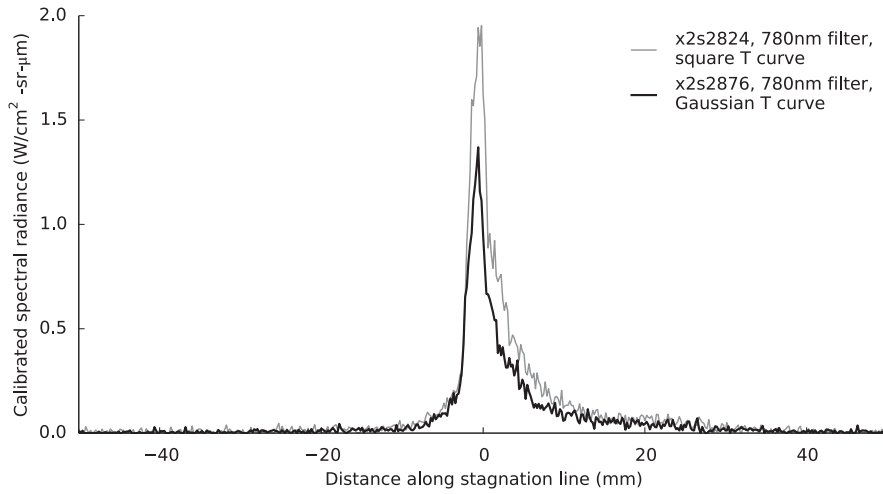


Figure 4.6: Calibrated radiance along stagnation line as imaged by 780 nm filters with square and Gaussian transmission curves.

filter. The reduction in the Gaussian filter as compared to the square filter illustrates that the Gaussian filter cannot be transmitting all of the light. Referring back to the 780 nm transmissivity curves in Figure 4.4, it can be concluded that the square filter is also not transmitting all of the incident light, but a higher percentage than the Gaussian filter. Thus, the measurements obtained by the 2D imaging system are not a direct radiance, but what can be termed an ‘incident’ or ‘filtered’ radiance. The filter transmission can be applied to the measured spectra over the same wavelength range as the corresponding filter through a convolution, enabling an appropriate comparison between the spectra and 2D images. The filter transmissivity could also be deconvolved from the 2D radiance data to compare to the original calibrated spectra.

The 2D intensity mapping method was verified by checking that the data is being calibrated correctly. The calibration procedure is detailed in the following section (4.2.3) but the verification experiment can be described here via relative spatial peak heights determined from calibrated values. The 600 nm centre wavelength filter was selected because this was one of the few available filter bands with minimal radiation from known flow species. There are a few minor atomic N and O lines, and the possibility of some atomic C contamination lines from the expansion tube. However, these should provide maximum peak heights that are about 2 % of the O 777 nm triplet spatial peak height at approximately 10 000 K, as calculated by *Photaura*. The raw counts from a Hayabusa shot with the 780 nm filter and one with the 600 nm filter at the same exposure time and gain were similar.

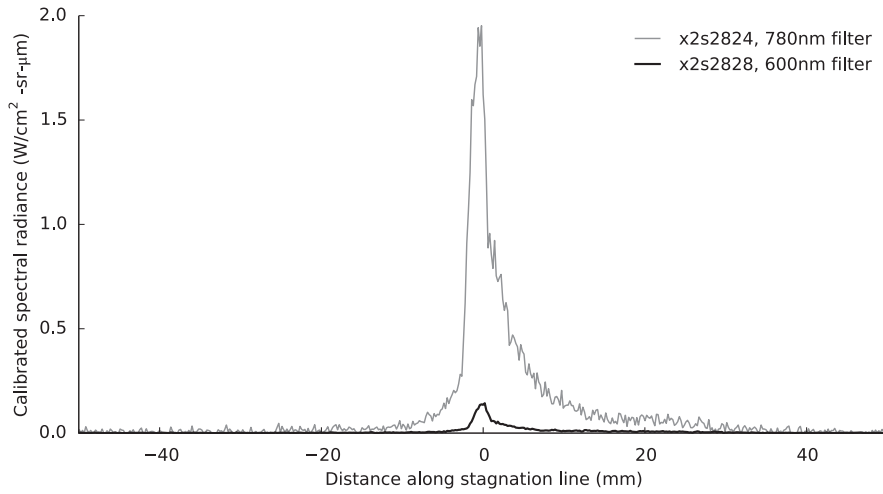


Figure 4.7: Comparison of calibrated relative intensity along stagnation line for 780 nm (square transmission curve) filter and 600 nm filter.

However, the calibrated data in Figure 4.7 shows a significant difference in the radiance, as the peak radiance through the 600 nm filter is about 7 % of the 780 nm peak radiance. The fact that there is still some emission from the 600 nm region indicates the possibility of higher atomic N and O levels than expected, or contributions from carbon contamination. The ICCD appears to be more sensitive in the 600 nm region but this was accounted for in the calibration.

4.2.3 Calibration

The calibration of optical systems assigns quantified values to raw data through a source of known intensity, and is necessary in this work to compare experimental data against quantified flight values. There are two calibration sources available in the lab: a tungsten filament lamp, which has known spectral irradiance at a 500 mm distance (measured in W · cm⁻² · μm⁻¹ or similar), and a Labsphere CSTM-LR-2Z-4 integrating sphere, which has known spectral radiance (measured in W · cm⁻² · sr⁻¹ · μm⁻¹ or similar). Calibration of a raw spectrometer image with a light source of known intensity is calculated by Equation 4.1. The experimental image f_{exp} is multiplied by a calibration factor and the ratio of exposure times t_{cal} and t_{exp} , and divided by the calibration image f_{cal} .

$$I(\lambda, z) = f_{exp}(\lambda, z) \times \frac{C}{f_{cal}(\lambda, z)} \frac{t_{cal}}{t_{exp}} \quad (4.1)$$

Calibration of the spectroscopy systems with the tungsten lamp exactly follows the procedure in Jacobs' thesis [57], including individual calibration of each optical component (i.e. all mirrors and windows, and the spectrometer), and the reader is directed there for further information. The calibration factor C accounts for the magnification M , the influence of reflectivity and transmissivity from optical components and air in the path ϵ , the lamp spectral irradiance as a function of wavelength E_{cal} , and the solid angle Ω , and is calculated in Equation 4.2.

$$C_t = M^2 \epsilon \frac{E_{cal}(\lambda)}{\Omega} \quad (4.2)$$

As the integrating sphere is a source of known spectral *radiance*, it can be placed at any distance from the spectrometer slit or camera and include all optical elements in the system. The solid angle, magnification, reflectivity and transmissivity of the whole system is accounted for in the calibration image when the integrating sphere is placed in the position of the object: in this case, at the location of the model stagnation point inside the test section. This simplifies both the calibration process, as it can be done *in situ* as a whole system, and the calibration factor C in Equation 4.1 reduces to the lamp spectral radiance as a function of wavelength L_{cal} , as shown in Equation 4.3.

$$C_i = L_{cal}(\lambda) \quad (4.3)$$

This is applicable for spectroscopy and 2D imaging systems, as the different optical elements and paths are accounted for in the calibration image. Both the tungsten lamp spectral irradiance and integrating sphere spectral radiance values are provided by the manufacturer and it is assumed that the deviation from these values is negligible. The preferred light source was the integrating sphere due to the simplified calibration process. The calibration curve is provided in Figure 4.8, and the calibration curve for the tungsten lamp can be found in Eichmann's thesis [33].

The tungsten lamp bulb is large enough at the calibration distance of 500 mm to illuminate the entire ICCD, and can be directly applied in Equation 4.1. At 1:1 magnification (horizontal images), the integrating sphere image through a spectroscopy system also illuminates the entire ICCD, but at a 1:4 magnification (vertical images), it only illuminates approximately half of the ICCD along

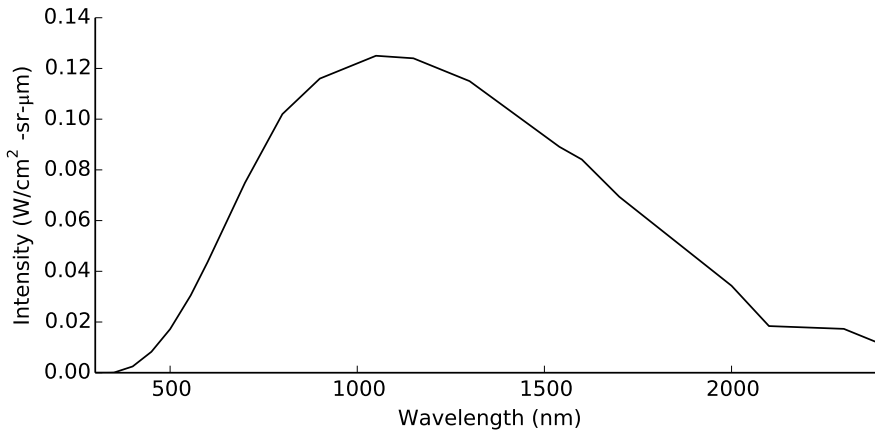


Figure 4.8: Calibration curve for the integrating sphere.

the distance dimension. Three calibration images were therefore stitched together for vertical slit measurement calibrations, where the lamp illuminated the top 50 %, the middle 50 % and the lower 50 % respectively, with generous overlap, to ensure no edge effects in the centre of the image.

2D intensity mapping calibration presents a different challenge. By imaging the circular integrating sphere outlet, with a radius of 12.5 mm, in two distance dimensions and through the same optical set-up as the experiments, the calibration image is of the small circular outlet, covering less than 2 % of the ICCD area. Instead of imaging small pieces of the ICCD and stitching near to 100 images together, calibration imaging follows the method presented by Sheikh *et al.* [52]. One image of the integrating sphere is taken in the same part of the ICCD as the experimental image, a rectangular section of pixels is selected from the centre of this image (as large as possible whilst neglecting the edges) and an average value of the intensity is calculated. There are inherent variations between calibration images even when considering the same pixel, due to variations in the ICCD response, and images should avoid regions bordering the edge of the ICCD where the response starts to fall away.

The intensity measured by the ICCD should be linear with increasing exposure time for a constant gain, regardless of the optical setup. This was confirmed by imaging both the integrating sphere and tungsten lamp, but care must be taken to remove the background counts from the calibration source images as discussed below in Section 4.2.4. The linearity of exposure time and intensity, using the

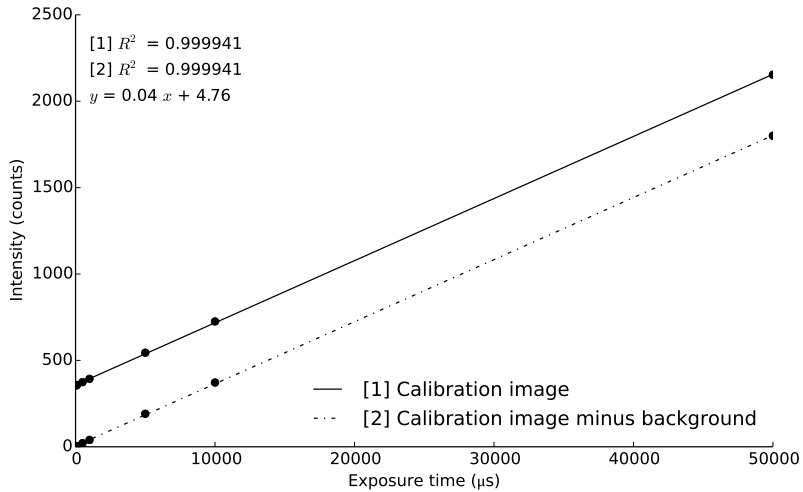


Figure 4.9: Linearity of exposure time for integrating sphere calibration images, and importance of background removal. Circular markers indicate measurement data.

integrating sphere as the calibration source, is demonstrated in Figure 4.9.

4.2.4 Background counts and cosmic ray removal

Every ICCD image contains background counts from charge on the ICCD, caused by thermal noise generation of electrons and electron holes (a location in the lattice structure where an electron could exist) without excitation from incident photons [89]. Although the Peltier coolers on the UV and IR ICCDs were set to 253 K, the IR ICCD had a high amount of background counts. It is important to subtract the background counts from both the raw experimental image and the calibration image to calculate the ratio of counts caused solely by incident photons. The background counts were found by extracting a region of the experimental or calibration image that is outside the capture area of the camera but still generates thermal noise [57]. Occasionally the ICCD picks up a cosmic ray, appearing as one pixel that is much brighter than the others, and is removed in the post-processing code [33]. This most commonly occurs when recording calibration images with longer exposure times and multiple accumulations.

4.2.5 High speed camera

The Shimadzu Hypervision HPV-1 high speed video camera recorded videos of expansion tube experiments, recording 100 frames at frame rates of 500 kHz or 1 MHz (maximum available). A Zoom Nikkor 100 - 300 mm f/5.6s lens was fitted to the camera for focusing through the IR side window at a maximum distance of 1 to 2 m from the model. The videos are qualitative in terms of intensity, but provide useful data about shock layer establishment, test time, arrival of unsteady flow and shock stand-off. The camera was carefully placed for the spectroscopy tests so that it could provide a secondary image set for alignment and checking for movement of the tube between aligning and firing. Unfortunately, the video camera could not be used in conjunction with the 2D imaging experiments because that optical system required the Zoom Nikkor lens, and there were no other suitable lenses available at the time of the experiments. A selection of high speed camera images are provided for flow visualisation in Appendix D.

4.3 Experimental Methodology

The conditions developed in Chapter 3 have X2 in its standard configuration: the reservoir, lightweight piston, primary driver, single 2 mm thick steel primary diaphragm, shock tube, single thin aluminium foil secondary diaphragm, acceleration tube, Mach 10 nozzle and test section. This was illustrated in Figure 2.6. The piston is seated on the launcher and the tube is sealed with intact primary and secondary diaphragms, separating the shock tube from adjacent sections. This occurs prior to evacuating the driver, shock tube and acceleration tube and taking alignment images.

If vertical spectra are to be captured, a separate alignment step is required with an aligning piece fitted to the front of the model, as mentioned in Section 4.2. Alignment images are captured by illuminating the model with a fluorescent lamp, before the tube is returned to atmospheric pressure. The alignment piece is removed by access through the top window so that the test section remains stationary and the alignment location is accurate to within 0.25 mm, then the tube is pumped down in preparation for the experiment with the top window re-fitted. The low pressure in the acceleration

	Hayabusa	Stardust
Mean primary shock speed ($\text{m} \cdot \text{s}^{-1}$)	4738	5108
Standard deviation of primary shock speed ($\text{m} \cdot \text{s}^{-1}$)	35	49
Mean secondary shock speed ($\text{m} \cdot \text{s}^{-1}$)	9905	11744
Standard deviation of secondary shock speed ($\text{m} \cdot \text{s}^{-1}$)	123	140

Table 4.3: Shock speed mean and standard deviation for each condition across the entire campaign.

tube and test section is maintained while the driver tube is filled with pure helium (Hayabusa) or a mixture of helium and argon (Stardust), the shock tube is filled with lab air, and finally, the reservoir is filled with compressed air. Fill pressures for both conditions were given in Table 3.2.

A National Instruments (NI) box running LabView software sent the initialising signal to the spectrometers once it and a trigger box were triggered by a photodiode pointed at the nozzle exit and a prescribed delay applied. The flow became sufficiently bright to push the photodiode voltage above a threshold value, and the rise time was a few microseconds. The shock speeds for each experiment were determined by the pressure rise against time as measured by PCB pressure transducers located along the shock and acceleration tube walls. The mean primary shock speeds, measured in the shock tube, and secondary shock speeds, measured across the last three transducer locations before the nozzle entrance, across the entire campaign are presented in Table 4.3. The standard deviation indicates that the Stardust condition has more variability in the shock speeds than Hayabusa, and this is due to the changed driver and difficulty in achieving the 3 Pa acceleration tube pressure, as discussed earlier. The Stardust campaign mean primary shock speed was lower than the condition test campaign average of $5444 \text{ m} \cdot \text{s}^{-1}$, while the mean secondary shock speed was higher. Hayabusas mean primary shock speed was slightly lower than the condition test campaign average of $4772 \text{ m} \cdot \text{s}^{-1}$, and the mean secondary shock speed is about $100 \text{ m} \cdot \text{s}^{-1}$ lower than the pitot campaign average of $10001 \text{ m} \cdot \text{s}^{-1}$. This, then, has ramifications for the nozzle exit parameters, and therefore the shock layer parameters.

Table 4.4 provides the most commonly used spectrometer settings over the experimental campaign.

Spectrometer	IR	IR	UV
Centre wavelength (nm)	780	840	374
Grating (lines/mm)	600	600	1800
Effective λ range (nm)	80	80	40
Slit width (μm)	50	50	50
Exposure time (μs)	10	10	15
Exposure delay (μs)	50	50	50

Table 4.4: Most common spectrometer settings for Earth re-entry experiments.

Vehicle/Model	Spectrometer	$\Delta\lambda$ (nm/pixel)	Δx (nm/pixel)
Hayabusa model	IR, vertical slit	0.13	1.04×10^{-4}
	IR, horizontal slit	0.13	2.61×10^{-5}
	UV, vertical slit	0.042	1.04×10^{-4}
Hayabusa flight	IR	0.48	n/a
	UV	0.19	n/a
Stardust model	IR, horizontal slit	0.13	2.61×10^{-5}
Stardust flight	ECHELLE	0.14 (at 370 nm) to 0.9 (at 880 nm)	

Table 4.5: Spectral and spatial resolution of experiments and flight data (where applicable).

A delay of 50 μs was required to avoid the flow establishment before the shock layer has steadied, and recording across about 10 μs gives a better average for the data but still fits comfortably within the steady test time. The 600 lines per mm grating captured a reasonable wavelength range in the IR with good resolution, and the 1800 lines per mm grating on the UV spectrometer allowed well resolved imaging of the N_2^+ band and bandhead while avoiding the extremely bright contamination lines in the following 5 nm, caused by excited aluminium and/or ionised calcium from the obliterated secondary diaphragm [59]. The 50 μm slit width was sufficiently large to avoid diffraction caused by the slit and to allow an adequate amount of light into the spectrometers, without a significant increase in broadening. Table 4.5 presents the spectral and spatial resolution for different spectrometer setups, combined with the X2 models and flight vehicles. The spatial resolution was not quoted for any flight results, but the spectral resolution for the Hayabusa IR is reported in McIntyre *et al.* [4], for the Hayabusa UV in Buttsworth, Morgan and Jenniskens [5], and for the Stardust ECHELLE in Jenniskens [15].

4.4 Summary

There are many aspects to preparing an experimental campaign in the X2 expansion tube following determination of the test conditions. The Hayabusa and Stardust models were designed, manufactured and mounted in the test section. All of the optical components were selected, set up, aligned and calibrated in readiness for measuring spectra or filtered intensity from the radiating shock layer in the extremely short steady test time. The 2D intensity mapping method was assessed for use, as it was a method new to the laboratory and for the first time, several filter bands were investigated. The experimental methodology outlined the procedure for recording the images, from which the results in Chapter 5 were obtained.

Chapter 5

Experimental Results and Analysis

The scaled Hayabusa and Stardust experimental campaign took place in the X2 expansion tube over several weeks and consisted of close to 50 shots, with the majority yielding good quality images. The successful measurements for Hayabusa comprised 2D images, and IR and UV 1D spectroscopic data in different directions, and the Stardust measurements included horizontal IR 1D spectroscopic data and 2D images. At least two shots were performed at nominally identical flow conditions for each set of measurement parameters, which include centre or filter wavelength and spatial location, and the intensity in raw counts were compared at the time of the experiments to check for repeatability. The best quality images that captured the steady test time with the closest to ideal shock speeds were selected for further analysis. The reasoning for only taking the best images for each set of parameters is that the focus of this work is not to analyse facility performance in detail, but to find out whether the closest to ideal experimental data can replicate flight, or be replicated in CFD. Each experimental image is presented with primary and secondary shock speeds for straightforward comparisons between images, or to ideal theoretical values. The results were calibrated and post-processed as outlined in Section 4.2.3; hence all spectroscopy and 2D intensity mapping data is presented in absolute units. Hayabusa vertical spectra in the IR and 2D images were compared across particular wavelength bands to assess the consistency between the two methods. Atomic emission lines were identified by referring to the NIST Atomic Spectra Database [90] and previous work (for example, [37]), and the UV N_2^+ band was known from previous work [5] [59]. Blackbody radiation has a negligible influence on the experimental spectra because the model has a cold wall of about 300 K.

Remembering that the major aim of this work is comparison of laboratory and flight data, the numerous axisymmetric vertical slices imaged in the 2D intensity maps will be used to construct flight rebuilding calculations in Chapter 7. Condition data and identified radiating species are inputs to the CFD and numerical spectra calculations that can directly compare to experimental data, or undergo the flight rebuilding process. Shock layer properties will be identified from CFD, and their accuracy in describing the experimental results will be shown in the comparison of spectra.

5.1 Near IR Spectroscopy

Many emission lines in the 700 to 900 nm near IR region of the flight spectra and these became the focus of IR emission spectroscopy during the X2 scaled re-entry experiments [4] [37] [15]. To image the desired wavelength range with reasonable detail, it was split in two and spectra had centre wavelengths of 780 nm or 840 nm. The other commonly used spectrometer settings can be viewed in Table 4.4. Measurements with a horizontal orientation were taken for Hayabusa and Stardust, to observe the change in spectra across the shock layer. Vertically oriented measurements, performed for Hayabusa only, can form a basic flight rebuilding calculation with several slices, and compare to 2D imaging data due to the axisymmetry of the measurement plane.

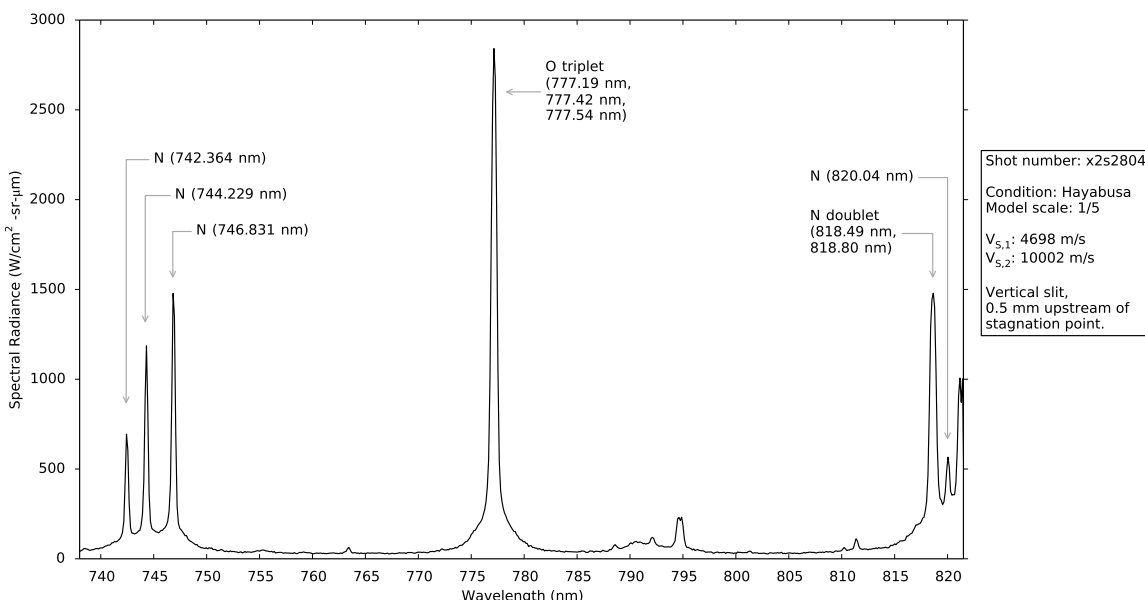


Figure 5.1: Hayabusa IR spectrum at 0.5 mm upstream of stagnation point, centre wavelength 780 nm.

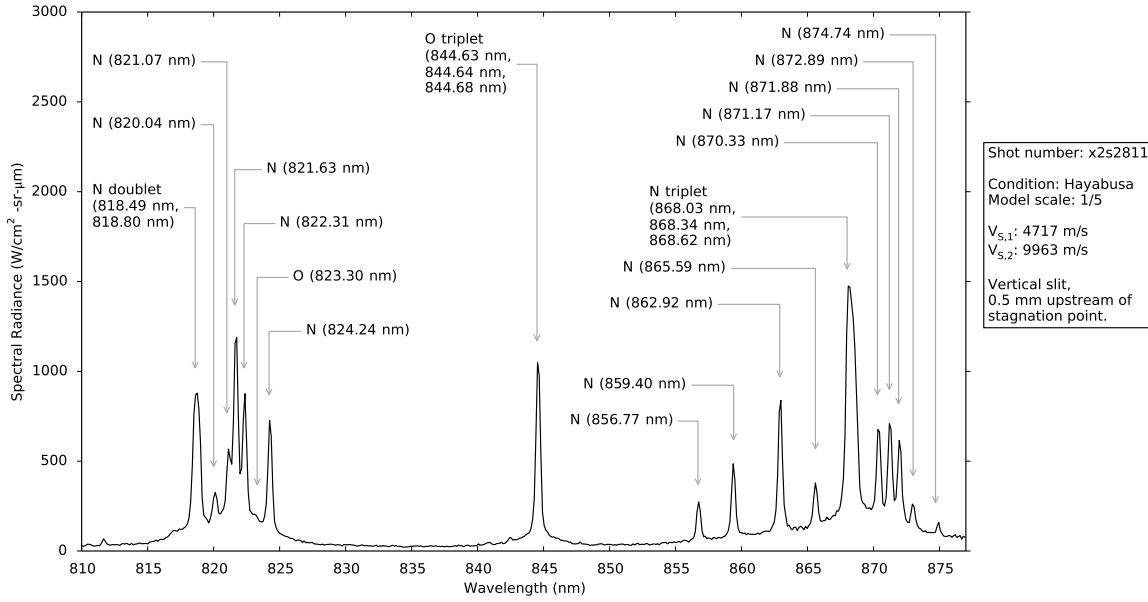


Figure 5.2: Hayabusa IR spectrum at 0.5 mm upstream of stagnation point, centre wavelength 840 nm.

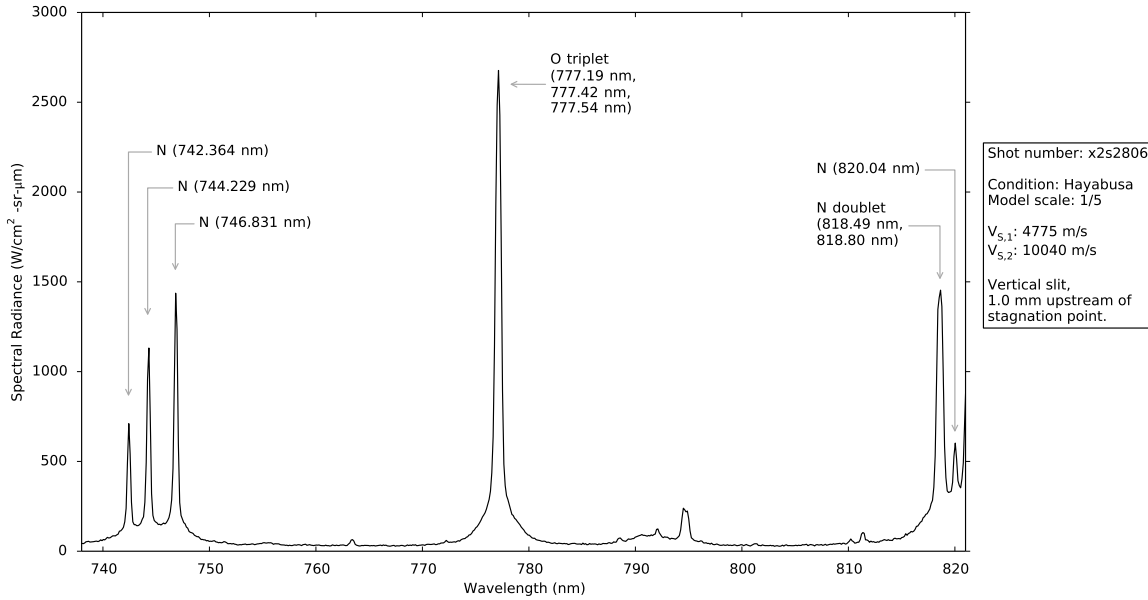


Figure 5.3: Hayabusa IR spectrum at 1 mm upstream of stagnation point, centre wavelength 780 nm.

5.1.1 Hayabusa: vertical orientation

Hayabusa was selected for vertical spectra measurements due to a larger shock stand-off distance and greater condition stability than Stardust, as determined by preliminary condition test shots and several

test shots with the Hayabusa model. As the number of shots in the campaign were limited, taking vertical spectra for each model was not possible. Five locations were originally tested: at the stagnation point ($x = 0$ mm), and $x = 0.5, 1, 1.5$ and 2 mm upstream of the stagnation point. The stagnation point measurements had excessive interference from the model surface, and as the shock stand-off distance was approximately 2.2 mm, the $x = 2$ mm location proved too close to the shock layer edge to produce useful data. Figures 5.1, 5.3 and 5.5 were recorded $0.5, 1$ and 1.5 mm upstream of the stagnation point and on the stagnation line, respectively. The centre wavelength of 780 nm highlighted the bright atomic O 777 nm triplet, a prominent feature of a high-temperature air spectrum. Three atomic N lines in the 740 to 750 nm range, as well as the lower end of a group of N lines around 820 nm, can be seen in these spectra. The shape of the spectral features throughout these images remains consistent with increasing distance from the stagnation point, while the peak spectral radiance decreases, especially around 1.5 mm.

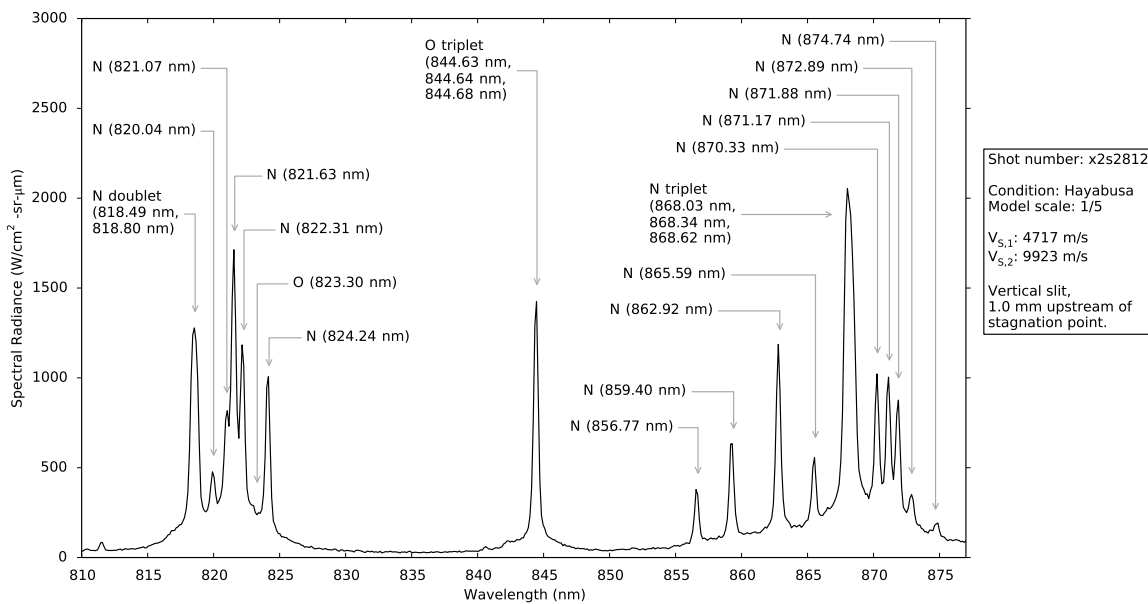


Figure 5.4: Hayabusa IR spectrum at 1 mm upstream of stagnation point, centre wavelength 840 nm.

The same shape and magnitude trends are also evident in the spectra with centre wavelength 840 nm, shown at $0.5, 1$ and 1.5 mm in Figures 5.2, 5.4 and 5.6, respectively. A second, less bright atomic O triplet sits near the centre of these spectra at 844 nm and two groups of several atomic N lines are captured around 820 nm and 870 nm. The atomic lines throughout the near IR have quite narrow peaks but appear to be affected by broadening around the base. There is approximately a 10 nm overlap

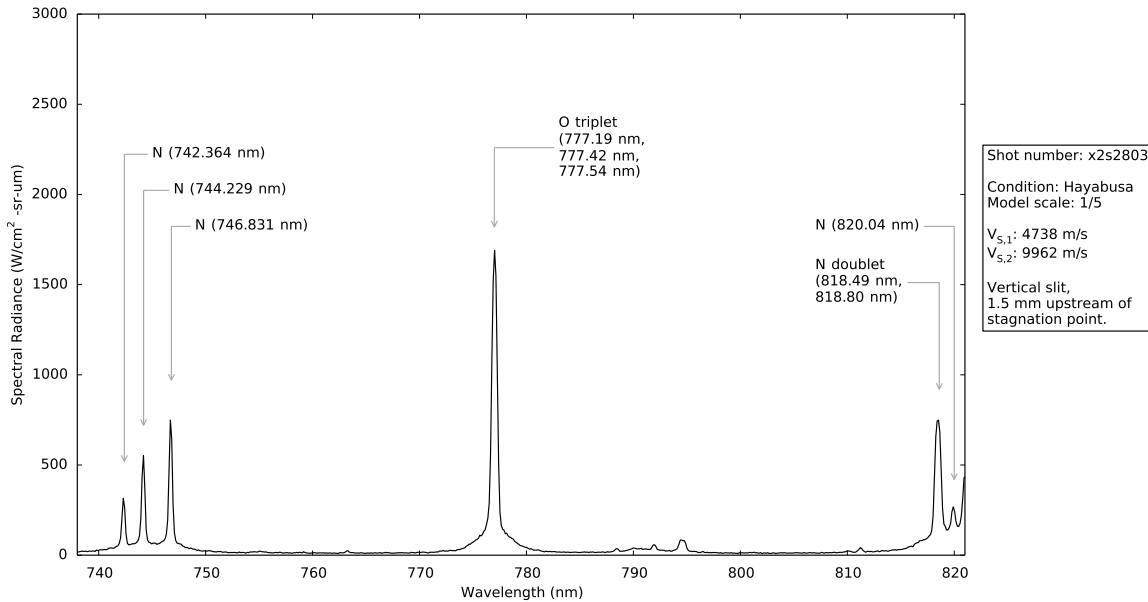


Figure 5.5: Hayabusa IR spectrum at 1.5 mm upstream of stagnation point, centre wavelength 780 nm.

between the images centred at 780 nm and 840 nm, and the 818 nm N doublet and N 820 nm line appear in every near IR spectra. There is some difference in the peak spectral radiance where the lines overlap, which can be attributed to differences in the secondary shock speed. The shock speed affects the post-shock temperature, and because of strong temperature dependence, atomic spectral emissions are affected. This is consistent with the results in Figures 5.3 and 5.4 at 1 mm, but not at 1.5 mm in Figures 5.5 and 5.6. In the images at 1.5 mm, the quoted v_{s2} values are almost identical but the N 818 nm peak differs significantly. The cause could be a shift in the imaging location under vacuum, or inconsistency in the pressure trace rise selection for the shock speed calculation. Variations in fill pressure, inconsistencies in the diaphragms or small leaks can cause the varying shock speeds between shots.

5.1.2 Hayabusa: horizontal orientation

Spectra were recorded with a horizontal slit orientation to capture variation along stagnation line from the stagnation point at the wall to the shock layer edge. This is the standard spectroscopy measurement for X2 experiments as it can be compared to point or line of sight radiation modelling, but the measured plane cannot be transformed for radiation analyses over the entire shock layer. As for the vertical spectra, the centre wavelengths were 780 nm and 840 nm to encompass all of the prominent

atomic N and O in the near IR. Figures 5.7 and 5.8 contain three spectra that were each averaged across approximately four pixels in the spatial dimension and illustrate the nonequilibrium (shock layer edge), equilibrium and near wall regions. Please note that the x distances referred to in Figures 5.7 and 5.8 refer to the distance in the direction parallel to the stagnation line, measured outwards from and upstream of the stagnation point. A point just upstream of $x = 0$ mm is allowed in the horizontal case because the location of the model edge can be identified, and therefore a point can be selected where it is almost the stagnation point, but there is no interference from the wall. This is not possible with the vertical alignment because the model is not captured in the image. The general trend is that the atomic emissions are maximum in the equilibrium region, and lower in the nonequilibrium region since the flow is not fully dissociated and there are not enough free electrons from ionisation. Emissions are also lower near the wall because of falling temperatures and recombination. The difference between peak heights in different regions is most pronounced in the three O 777 nm triplets in Figure 5.7, and the decline between equilibrium and nonequilibrium in all features of Figure 5.8. The peak heights in Figure 5.7 compare favourably with the vertical spectra in Figures 5.1, 5.3 and 5.5, taken at similar distances from the stagnation point, and averaged across the stagnation line pixels.

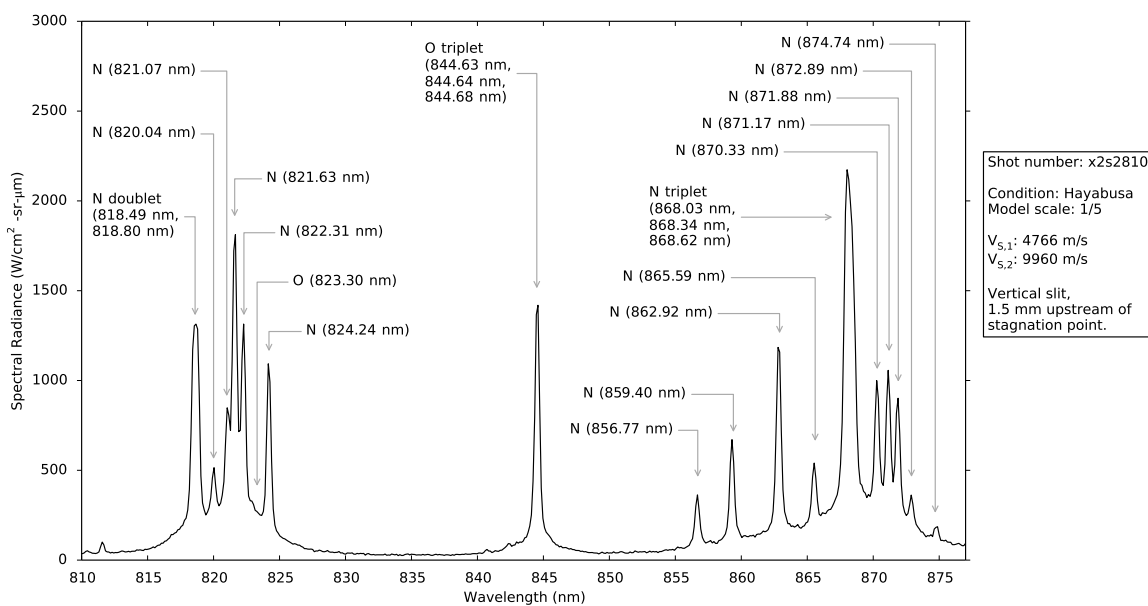


Figure 5.6: Hayabusa IR spectrum at 1.5 mm upstream of stagnation point, centre wavelength 840 nm.

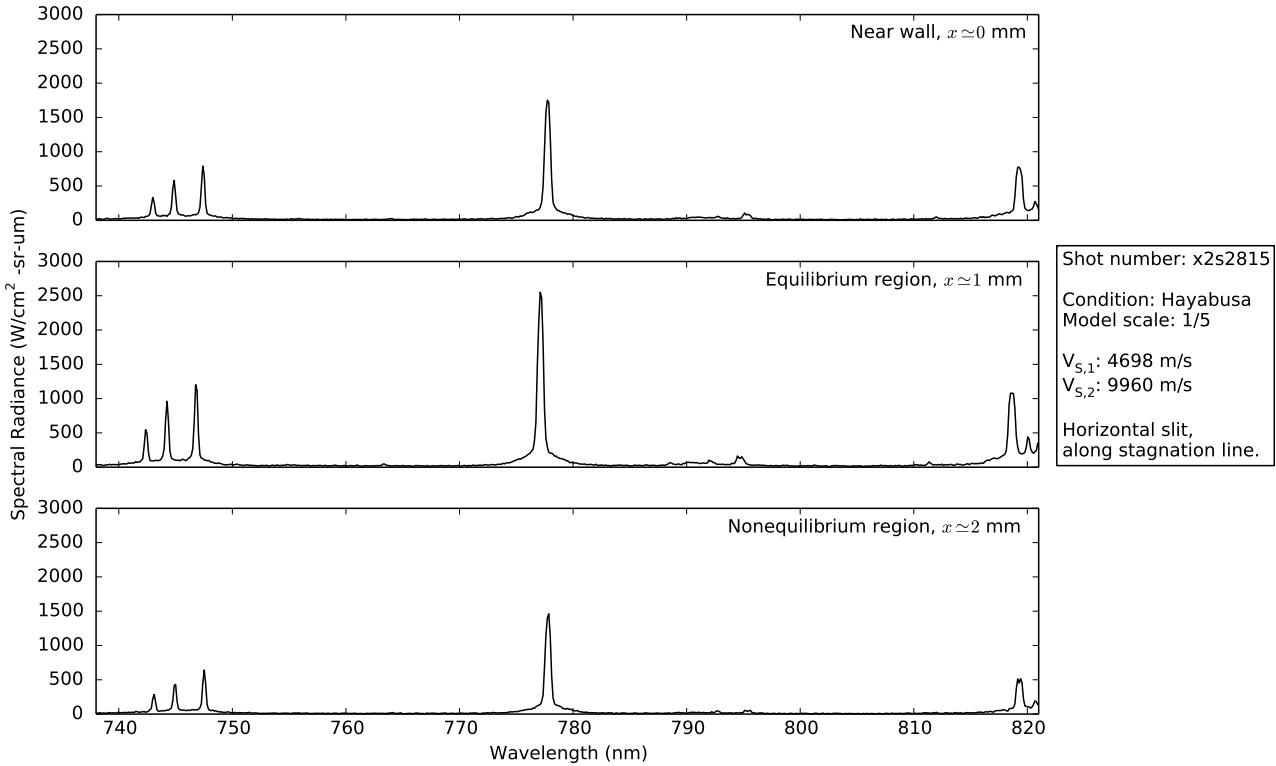


Figure 5.7: Hayabusa IR spectrum from wall, equilibrium and nonequilibrium region on stagnation line, centre wavelength 780 nm.

5.1.3 Stardust: horizontal orientation

This is the first time that Stardust spectra has been produced in X2 expansion tube experiments at a condition close to being binary scaled and enthalpy matched for a 1/10 scale model. It was assumed that the comparison between Hayabusa vertical spectra and 2D images would be enough to show consistency between the methods, without the extra shots necessary for the same comparison with Stardust. Due to time limitations, four shots were assigned to recording horizontal slit spectra for Stardust, to show a profile across the shock layer and along the stagnation line. The near wall, equilibrium and nonequilibrium were chosen from the raw spectrometer images at locations indicated by CFD results. Figure 5.9 centres on 780 nm and Figure 5.10 centres on 840 nm, showing the difference in spectra at varying distances from the stagnation point. Immediately evident is the reduction in intensity in reference to the Hayabusa stagnation line images, which had the same range on the y-axis, and the only standout feature is the equilibrium region O 777 nm triplet in the equilibrium region of Figure 5.9. The Stardust condition was about $1.5 \text{ km} \cdot \text{s}^{-1}$ faster than Hayabusa as the flight equivalent

speed was $12 \text{ km} \cdot \text{s}^{-1}$, hence the decrease in atomic species could be driven by increased ionisation across the entire shock layer, most likely to N^+ and O^+ . This will be addressed in CFD simulations in Chapter 6. Stardust's nose radius and sphere-cone angle, combined with the high flight equivalent speed, resulted in a smaller shock stand-off distance than Hayabusa and distinguishing discrete regions across the shock layer was made difficult by the choice of magnification, indicating a higher magnification than 1:1 would be useful in future experiments.

5.2 Hayabusa UV Spectroscopy

The only air species that radiates in the UV region within the Hayabusa shock layer is N_2^+ , which has a bandhead at 391.22 nm combined with N_2^+ First Negative (B-X) $\Delta v = 0$ band that extends back to about 370 nm. There is also the N_2^+ First Negative (B-X) $\Delta v = -1$ band that extends from about 340 to 360 nm, which is partially cut off by the spectrometer as the focus was on the First Negative band. Unfortunately, the bands may be contaminated by CN or Fe that comes from the tube or diaphragm materials and also radiates in this region, and this needs to be taken into consideration when assessing

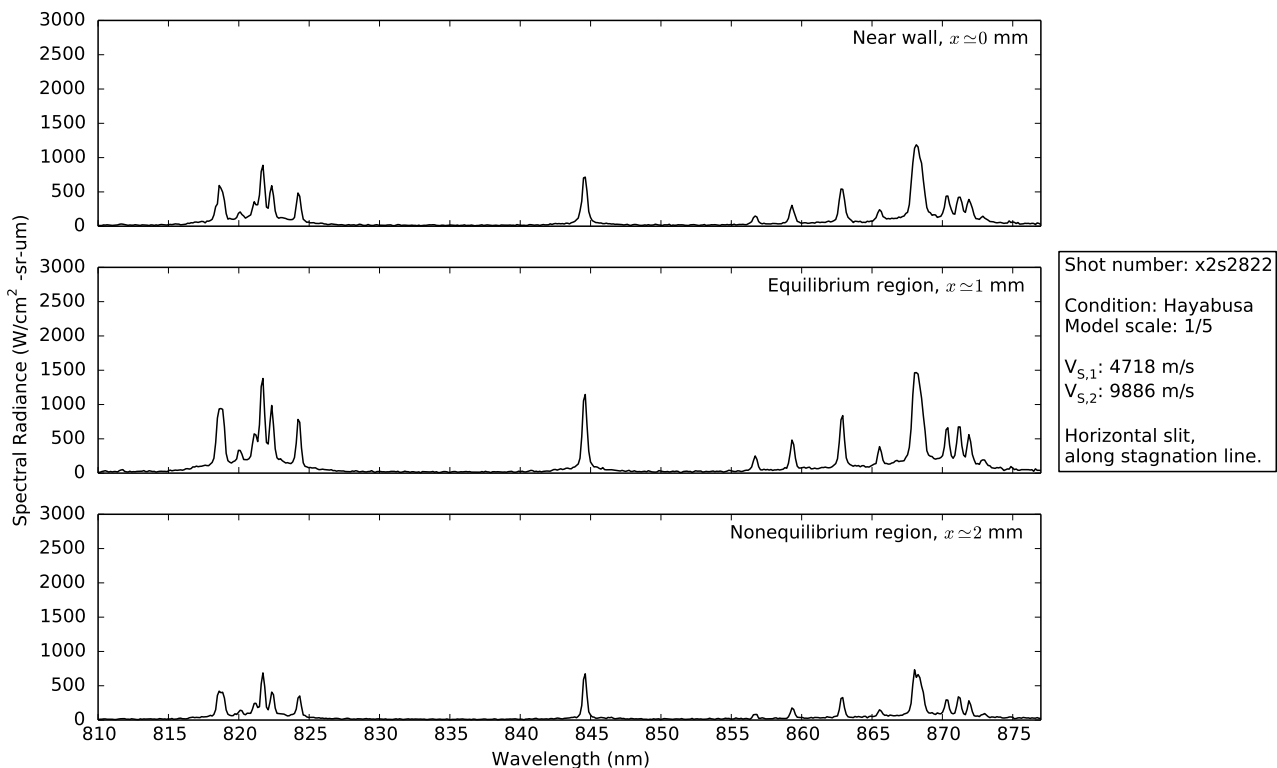


Figure 5.8: Hayabusa IR spectrum from equilibrium region on stagnation line, centre wavelength 840 nm.

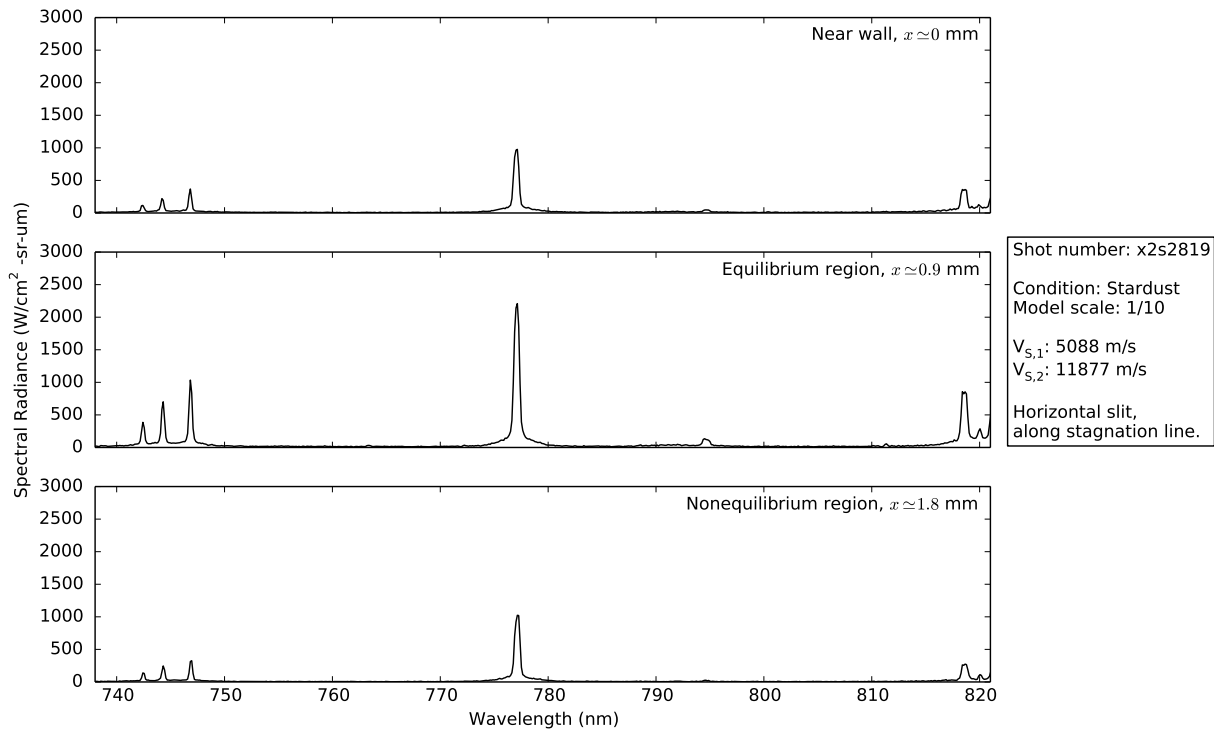


Figure 5.9: Stardust IR spectrum from equilibrium region on stagnation line, centre wavelength 780 nm.

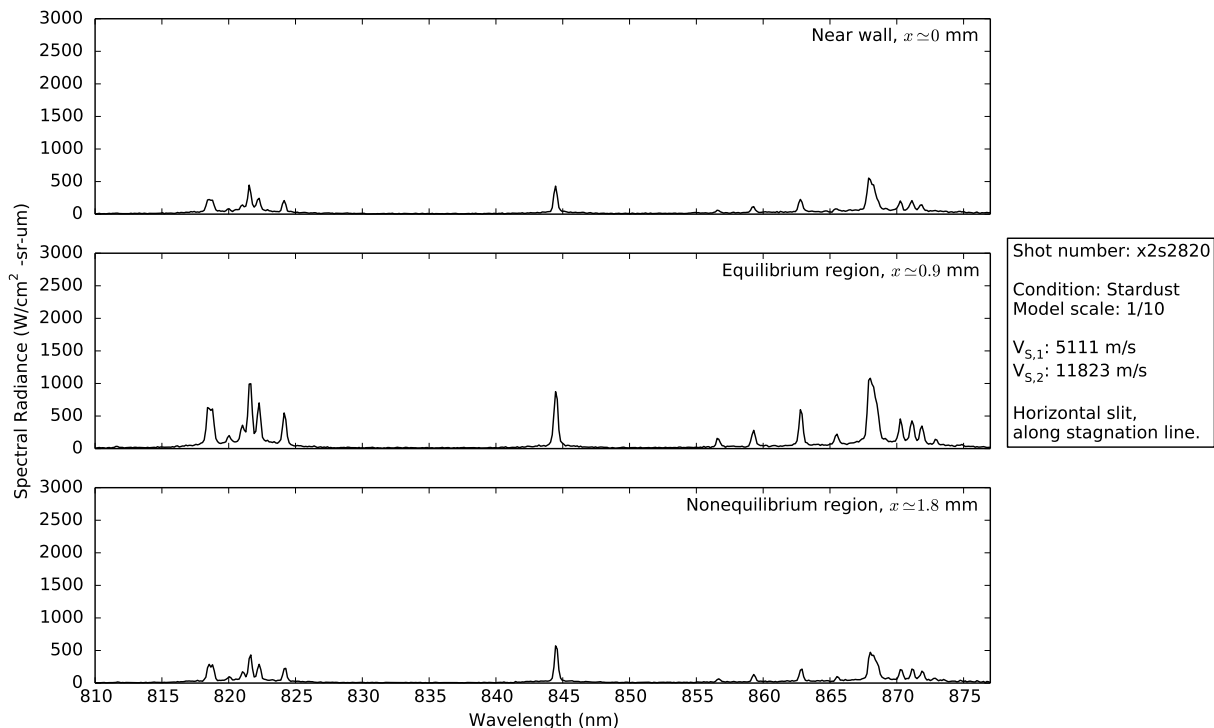


Figure 5.10: Stardust IR spectrum from equilibrium region on stagnation line, centre wavelength 840 nm.

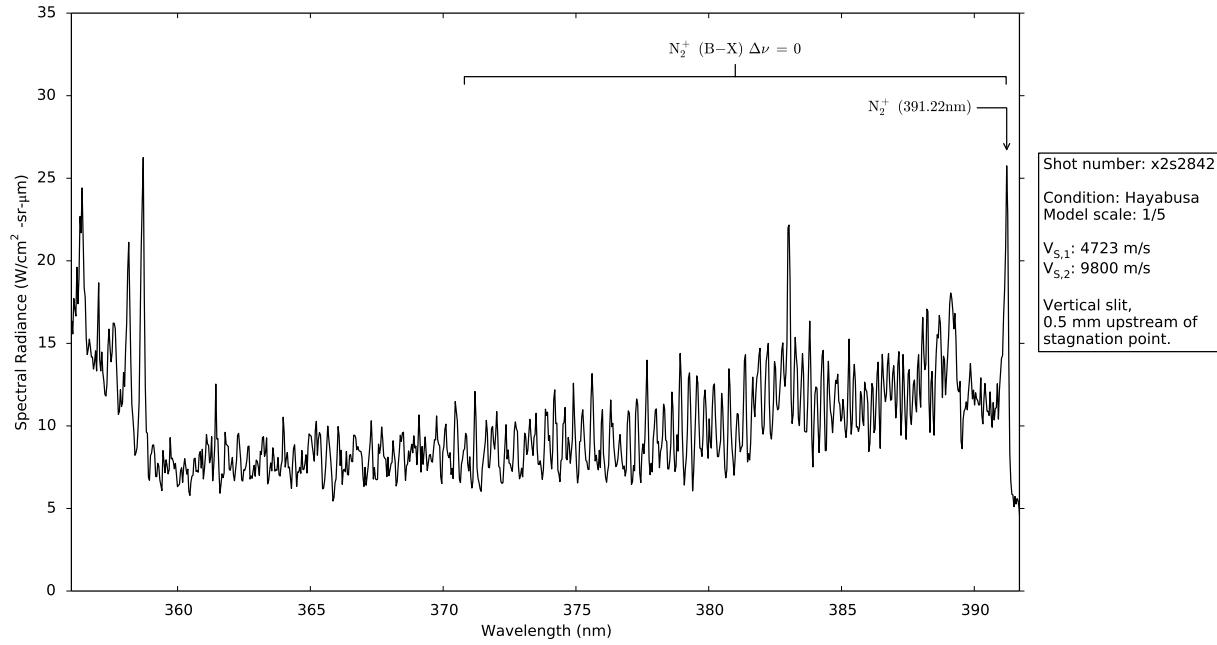


Figure 5.11: Hayabusa UV spectrum at 0.5 mm upstream of stagnation point, centre wavelength 374 nm.

the data. The bandhead stands clear of any contamination lines, therefore there can be more confidence in the measurement. It is identified as the main feature on the right side of Figures 5.11, 5.12 and 5.13 at 0.5 mm, 1 mm and 1.5 mm upstream of the stagnation point. The spectra look vertically through

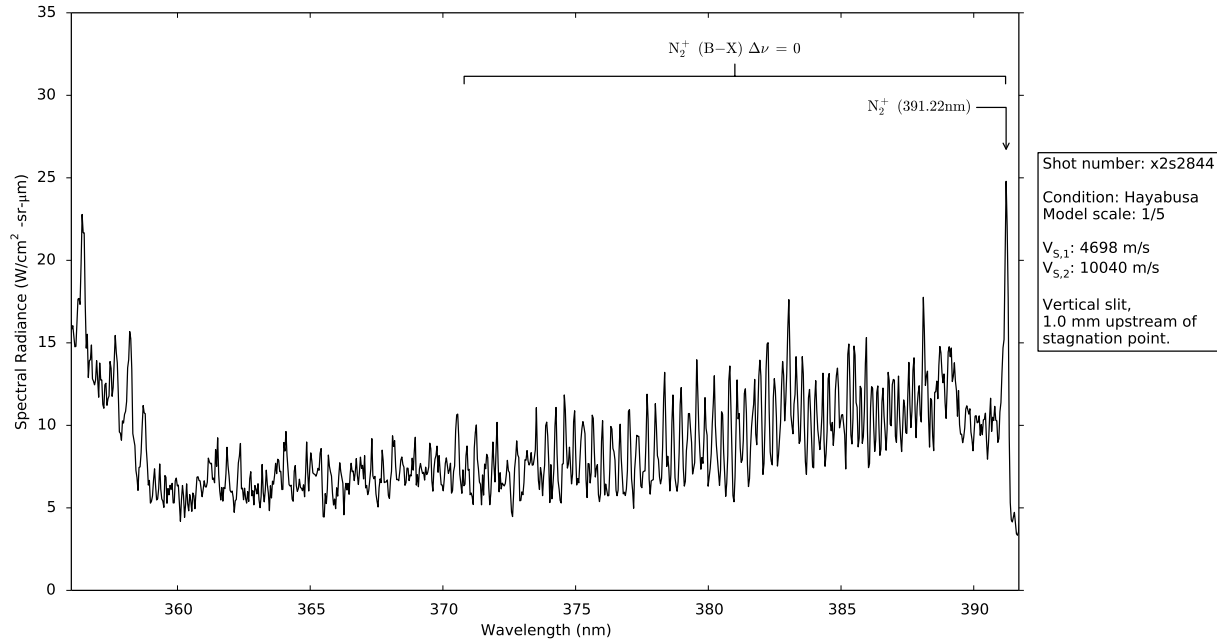


Figure 5.12: Hayabusa UV spectrum at 1.0 mm upstream of stagnation point, centre wavelength 374 nm.

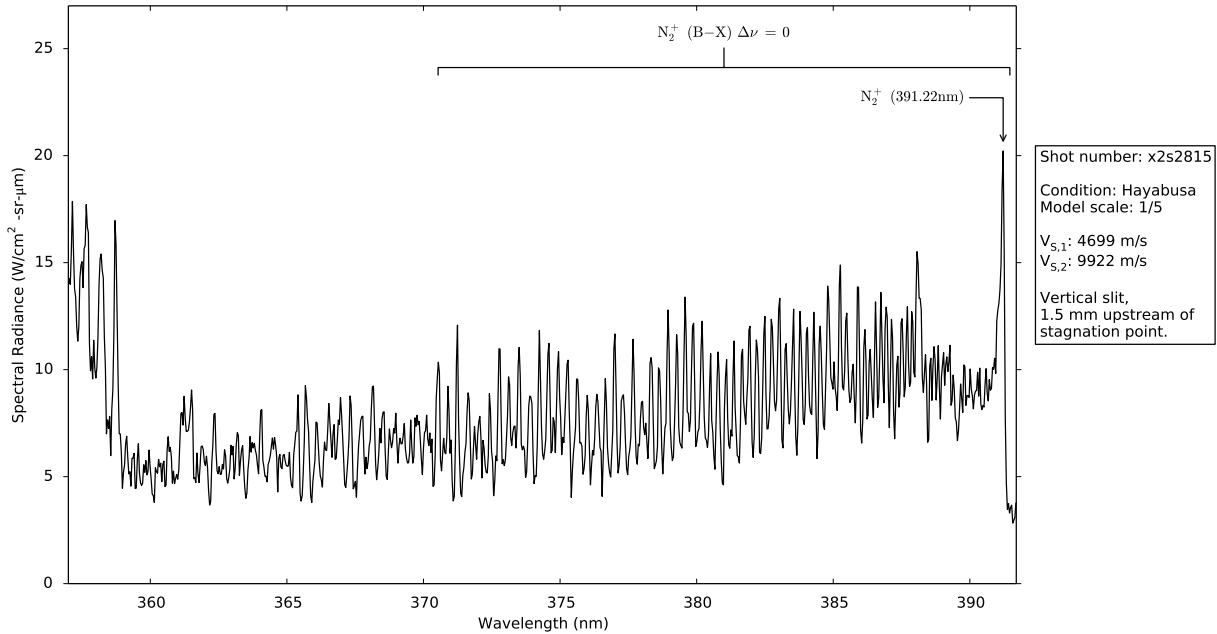


Figure 5.13: Hayabusa UV spectrum at 1.5 mm upstream of stagnation point, centre wavelength 374 nm.

the shock layer and the high-resolution grating, centred at 374 nm, produces distinct emission lines that define the N₂⁺ rovibronic transitions in this energy range. The magnitudes of these peaks are one to two orders of magnitude smaller than in the IR, and it is only the presence of ablated carbonaceous species, primarily CN that increases the UV emissions for an Earth environment. A comparison of the N₂⁺ bandhead peak magnitude across Figures 5.11, 5.12 and 5.13 shows that it remains fairly constant, and falls slowly from the 0.5 mm location to the 1.5 mm location. N₂⁺ is a species created in the abrupt temperature rise of the nonequilibrium shock layer [13], and because it mainly exists in the narrow nonequilibrium region on either side of the line of sight, its variation is most affected by the shock layer width changing with distance from the stagnation point. This contrasts with the atomic species in the near IR region, which vary with the region as well as the differing path lengths.

5.3 2D Intensity Mapping

The narrow band filter centre wavelengths were selected based on the five regions with major features from spectra in Section 5.1: the 780 nm and 840 nm filters captured the two atomic oxygen triplets, and the groups of atomic nitrogen lines were captured by filters centred on 740 nm, 820 nm and 870 nm. The zoom lens was aligned to capture just over half of the shock layer in the vertical direction

and based on the assumption of an axisymmetric profile, the experimental image was mirrored along the stagnation line, which was identified from alignment images. Under this assumption, and if the raw intensity-distance profile showed uniformity on either side of the stagnation line, the shock layer could be captured in more detail because the magnification could be greater. The calibrated images have the horizontal and vertical distances on the x - and y -axes, respectively, and the radiance as coloured contours. There is one contour scale per set of Hayabusa or Stardust images, extending to the maximum radiance value for any of the filters for that model. This is to visualise the difference in intensity between the filter bands, even though the shock layer details are not as evident for the bands with lowest radiance.

5.3.1 Hayabusa

Immediately apparent from the frames of Figure 5.14 is the variation in radiance across the filters. The 820 nm and 870 nm centre wavelength filters produce the most radiance due to the many lines within the filter band, and the 780 nm filter contains the brightest line in the near IR. These features can be referred to in Figures 5.7 and 5.8, for example. Figure 5.14 also shows that the spatial distribution of radiance for each filter band is very similar, as it follows the spatial distribution of the atomic species undergoing the relevant transitions. The highest magnitude emissions were in the thermochemical equilibrium region surrounding the stagnation line, and the radiance decreases going outwards as the sonic line moves toward the model surface from the shock layer edge. The increase in emissions across the shock illustrates the dissociation of molecular nitrogen and oxygen into atomic species, and the excitation of these atoms.

5.3.2 Stardust

The highest radiance values for the Stardust shock layer in Figure 5.15 are from the 870 nm filter and the 820 nm filter, imaging groups of atomic N lines and the 780 nm filter, imaging that bright atomic O triplet. The 840 nm atomic O triplet and the N lines in the 740 nm range produce low radiance; consistent at first glance with spectra in Figures 5.9 and 5.10. There are pronounced differences in

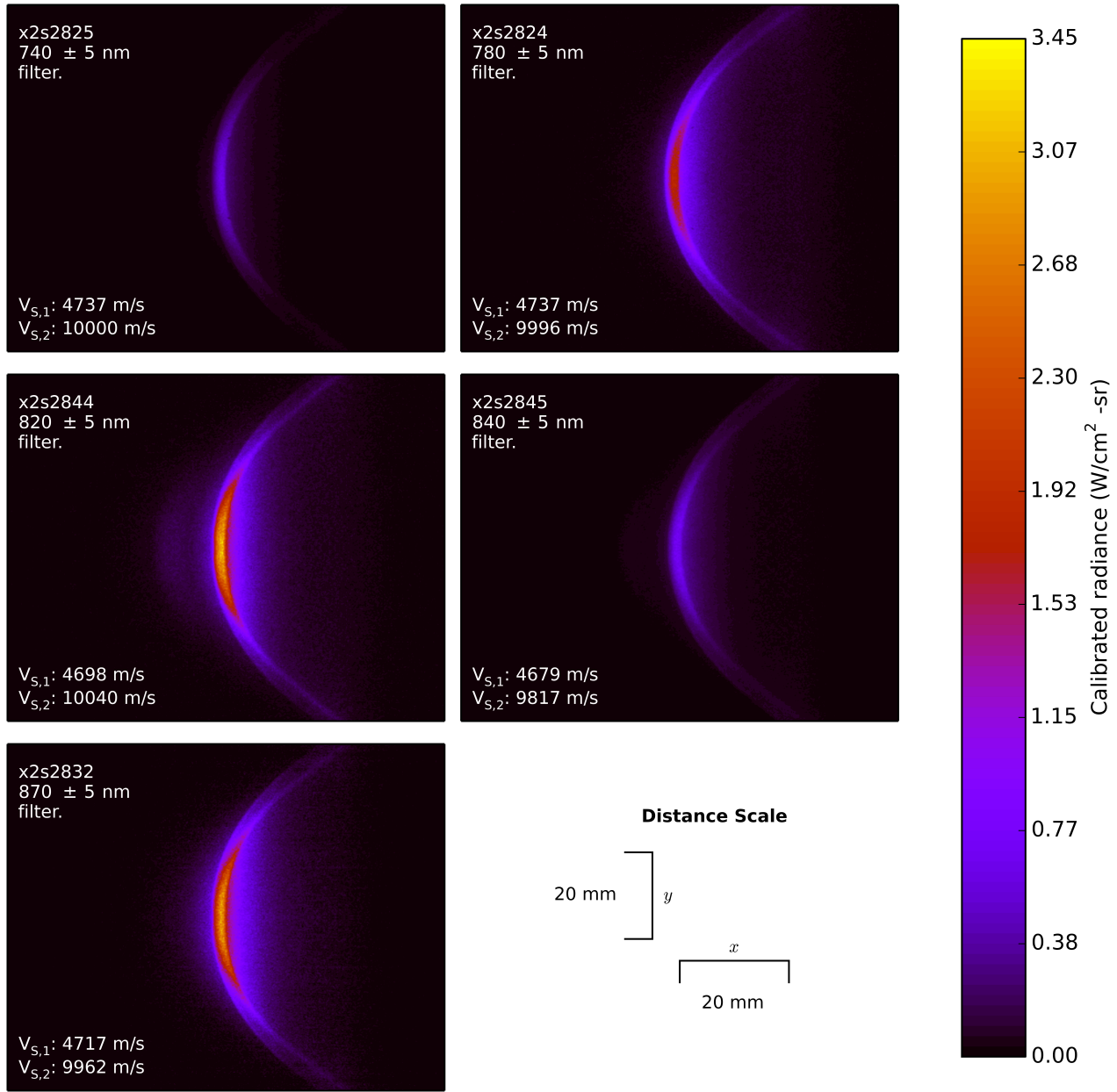


Figure 5.14: Hayabusa shock layer radiance, imaged through various narrow band filters.

the Stardust images relative to Hayabusa, due to the model shape and condition. Stardust's sharper sphere-cone angle, smaller nose radius and faster shock speed produces a smaller shock stand-off than with Hayabusa's more rounded features and slower speed. Stardust shows lower radiance in the region surrounding the stagnation line than Hayabusa for the equivalent filter, indicating that the faster speed is not necessarily decreasing the amount of dissociation from molecular to atomic species, but is likely causing the atomic species to ionise (this is investigated in Chapter 6's CFD simulations). The

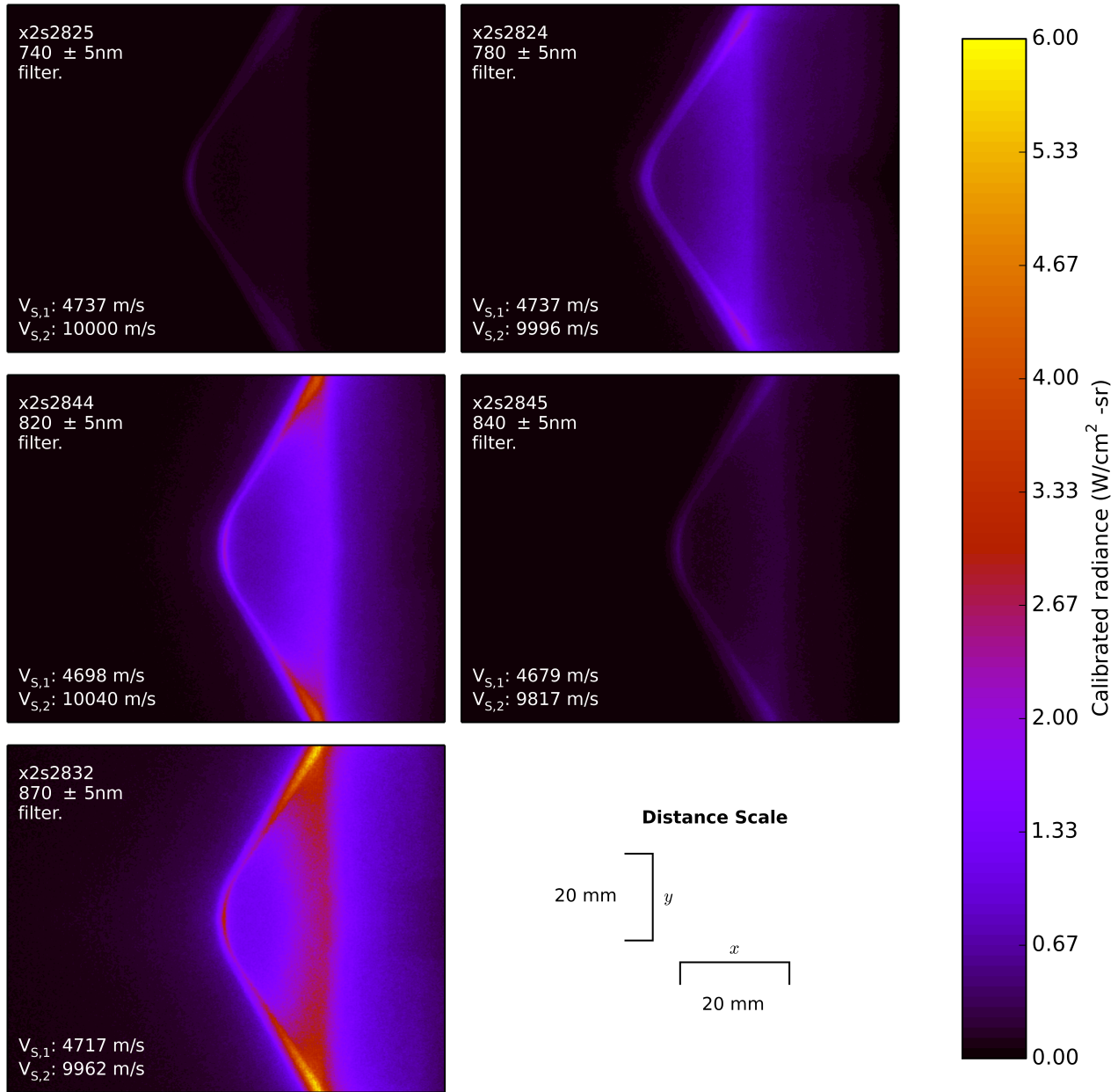


Figure 5.15: Stardust shock layer radiance, imaged through various narrow band filters.

highest radiance values are produced adjacent to the corner at the edge of the vehicle forebody. The relative contribution of the abundance of radiating atomic species in the shoulder region measured against the longest lines of sight is investigated through application of the Abel inversion in Chapter 7.

5.4 Comparing Integrated Spectra and 2D Results

5.4.1 Hayabusa

The comparison between a spectrum measured along a particular vertical slice through the shock layer and a 2D intensity map requires the spectrum to be integrated over the narrow band filter wavelength range from post-processing of the 2D image, and convolved with the transmission function of the filter. The convolution is necessary as the filter was not part of the spectroscopy system but the sizeable impact of the filter transmission functions must be applied to the spectra to make a just comparison with the filtered 2D images. Other optical elements, such as mirrors, lenses and spectrometers, also differ between the two systems but are accounted for in calibration and do not have the same effect on transmission as the narrow band filters. The transmission function, spectral radiance and convolution for the 780 nm region and the 840 nm region are shown in Figures 5.16 and 5.17, respectively, mapping filter transmission on the left y-axis and spectral radiance on the right. The need for the spectral radiance convoluted with transmission is illustrated against the original experimental values.

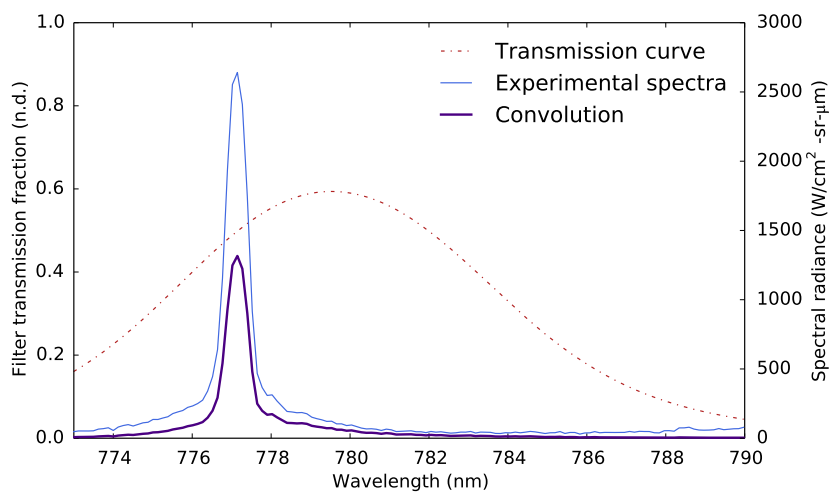


Figure 5.16: Convolving the 780 nm filter transmission curve (left y-axis) with the experimental spectrum in the filter wavelength range (right y-axis) to illustrate reduction in intensity.

The vertical spectrum section with transmission function applied was integrated across the applicable filter wavelength range, along the entire length of the distance axis in the calibrated experimental

image. Wavelength was on the x -axis, distance on the y -axis, and intensity on the z -axis. The integrated spectrum, as an intensity versus vertical distance data set, was mapped over 3D line plots of each column of pixels from the corresponding 2D image, and finally plotted overlapping the column it shared the greatest similarity with. The selected columns of pixels were plotted with the matched integrated spectra at three locations upstream of the stagnation point against vertical distance from the stagnation line in Figures 5.18a and 5.18b, for the regions surrounding 780 nm and 840 nm, respectively. The distances do not match because the vertical spectra were matched to the most similar vertical slice. All slices have strong similarities to the integrated spectra in curve shape and peak magnitude except the 0.5 mm location in Figure 5.18b, which could be caused by different properties in that region of the shock layer, interference by the wall, or variation in the observation depth between the two systems.

Figures 5.18a and 5.18b are the easiest comparisons to make because essentially, one line is being imaged in both systems. The 2D images that group the nitrogen lines image them together by some mechanism, and the effects of broadening are not known. In the spectra, the wings of the discrete lines overlap in a certain way, and this directly influences the integration over the wavelength band. More smearing in the 2D image could increase the observed radiance due to the widened lines overlapping. The O 777 nm and 844 nm triplets are affected by broadening, shown by the line shape and wings, but should still be comparable to the 2D data if the camera and instrument functions of the

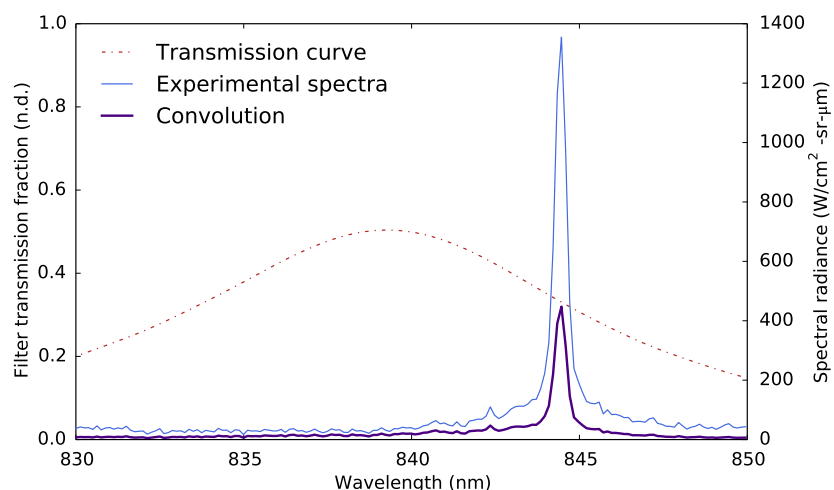


Figure 5.17: Convolving the 840 nm filter transmission curve (left y-axis) with the experimental spectrum in the filter wavelength range (right y-axis) to illustrate reduction in intensity.

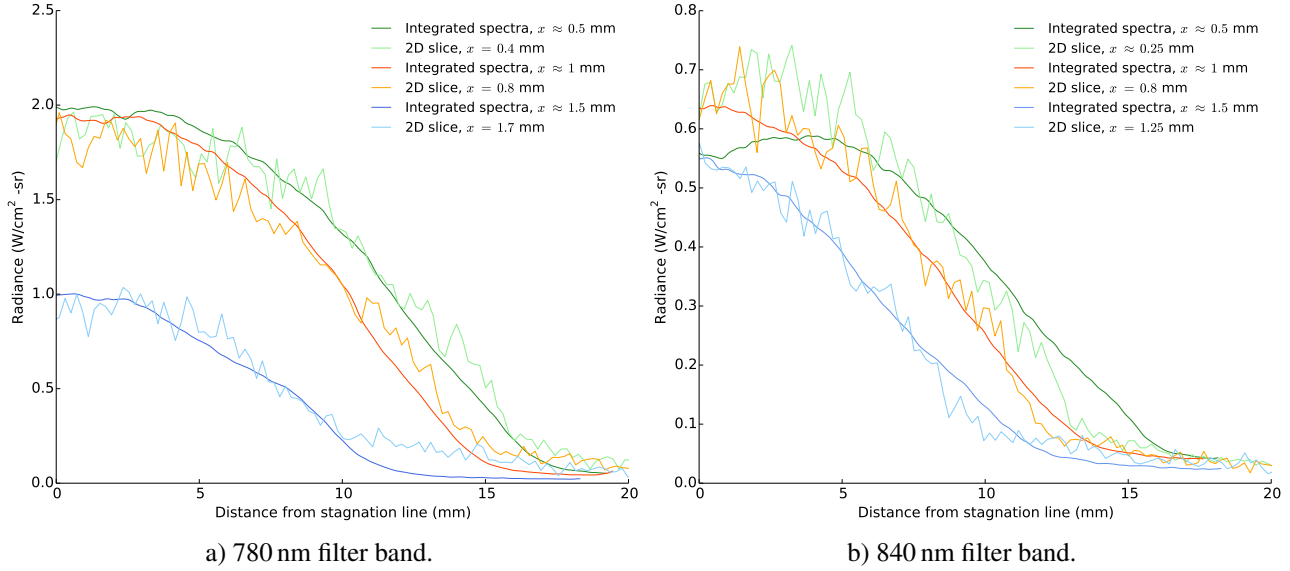


Figure 5.18: Comparison between integrated spectra and slices from 2D images for several vertical locations.

spectroscopy and 2D systems are reasonably similar. Comparisons are also difficult for the line sets around 740 nm and 870 nm because the wavelength range of the comparable spectra cuts off inside the filter integration band. It is encouraging to note that the similarities in the results were achieved even though each 1D result came from a different shot, and the 2D result from a separate shot again.

5.5 Summary

This chapter presented a representative selection of the calibrated IR and UV spectra, and 2D images, that were recorded during the Hayabusa and Stardust X2 experimental campaign. The spectral lines were identified and the strength of the lines in the equilibrium or nonequilibrium regions of the shock layer could be seen. The calibrated 2D images, recorded over five filter bands that correspond to the five main groups of spectral features between 700 and 900 nm, will be used in the flight rebuild in Chapter 7. The calibrated spectra provide good comparison data for CFD spectra, which will be simulated over the next two chapters. Each image was displayed with shot data, including the measured shock speeds, as an indication that every shot is different and the variation in shock speeds from the ideal value has an influence on the resulting spectra. The variation of imaging locations due to unforeseen movement of the test section can also influence the measured spectra. This must be considered

when final comparisons take place with numerical and flight data, and are factors of expansion tube experiments that are difficult to reduce, let alone remove. The comparisons between 1D spectra integrated over a wavelength band and convolved with the filter transmissivity, and the corresponding filtered 2D image sliced at the 1D spectra location, were sufficient considering shot-to-shot variation.

Chapter 6

Computational Fluid Dynamics of Aeroshells in *eilmer3*

The *eilmer3* compressible flow CFD code was implemented to simulate certain trajectory points on the Hayabusa and Stardust re-entries, as well as scaled simulations of expansion tube aeroshell models. As highlighted in Chapter 2, *eilmer3* is capable of capturing the nonequilibrium thermochemistry and viscous flux components that are necessary for modelling hypervelocity flows, and these simulation parameters are detailed. The shock layer surrounding the aeroshells is of interest in understanding the behaviour of air in such high-enthalpy reacting flows, and flowfield properties can be compared to results from other works, using other programs, to assess performance and points of difference. The converged solutions will become inputs for radiation modelling and to produce radiative properties that can compare to experiment and flight. The problems of using high-enthalpy facility data to validate CFD are well known due to the inherent uncertainties in expansion tube flows [7] [91]. These problems can extend to flight data, which may only be available in the form of spectra or heat flux gauge measurements, and requires radiation modelling following the CFD solution, therefore adding to potential uncertainties. In this work, the aim is not to attempt to validate the CFD, but to try to achieve reasonable quality simulations of experiments and identify the differences, in order to improve future experiments and simulations.

eilmer3 is based on the integral form of the Navier-Stokes equations, given in Equation 6.1, and a cell-centred, finite-volume approach is applied to produce solutions in 2D or 3D. The conserved

quantities, U , include total and species density, momentum per volume, and total, vibrational and electron-electronic energy per volume. The inviscid flux vector accounts for mass, momentum and energy flux, while shear stress, heat flux and diffusion are included in the viscous flux vector. The source terms are an amalgamation of geometry, chemistry, thermal energy exchange and radiation components, and their form is determined by the axisymmetry of the model, selected chemical kinetics, thermodynamics and transport models [65].

$$\frac{\partial}{\partial t} \int_V U dV = - \oint_S (\bar{F}_i - \bar{F}_v) \cdot \hat{n} dA + \int_V Q dV \quad (6.1)$$

Performing a simulation in *eilmer3* is illustrated in a greatly simplified manner in Figure 6.1 to introduce the structure and parameters discussed in Section 6.1. The input script defines the grid, mesh and blocking, thermochemistry, transport, inflow and boundary conditions, and control parameters. The pre-processor then forms files that define each aspect of the simulation ready for run time. The simulation can be run in serial or parallel using the relevant executable, and usually for aeroshell calculations, the parallel version is required to handle the fine mesh and hypervelocity conditions. The energy exchange and reaction scheme files are accessed during run time, and the radiation file is also required in a calculation including the radiative source term. Once the simulation is completed, the post-processor writes out the results in formats for visualisation, or in data files following a specified slice through the shock layer. Most commonly, these slices are taken along the stagnation line or around the vehicle surface, but can be in any direction. A more detailed description of the pre- and post-processing and simulation execution is provided in the *eilmer3* user guide [66].

6.1 Simulation Parameters

The parameters selected for the Hayabusa and Stardust simulations are presented as an example of constructing a typical aeroshell calculation in *eilmer3*. Many parameters were the same for the two vehicles and the subsequent scaled models, as both cases were small Earth re-entry capsules with a focus on the radiating air shock layer. Where selections have been stated and reasons have not been expanded upon, it reflects the best available in *eilmer3* and, in general, the current standard for aeroshell calculations.

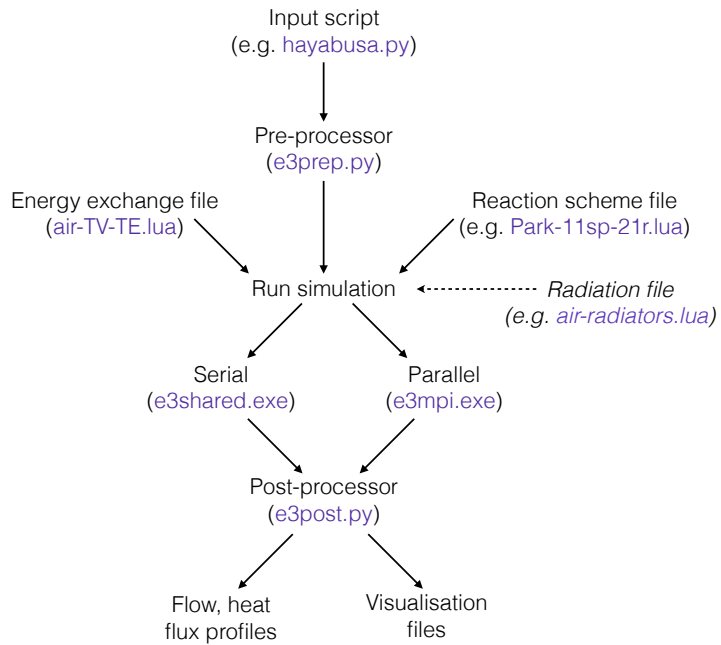
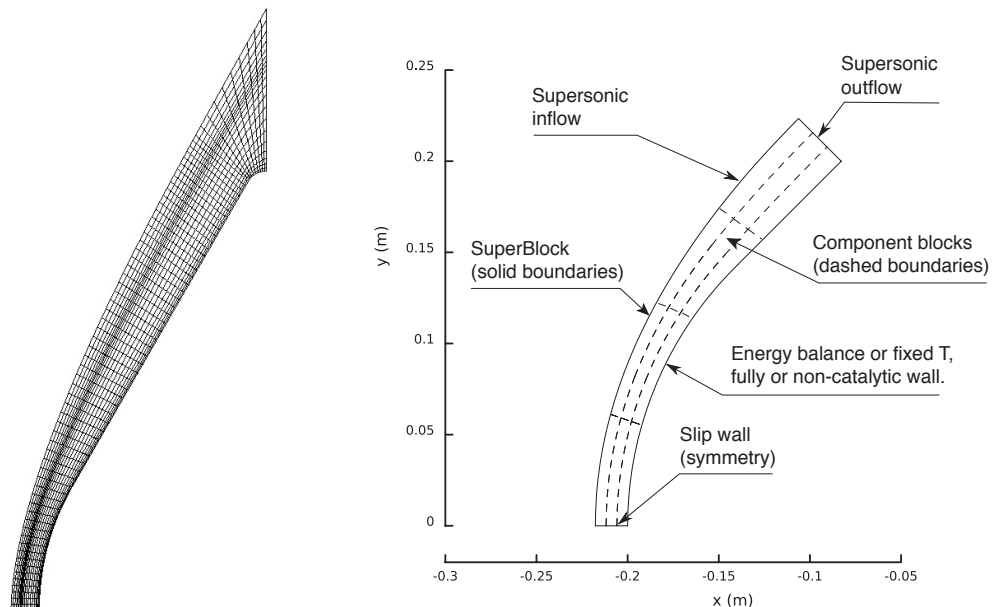


Figure 6.1: Running a simulation in *eilmer3*: a brief overview.

6.1.1 Grid, Meshing and Block Structure

The axisymmetry of the aeroshell and X2 model shock layers is exploited so that simulations can be performed in 2D, with a symmetry axis at the stagnation line. This extends from the assumption that Hayabusa and Stardust follow ballistic trajectories at high altitudes, hence the simulated flowfield can be oriented with zero angle of attack [35] [1]. The grid has been sized to include the forebody shock layer only, extending slightly around the shoulder for Stardust as the shoulder radius is commonly defined [25]. It is assumed that the majority of the radiation captured in flight observations emanates from the forebody and the expansion tube measurements followed this assumption, imaging only the forebody region. The current set-up of expansion tube models precludes afterbody imaging or comparable modelling due to the mounting arrangement. Potter [13] demonstrated that excluding the afterbody flow did not affect the forebody flow around a Hayabusa model. The added computational expense and complexity from turbulence and separation zones is not necessary for the present calculations.

The grid is defined by nodes and bounding curves placed along the surface, extending outwards from the shoulder and the stagnation point to a similarly curved upstream boundary located beyond the shock front. This arrangement is shown in Figure 6.2b. Positioning the upstream boundary to sufficiently capture the shock requires some trial and error during the first attempt at simulating each condition, as the shock stand-off will change. The number of structured, quadrilateral cells in the x and y directions are specified and clustering functions can skew the width and number of cells in critical areas, based on positioning and strength coefficients. Clustering is generally applied near the wall to resolve the viscous boundary layer, around the shock for better detail in the nonequilibrium region and towards the stagnation line to lower the aspect ratio of cells in this critical region. A mesh over the Stardust flow domain is shown in Figure 6.2a and the cell numbers and strength of clustering have been reduced to better illustrate these features. The Hayabusa mesh is similarly structured and is therefore not shown.



a) Typical Stardust cell and domain layout,b) Typical Hayabusa block layout using SuperBlock constructor with reduced number of cells and reduced boundary conditions.
clustering.

Figure 6.2: Aeroshell cell, domain and block layout examples.

The number of blocks specified in the x and y directions define the total number of blocks and their placement as they are overlaid on the cells. The ‘SuperBlock’ constructor is used in the aeroshell

calculations to define properties of whole areas, such as boundary conditions for the entire forebody domain, and partition these into sub-blocks. This method allows easy assignment of blocks to processors, and as the machines used to run these simulations had 16 processors per node and few restrictions on allowed hours, the number of blocks was a multiple of 16 and were assigned 1:1 to the processors. The maximum number of blocks used in the current simulations was 64, and they would generally run to completion in less than 48 hours, barring errors. The assignment of a SuperBlock, sub-blocks and boundary conditions to a Hayabusa forebody domain is presented in Figure 6.2b, without showing the cell layout. The same boundary conditions and similar blocking structure were also applied to Stardust. The boundary conditions are expanded upon in Section 6.1.4.

The final Hayabusa grid resolution was 100×100 cells, including strong clustering in the x -direction around the shock and near the wall, and weak clustering towards the symmetry axis in the y -direction. Richardson extrapolation was used to test the convergence based on grids with 25 % and 6.25 % of the cells, where the number of cells in the x - and y -direction were each reduced by a factor of 2 in each grid to give an overall grid refinement ratio of 4. The test parameter is extrapolated based on the values from each grid to a theoretical ideal value at zero grid spacing [85]. The test parameter was temperature at the edge of the thermal equilibrium region closest to the wall, about 2.6 mm upstream of the stagnation point and on the stagnation line. The two temperatures in each simulation were seen to be in equilibrium at that point before temperatures decreased approaching the wall. The converging temperature values determined that the grid was sufficiently resolved and the ideal extrapolated value is shown in Figure 6.3. Grid spacing on the x -axis refers to the normalised size of the cells relative to the most refined grid, which has a value of 1. The scaled Hayabusa grids have the same set-up as the full scale grid and show the same trends in convergence.

The final Stardust grid resolution was 90×210 cells; 180 cells in the y -direction mapping the sphere-cone and 30 in the small SuperBlock around the shoulder. Strong clustering is applied around the shock and near the wall as for Hayabusa. Cells are weakly clustered towards the stagnation line, outflow, and adjacent boundary between SuperBlocks, as the flow begins to pass around the shoulder. Richardson extrapolation was applied at 2.6 mm on the stagnation line and upstream of the stagnation point, and results are calculated and plotted in Figure 6.4 following the same procedure described

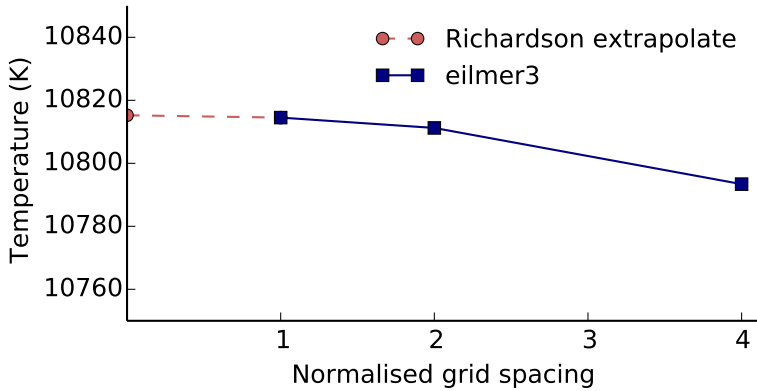


Figure 6.3: Hayabusa grid convergence study using Richardson extrapolation to calculate temperature at zero grid spacing.

for Hayabusa. The scaled Stardust simulations show the same convergence trends as the full scale because the same number of cells and cell layout was implemented.

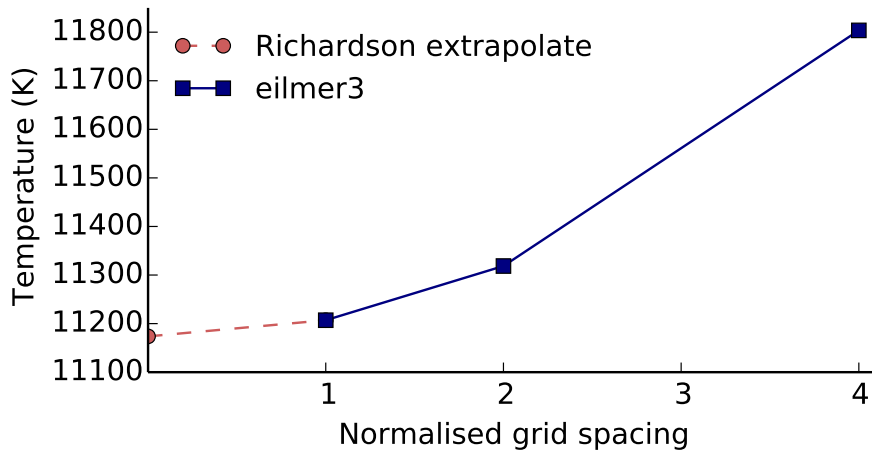


Figure 6.4: Stardust grid convergence study using Richardson extrapolation to calculate temperature at zero grid spacing.

Against a theoretical order of convergence of $r = 1$, the calculated orders of convergence, p , were 1.06 for Stardust and 1.22 for Hayabusa, and differences can be caused by the presence of shocks, grid stretching and shape, and any non-linearities in the solution [85]. The results are within the asymptotic range of convergence since 1.0003 (Hayabusa) and 0.99 (Stardust) are both sufficiently close to the theoretical value of 1, as expected for a shock-capturing scheme with limiters. For the selected points, the Hayabusa result can be quoted as 10815.2 K with an error of 0.0085 %, and the

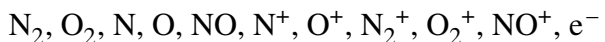
Stardust result as 11 173.7 K with an error of 0.37 %. The uncertainties are calculated by the finest grid convergence index [92], provided in Equation 6.2. The safety factor G_s was selected to be 1.25 as the comparison was over three grids [85].

$$GCI_{fine} = \frac{G_s}{r^p - 1} \frac{g_1 - g_2}{g_1} \quad (6.2)$$

The Hayabusa solution is more converged than Stardust in terms of the ideal value at zero grid spacing and the uncertainty, but the Stardust outcomes are likely a consequence of the high velocity, high altitude condition that is approaching non-continuum. As will be discussed in Section 6.2.4, the Stardust shock layer is almost entirely nonequilibrium apart from one cross-over region at which the data above were taken, and the temperatures are far beyond reasonable extrapolation limits in thermodynamic data. Therefore, the higher level of uncertainty and range to the ideal Stardust result in terms of the grid is fine given the other uncertainties that are impacting the simulation. The coarser grids move away from the ideal value more rapidly in the Stardust case because the loss of cells, especially in the x -direction, has a greater effect on the highly nonequilibrium shock layer for the Hayabusa shock layer where the nonequilibrium portion is only half of the shock layer.

6.1.2 Thermochemistry

At a user level, specifying thermochemical parameters is straightforward: define a list of species, the thermal model, the energy exchange file when considering multiple thermal modes, and reaction scheme file if the reacting flag is set. A gas model file is generated in *lua* format and is read in by the thermochemistry module during the simulation, containing details from the top-level choices. The same gas model parameters were used throughout the Hayabusa and Stardust simulations. The high-temperature nature of hypervelocity Earth re-entry flows meant that the 11 species air model with molecules and atoms, and their associated ions plus electrons, was required as evidenced by Gupta *et al.* [93]. These species are:



Species that exist in trace amounts, including water and carbon dioxide, were omitted.

The necessity of thermochemical nonequilibrium modelling for aeroshells at entry speeds of over $10 \text{ km} \cdot \text{s}^{-1}$ was illustrated by Tirskey [8] in the image reproduced by Gollan [7], and included here in Figure 6.5. A nonequilibrium, two-temperature thermal model combined the translational-rotational modes and the vibrational-electron-electronic modes as suggested by Park [67]. The two-temperature model calculates viscous transport and thermal conductivity by implementing Gupta *et al.*'s mixing rules [93], which calculate viscosity coefficients, modal conductivities, mixture coefficients and binary diffusion coefficients through collision integrals [13]. As Boyd *et al.* stated, this approach sufficiently approximated the more accurate Chapman-Enskog relations for the Stardust flow regime [68] when compared by Palmer and Wright [94]. As Gupta *et al.*'s mixing rules are meant for continuum, it is certainly appropriate for the lower altitude, lower velocity Hayabusa conditions considered herein.

Thermal energy exchange is caused by interaction between individual thermal modes of colliding species and chemical reactions, and is presently modelled for air species only in *eilmer3*. A supplementary *lua* file defines interactions between certain species as well as parameters to calculate the relaxation time. Vibrational-translational energy exchange is modelled by the Landau-Teller equation [7], and the relaxation time is calculated using the Millikan and White [95] correlation with the Park high-temperature correction applied [67]. The Appleton and Bray [96] rate equation is applied for exchanges between electrons and heavy particles' translational modes (ion or neutral) through elastic collisions [13]. Exchanges with the rotational mode are not considered because it relaxes to the translational temperature in the order of tens of collisions, compared to the tens of thousands of collisions required to bring the translational and vibrational modes to equilibrium [7]. Vibration-electron exchanges only become important when these two modes are separated and in nonequilibrium [13], but these exchanges are not accommodated in a two-temperature model; instead, a three temperature model would be necessary if the vibration and electronic modes are not equilibrated.

Chemical reactions describe how shock-processed gas dissociates, ionises, and exchanges molecules or charge. Park's 21 reaction scheme [67] and Gupta's 20 reaction scheme [93] (or slight variations

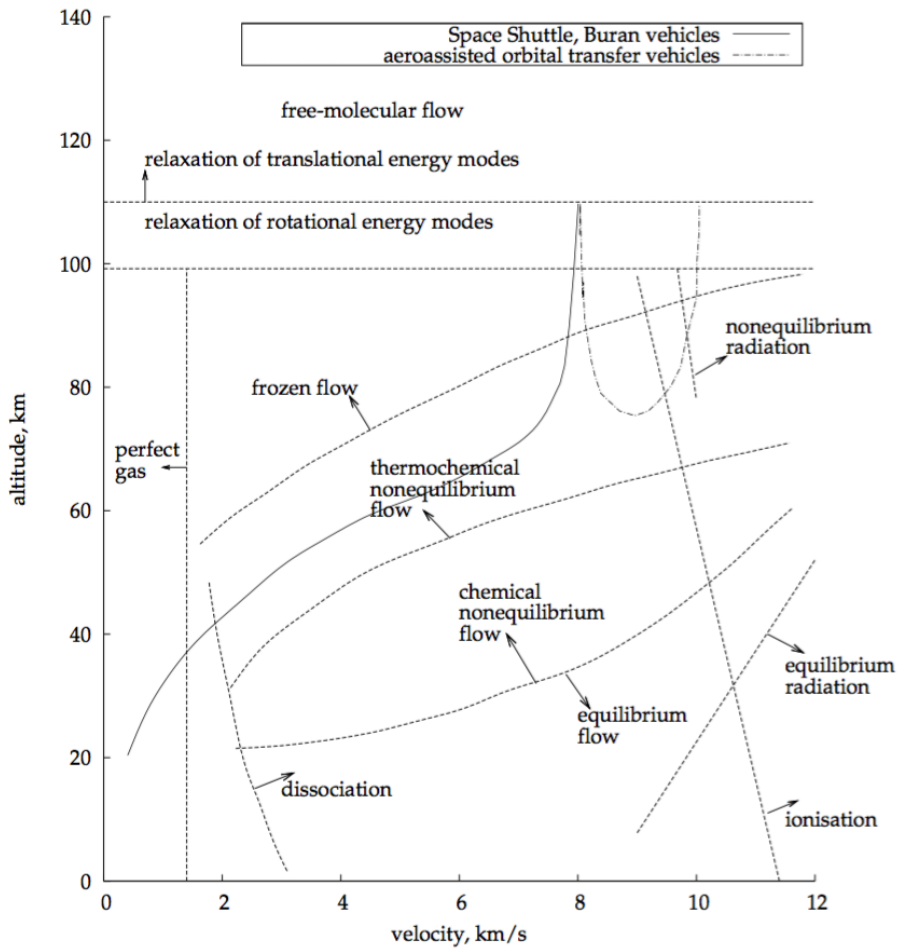


Figure 6.5: The trajectories of (1) Space Shuttle and Buran vehicles, and (2) aeroassisted orbital transfer vehicles, mapped by velocity and altitude to indicate important regions for physical and chemical processes. Reproduced from Gollan [7], who redrew the original figure from Tirsky [8].

of these) are the most common models to describe finite-rate air chemistry with 11 species. The schemes, documented in a supplementary *lua* file, give the species involved in the reaction, the model for calculating the forward reaction rate, and an equation for either an equilibrium rate constant or backward reaction rate. The generalised Arrhenius form for forward rate coefficients is presented in Equation 6.3, where E_a is the activation energy, A and n are model-specific parameters, and k_B is the Boltzmann constant. E_a , A and n are all documented per reaction in the *lua* file for each scheme.

$$k_f = AT^n \exp \frac{-E_a}{k_B T} \quad (6.3)$$

Dissociation reactions are governed by a weighted version of Park's geometric average temperature [67] as given in Equation 6.4, due to improvement in N_2 dissociation rates with this weighting [13]

[97]. Forward rates for neutral exchange reactions, charge exchange reactions, and associative ionisation reactions use T_{tr} with the Arrhenius equation (Equation 6.3), while electron impact ionisation reactions set T_{ve} as the governing temperature. The Park formulation allows efficiencies to be set for third-body species assisting in dissociation reactions, and chemistry-energy coupling can be included to account for the thermal energy change during formation or destruction of species [13]. Backward reaction rates follow an Arrhenius form similar to Equation 6.3, and are governed by T_{tr} only if applied to recombination reactions. The equilibrium constant can be formulated following the procedure in the *eilmer3* theory book [98].

$$T = \sqrt{T_{tr}^{0.7} T_{ve}^{0.3}} \quad (6.4)$$

The limitations of the two-temperature model are known in literature (see, for example, [91]) and so comparing two reaction schemes with the apparent thermal model limitations may be a futile exercise. Each reaction scheme was applied in an attempt to make the process of numerical rebuilding of flight or experiments as straightforward as possible. Park was easier to work with in terms of general numerical stability, adaptability to grid refinement and computational time, especially for Stardust, as Gupta was unable to produce sufficiently refined results. The results of modelling Hayabusa with the two reaction schemes, including flow parameters and numerical spectra, are presented in Section 6.2.1.

6.1.3 Diffusion, Turbulence and Non-Continuum Effects

Diffusion between air species forms the final term in the viscous flux vector and can be modelled most simply by assuming a binary mixture of species i and an aggregate of all remaining species. Fick's law is the basis for calculating diffusive flux J_s from the binary diffusion coefficient D_i , but only applies to binary diffusion of two gases [99]. Ramshaw and Chang's self-consistent effective binary diffusion approximation to the Stefan-Maxwell equations [100] allows calculation of multicomponent diffusion, as an extension to Fick's law, and calculates the multicomponent diffusion coefficients from their binary counterparts, which come from Gupta *et al.*'s collision integrals [93]. The multicomponent model should better represent the physical problem than the constant Lewis number approximation

previously implemented in *eilmer3*, which assumed the same binary diffusion coefficient for each species pair, as demonstrated by Sutton and Gnoffo [99].

The flows around the blunt Hayabusa and Stardust forebodies are assumed to be laminar, based on calculations by Winter *et al.* showing that the Hayabusa wall Reynolds number at varying altitudes, calculated with an assumed roughness height, remained less than its critical value [35]. Liu *et al.* made the same assumption in their Stardust simulations [70]. As discussed in Chapter 3, the Knudsen number indicates that while the X2 flow over a scaled Stardust model should be continuum, the full scale trajectory point may be non-continuum. Boyd *et al.* show that the overall Knudsen number is not good enough for evaluating local non-continuum effects, especially in the Stardust stagnation point region [68], and could have an effect on the results in Section 6.2.4.

6.1.4 Boundary Conditions

The forebody flow domains are bounded by an inflow boundary a symmetry axis, the vehicle wall and an outflow boundary. The stagnation line symmetry axis can be represented by a slip wall boundary condition with no viscous effects due to no shear stress. The inflow boundary must have at least supersonic velocity and is defined by the freestream conditions either at the flight trajectory point or from the nozzle exit flow in X2. The outflow boundary condition extrapolates the values from cells adjacent to the outflow boundary, and performs best with supersonic flow, which is generally achieved by the shoulder region. The vehicle wall has a fixed temperature for the X2 model simulations because the stainless steel wall begins at room temperature (about 300 K) and the extremely short test times only raise the wall temperature by 100 K at most [101]. In that temperature range, there are negligible effects on the flowfield or heat flux. For flight simulations, the vehicle walls are modelled by a surface energy balance, where the dynamic wall temperature is updated every step from the heat flux incident on the wall and re-radiated heat flux, assuming the wall acts as a black-body [13]. The emissivity of the wall is assumed to be 0.9 and the temperature calculation is given in Equation 6.5, as a rearrangement of the heat flux balance. The wall catalycity can currently be modelled as non-catalytic, or super-catalytic, which in *eilmer3* is an attempt to push full recombination to freestream values of N₂ and O₂. These can be viewed as the bounding cases for wall catalycity and both were investigated to

provide an idea of the impact of catalycity on the flow near the wall. The super-catalytic assumption holds more validity for the X2 model, since the low-temperature steel surface could potentially drive such extreme recombination in the short test time.

$$T_w = \left(\frac{-q_{cond} \cdot \hat{n} - q_{diff} \cdot \hat{n} - q_{rad} \cdot \hat{n}}{\epsilon \sigma} \right)^{1/4} \quad (6.5)$$

In Section 3.1.5.2, nozzle calculations were performed with equilibrium thermochemistry or a single temperature and 5 reacting air species. The different thermochemistry models had some effect on the flow parameters at the model location, including a decreased temperature and increased density through the test time for the Park 5 species, one temperature (1T) case. To investigate if the changed flow conditions would affect the post-shock results, two coarse grid scaled Hayabusa simulations were conducted, with one inflow constructed from the equilibrium thermochemistry case, and the other from the Park 5 species, 1T case. The inflow mole fractions for the equilibrium case were calculated in CEA [82].

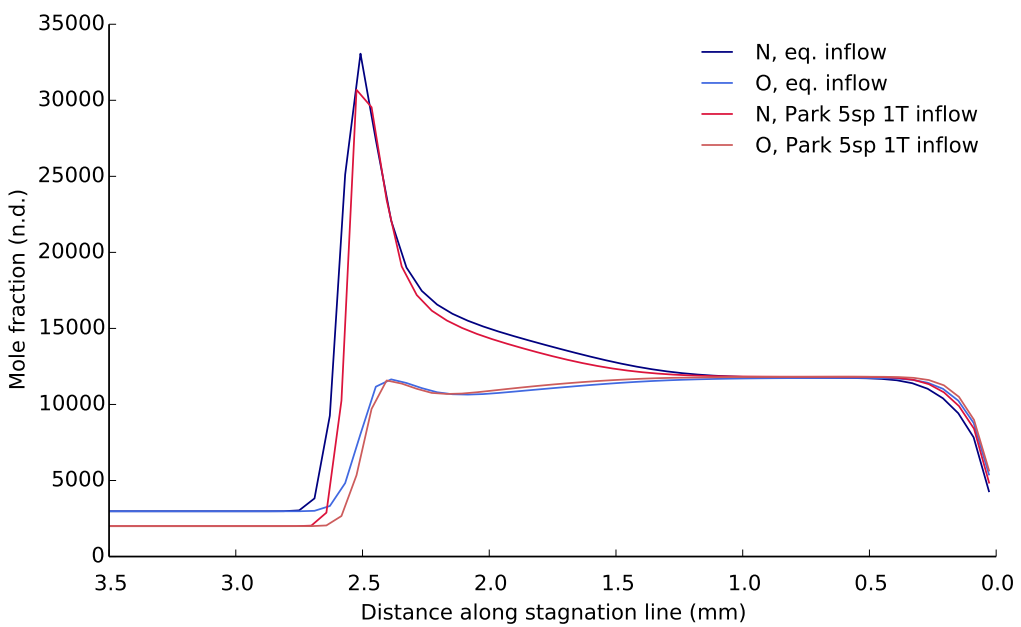


Figure 6.6: Temperatures along stagnation line for Hayabusa scaled simulation, comparing inflow conditions constructed from equilibrium (eq.) and Park 5 species (sp) 1T facility simulations.

Figure 6.6 compares the two temperatures through the shock layer for each inflow condition, and Figure 6.7 compares the mole fractions for N and O. Mole fractions are non-dimensional, and are

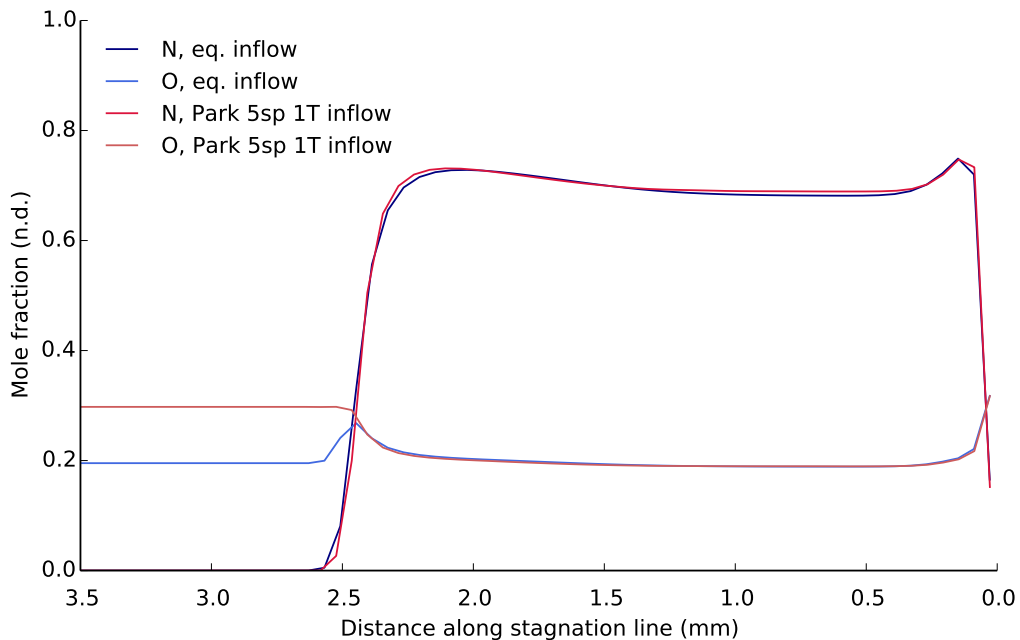


Figure 6.7: N and O mole fractions along stagnation line for Hayabusa scaled simulation, comparing inflow conditions constructed from equilibrium (eq.) and Park 5 species (sp) 1T facility simulations.

labelled in Figure 6.7 and following plots as ‘n.d.’. There are small differences in the temperature rise across the shock that can be attributed to the grid, but any differences due to the inflow conditions are slight, especially when the shock layer is in thermochemical equilibrium. Observing the pre-shock differences in temperature and mole fractions, the post-shock results are significant, confirming the use of the equilibrium facility simulations as inflow for the scaled Hayabusa simulations. It is assumed that this applies to the Stardust simulations also. Any differences that then occur with the full scale or ideal scaled simulations are based on the condition itself and how well it has been scaled, rather than the thermochemistry models used for the facility simulations.

6.1.5 Summary

Selections of simulation parameters or example values for flowfield calculations that have been discussed above are summarised in Table 6.1 as a reference.

Gas model	11 species air
Reaction scheme	Park, Gupta
Thermal model	Nonequilibrium, two-temperature. Park's geometric average for rate-controlling T.
Thermal energy exchange	Vibrational-translational: Millikan-White. Electronic-translational: Appleton-Bray.
Transport properties	Gupta <i>et al.</i> mixing rule with collision integrals for viscosity and diffusion coefficients.
Diffusion model	Ramshaw-Chang self-consistent effective binary diffusion.
Turbulence	None.
Wall boundary conditions	Fixed temperature or surface energy balance. Super- or non-catalytic.

Table 6.1: Summary of flowfield parameters for CFD aeroshell simulations in *eilmer3*.

6.2 Flowfield Results

6.2.1 Hayabusa full scale simulation

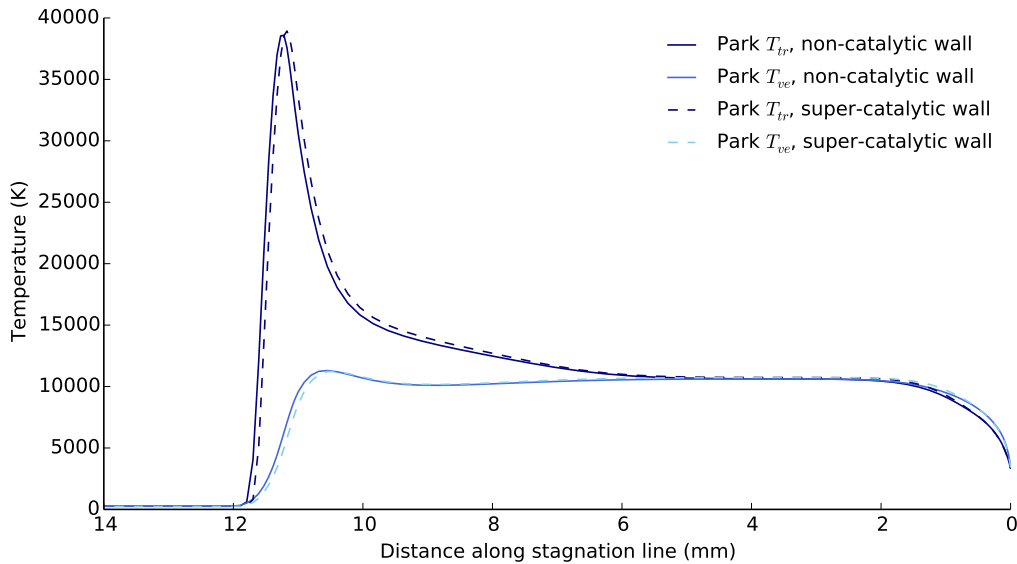


Figure 6.8: Temperatures along stagnation line for Hayabusa full scale simulation, comparing Park with non-catalytic and super-catalytic wall.

The super-catalytic and non-catalytic wall boundary conditions were tested on the refined Hayabusa grid and the effect on temperature along the stagnation line is plotted in Figure 6.8. The temperature

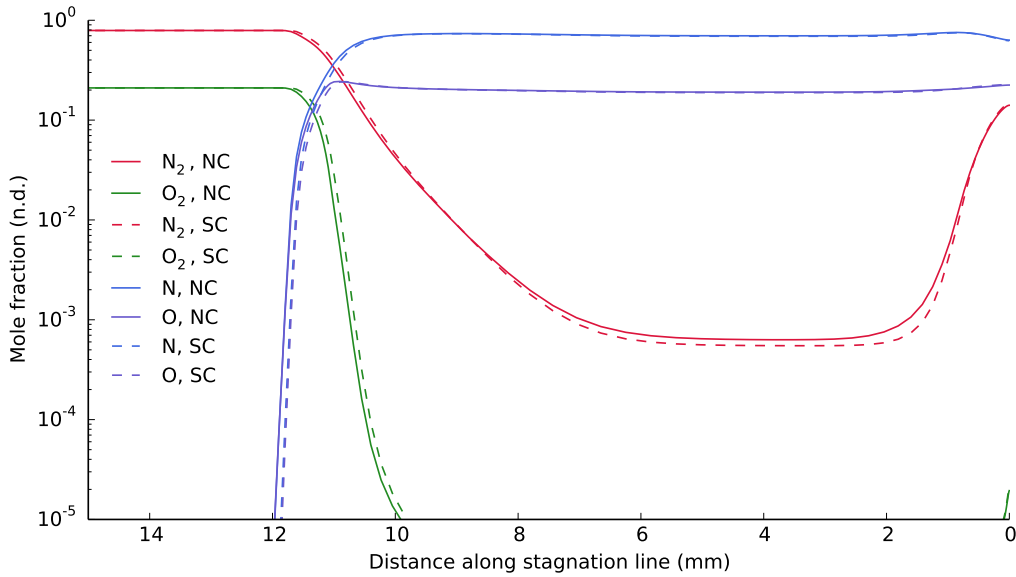


Figure 6.9: Selected mole fractions along stagnation line for Hayabusa full scale simulation, comparing Park with non-catalytic and super-catalytic wall.

change throughout the shock layer is around 0.1 % and the wall has not significantly influenced the boundary layer, as the radiative equilibrium wall temperature is too high for forced recombination to occur. Figure 6.12 demonstrates the lack of recombination in both cases, in terms of N and O atoms and molecules that dominate the shock layer and freestream, respectively. These results are consistent with the comparison of catalytic walls for a lower altitude, theoretical Hayabusa trajectory point, simulated by Potter using *eilm3* [13]. Catalytic walls may have a greater impact on the boundary layer if the wall temperature drops, or in combination with ablation and pyrolysis. The super-catalytic wall simulation will be the default solution for the remaining results in this section.

The Park and Gupta reaction schemes do influence many flowfield parameters, and this is demonstrated by plotting the temperatures along the stagnation line in Figure 6.10. The Park peak T_{tr} and T_{ve} temperatures are higher than Gupta, the shock stand-off distance is greater using the Park scheme, and T_{tr} takes longer to relax. The Gupta thermal equilibrium region extends from the boundary layer edge to 1 mm downstream of the shock, whereas the Park temperatures are in equilibrium for about 4 mm in total. There is also some temperature separation in the boundary layer, as the modes relax differently to the radiative equilibrium wall temperature. Winter *et al.*'s temperature plots show a highly equilibrium shock layer that is near the same temperature as the present calculations

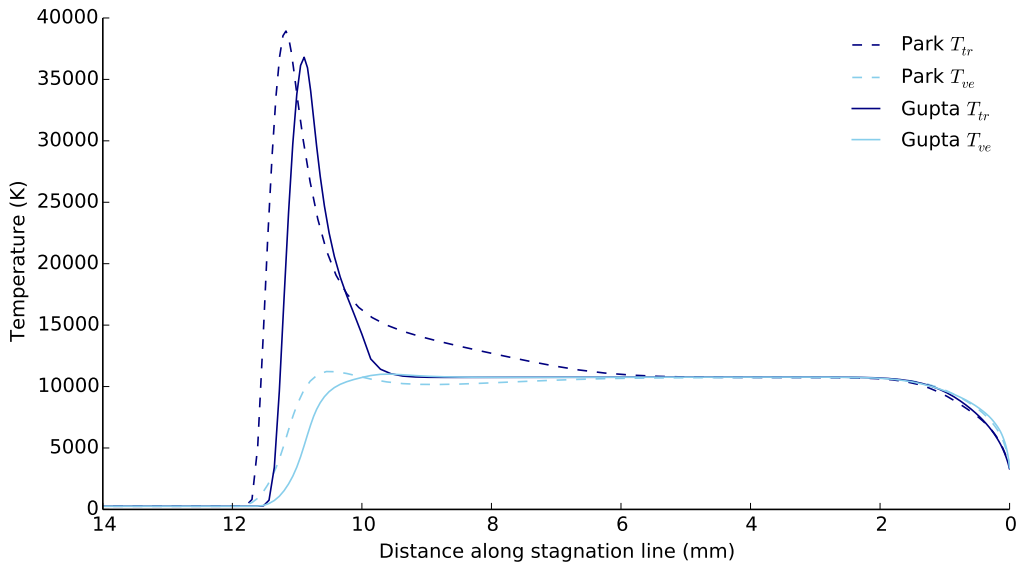


Figure 6.10: Temperatures along stagnation line for Hayabusa full scale simulation, using Park and Gupta reaction schemes. Super-catalytic wall.

(the figure scale prevents any exact comparisons), lower peaks in T_{tr} and T_{ve} , less separation of temperatures in the boundary layer and similar shock stand-off distance [35]. The temperatures along the stagnation line that were calculated by Kihara *et al.* [75] and Suzuki *et al.* [74] look very similar to the present results using the Park reaction scheme, albeit at one second later in the Hayabusa trajectory (13:52:21 UTC). The higher resolution grid in Kihara *et al.* shows a T_{tr} peak at nearly 40 000 K, compared to about 39 000 K in Figure 6.10. The equilibrium regions are about 4 mm wide in both cases, and the shock standoff is approximately 11 mm in Figure 6.10 and 12 mm in Kihara *et al.* [75] and Suzuki *et al.* [74]. Although the Gupta results are closer to Winter *et al.*'s results, the initial decision of going forward with the Hayabusa condition was based on the nonequilibrium shown in the Park simulation, which compare favourably with Kihara *et al.*'s and Suzuki *et al.*'s results.

The Park and Gupta reaction schemes impact the mole fractions across the shock layer, exemplified by atomic and molecular N and O, and N_2^+ , mole fractions in Figure 6.11. The main difference is in the approach to modelling equilibrium between the two reaction schemes, which affects the average flow properties, including density, across the shock layer. This, in turn, causes the larger shock stand-off distance with the Park model, although the length of the dissociation regions are nearly identical, simply translated by that difference in shock stand-off. The atomic mole fraction

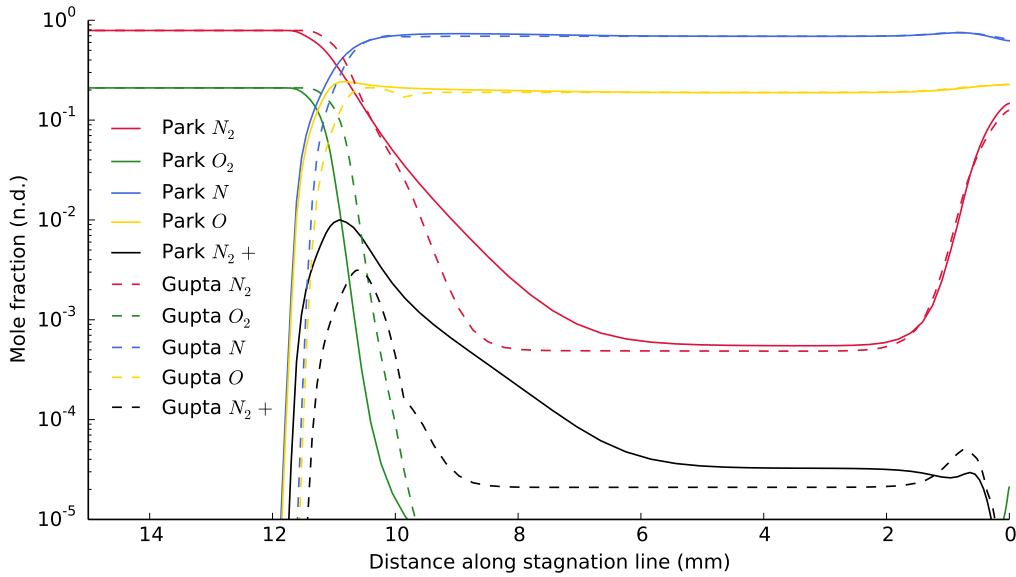


Figure 6.11: Mole fractions for atomic and molecular N and O, and N_2^+ , along stagnation line for Hayabusa full scale simulation, comparison between Park (solid line) and Gupta (dashed line) reaction schemes.

magnitudes are also almost identical, and when considering the similarities in temperature and other flow properties, the reaction scheme should have a minor impact on calculation of atomic radiation in the IR. Therefore, for Hayabusa and Stardust in the IR, the Park reaction scheme was implemented and forms the exemplary results shown for the continuation of this chapter. The major species in UV spectra when considering air only is N_2^+ , and it is clear from Figure 6.11 that the two reaction schemes model the creation and destruction of this species quite differently. Therefore, for the Hayabusa UV numerical spectra, the Gupta reaction scheme will be used for the flowfield calculation as well as Park, to investigate the differences between the models.

The mole fractions of all 11 species are plotted in Figure 6.12, and were calculated using the Park scheme. O_2^+ is the only species created across the shock that virtually disappears once the temperatures fall, but the other ionic species persist through the shock layer to the wall. N, O, and their ions and free electrons dominate the shock layer, reaching a chemical equilibrium state between approximately 2 and 6 mm from the wall, as stated previously.

Figure 6.13 depicts temperature and pressure around the aeroshell surface, from the stagnation point to the shoulder following the sphere-cone shape. The stagnation point pressure is just over half an

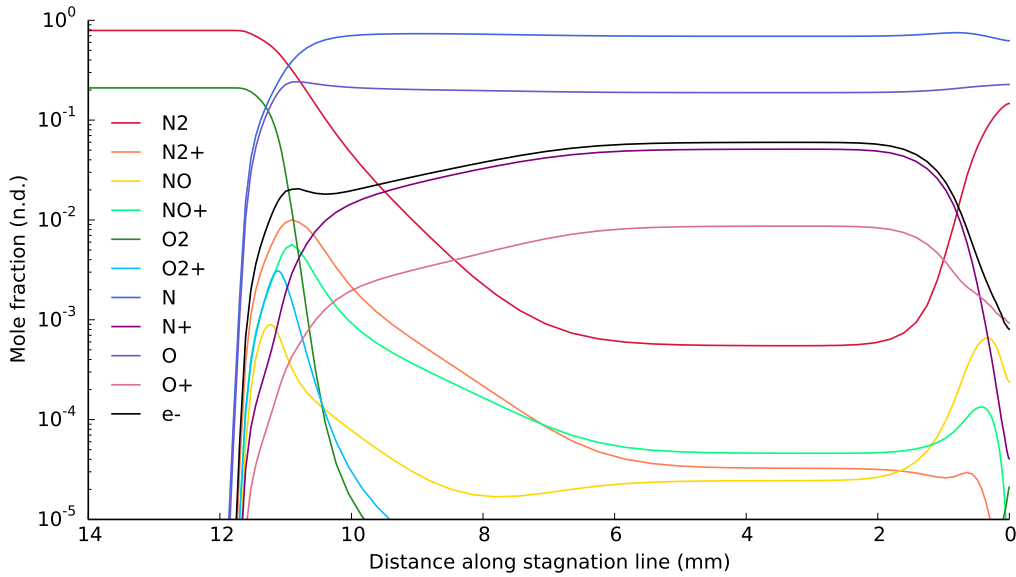


Figure 6.12: Mole fractions along stagnation line for Hayabusa full scale simulation, Park reaction scheme.

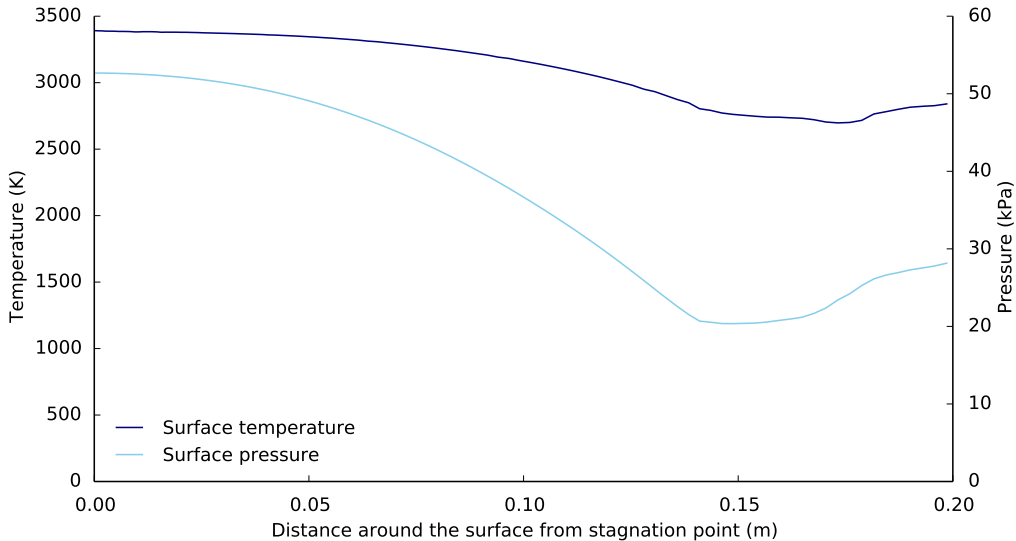


Figure 6.13: Temperature and pressure along the vehicle surface from the stagnation point for Hayabusa full scale simulation.

atmosphere, and radiative equilibrium temperature is about 3400 K. Both parameters decrease with the distance around the surface, until just before the shoulder, where an inflection point is reached and p and T increase until the outflow boundary. The peak temperature is higher than the temperature calculated from thermal radiation in Winter *et al.* (≈ 3100 K) [35], from IR data in McInytre *et al.* (≈ 3090 K) [4] and across the spectrum in Loehle *et al.* (≈ 3200 K) [77]. This could be due to the simulated conditions in the boundary layer, combined with the modelling of the radiative equilibrium

wall. In Suzuki *et al.*'s CFD simulations with surface reactions included, the maximum surface temperature around the stagnation point was about 3250 K [74]. Furthermore, the temperatures measured in flight that are plotted as a comparison to Suzuki *et al.*'s CFD results seem to indicate the mean temperature is somewhere around 3300 K [74]. Increasing the emissivity value, or including surface ablation and pyrolysis, are possible mechanisms by which the surface temperature may be lowered, but the variations in measured re-entry temperatures exemplify the uncertainties that exist in the comparison of parameters between CFD solvers, and the flight data.

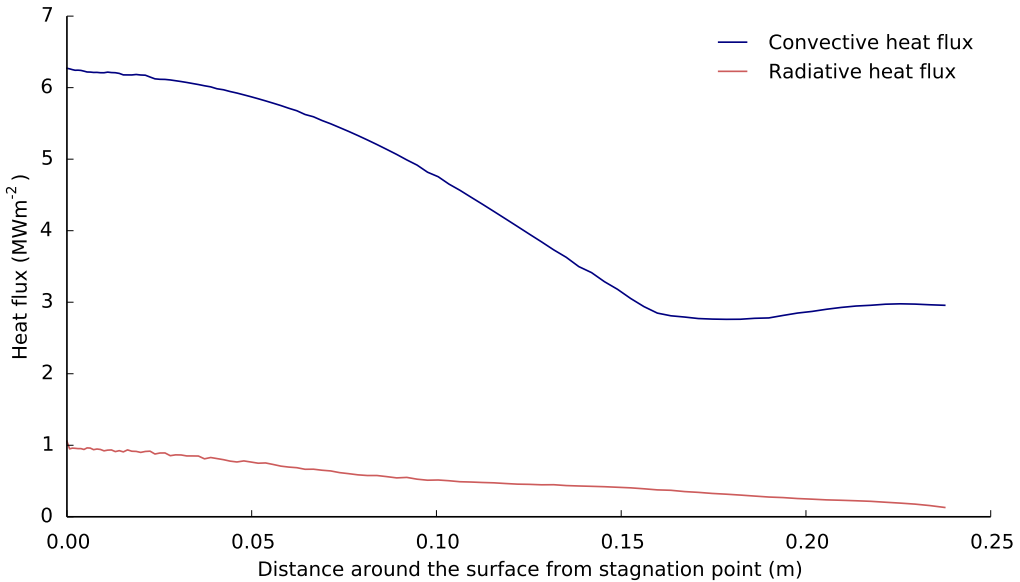


Figure 6.14: Convective and radiative heat flux along the vehicle surface from the stagnation point for Hayabusa full scale simulation. Radiative heat flux calculated at the end of converged flowfield simulation.

The convective heat flux around the aeroshell surface, shown in Figure 6.14, is the sum of the conductive and diffusive heat fluxes. It follows the same trend as the surface temperature in Figure 6.13, decreasing from the stagnation point value of $6.2 \text{ MW} \cdot \text{m}^{-2}$ to a minimum near the shoulder, where it increases slightly before the outflow boundary. The maximum q_{conv} is much lower than the $12 \text{ MW} \cdot \text{m}^{-2}$ predicted by Suzuki *et al.*'s implementation of the Detra-Kemp-Riddell model, and still somewhat lower than their initial CFD solution of $8 \text{ MW} \cdot \text{m}^{-2}$, but higher than the $5.3 \text{ MW} \cdot \text{m}^{-2}$ obtained when surface reactions (except nitridation) were included [74]. Winter *et al.* also predicted a q_{conv} of $9 \text{ MW} \cdot \text{m}^{-2}$ using engineering methods, inferring that predictive methods are overestimating the simulated convective heat flux [35].

The radiative heat flux is also presented in Figure 6.14, and was calculated using *e3rad* monte-carlo ray tracing with 1000 rays per cell, on the converged flowfield solution. The radiative heat flux peaks at close to $1 \text{ MW} \cdot \text{m}^{-2}$ at the stagnation point, and gradually decreases around the aeroshell surface. There are some small cell-to-cell fluctuations, especially near the stagnation point, which are not resolved by altering the number of rays. The stagnation point radiative heat flux calculated by Suzuki *et al.* is very similar to the present value, at just below $1 \text{ MW} \cdot \text{m}^{-2}$, and from a tangent-slab method [74]. Kihara *et al.* calculated a higher stagnation point radiative heat flux of about $1.5 \text{ MW} \cdot \text{m}^{-2}$, but the calculation method was not specified [75].

6.2.2 Inclusion of mass flux boundary condition

The Hayabusa vehicle had a carbon phenolic TPS that underwent ablation and pyrolysis under the extreme heat loads experienced re-entry. Ablation is the reaction of the carbon fibres with the air boundary layer, and pyrolysis is the disintegration and outgassing of the matrix phase due to temperature increase through the material. In the UV spectra recorded by Buttsworth, Morgan and Jenniskens [5], the ablative species CN is dominant, and so attempts to fully replicate these spectra must include gas-surface interactions. As part of the ESA Ablation-Radiation Coupling project, boundary conditions were developed by the author to model ablation and pyrolysis [101]. Ablation involves the modelling of nitridation, oxidation and sublimation of surface carbon using Arrhenius equations, depleting the required air species and introducing the ablative products through addition to the total and species mass flux. It was assumed for Hayabusa that surface reactions only, without pyrolysis, would suffice since CN is most likely created through ablation. The implementation of the boundary condition is simplistic, following the structure presented by Park, Jaffe and Partridge [9], but provides a good first attempt in *eilmer3*. A mass flux boundary condition had not previously been developed for aeroshell simulations, and more complex and possibly more accurate implementations can be built from the current structure. Currently, validation and verification of the boundary condition has not been completed and is a target for future work, but will be assumed to perform adequately based on Park, Jaffe and Partridge's work [9]. Discussion of the implementation and boundary condition structure is provided in Appendix B. The simulations were run for the same five body lengths as the

air only simulations, and the key result is the mole fractions along the stagnation line in Figure 6.15. The ablative species are entering and diffusing through the boundary layer, and some reach as far as 5 mm from the wall, albeit in small quantities. CN increases to a maximum at about 1 mm from the wall, and its influence on the UV radiation will be investigated in the next chapter.

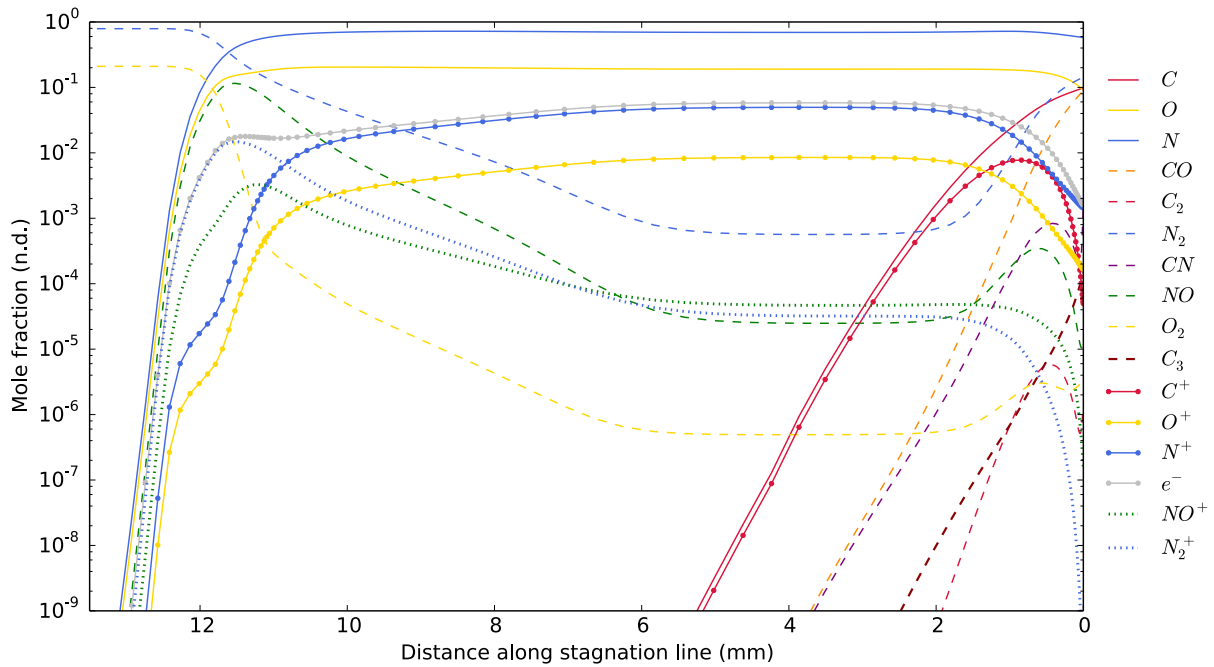


Figure 6.15: Mole fractions along stagnation line for Hayabusa full scale simulation, using mass flux boundary condition, 20 species and Park's 24 reaction scheme [9].

6.2.3 Hayabusa scaled simulations

Two different simulations were conducted at scaled conditions and with a scaled geometry to compare to the full scale Hayabusa simulations. The one-fifth scale Hayabusa model was simulated with an idealised inflow as well as an inflow created from a combined facility simulation. The ideal scaled case alters the length dimensions and the density only, keeping all other parameters the same as the flight scale simulation and eliminating the shock heating of inflow gas. This is called idealised inflow because it is binary scaling applied perfectly, assuming an ideal wind tunnel existed that could produce such flow. The combined facility simulation results in flow exiting the nozzle and passing through the test section, without the model present. The flow properties were extracted at the location

of the model and by estimating when the photodiode would trigger, the properties were averaged over the approximate spectrometer gate time to create the inflow condition. In Figure 3.10, showing the model location flow parameters, the test time is marked as $t = 26540 \pm 5 \mu\text{s}$. The simulation was converted from five species and thermochemical equilibrium, or single temperature chemical nonequilibrium, to 11 species and two-temperature nonequilibrium, as required in the Hayabusa bow shock. The expanding flow exiting the nozzle is partially dissociated and shock heated, and these properties are carried through to the inflow over the model. The simulations using the facility simulation results in the inflow are labelled ‘nozzle inflow’ in the results plots.

Simulations at all scales were performed with the Park reaction scheme and a super-catalytic wall. The distance axis has been scaled by the nose radius of the vehicle or model (for reference, the nose radii are 0.2 m for the full scale vehicle and 0.04 m for the scaled model) to enable straightforward comparison along the same non-dimensionalised length. The plots therefore show the behaviour of a variable at the same relative location in the shock layer. Note the different scales on each y-axis, as each plot has a mole fraction range to suit the particular species and show their behaviour as clearly as possible.

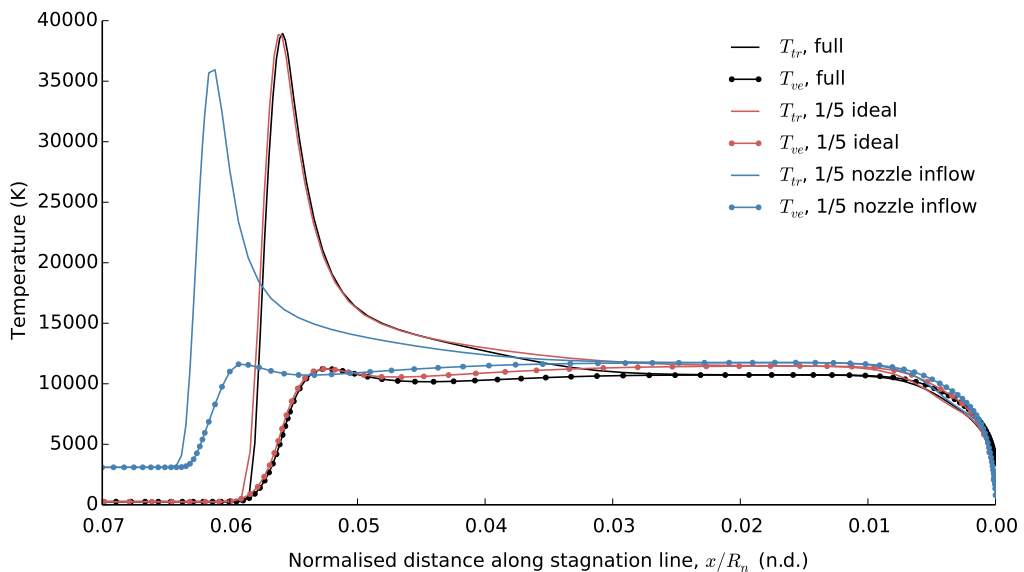


Figure 6.16: Temperatures along stagnation line for Hayabusa full scale, 1/5 ideal and 1/5 nozzle inflow simulations.

Figure 6.16 illustrates the translational-rotational and vibrational-electron-electronic temperatures along a normalised stagnation line, where $x/R_n = 0$ corresponds to the stagnation point. As the distance is normalised, it is also non-dimensionalised (n.d.). There is some separation of the temperatures approaching the wall in each simulation, as recombination becomes the prominent reaction type. The full scale and ideal scaled temperatures rise almost identically across the shock front, which indicates that binary scaling is holding, but they separate as they relax to different equilibrium values. The two simulations do not have identical temperature behaviour as the flowfields are not entirely binary reaction dominated: the area of equilibrium, however small, means that binary and ternary processes are matched and one does not dominate the other. The heated freestream of the nozzle inflow scaled simulation caused higher shock layer equilibrium temperatures and a larger relative shock stand-off, demonstrating that the condition scaling is not perfect. The T_{tr} peak is lower than the full and ideal scaled cases, but the equilibrium temperature is the highest of the three at about 11750 K, followed by the ideal scaled at 11475 K and the full scale at 10732 K. A major consequence of the increased temperature in the scaled cases is the direct effect on atomic emissions, including those that were the focus of experimental measurements, hence having even a small equilibrium region may be more detrimental to CFD and experimental results than first thought. However, it is unlikely given the conditions during Hayabusa observations [4] that any observed trajectory point would be in full nonequilibrium, thus the effort must go towards understanding where and how these flowfield effects are impacting on the results.

The mole fractions of the 11 air species considered have been grouped into four figures by type. In each plot, the difference in shock stand-off distance between the nozzle inflow scaled simulation and full and ideal scaled simulations is clear, but the focus will be on the mole fraction magnitudes at specific points in the shock layer, including the equilibrium region and across the shock. The atomic species and dominant radiators in the IR, N and O, are shown in Figure 6.17. The O mole fractions differ by about 0.05 in the equilibrium region, but equilibrium N mole fractions range from 0.68 for nozzle inflow scaled, to 0.691 for full scale and 0.709 for ideal scaled. The nozzle inflow scaled case has less N than the other two cases because the higher temperature is causing N to ionise into N^+ and e^- , and increased mole fractions of these species for the nozzle inflow case is seen in Figure 6.18, which plots ions of atomic species, and electrons.

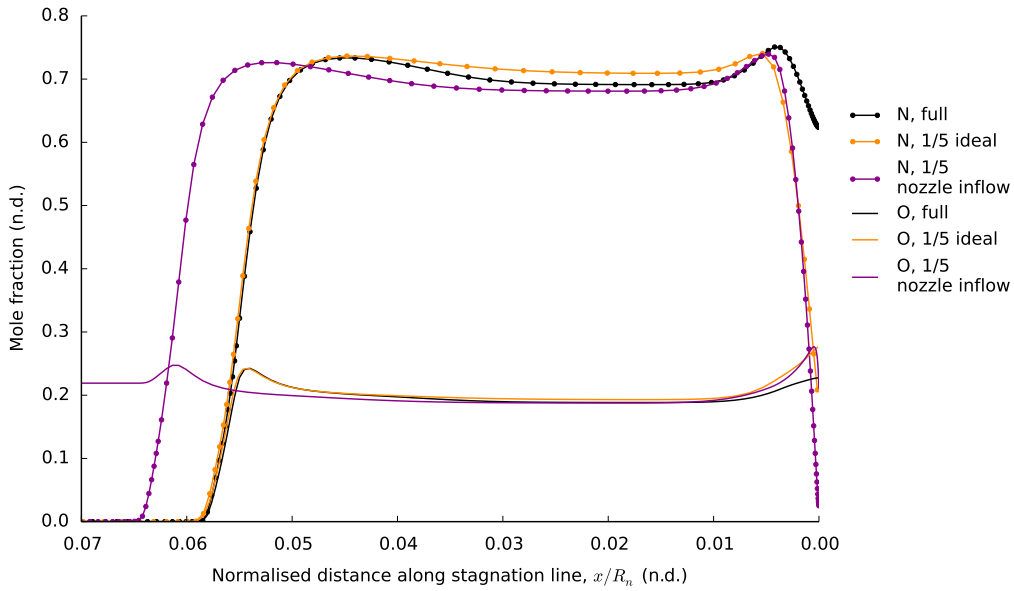


Figure 6.17: Mole fractions of atomic species along stagnation line for Hayabusa full scale, 1/5 ideal and 1/5 nozzle inflow simulations.

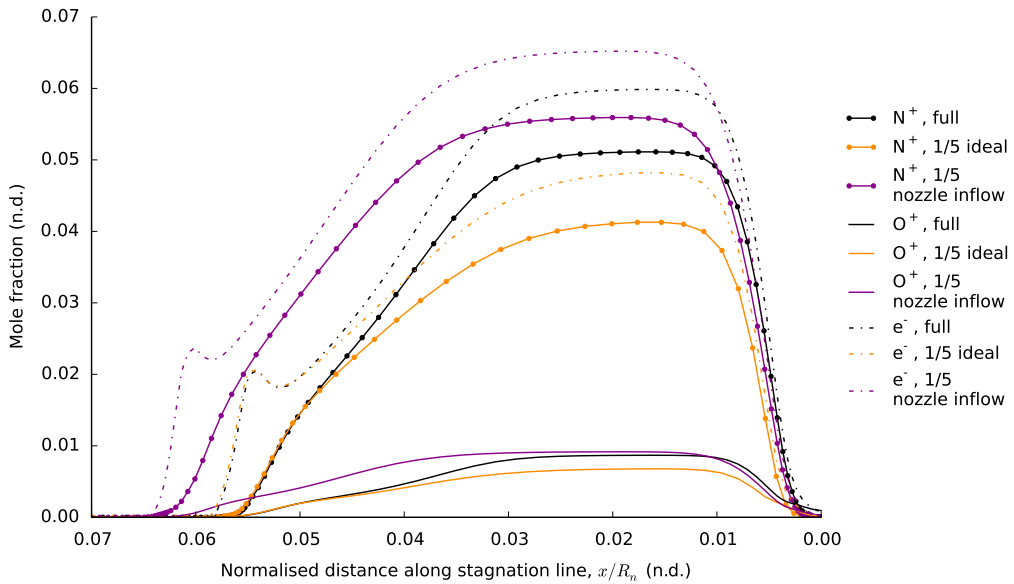


Figure 6.18: Mole fractions of atomic ions and electrons along stagnation line for Hayabusa full scale, 1/5 ideal and 1/5 nozzle inflow simulations.

The lower amounts of O^+ in the ideal scaled case, given in Figure 6.18, could be due to the difference in thermodynamic parameters through the equilibrium region. Although the temperature is higher in the ideal scaled than the full scale case, the ionisation is reduced with the pressure elevation. The

recombination of O^+ and e^- to O near the wall in Figure 6.18 causes an increase in O in Figure 6.17 that is more pronounced for the scaled cases. N^+ recombines to N , which then recombines to N_2 , and Figure 6.17 shows a much more dramatic effect for the scaled models, with a 300 K wall to replicate expansion tube conditions.

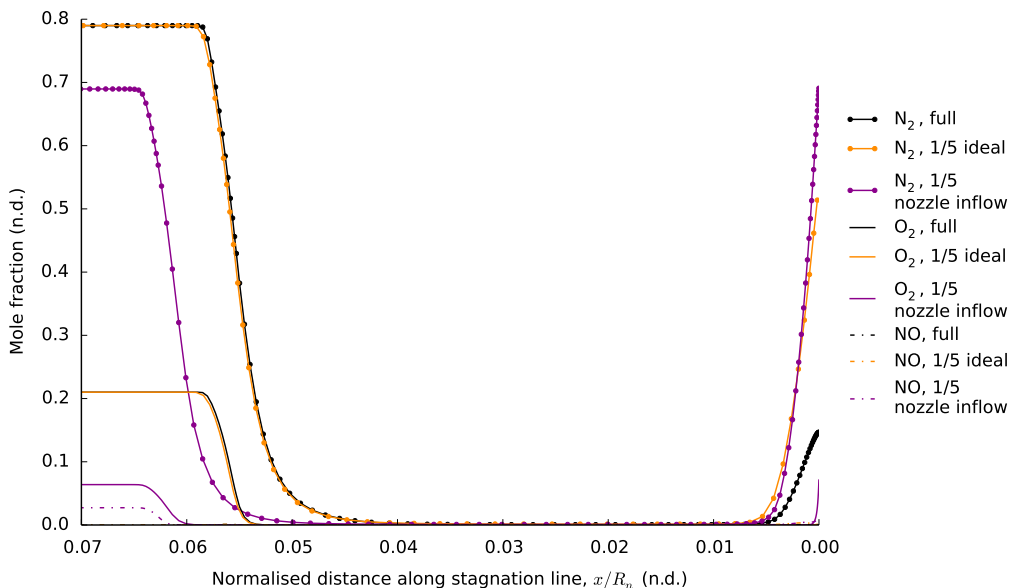


Figure 6.19: Mole fractions of molecular species along stagnation line for Hayabusa full scale, 1/5 ideal and 1/5 nozzle inflow simulations.

N_2 and O_2 follow similar patterns of dissociation and recombination at each scale in Figure 6.19, and NO barely features. It is only visible above trace amounts in the partially dissociated nozzle inflow freestream. The creation and destruction of molecular ions, as illustrated in Figure 6.20, also progress in similar fashion between scales, and the ideal scaled and full scale cases are identical for these species. The most interesting species for UV measurements is N_2^+ , which has a higher peak magnitude in the nozzle inflow case.

The pressure along the surface of the Hayabusa vehicle or model, extending from the stagnation point around the sphere-cone to the shoulder, is plotted in Figure 6.20. Due to binary scaling, surface pressure in the scaled cases should be approximately five times greater than the full scale case, so the full scale result multiplied by five is provided as a reference. The flight reference pressure and ideal scaled pressure are extremely similar until the minimum that occurs on the cone prior to the

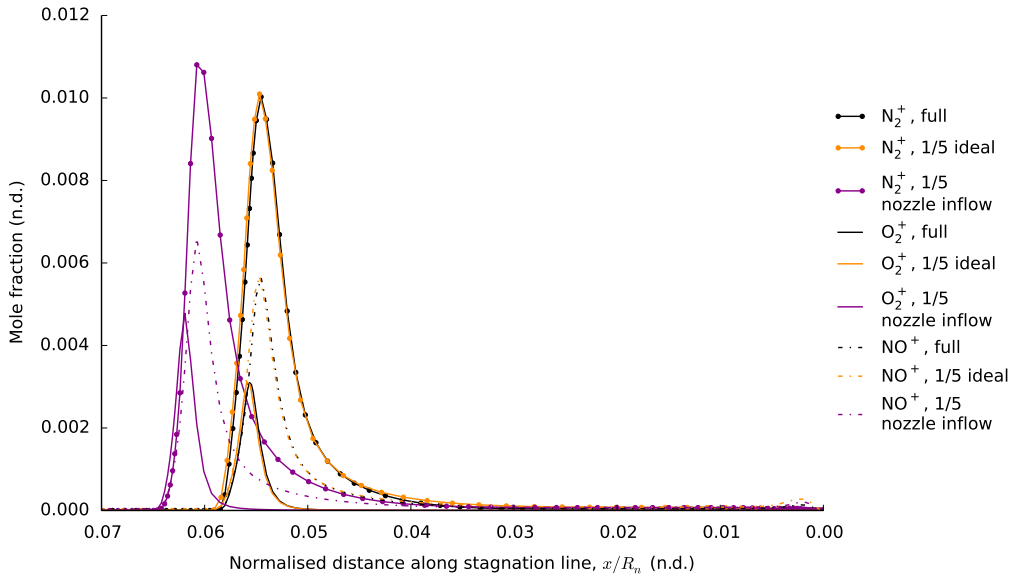


Figure 6.20: Mole fractions of molecular ions along stagnation line for Hayabusa full scale, 1/5 ideal and 1/5 nozzle inflow simulations.

exit boundary, where the ideal scaled and nozzle inflow scaled pressures overlap. The nozzle inflow pressure, for the most part, remains about 10 to 20 kPa above the other values, due to the mismatch in condition scaling. Measuring the surface pressure in future aeroshell tests, even at a single point prior to the conical section minimum, could give feedback on the condition's performance.

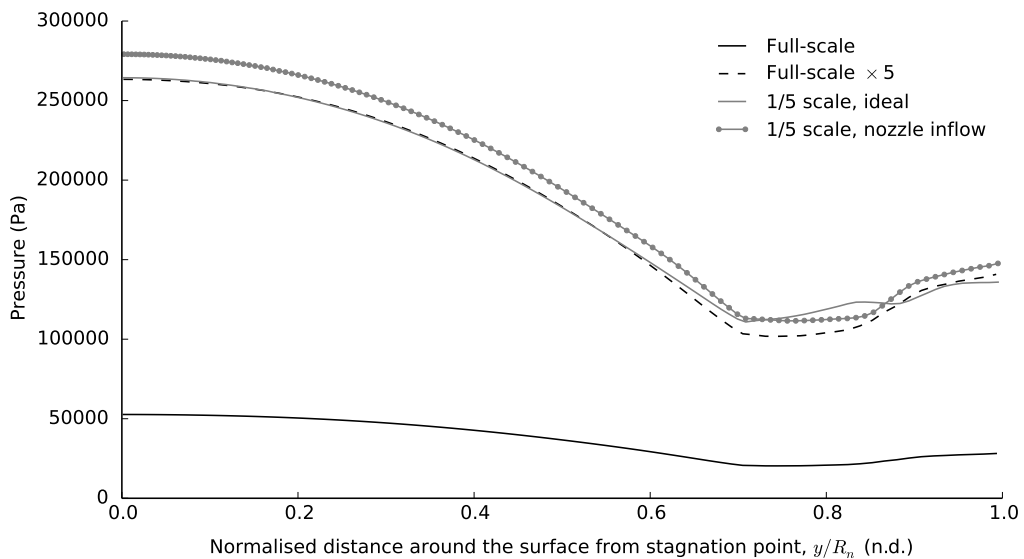


Figure 6.21: Pressure over the vehicle surface for Hayabusa full scale, 1/5 ideal and 1/5 nozzle inflow simulations.

The convective heat fluxes in Figure 6.22 are also plotted with a scaled flight value ($5\times$ greater) as a reference, but this is a more difficult comparison because the full scale case had a radiative equilibrium wall at over 3000 K, and the scaled cases had a fixed temperature wall at 300 K to represent the cold steel model. Hence, the heat flux of the ideal scaled case is nearly twice the full scale reference value. The higher temperature shock layer of the nozzle inflow scaled case increases the heat flux to the surface by another $20 \text{ MW} \cdot \text{m}^{-2}$ as compared to the ideal scaled heat flux.

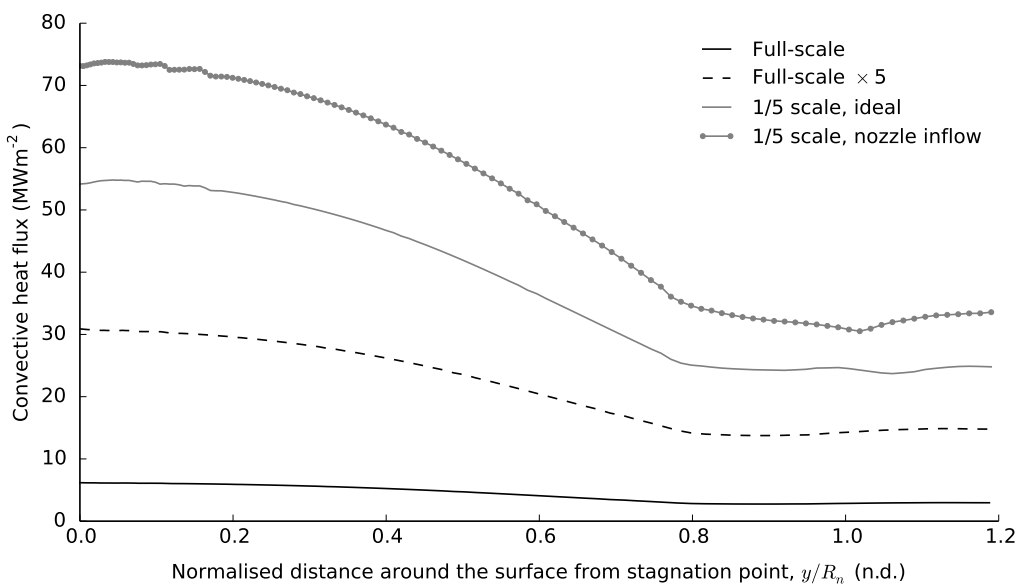


Figure 6.22: Convective heat flux over the vehicle surface from the stagnation point for Hayabusa full scale, 1/5 ideal and 1/5 nozzle inflow simulations.

The comparison between the two focus species for IR spectra calculations, N and O, and the UV spectra focus species N_2^+ when using different reaction schemes is shown in Figure 6.23 for the ideal scaled case, and Figure 6.24 for the X2 scaled case. In the ideal scaled simulation, N and O have comparable mole fractions within the shock layer between Park and Gupta reaction schemes, but N_2^+ differs quite substantially, with Gupta producing a much lower mole fraction for the majority of the shock layer. In the X2 scaled simulation, the comparison between N and O mole fractions is again satisfactory, and the difference between Park and Gupta for N_2^+ occurs across about half of the shock layer, which is less than in the ideal scaled case. There should be less of a difference between UV spectra for the X2 scaled case due to reaction schemes than for the ideal scaled case, because of the reduced discrepancy between the two reaction schemes for the X2 scaled case.

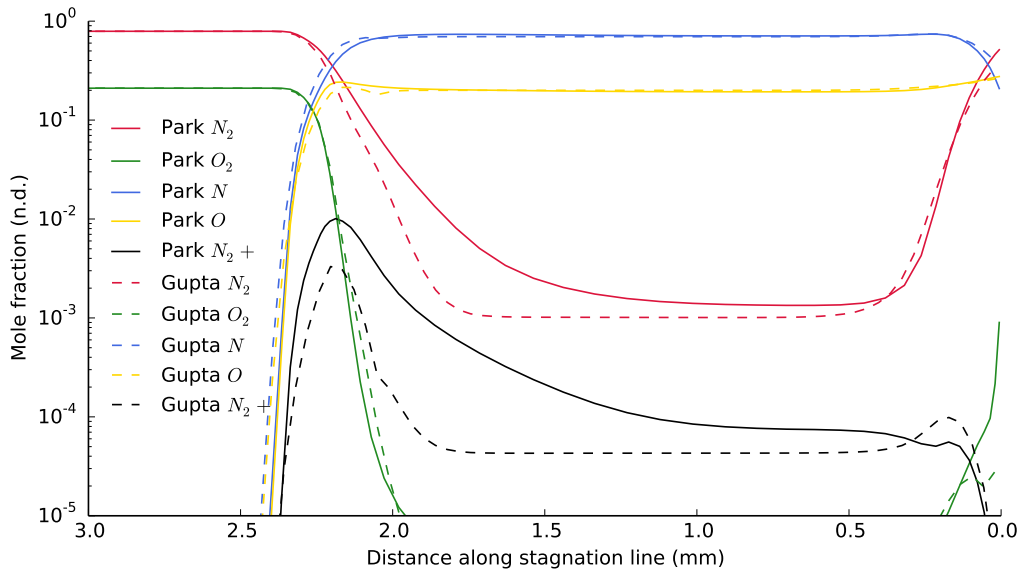


Figure 6.23: Mole fractions for atomic and molecular N and O, and N_2^+ , along stagnation line for Hayabusa ideal scaled simulation, comparison between Park (solid line) and Gupta (dashed line) reaction schemes.

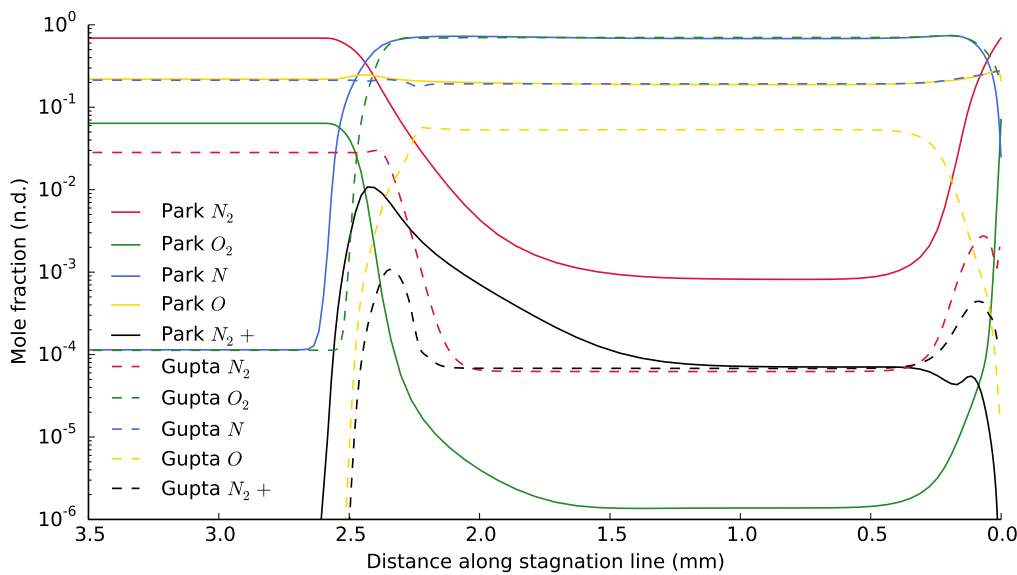


Figure 6.24: Mole fractions for atomic and molecular N and O, and N_2^+ , along stagnation line for Hayabusa X2 scaled simulation, comparison between Park (solid line) and Gupta (dashed line) reaction schemes.

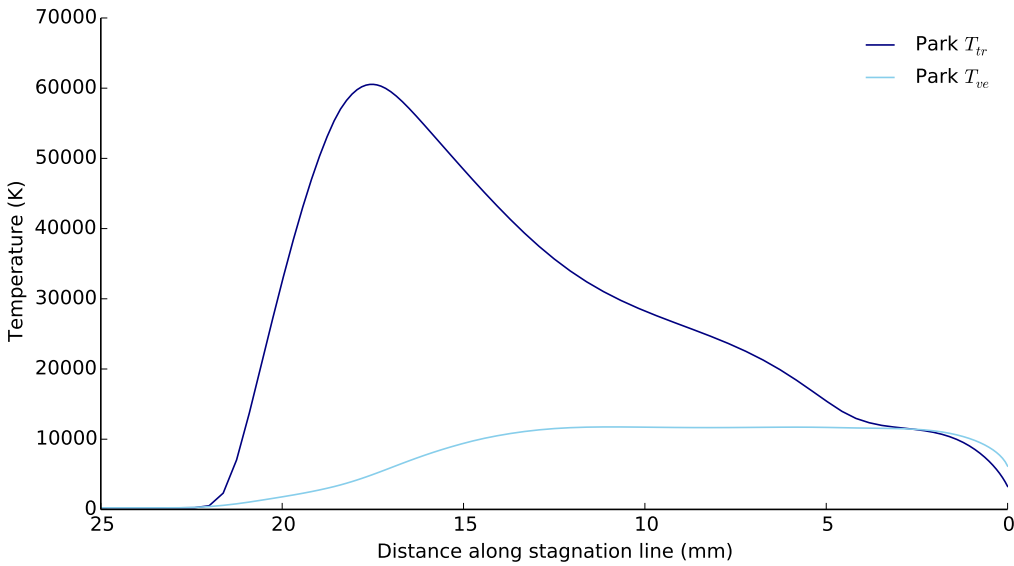


Figure 6.25: Temperatures along stagnation line for Stardust full scale simulation, Park reaction scheme, supercatalytic wall.

6.2.4 Stardust full scale simulation

The contrast between the lower altitude, higher density Hayabusa condition and the higher altitude, lower density Stardust condition is apparent upon observation of the temperatures along the Stardust stagnation line in Figure 6.25. Based on the Hayabusa results, Stardust was simulated with a supercatalytic wall boundary and the Park reaction scheme. The shock layer is largely nonequilibrium, except for a brief area around 2.5 mm upstream of the stagnation point where the temperatures meet. T_{tr} rises to about 60 000 K; vastly higher than the maximum temperature of 20 000 K in the thermodynamic tables and far beyond any reasonable limits for extrapolation. T_{ve} rises slowly across the shock to a more reasonable maximum of above 11 600 K. The shock front is smeared over several millimetres, and the shock stand-off distance is almost double that of Hayabusa. The solutions from Boyd, Trumble and Wright [68], Liu *et al.* [70] and Martin, Farbar and Boyd [69] are at 71 km altitude rather than the 69 km altitude for the Stardust condition considered in this work, but still provide useful comparisons. Liu *et al.* have a fully nonequilibrium flowfield but the peak T_{tr} is between 25 000 and 27 000 K, and T_{ve} barely exceeds 10 000 K in the middle of the shock layer while T_{tr} remains closer to 12 000 K [70]. The shock stand-off distance is much smaller at 15 mm, a similar value to Boyd, Trumble and Wright at 71 km [68]. The modified DPLR T_{tr} reaches approximately 50 000 K, which is closer to the Figure 6.25 value, but T_{ve} sits between the DPLR baseline and

modified peak values (for further explanation, see the paper [68]). The stagnation line temperature plot in Martin, Farbar and Boyd is the closest, visually, to Figure 6.25. The largely nonequilibrium shock layer extends to just beyond 26 mm upstream of the stagnation point, T_{tr} peaks at about 55 000 K and T_{ve} slowly rises to a maximum of near 12 000 K [69]. The two temperatures meet at about 4 mm from the wall, and unlike Figure 6.25, remain the same through the boundary layer. It is inferred that an *eilmer3* simulation at 71 km would compare closely with Martin, Farbar and Boyd's result, which is reassuring given the complexity of CFD simulations at such conditions.

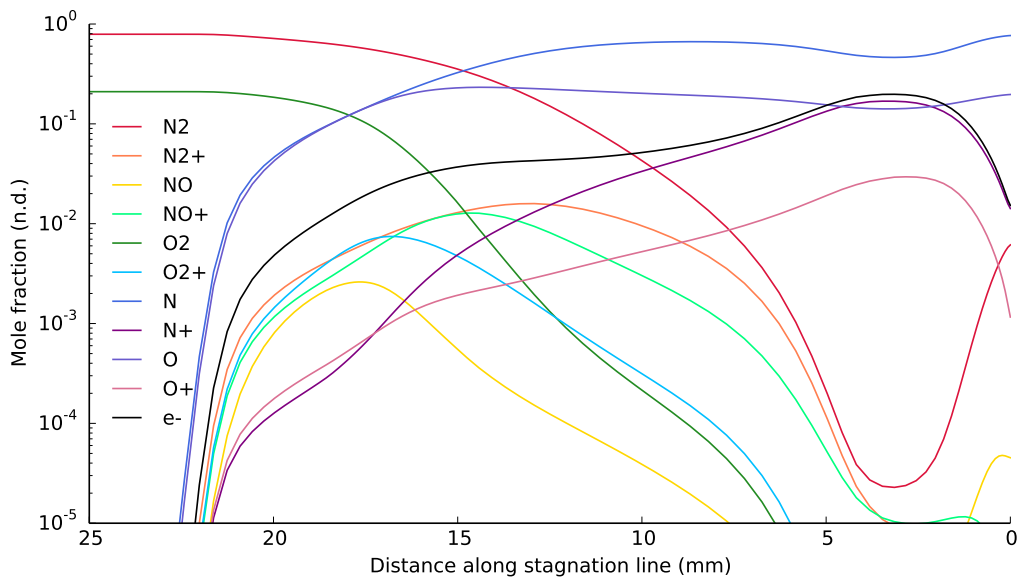


Figure 6.26: Mole fractions along stagnation line for Stardust full scale simulation, Park reaction scheme, super-catalytic wall.

The mole fractions in Figure 6.26 do not exhibit a clearly defined chemical equilibrium region; rather, they vary across the whole shock layer. Most species rise or fall quite slowly, except for the region around 3 mm, where equilibrium may occur briefly. N^+ , O^+ and e^- increase through the shock layer to the point where there is more N^+ than N , showing the importance of atomic ionic species in high altitude hypervelocity flows.

The surface temperature and pressure extend from the stagnation point, around the 60° sphere-cone and the modelled small radius shoulder, in Figure 6.27. The stagnation point surface pressure, at nearly 11 kPa, is about five times lower than the Hayabusa value, and drops until the transition from

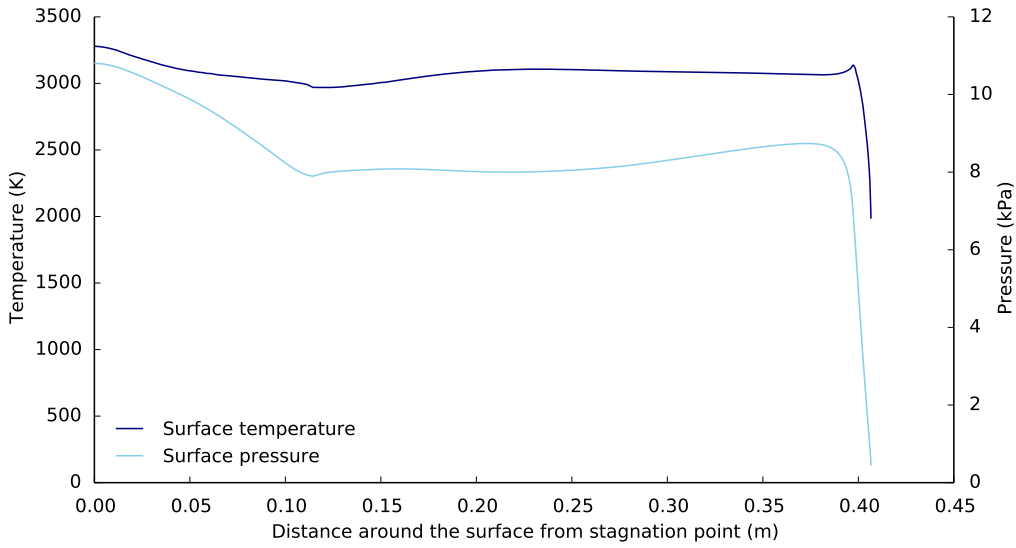


Figure 6.27: Temperature and pressure along the vehicle surface from the stagnation point for Stardust full scale simulation.

the spherical into the conical geometry, then rises from about 8 kPa until the expansion around the corner causes a rapid drop. Boyd, Trumble and Wright report a stagnation point surface pressure of just below 8 kPa and although their plot follows the same trend as Figure 6.27, the pressure minimum is nearer to 6 kPa. The stagnation point surface temperature is approximately 3300 K, which is about 50 K higher than in Martin, Farbar and Boyd, but remains above 3000 K until the shoulder, whereas Martin, Farbar and Boyd's falls to near 2900 K [69]. The profiles are reasonably alike in shape and also compare well with Liu *et al.*'s surface temperature profiles [70], which sit very close to, or between, the Martin, Farbar and Boyd data and Figure 6.27.

Figure 6.28 shows the convective heat flux around the Stardust sphere-cone shape, dropping from a maximum at the stagnation point to a minimum at the edge of the rounded shoulder. Although the curve shape is similar to that of Martin, Farbar and Boyd [69], the values are much closer to their ablating wall case ($2.8 \text{ MW} \cdot \text{m}^{-2}$ peak) than the flowfield only case with a super-catalytic wall ($7 \text{ MW} \cdot \text{m}^{-2}$ peak). Gupta's super-catalytic wall case is similar to the current maximum value and Martin, Farbar and Boyd's ablating wall value at $4 \text{ MW} \cdot \text{m}^{-2}$, albeit at the 42 s trajectory point [71]. Gupta's non-catalytic wall convective heat flux, at $7 \text{ MW} \cdot \text{m}^{-2}$, is almost double the present value but very similar to values given by Park [73], and Olynick, Chen and Tauber [72]. There are acceptable discrepancies in the heat flux value due to different solvers and a range of wall boundary conditions.

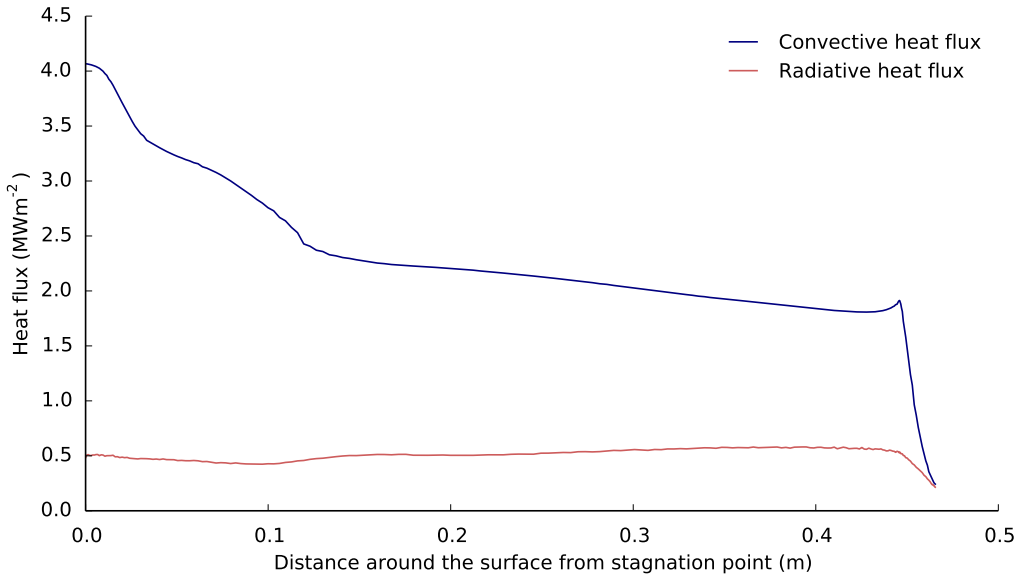


Figure 6.28: Convective and radiative heat flux along the vehicle surface from the stagnation point for Stardust full scale simulation.

Figure 6.28 also presents the radiative heat flux, calculated from the converged flowfield solution using *e3rad* monte-carlo ray tracing with 1000 rays per cell. The stagnation point radiative heat flux is $0.5 \text{ MW} \cdot \text{m}^{-2}$, similar to the $0.6 \text{ MW} \cdot \text{m}^{-2}$ calculated by Liu *et al.* and more than double Olynick's value of about $0.2 \text{ MW} \cdot \text{m}^{-2}$. At the stagnation point, the radiative heat flux is slightly more than 10 % of the convective heat flux. The radiative heat flux curve around the aeroshell body is also similar to Liu *et al.* [70], and the peak value is towards the shoulder rather than at the stagnation point.

6.2.5 Stardust scaled simulations

The one-tenth scale Stardust simulations followed the structure of the Hayabusa simulations: an ideal scaled version, with only density and length changed, and a nozzle inflow version, using the model location plane results of an X2 facility simulation at nominal fill pressures and during the nominated test time (see Figure 3.17). Parameters from the scaled simulations are compared to the full scale case to assess the effect of scaling and inflow conditions, and as for Hayabusa, all simulations had Park reactions and a super-catalytic wall.

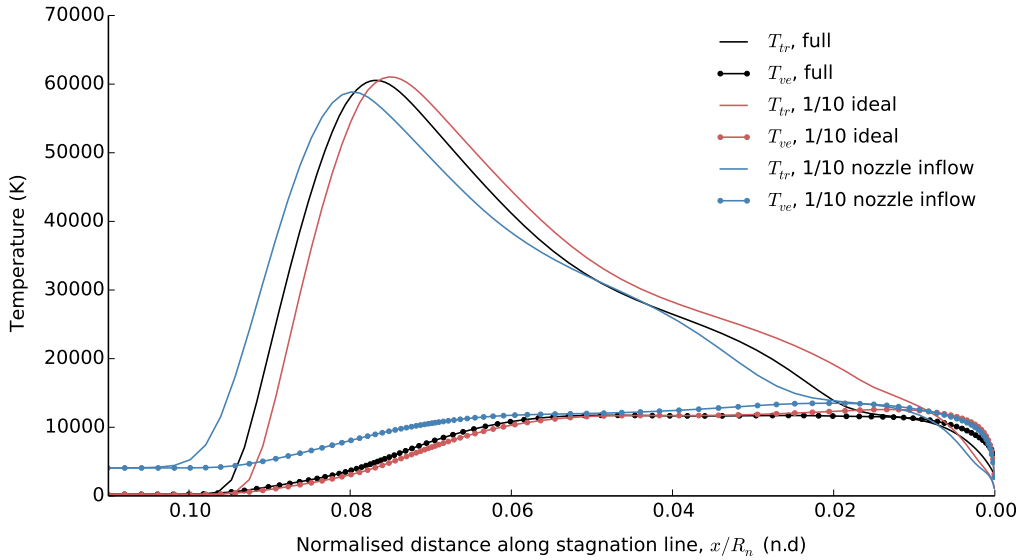


Figure 6.29: Temperatures along stagnation line for Stardust full scale, 1/10 ideal and 1/10 nozzle inflow simulations.

The heavily nonequilibrium nature of the Stardust shock layer carries through to the scaled simulations, as shown in the two-temperature modes plotted along the normalised stagnation line in Figure 6.29. The Hayabusa results showed matching of the T_{tr} curve across the shock and separation of equilibrium temperatures between scales, hence the fact that the Stardust T_{tr} curves do not match is surprising. The shock stand-off distance varies between the ideal scaled and full scale cases, affecting the temperature modes as if one was translated for most of the shock layer. T_{ve} is very similar for the full and ideal scaled cases, and they are virtually identical between $x/R_n = 0.03$ and 0.05. The behaviour of both temperature modes differ near the wall, as the full scale T_{tr} relaxes further upstream than the ideal scaled T_{Tr} . This could be driving the difference in T_{tr} as it extends back to the shock front. A difference in Knudsen number between the flight and scaled condition could also be driving the differences since the flight condition is nearing the non-continuum regime. Shock stand-off for the nozzle inflow case is larger and the inflow temperatures are high, causing higher T_{ve} across the shock layer and yet another difference in the T_{tr} curve, including relaxation to the T_{ve} value further upstream of the other two simulations. As the values for T_{tr} are extrapolated so far beyond tabulated values, it is difficult to comment on the behaviour between scales, beyond following a similar shape and ranging by a few thousand Kelvin at a given point along the stagnation line. The influence of the differences in temperature will be investigated in Stardust spectra modelling.

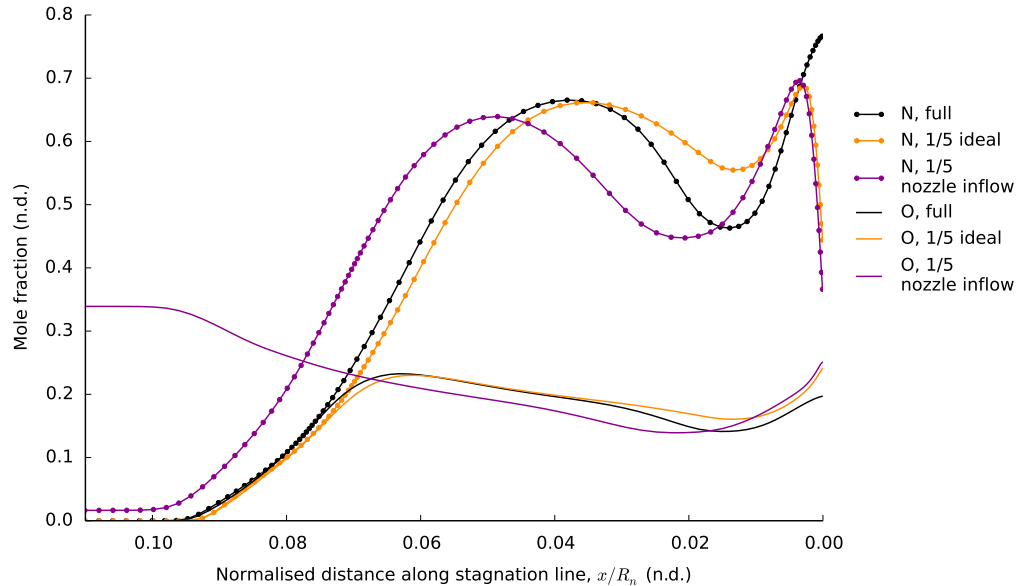


Figure 6.30: Mole fractions of atomic species along stagnation line for Stardust full scale, 1/10 ideal and 1/10 nozzle inflow simulations.

The mole fractions of atomic N and O across the shock layer are shown in Figure 6.30. From the edge of the shock to near $x/R_n = 0.04$, the full scale and ideal scaled plots are very similar, but there is more ionisation around $x/R_n = 0.02$ in the full scale case. The gradual decrease of O after an initial rise shows gradual ionisation to O^+ , which is also observed in Figure 6.31. N recombines at the wall in the scaled cases only due to the 300 K wall temperature, while recombination is seen in all cases for O, O^+ and N^+ . The mole fractions of N^+ , O^+ and e^- all peak just prior to this recombination region near the wall, which would reduce the emission from atomic species.

N_2 and O_2 have a fairly gradual decline across the Stardust shock front in Figure 6.32, and full dissociation is not reached until the flow is close to the wall. The molecular mole fractions in the full scale and ideal scaled cases differ at most by 5 % at any given point, and the freestream dissociation in the nozzle inflow case is evident, particularly for O_2 . NO does not feature in comparison to the other molecular species. The creation and depletion of molecular ions, as shown in Figure 6.33, spreads over a large area of the shock layer, following the nonequilibrium in the two temperature modes. The peak mole fractions for each species differs between simulation cases, but is always greatest in the nozzle inflow case as the shock layer temperatures are highest. N_2^+ is an important nonequilibrium

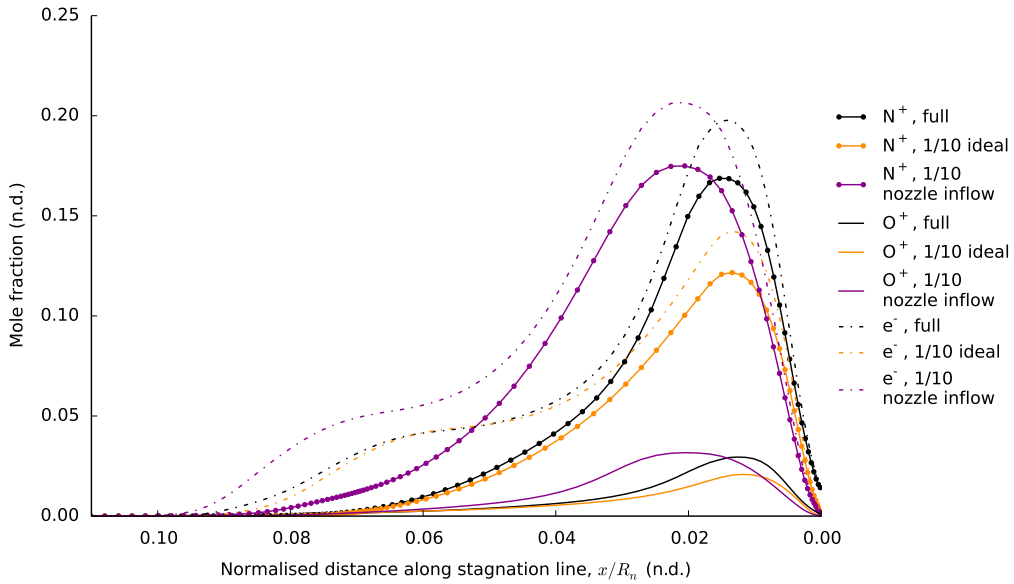


Figure 6.31: Mole fractions of atomic ions and electrons along stagnation line for Stardust full scale, 1/10 ideal and 1/10 nozzle inflow simulations.

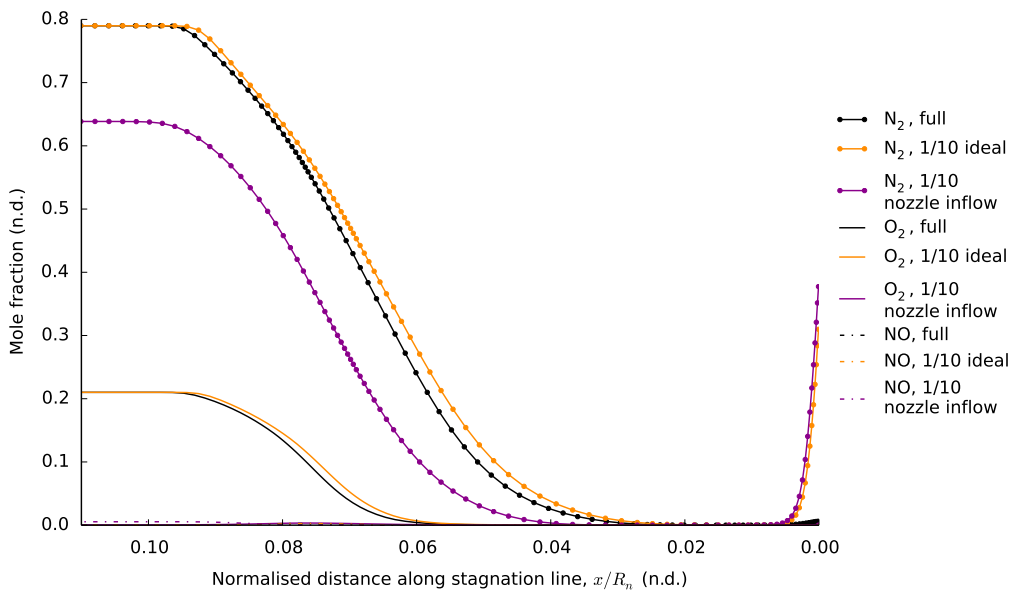


Figure 6.32: Mole fractions of molecular species along stagnation line for Stardust full scale, 1/10 ideal and 1/10 nozzle inflow simulations.

species and radiator in the UV, and will feature in spectra calculations and comparisons.

Pressure across the surface of the Stardust vehicle and 1/10 scale models is plotted in Figure 6.34, including the full scale pressure multiplied by 10 for easier comparison with the scaled cases.

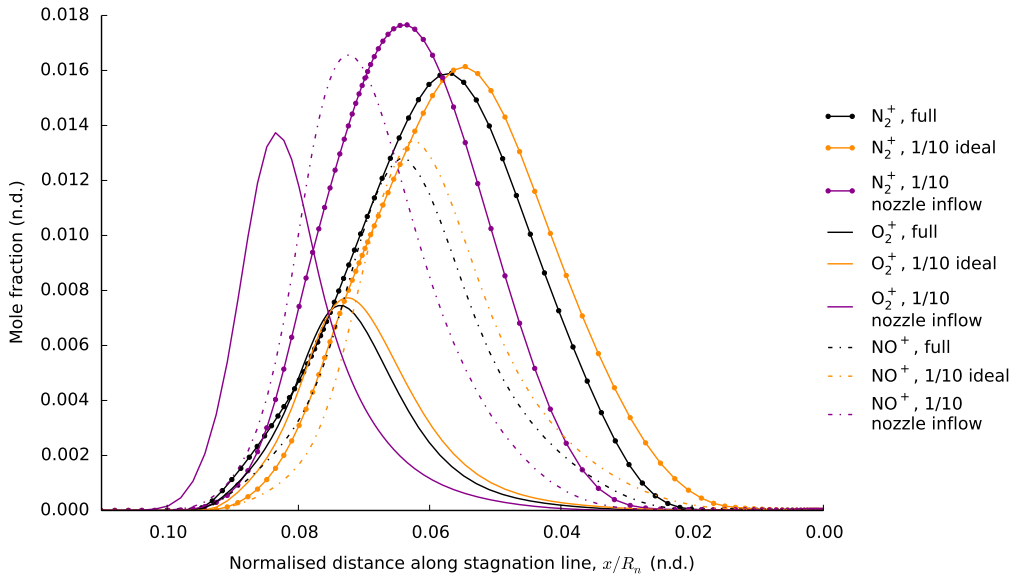


Figure 6.33: Mole fractions of molecular ions along stagnation line for Stardust full scale, 1/10 ideal and 1/10 nozzle inflow simulations.

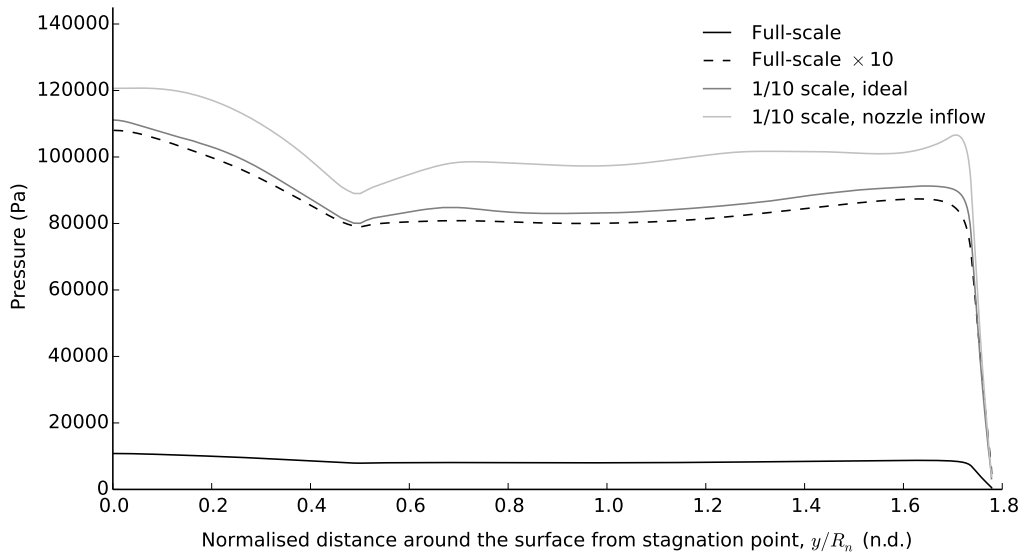


Figure 6.34: Pressure over the vehicle surface for Stardust full scale, 1/10 ideal and 1/10 nozzle inflow simulations.

All cases follow roughly the same shape, decreasing from a stagnation point maximum to a local minimum where the geometry transitions from spherical to conical, and increasing to the curved shoulder before decreasing dramatically near the outflow boundary. The ideal scaled pressure is around 2 % higher than the multiplied full scale pressure over the length of the surface, whereas the nozzle inflow case is higher again by 10 to 15 %. The difference in inflow conditions due to imprecise

scaling of the condition has impacted many flow parameters, including the surface pressure and the convective heat flux, shown in Figure 6.35. The full scale reference value ($\times 10$ of the actual value) cannot be properly compared as the full scale simulation had a radiative equilibrium wall, while the scaled simulations had fixed temperature walls at 300 K. The nozzle inflow case heat flux is greater than the ideal case by close to $10 \text{ MW} \cdot \text{m}^{-2}$ over much of the surface, except around the stagnation point. This decrease is a purely numerical error.

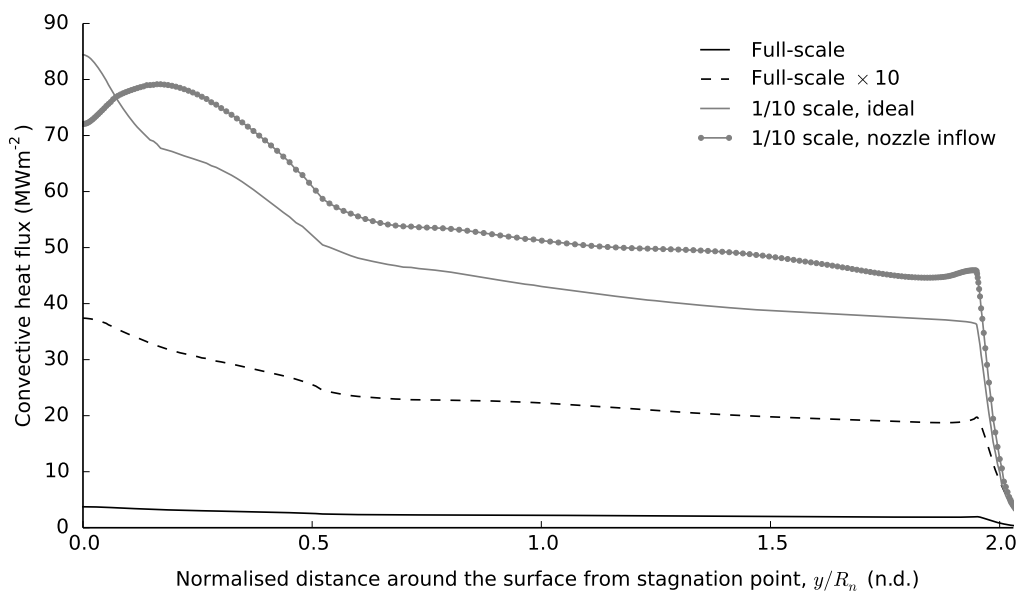


Figure 6.35: Convective heat flux over the vehicle surface from the stagnation point for Stardust full scale, 1/10 ideal and 1/10 nozzle inflow simulations.

6.3 Conclusion

Hayabusa and Stardust CFD 2D axisymmetric simulations were performed using *eilmer3* at full scale and flight trajectory points, scaled with ideal inflow conditions, and scaled with X2 nozzle simulation inflow conditions. A range of simulation parameters were selected to define the thermodynamics, chemical kinetics, diffusion, boundary conditions, and mesh and blocking structures. A grid resolution study, based on temperature as a primary flow parameter, showed that the Hayabusa and Stardust grids had a sufficient theoretical order of convergence and theoretical value at zero grid spacing to

demonstrate convergence. Continuing from the facility simulations in Chapter 3, the impact of equilibrium or 5 air species inflow, with flow properties from the nozzle exit, on shock layer properties was assessed as negligible. A range of results were presented for Hayabusa and Stardust at full scale, ideal scaled, and X2 nozzle inflow scaled conditions, including stagnation line temperatures and mole fractions, and surface temperature, pressure and heat flux. Where possible, the full scale results were compared to other simulation results published in literature, and similarities and differences in results were identified. Comparisons were also made between the full scale and scaled cases, and although binary scaling appeared to hold across the shock in the Hayabusa ideal scaled case, the scaling was not maintained entirely in all cases and therefore differences in the flowfield were evident. The flowfield results from this chapter become inputs for the radiation calculations and flight rebuilding in Chapter 7, and the final comparisons will be formulated from the radiation results. The less than ideal flowfield results from the scaled simulations, especially with the X2 nozzle inflow, suggest that the spectra calculated in Chapter 7 will also be flawed. Future work could involve investigating the facility simulations in more detail, including attempts to measure nozzle exit parameters other than the conehead pressure to characterise the flow for comparison with simulations. The effect of increasing nonequilibrium regions on binary scaled shock layer parameters for Hayabusa could be studied, as well as the influence of non-continuum effects on binary scaling in the Stardust shock layer.

Chapter 7

Experimental and Numerical Rebuilding of Hayabusa and Stardust Flight Data

7.1 Motivation

Flight data collected during the Hayabusa and Stardust re-entries is crucial for understanding the hypersonic flight environment, and is more significant if it can be recreated on the ground. The glowing fireballs fitted onto one pixel of the ICCD cameras based on geometric optics and magnification, but imperfections in the optics and motion tracking, either from the aircraft or on the ground, typically distributed the emissions over several pixels. Although the total radiation was received over several pixels, the net radiation can still be summed. The experimental set-up that was available in the laboratory allowed measurements along one or many lines of sight, from side access windows that oriented the viewing direction perpendicular to the flow. As presented in Chapters 4 and 5, the spectrometers produced spectrally resolved radiation measurements along a single vertical or horizontal line of sight, and the 2D images produced filter band integrated measurements that were essentially a series of line of sight measurements in the one image. The subject of the measurement differs from the whole capsule in Figure 7.1 to a single or group of slices through the shock layer in Figure 7.2, due to optical set-up constraints in each case. To achieve the equivalent cumulative intensity as the flight data, the experimental data needs to be transformed in a way that the radiation can be known at every point within the shock layer, allowing lines of sight to be traced in any direction and summed for a cumulative result. This field of radiating points will be the local emission,

per wavelength and/or solid angle where required. Generating a field of radiating points from CFD is somewhat simpler, as the intensity is calculated as a per unit volume quantity at each grid point prior to integration along defined lines of sight.

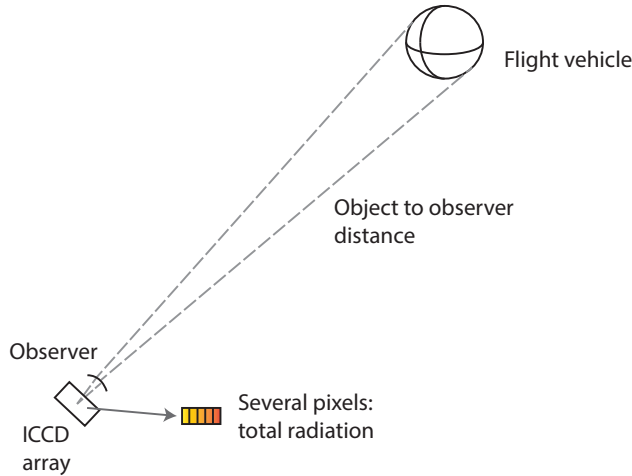


Figure 7.1: Imaging the whole radiating shock layer of a vehicle during re-entry, onto a small number of pixels. Not to scale.

Flight rebuilding has been performed for CFD results before, for both Stardust and Hayabusa. From 2D simulations of the Stardust capsule, Winter *et al.* evaluated the visible surface and view factor, followed by the thermal radiation, to apply to the flight spectra, but plasma emissions were only simulated by iterating through temperatures in a stand-alone, line-by-line spectral code [24]. The methodology is expanded in Winter *et al.*'s Hayabusa analysis, revolving a 2D solution into 3D and tracing lines of sight at various view angles, followed by a spatial sensitivity study [35]. However, the application of this methodology to the CFD results is not described in enough detail for reproduction. Flight rebuilding of Stardust CFD results was also performed by Liu *et al.* by revolving the 2D solution into 3D and tracing the lines of sight as Winter *et al.* had outlined [70]. Liu *et al.* noted, importantly, that the temperatures and number densities were known or interpolated at every point, prior to integration of the radiative transfer equation (RTE) along each line of sight using the radiation solver NEQAIR. Summation of the line of sight radiation, multiplied by the solid angle of a single cell, produced the total emission. Loehle *et al.* compare spectral data from the Hayabusa flight to rebuilt data from the NASA EAST facility through scaling of geometric parameters (experiment, relative to flight) and the IRS plasma wind tunnel PWK1, for which the method is not described in

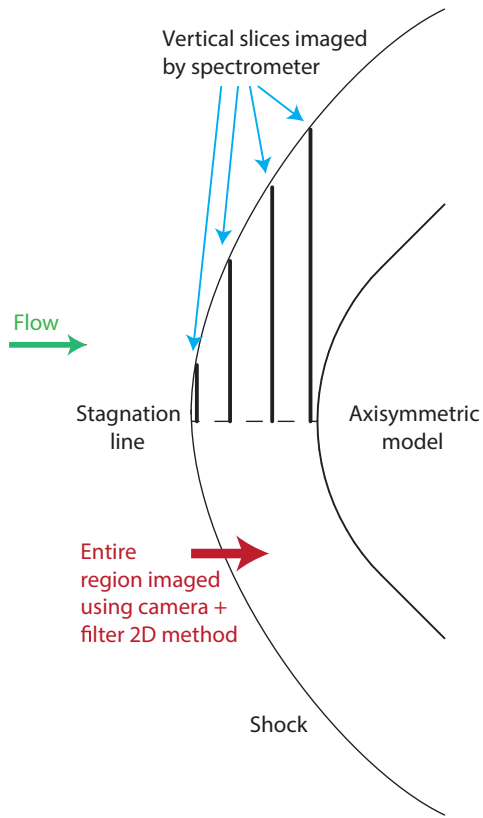


Figure 7.2: 2D illustration of imaging the radiating shock layer around an aeroshell model in X2, using a spectrometer along a single line of sight, or taking a 2D image of an entire section.

detail [77]. The line-integrated spectral measurement initially recorded in EAST has been divided by the line of sight (LOS) length to find the volumetric power density, due to an assumed uniform shock profile, rather than applying a more complex transform. Surface temperatures are compared between flight and CFD simulations at various trajectory points using a method to calculate surface heat flux and temperature that is described, including equations, and temperatures from the material response code FABL are also plotted featuring several different heat shield materials. The current analysis focuses on the flowfield radiation, so the CFD rebuilding and the geometric transformation of the EAST data are most relevant, and were used as a starting point for constructing the methodology. The key difference for experimental rebuilding is that X2 experiments were performed using a model and attempts were made to fully recreate the flight shock layer, including geometry and flow conditions under binary scaling.

7.2 Flight Rebuilding Objectives

The overall aim of the thesis is realised in these analyses: namely, a three-point comparison between experimental, CFD, and flight data. The experimental spectra and 2D intensity maps, measured in the X2 expansion tube, are now rebuilt into quantities that can compare to flight. The numerical flight rebuilds calculate radiative properties from the flowfield results of full scale, ideal scaled and nozzle inflow scaled simulations and construct flight-equivalent radiating fields. A comparison between CFD and experiment is also performed, in order to assess the performance of the simulations at all scales against the experimental results. The IR spectra from McIntyre *et al.* [4] are presented in terms of spectral radiance ($\text{W} \cdot \text{cm}^{-2} \cdot \mu\text{m}^{-1} \cdot \text{sr}^{-1}$), and the UV data in terms of spectral irradiance ($\text{W} \cdot \text{m}^{-2} \cdot \text{nm}^{-1}$) [64]. The experimental spectra in previous chapters and numerical spectra in this chapter are presented as spectral radiance, and the 2D image values and integrated spectra are in terms of radiance ($\text{W} \cdot \text{cm}^{-2} \cdot \text{sr}^{-1}$). To consolidate the units, the final quantities will be presented as radiance ($\text{W} \cdot \text{m}^{-2} \cdot \text{sr}^{-1}$) or spectral radiance, so that the solution is not dependent upon knowledge of the flight (or experimental) solid angle. Since the solutions will be wavelength integrated in most cases, the particular wavelength range will be noted. The intensity per unit volume that is defined at each point in the radiating field is equivalently known as the plasma emissivity or (spectral, if wavelength resolved) power density, and will be given per solid angle ($\text{W} \cdot \text{m}^{-3} \cdot \text{sr}^{-1}$).

7.3 Assumptions

The assumptions for the flight rebuild are:

- In flight, the lines of sight are parallel, since the flight vehicle was far enough from the observer for this to be a sufficiently good approximation.
- In X2 experiments and flight, the flowfield is optically thin in the IR region. This is valid for flight and experimental scale, after extensive numerical analysis tracking the emission and absorption coefficients in each calculation.
- Since the flowfield is optically thin in X2 experiments and flight, the lines of sight can be forward-facing; that is, from the body outwards in an upstream direction, because emission is

independent of direction. If there was significant absorption, then the particular lines of sight would become important.

- All of the integrated intensities from CFD results are calculated with the projected frontal area of the capsule or scaled model, so it gives the maximum possible radiance or radiant intensity value. Including a reduced area will then reduce this value, but for the Hayabusa and Stardust flight path angles quoted at the time of observation, the area change would be less than 5 %, so quoting the ‘worst case’ full capture area value is suitable.
- Line broadening will be included within the wavelength integration limits for flight and X2 scaled numerical spectra. Even if the broadening functions are different, which is certainly the case between flight and experiment, the area under the curve and therefore the integrated intensity remains the same. Appropriate functions can be specified and adjusted in numerical spectra.
- The maximum number of points and the spacing between them, radially and along the LOS, is determined by the pixel resolution in the experimental images. The smallest possible distance is the width of a pixel, because intensity is only recorded once in each pixel. Lower resolution is possible by averaging over several pixels.

7.4 Background

Further processing of the experimental images and CFD flowfield data is required to generate results that are comparable with flight and each other. Radiation transport and spectra modelling are combined with the *eilmer3* CFD simulations to calculate the impact of radiation on the flowfield and couple the two where necessary, and to create numerical spectra. An overview of radiation modelling is presented and summarised by the parameters selected for generating numerical spectra in this work. The Abel inversion, a mathematical transformation required for processing the experimental data, is outlined along with the method implemented to solve it numerically.

7.4.1 Radiation Transport Modelling

High temperatures in the shock layer cause air species to radiate, introducing a radiative heat flux that adds to the convective heat flux incident on the vehicle surface. Radiative emission depends on flowfield properties such as temperature and density, and in re-entry scenarios where the heat transfer becomes non-adiabatic, the radiation alters the flow. This is termed radiation-flowfield coupling and its strength can be assessed through the Goulard number, the non-dimensional ratio of radiative energy flux to the total energy flux [102] given in Equation 7.1. From an *eilmer3* point of view, the Goulard number can be calculated from preliminary flowfield calculations by sourcing the stagnation point radiative heat flux through a tangent-slab calculation performed in post-processing, as this is assumed to be the point at which the largest heat flux occurs for an axisymmetric vehicle [40]. The general rule-of-thumb states that radiation-flowfield coupling becomes significant for a Goulard number above 0.01 [103] [60].

$$\Gamma = \frac{2q_{rad}}{\frac{1}{2}\rho_\infty u_\infty^3} \quad (7.1)$$

The nominal Goulard numbers calculated from simulations of Hayabusa and Stardust full scale vehicles and X2 scaled models are given in Table 7.1. Binary scaling causes the model shock layer Goulard numbers to be much less than the threshold, as radiative heat transfer is proportional to the nose radius of a blunt body vehicle [60]. The full scale Hayabusa simulation could experience some loose coupling since its Goulard number is just below the threshold. The high altitude of the Stardust flight condition produces a Goulard number that indicates significant radiation-flowfield coupling. If there is noticeable alteration to the flowfield as a consequence of strong coupling, the binary scaling assumption can cease to hold [17], then questioning the validity of the methodology adopted to establish ground reproduction.

	Hayabusa full scale	Hayabusa 1/5 scale (ideal)	Stardust full scale	Stardust 1/10 scale (ideal)
Goulard number	0.008	0.003	0.016	0.005

Table 7.1: Goulard numbers for Hayabusa and Stardust at two scales, calculated from preliminary *eilmer3* simulations and tangent-slab calculation along the stagnation line.

Radiation transport is included in the Navier-Stokes equations via the radiative source term, given by the divergence of the radiative heat flux in Equation 7.2. The emission and absorption coefficients are calculated from the nominated spectral database as discussed in Section 7.4.2 and the overall equation is solved through numerical methods. The monte-carlo ray tracing method traces a specified number of rays through the flowfield in any direction and at random, and solves Equation 7.2 across the generated field of rays. It can be spectrally resolved if the focus is on calculating numerical spectra, as it is in this work, or as a bulk transport property if the focus is on radiative heat flux only. The simpler tangent-slab and more comprehensive monte-carlo ray tracing methods are available in *eilmer3*, and Potter provides a detailed discussion about their implementation and testing, including the analysis that tangent-slab was only a reasonable approach near the stagnation line [13]. The radiation-flowfield coupling test later in this section used the Stardust flowfield and geometry, which changes considerably away from the stagnation line, therefore Potter's analysis informed the selection of the monte-carlo method for these calculations.

$$-\nabla \cdot \vec{q}_{rad} = 4\pi \int_{\infty} j_v dv - \int_{\infty} \int_{4\pi} \kappa_v I_v d\Omega dv \quad (7.2)$$

Starting from a flowfield solution, the iterative radiation transport calculation procedure is shown in Figure 7.3. The source term is calculated in *e3rad* and included in the next run of *eilmer3*, and convergence is checked after a certain time or number of steps. If there is no difference between the current and previous solution, the numerical spectra can then be determined.

Preliminary radiation-flowfield coupling tests with Stardust showed change occurring in flowfield variables due to the influence of radiation, but over periods of time much longer than hundreds of steps, thus the condition was loosely coupled. The update time was selected to be one body length (R_n/u_{∞}) of flow or about 1.9×10^{-5} s; enough time to see a change between iterations but sufficiently small that the updated source term did not adversely affect the flowfield simulation. The monte-carlo ray tracing transport model was chosen, as it is the most rigorous method, and the accuracy of the tangent slab model decreases away from the stagnation line [13]. The number of rays and number of

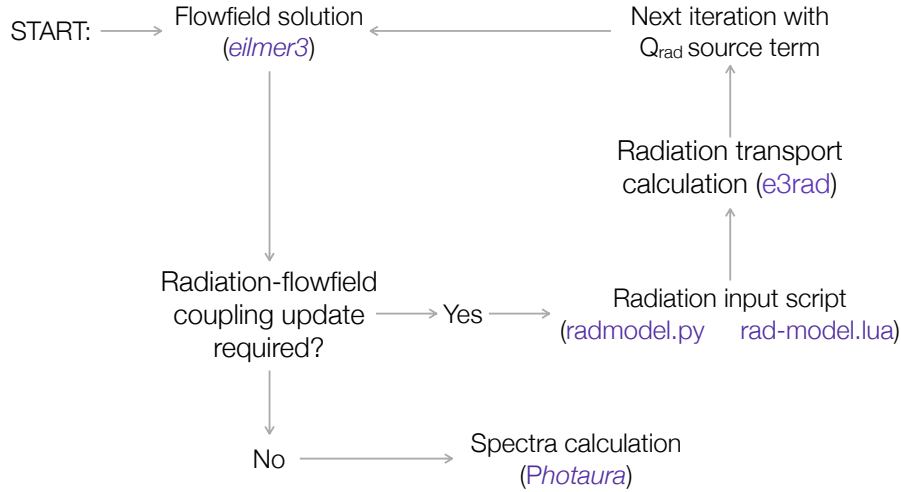


Figure 7.3: Radiation transport and flowfield coupling calculations.

spectral points were restricted by memory limitations on the available clusters. An example calculation used 1000 rays per cell and 30 points per nm over a spectral range of 50 to 1200 nm and *Photaura* was the database, following the parameters in Table 7.2. The uncoupled calculation, converged after five body lengths of flow, became the start of the coupled calculation. The temperature modes from the beginning and the end of the coupled calculation, converged five body lengths of flow later, are presented in Figure 7.4. There is a slight difference to the temperature profile, especially around the middle of the shock layer, but a 0.8 % variation at a temperature of nearly 12000 K is assumed to be insignificant with regards to spectral calculations. Taken as a representation of how all parameters vary with the inclusion of a radiative source term, the coupling does not have a considerable enough influence to include it further in the radiation spectra calculations, and so the uncoupled results shall be used.

7.4.2 Radiation Spectra Modelling

Numerical spectra are created by modelling physical processes that cause radiative emission and absorption, based on data from the flowfield. The radiative transfer equation defines the spatial and temporal variation of radiative intensity as a function of emission, absorption and scattering. Equation 7.3 presents the radiative transfer equation ignoring scattering, due to the low gas density and inability to model particles released during ablation, and neglecting temporal variation as the shock speed is

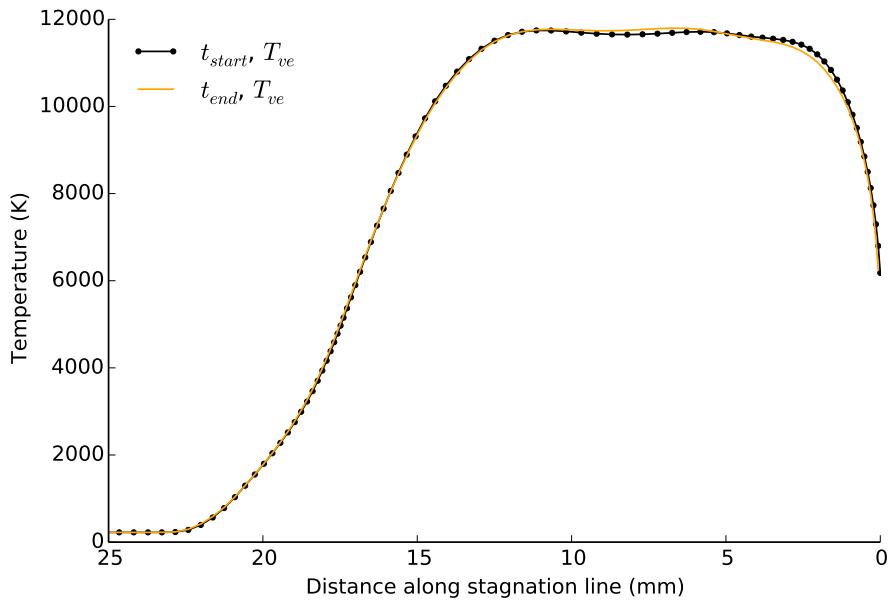


Figure 7.4: T_{ve} along the stagnation line at the beginning and end of the Stardust radiation-flowfield coupled calculation, with a radiation source term update every one body length of flow.

much less than the speed of light.

$$\frac{\partial I_v}{\partial s} = j_v - \kappa_v I_v \quad (7.3)$$

The emission and absorption coefficients, j_v and κ_v , are determined by a radiation database from the flow properties at a particular point, combined with the transition type, the electronic level populations and the radiative mechanism [13]. *Photaura* is the radiation database within *eilmer3* [13] and is the principal database in use for the present numerical spectra calculations. *PARADE*, the radiation database developed by Fluid Gravity Engineering, the European Space Agency and IRS Stuttgart has been linked to *eilmer3* in the Ablation-Radiation Coupling project (see, for example, reporting about PARADE [104] and its use in the project [105] [106]) and is also used in this work. Both databases can calculate radiation from thermal equilibrium, using a Boltzmann distribution, or from thermal nonequilibrium with a quasi-steady state (QSS) approach that involves collisional-radiative modelling of dissociation, ionisation, impact excitation and radiative transition [13].

Solving the radiative transfer equation along a particular line of sight yields spectral radiance in

terms of wavelength, units $\text{W} \cdot \text{m}^{-2} \cdot \text{nm}^{-1} \cdot \text{sr}^{-1}$, after conversion from the native value in terms of frequency (as denoted by the subscript ν). Equation 7.4 illustrates the general solution of Equation 7.3, showing the necessity of calculating j_ν and κ_ν . If the flowfield is optically thin, that is, none of the radiation that is emitted is (re-)absorbed, the problem simplifies to integrating the emission coefficients along the line of sight length. The calculated spectral radiance can compare directly to experimental measurements if the line of sight is the same. Once the line of sight coordinates are selected; for example, to replicate a vertical spectra measurement in X2, a script post-processes the flowfield data and carries out the radiation calculations to produce the spectral radiance in terms of wavelength (units $\text{W} \cdot \text{m}^{-2} \cdot \text{nm}^{-1} \cdot \text{sr}^{-1}$), as well as plasma emissivity (units $\text{W} \cdot \text{m}^{-3} \cdot \text{nm}^{-1} \cdot \text{sr}^{-1}$), which is essentially the emission coefficient of each cell. These values can then be used in flight rebuilding in the same way as the experimental measurements.

$$I_\nu(s) = I_\nu(s_0)e^{-\kappa_\nu(s_0,s)} + \int_{s_0}^s j_\nu(s')e^{-\kappa_\nu(s',s)}ds' \quad (7.4)$$

The numerical spectra calculations are carried out over a defined wavelength range with a given resolution, in terms of points per nanometre. The radiating species can be a subset or the complete set of flowfield species, and these can be modelled considering thermochemical equilibrium or nonequilibrium. Particular transitions and types of radiation can be selected in some instances (for example, the user can select particular bands in PARADE) and the radiation can be line-resolved if the desired result is a full spectrum, rather than just cumulative intensity. Figure 7.5 illustrates the calculation of numerical spectra along a line of sight created from a CFD solution, as well as a simpler process when flow properties are assumed constant along a given path length. In this case, the flow properties can be taken from one cell in the equilibrium region, instead of including the variation of properties that occur along a line of sight that traverses the shock layer.

Broadening functions must be applied to numerical spectra in an attempt to create the same effects that various broadening mechanisms have on the physical flow, including Doppler broadening due to velocity, pressure broadening, and effects introduced by the instrument. In-built methods include a Voigt function or square-root Voigt function, both with Gaussian and Lorentzian components for which the full width at half-maximum (FWHM) is specified. The procedures of Cruden *et al.* [107]

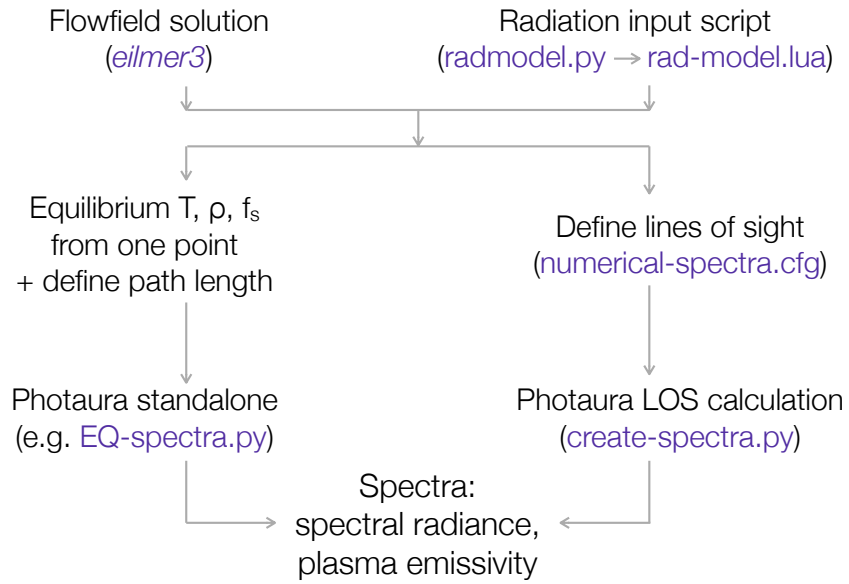


Figure 7.5: Calculating spectra from an *eilmer3* solution along a line of sight, or assuming constant properties in a ‘single-cell’ methodology.

were followed to determine the camera and instrument functions from experimental measurements. The same functions can be applied to CFD in order to include the instrument broadening seen in experiment. The best fit to the shape of the experimental measurements was a square-root Voigt function, but mainly because of extra background that is not simulated fully in CFD. The best fit to the flight data appeared to be the standard Voigt function. Thus, all numerical spectra have been calculated with a standard Voigt function, and Gaussian and Lorentzian FWHMs were determined by experiment or iterative methods.

7.4.3 Abel Inversion

The Abel inversion is a mathematical transform that takes an integrated value, $F(y)$ at a certain height, y and yields the radial function per unit length, $f(r)$, as given in Equation 7.5.

$$f(r) = -\frac{1}{\pi} \int_r^\infty \frac{dF}{dy} \frac{dy}{\sqrt{y^2 - r^2}} \quad (7.5)$$

Spherical symmetry (or axisymmetry) is assumed, which is why it was necessary for experimental measurements to be taken vertically through the shock layer, rather than the standard horizontal stagnation line measurements. The vertical and horizontal imaging planes in Figure 7.6 emphasise the axisymmetry of vertical slit spectroscopy measurements or each column in a 2D image. By taking a series of vertical images at different locations along the direction of flow, the radiation per unit volume is then revealed by the Abel inversion at discrete points throughout the entire 3D forebody shock layer. Placement of vertical slices, as captured in X2, were shown in Figure 7.2.

When the Abel inversion is applied to optical measurements, the integrated value is the spectral radiance from 1D spectroscopy or radiance from 2D images, and the y value is the height from the stagnation line. The Abel inverted value is the local plasma emissivity per wavelength or the wavelength integrated emissivity, and is defined radially from the centre of the circular plane, which is the stagnation line in this case. Once the Abel inversion is performed for each vertical slice, the radial plasma emissivity is known for each slice, creating a 3D field of radiating points defined by their position from the stagnation line in y and z , and stagnation point in x .

The Abel inversion requires numerical methods to solve, especially with discrete data sets. The simplest method is the geometric onion peeling method, where a series of concentric circles are

Database	<i>Photaura</i> , PARADE
Wavelength range	All: 50 - 1200 nm UV: 300 - 400 nm IR: 700 - 900 nm
Number of spectral points	All: 115 000 UV: 10 000 IR: 20 000
Radiating species	Subset or full set of flowfield species, e.g. atoms only: N, N ⁺ , O, O ⁺ , e ⁻
Thermochemical equilibrium (Boltzmann) or nonequilibrium (QSS)	<i>Photaura</i> : set by species, PARADE: <i>parade_population</i>
Transport model	Tangent-slab, monte-carlo (MC) ray tracing
Number of rays	100, 1000, 10 000 (for MC only)
Spectrally resolved	Yes, for creating numerical spectra

Table 7.2: Summary of radiation spectra and transport parameters for CFD aeroshell simulations in *eilmer3*.

used to distribute $F(y)$ and working from the outside in, can define $f(r)$ for each circle, finishing at the centre [108]. This method was used for initial analysis but is extremely inaccurate and was excluded from the final methodology. Polynomial fitting methods and Fourier methods have varying degrees of accuracy and success, but the spline method developed by Fulge *et al.* performs well, and was the preferred choice [109]. The method approximates the local distribution by a set of splines, applying specific boundary conditions between the connecting spline points and their first derivatives as well as the centre and outer boundaries. The resulting set of over-determined equations is solved by applying a least-squares method, producing the coefficients to describe the inverted function. Fulge *et al.*'s analysis shows that the spline method performs consistently better than the other Abel inversion methods for their plasma wind tunnel spectroscopic data, and the same will be assumed for the data considered in the flight rebuild [109]. Similarly formulated spline algorithms for numerical Abel inversion were used by Sainz *et al.* for microwave emission plasmas and Glasser, Chapelle and Boettner for plasma spectroscopy test functions. Both showed good results, including good smoothing of the data where noise may exist [110] and superior performance over polynomial methods [111].

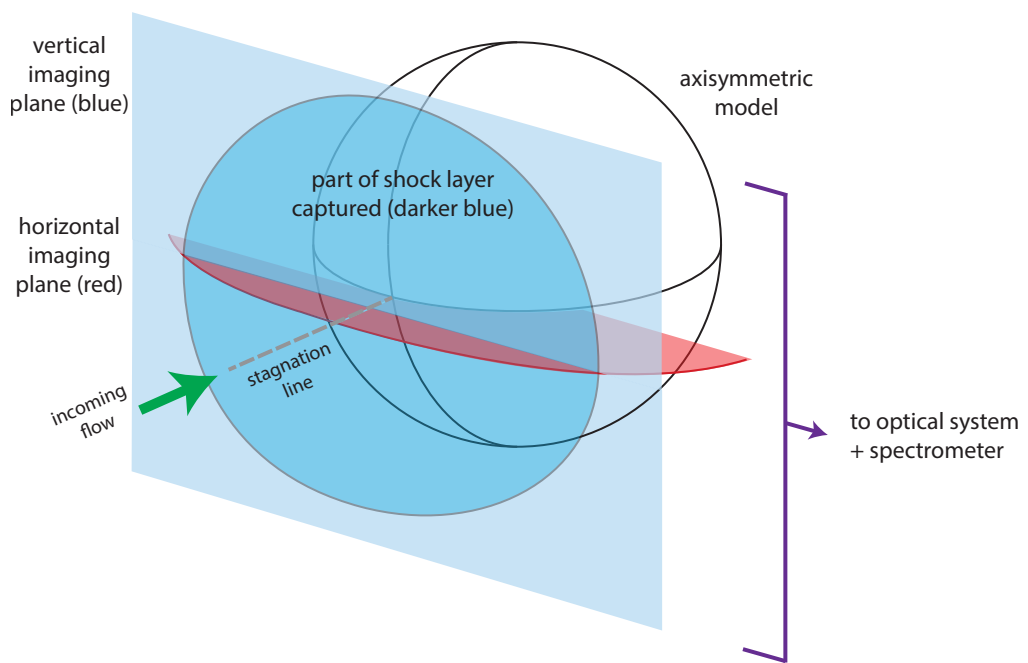


Figure 7.6: Vertical and horizontal slices through the shock layer in front of an axisymmetric model.

7.5 Hypothesis: Scaling Models and Radiation

Capra postulated, from her investigation of radiative heat flux for Titan entry in an expansion tube, that radiative heat flux received at the surface is invariant under binary scaling, in a transparent gas [17]. This can be extended and generalised to assess the radiative energy per unit area in the same relative location; for example, along a line of sight through the shock layer, at different scales. Take the total radiant energy in the flowfield as proportional to the total amount of mass in a control volume, for the flight case (subscript f) in Equation 7.6 and scaled case (subscript sc) at identical thermal conditions but a different physical size in Equation 7.7.

$$E_f \propto m_f = \rho_f L_f^3 \quad (7.6)$$

$$E_{sc} \propto m_{sc} = \rho_{sc} L_{sc}^3 \quad (7.7)$$

Recall the binary scaling equation as declared in Chapter 3, and re-stated in Equation 7.8, to maintain the product of density and length and preserve mass fractions along a streamline.

$$\rho_f L_f = \rho_{sc} L_{sc} \quad (7.8)$$

The ratio between the radiant energy in the flight and scaled flowfields can be calculated in terms of the ρL parameter, as in Equation 7.9.

$$\frac{E_f}{E_{sc}} = \frac{(\rho_f L_f) L_f^2}{(\rho_{sc} L_{sc}) L_{sc}^2} \quad (7.9)$$

Applying Equation 7.8, the ρL parameters cancel out, and the ratio of flight to scaled total radiant energy is given in Equation 7.10.

$$\frac{E_f}{E_{sc}} = \left(\frac{L_f}{L_{sc}} \right)^2 \quad (7.10)$$

For Hayabusa, $L_f/L_{sc} = 5$ and for Stardust, $L_f/L_{sc} = 10$. Thus, it is expected that the flight results

over the entire flowfield (flight data and CFD) will be greater than the scaled results over the entire flowfield (X2 experiments and CFD) by a factor of 25 for Hayabusa, and a factor of 100 for Stardust. Equation 7.10, when rearranged to Equation 7.11, shows that the energy per unit surface area is equal, illustrating the invariance of radiative heat flux (an energy per unit area quantity) under binary scaling assumptions. This extends to spectral radiance, the quantity measured in calibrated spectra, because when considering the radiation reaching the area subtended by the same relative solid angle the invariance is maintained, as is the per unit wavelength quantity. Over the same wavelength range and along the same relative line of sight, including the observing area and the subtended solid angle, the spectra in flight or full scale CFD cases should be equivalent to scaled experimental and numerical spectra.

$$\frac{E_f}{L_f^2} = \frac{E_{sc}}{L_{sc}^2} \quad (7.11)$$

Therefore, radiation flux over the entire forebody shock layer will be presented in radiant intensity ($\text{W} \cdot \text{sr}^{-1}$) and comparisons will be assessed against the target length scale factor: 25 for Hayabusa, and 100 for Stardust. The spectra will be compared in terms of spectral radiance ($\text{W} \cdot \text{m}^{-2} \cdot \text{sr}^{-1} \cdot \text{nm}^{-1}$) and should be equal along the same relative line of sight.

7.6 Methodology

Several methods were implemented to compare CFD to experiment, flight to CFD, and experiment to flight, and are outlined below as pertaining to each comparison.

7.6.1 Comparing experiment and flight

The process of finding the equivalent flight intensity from an experimental measurement is outlined.

1. As discussed in Chapter 4, vertical measurements are taken through the shock layer around a Hayabusa or Stardust scaled model, as axisymmetric vertical profiles are necessary for the Abel inversion. The measurements have been calibrated in intensity, wavelength and distance

and presented in 5. If necessary, the images are cut at the stagnation line, so that the y profile extends from the centreline to the shock layer edge.

2. For 1D spectra images only, the wavelength band is selected (usually the same as the filter wavelength for that feature) and the image is integrated over the wavelength band for every y . The result is an array of radiance vs distance, where the vertical spacing dy is defined by the pixel width and magnification, and number of vertical points ny is defined by the spatial extent of the image. The horizontal spacing dx is defined by distance along stagnation line between two vertical spectra, and number of horizontal points nx is defined by the spatial extent of the image.
3. For 2D images only, each column can be treated separately as an array of radiance vs distance. Vertical spacing dy and horizontal spacing dx are defined by the pixel width and magnification in each direction, and the number of points in x and y direction, nx and ny , are defined by the spatial extent of the image.
4. Final input arrays are 2D arrays of radiance, with each cell location attributed to an x and y coordinate, stored in separate arrays.
5. The Abel inversion spline method is applied to each column of the input array, following the axisymmetry in the vertical dimension, to produce a 2D array of plasma emissivity, or j ($\text{W} \cdot \text{m}^{-3} \cdot \text{sr}^{-1}$). CFD results come directly from the radiation calculation in the form of plasma emissivity, and so the rebuilding process for CFD solutions begins here.
6. The x dimension becomes the axial dimension s , and the y dimension becomes the radial dimension r , and dx , nx , dy and ny map to ds , ns , dr and nr , respectively. The small area around one radiating point is approximated by $dA = dr^2$, and the small radiating volume by $dV = dr^2 \times ds$.
7. The 2D plane is rotated into 3D, with dr the spacing around the circumference of each ring. The number of segments around each ring varies with dr , and in cases where there are non-integer numbers of segments, the value is rounded to the next highest integer.
8. To calculate radiant intensity, plasma emissivity at every point is integrated in a small volume

element, so that the value at each point is now in $\text{W} \cdot \text{sr}^{-1}$.

$$I [\text{W sr}^{-1}] = \sum_{i=1}^n j_i [\text{W m}^{-3} \text{sr}^{-1}] \times dV_i [\text{m}^3] \quad (7.12)$$

9. The comparative flight values are calculated from their published values, depending on the region of the spectrum and the vehicle.

- (a) Hayabusa IR: as the values are published in $\text{W} \cdot \text{cm}^{-2} \cdot \mu\text{m}^{-1} \cdot \text{sr}^{-1}$, convert to $\text{W} \cdot \text{m}^{-2} \cdot \text{nm}^{-1} \cdot \text{sr}^{-1}$, and integrate over the prescribed filter range that matches the feature, e.g. 773-790 nm for the 777 nm O triplet.
- (b) Hayabusa UV: values are published in $\text{W} \cdot \text{m}^{-2} \cdot \text{nm}^{-1}$ and referenced to a standard 100 km observation distance. Integrate over the selected wavelength range to match that used for the experimental or CFD part of the rebuild, then divide by the solid angle in Equation 7.13 using $d_{obs} = 100 \text{ km}$ for radiance in $\text{W} \cdot \text{m}^{-2} \cdot \text{sr}^{-1}$.

$$\Omega_f = \frac{\pi R_{capsule}^2}{d_{obs}^2} \quad (7.13)$$

- (c) Stardust: values are also published in $\text{W} \cdot \text{m}^{-2} \cdot \text{nm}^{-1}$ and the flight observation distance is given in Jenniskens [15]. Integrate over the selected wavelength range to match that used for the experimental or CFD part of the rebuild, then divide by the solid angle in Equation 7.13 using the published distance for radiance in $\text{W} \cdot \text{m}^{-2} \cdot \text{sr}^{-1}$.

7.6.2 Comparing CFD and flight

Radiation calculated from the results of CFD simulations can be compared to flight in a wavelength-resolved or wavelength-integrated manner. The wavelength-integrated radiance can be determined for flight by integrating over the desired wavelength band, as suggested in Section 7.6.1. *Photaura* calculates j at each radiating point based on the flowfield properties, before looking to integrate along a line of sight and return spectral radiance. The field of radiating points can be rotated into 3D and summed along lines of sight, following steps 7 and 8 in the experimental calculation method above, to

achieve a radiance value across the entire radiating volume, which can be compared to the flight value.

The wavelength-integrated method requires a result from CFD and radiation modelling to compare directly to the flight spectra. Following a similar procedure to Liu *et al.* [70] and Winter *et al.* [35], spectral radiance was calculated along many lines of sight emanating outwards from the vehicle surface through the shock layer, and averaged to produce a spectrum comparable to flight. It was assumed that the lines of sight would be parallel to the stagnation line, outwards from the vehicle towards an observer location. A viewing angle can be introduced if desired, but the current results will not include an angle, therefore defining the upper limit for the radiation modelling. In the case of Hayabusa, there was no shadowing from the capsule body and the shock layer was optically thin, making the view angle irrelevant [5]. Through a sensitivity analysis it was discovered that 100 lines of sight with 100 points along each line was sufficient for a grid-independent solution.

7.6.3 Comparing CFD and experiment

Experimental spectra were recorded and calibrated to produce spectral radiance, which can be compared directly to numerical spectra integrated along lines of sight to also give spectral radiance. The comparisons take place at the same location, vertically or horizontally, in the shock layer for experiment and scaled CFD simulations, and at the same relative location for the full scale CFD simulation, accounting for the length scaling factor. As an example, the experimentally measured spectra that were recorded on a vertical plane located 1 mm upstream of the stagnation point can be compared to the same plane in the scaled CFD simulations, and a plane located 5 mm upstream of the stagnation point in the full scale CFD simulation.

The plasma emissivity, j , can also be compared between experiment and CFD, and as stated above, j is the native radiation value calculated from the flowfield properties in a radiation solver. The experimental 2D images can be Abel-inverted, following the procedure in Section 7.6.1, to produce a wavelength-integrated plasma emissivity. Hence, the two fields of radiating points can be compared once the numerical result has been integrated over the same wavelength range as the filter applied to the experimental image.

7.7 Results and Analysis

7.7.1 Comparing CFD and experiment

The comparison of CFD results to X2 experiments will consist of two parts: full scale CFD against experiment, and scaled CFD, including ideal scaled and X2 inflow scaled, against experiment. The results from each set of CFD simulations show some intriguing differences, thus it is best to separate them. As spectra were recorded along vertical slices upstream of the model location in experiment, slices at the same location for scaled CFD, or relative location for full scale CFD, will be presented.

7.7.1.1 Hayabusa

Numerically generated spectra from radiation modelling and CFD of the Hayabusa flight vehicle, using the *Photaura* and PARADE databases, are presented alongside experimental spectra for the 1/5 scale Hayabusa model in Figure 7.7. The magnitudes of the peaks in parts 7.7a through 7.7d compare well between the *Photaura* and PARADE cases, and the experimental case. The higher magnitudes in part 7.7e, and especially in part 7.7f, could possibly be attributed to error in the optics positioning, or a higher incident velocity than calculated for those shots. PARADE overestimates the peak magnitudes from *Photaura* for most of the lines considered, but there is a high level of consistency between the two databases. The FWHM of the Voigt function in the IR numerical spectra is approximately 0.33 nm. The additional background and subsequent extra broadening in the experimental spectra, especially between closely spaced spectral lines, is attributed to extra contributions from free-free neutral-ion interactions, from a study conducted by Cruden *et al.* in the NASA EAST facility [107]. Their spectra showed the same increased background, and once it was determined to be real radiation by placement of a notch filter, analytical calculations of electron number density were performed following a chosen parameterisation [107]. The result showed that the electron number density should be more than predicted by simulations. Tests were carried out on the current numerical results to ensure that it was not the full-width at half-maximum in use for the Gaussian or Lorentzian component, or indeed the broadening function shape itself, that were causing the discrepancies. Hence, it is hypothesised that the effect of electron number density and subsequent free-free radiation is impacting the results for the full scale Hayabusa simulations. Overall, the

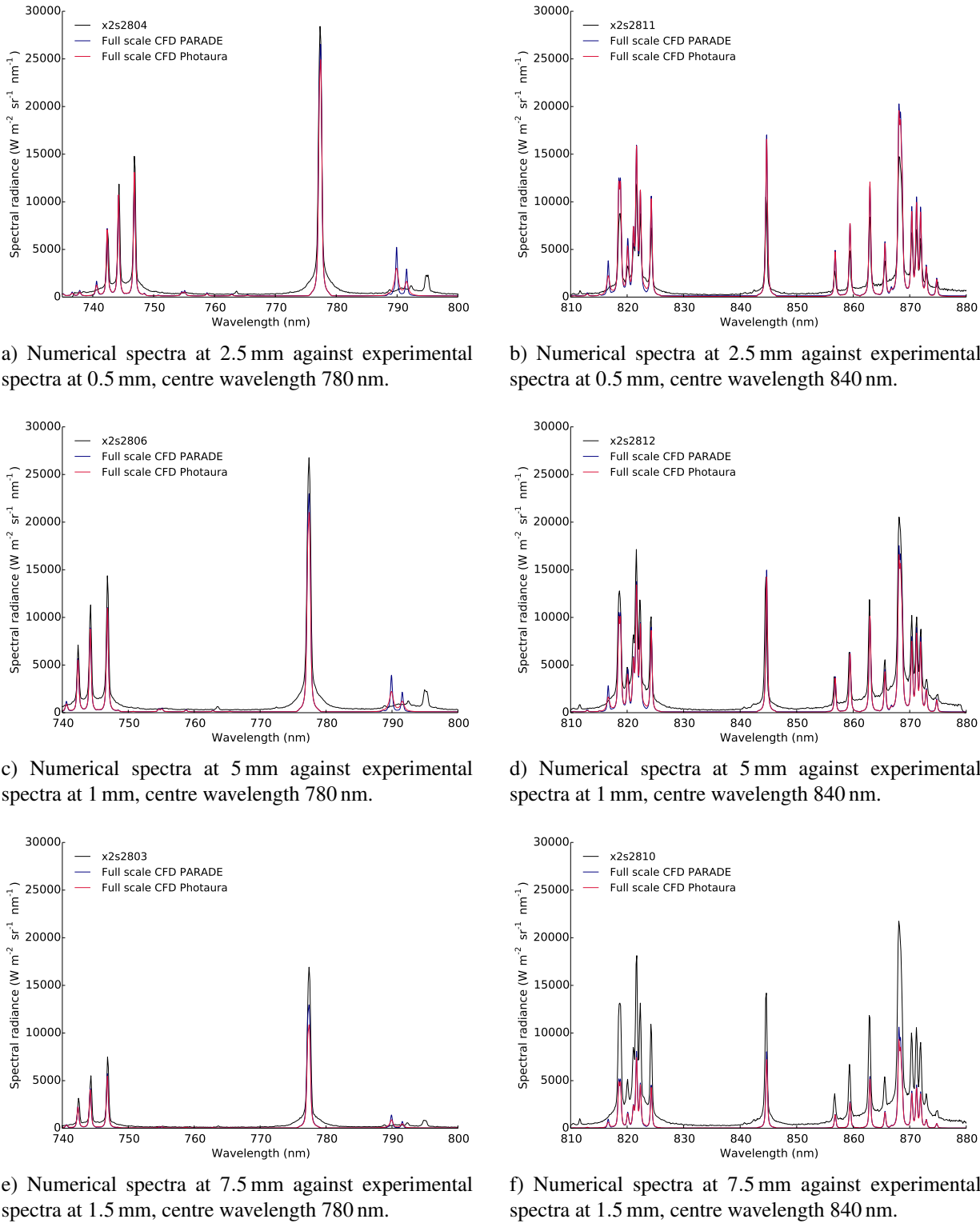


Figure 7.7: Comparison of full scale simulated Hayabusa numerical spectra, sliced vertically, compared to the same scaled location for the vertical experimental spectra.

similarity of the full scale CFD spectra and the experimental spectra looks promising for flight comparisons at a first glance. It appears to indicate that even though the summed flowfield emissions are expected to differ by 25 as postulated in Section 7.5, measurements of the volume integrated intensity (in this case, spectral radiance) along a line of sight will be very similar.

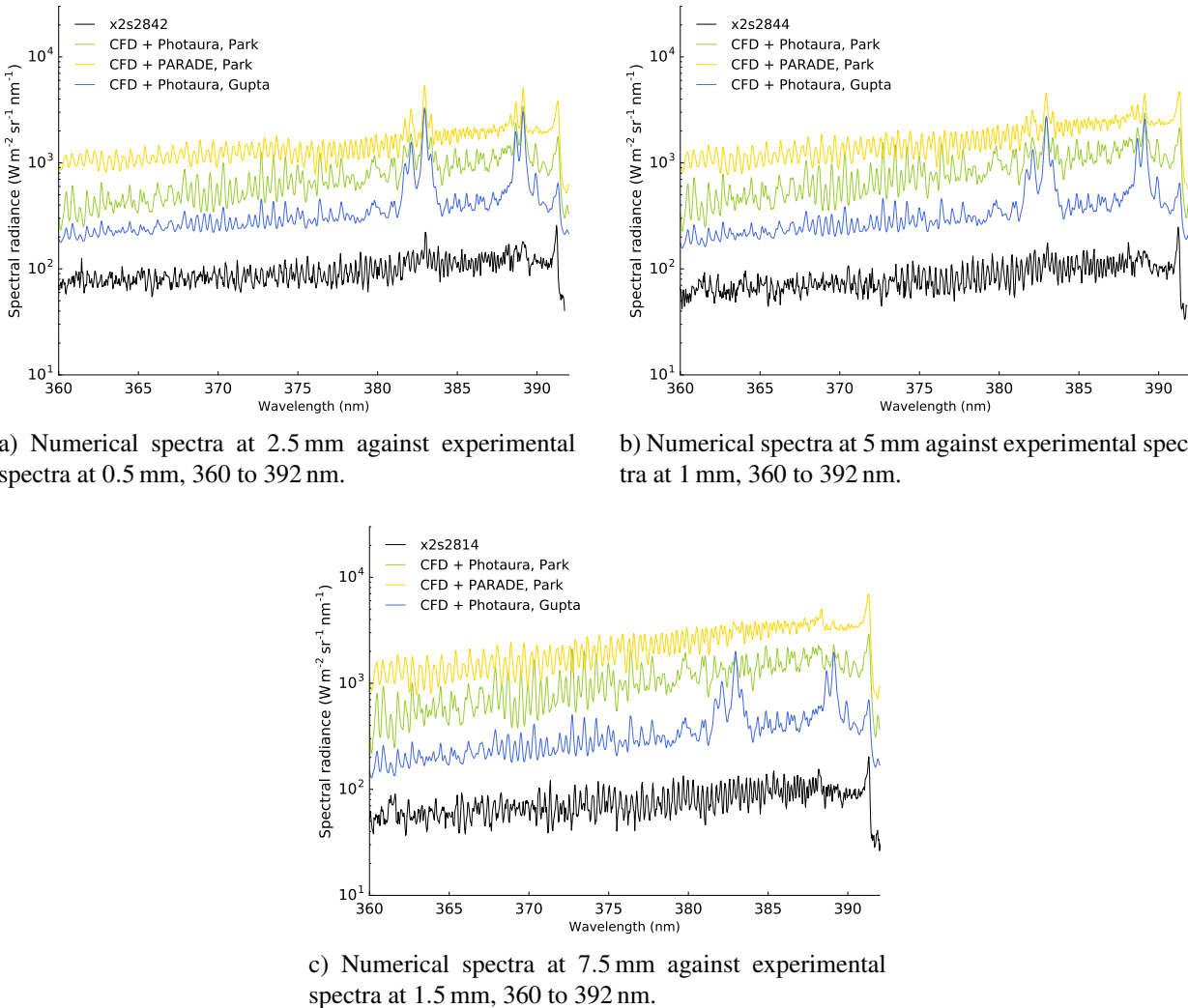


Figure 7.8: Comparison of full scale simulated Hayabusa numerical spectra in the UV, sliced vertically, compared to the same location for the vertical experimental spectra.

The Hayabusa experimental and full scale CFD UV spectra are plotted on a log scale in Figure 7.8, and the main feature to compare is the N_2^+ bandhead at approximately 391 nm. The FWHM of the numerical spectra, at 0.16 nm, is similar to the well-resolved experimental spectra. As N_2^+ is a largely nonequilibrium species that appears and depletes across the shock front, it is a difficult species to

model. Immediately obvious is the order of magnitude difference between the experimental results and CFD results using the Park reaction scheme, made worse in the PARADE calculations. The overprediction of N_2^+ emission is affected by both choice of reaction scheme and database, as Gupta and Photaura are the best available choices, respectively. However, even the best selections cannot replicate the experimental results and more investigation is necessary to resolve the differences to experiment. Overall, N_2^+ does not contribute substantially to the overall radiation in the Hayabusa shock layer, but it is an important marker for nonequilibrium.

Figure 7.9 presents numerical spectra from ideal scaled and X2 nozzle inflow scaled Hayabusa CFD simulations against spectra from experiment. The experimental spectra are the same as that presented against full scale CFD spectra in Figure 7.7, and now it is apparent that although the full scale spectra compared well to experiment, the scaled CFD spectra, in general, do not. The ideal scaled CFD spectra come closer to the experimental spectra than the nozzle inflow scaled case, and the best comparisons are at 1.5 mm upstream of the stagnation point. At this location, the ideal scaled and experimental spectra are nearly identical in the 810 to 880 nm region. However, the background and wings between adjacent spectral lines are simulated much better in these cases than in the full scale case, suggesting that the higher temperatures of the shock layer (c.f. Figure 6.16) are not only increasing the atomic line peak heights, but the free electrons and resultant free-free radiation. The disagreement between spectra from the ideal scaled and nozzle inflow scaled CFD highlights the difference in conditions brought about by the facility simulation, and that the selected test time to create the inflow seems to be far from ideal: at worst, the ideal case peak magnitudes are about 50 % of the nozzle inflow case, e.g. in part 7.9e. Experiment and scaled CFD spectra should, ideally, be the same for the same models, locations and conditions, and these should be very similar to full scale CFD spectra. The consequences of uncertainties in the experimental flow over the model and the inability to measure anything other than conehead pressure beyond the acceleration tube are CFD flow properties that can quickly diverge from actual values. As stated in Chapter 3, the changes in v or ρ are masked by the conehead pressure and any consistency in that measurement can be misleading. Comparisons between IR spectra from air shock layer experiments in the NASA EAST facility and NEQAIR numerical spectra have also proved problematic, as exemplified by Bose *et al.* [62]. The differences were attributed to thermochemical equilibrium not being achieved, although it is assumed

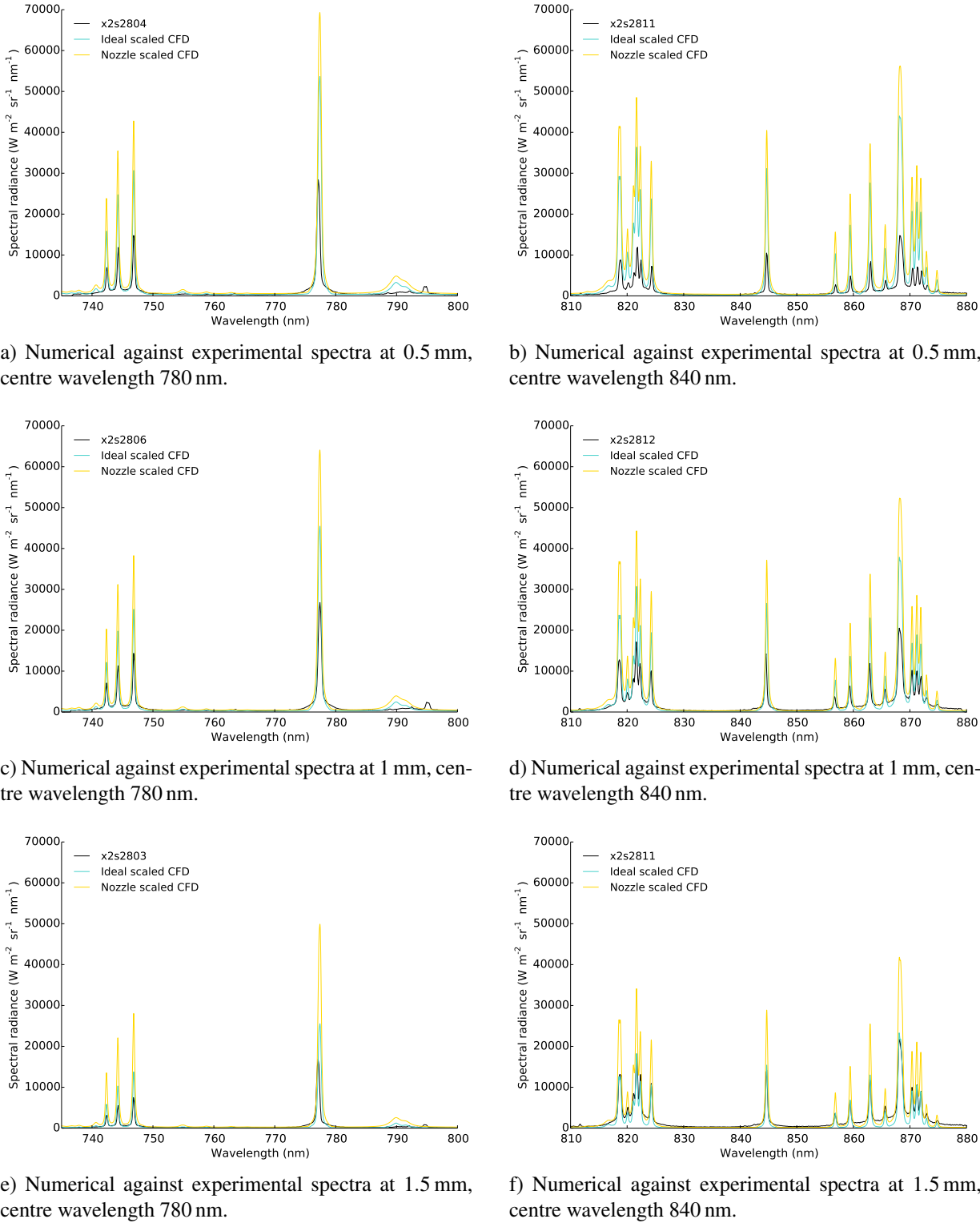


Figure 7.9: Comparison of ideal and nozzle inflow scaled simulated Hayabusa numerical spectra, sliced vertically, compared to the same location for the vertical experimental spectra.

in the radiation modelling process. Bose *et al.* also suggested that boundary layer interaction with cold walls or radiative cooling could affect the flow in the EAST facility [62], which should not pose a problem in the case of the current experiments, given the large diameter of the X2 test section. It is possible that the modelling of thermochemical equilibrium and nonequilibrium, and associated radiation, is not accurately reflecting the experimental flow.

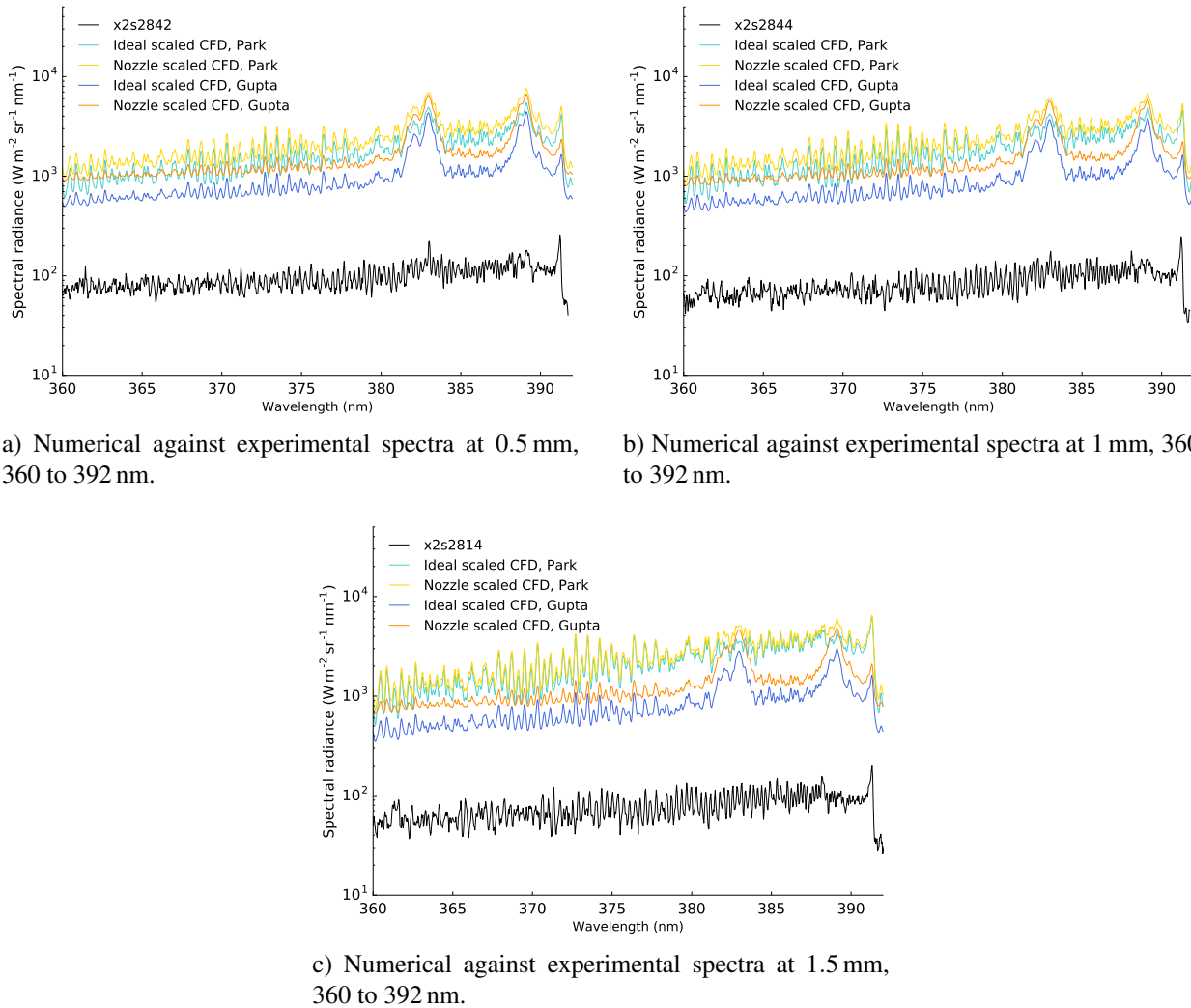


Figure 7.10: Comparison of ideal and nozzle inflow scaled simulated Hayabusa numerical spectra in the UV, sliced vertically, compared to the same location for the vertical experimental spectra.

The comparison of UV spectra at three vertical locations for experiment and scaled CFD, shown in Figure 7.10, produces a similar order of magnitude difference that was seen in the full scale CFD to experiment comparison. The FWHM of 0.16 nm produces a resolution similar to experiment, and the

use of the Gupta reaction scheme brings the spectral radiance due to N_2^+ closer to the experimental value. The scaled CFD spectra peak magnitudes are again greater than the full scale CFD in Figure 7.8, but it is the discrepancy to the experimental spectra that illustrates the further investigation that is needed into modelling nonequilibrium species.

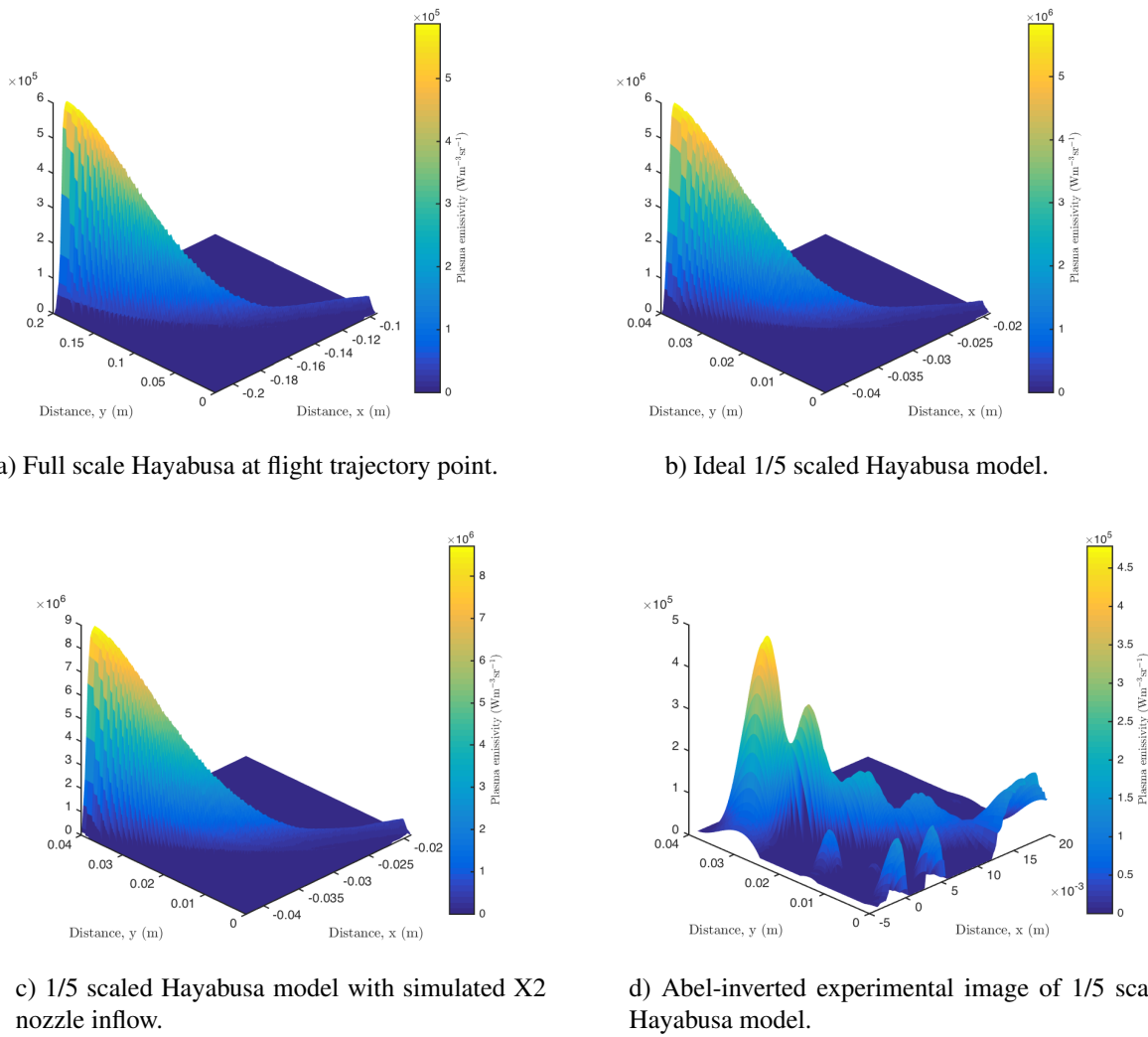


Figure 7.11: Plasma emissivity of Hayabusa simulated shock layers, 773 to 790 nm using *eilmer3* and *Photaura*, compared to the Abel-inverted experimental image (2D intensity mapping). Please note the differences in axes scales between each image, to account for the orders of magnitude.

The plasma emissivity across the axisymmetric shock layer plane in Hayabusa CFD simulations and experiment is shown in Figure 7.11. These images display j calculated between 773 and 790 nm but are examples of the radiation profile across all considered spectral features in the IR. The filter

transmissivity has been applied to the experiment as well as the CFD calculations. The main feature to note is the difference in magnitude of the peak value of j : the scaled CFD values are just over an order of magnitude larger than the flight CFD value and the experimental value. This is consistent with the emission over the entire flowfield differing by a factor that, ideally, is equal to the length scale squared. However, as evidenced by the line of sight integrated spectra comparisons in Figure 7.9, the j values are ultimately too high in the scaled CFD cases to fulfil this expected ratio, due to factors previously postulated. The peak experimental j is slightly less than the flight CFD peak j , but the eventual similarity along a particular vertical line of sight is explained by the different profiles of j along the remainder of that line of sight. It is difficult to tell from the 3D images, but the experimental j maintains a higher value for a longer relative distance along the same relative line of sight as the flight CFD, and therefore when integrated alone that line, the integrated intensity is very similar. The Abel inversions are not properly processing the input due to noise in the experimental images, and the resolution is limited to one pixel width. A study of Abel inversions applied to plasma emissivity from a plasma torch showed that the addition of noise to a hypothetical smooth data set changed the results of the Abel inversion towards the outer edges of the radial dimension [112], similar to the effects in Figure 7.11d, but did not have a significant effect compared to the main inversion profile. There will be imperfections with numerical transformations applied to experimental data sets, and the spline method still produced the best numerical Abel inversion results for the current data.

7.7.1.2 Stardust

The plasma emissivity of the Stardust axisymmetric shock layer plane imaged in experiment and simulated at various scales is shown in Figure 7.12. As for Hayabusa, j is calculated between 773 and 790 nm, which focuses on the O 777 nm triplet, and the filter transmission function is applied in the experimental and numerical cases. The experimental peak magnitude is higher than the full scale CFD and closer to the scaled CFD values than Hayabusa, but the CFD j distribution across the flowfield is much more uniform than in experiment, which is hampered by the prominence of the Abel inversion around the stagnation line and its decay further around the vehicle. The order of magnitude difference from the flight CFD to the scaled CFD j peak values is feasible given the target ratio between full scale and scaled flowfields. However, the high values remain across the flowfield,

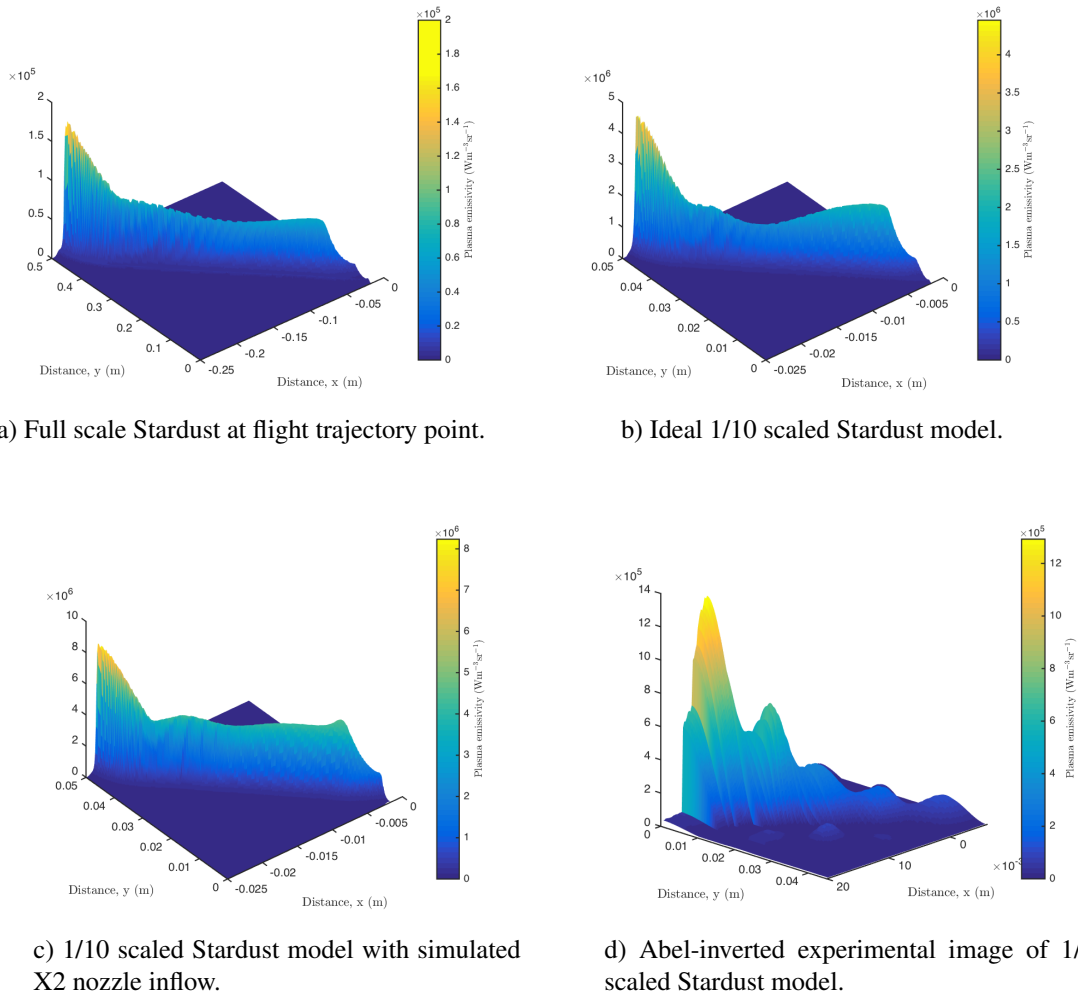


Figure 7.12: Plasma emissivity of Stardust simulated shock layers, 773 to 790 nm using *eilmer3* and *Photaura*, compared to the Abel-inverted experimental image (2D intensity mapping with filter). Please note the differences in axes scales between each image, to account for the orders of magnitude.

unlike in experiment, and therefore contribute to excessive emissions, as in the Hayabusa case. As the Abel-inverted flowfield displays local plasma emission, it is clear that the extra line of sight spectral radiance seen in Figure 5.15 is just an artefact of the line of sight integration, rather than extra intensity due to the expansion around the shoulder.

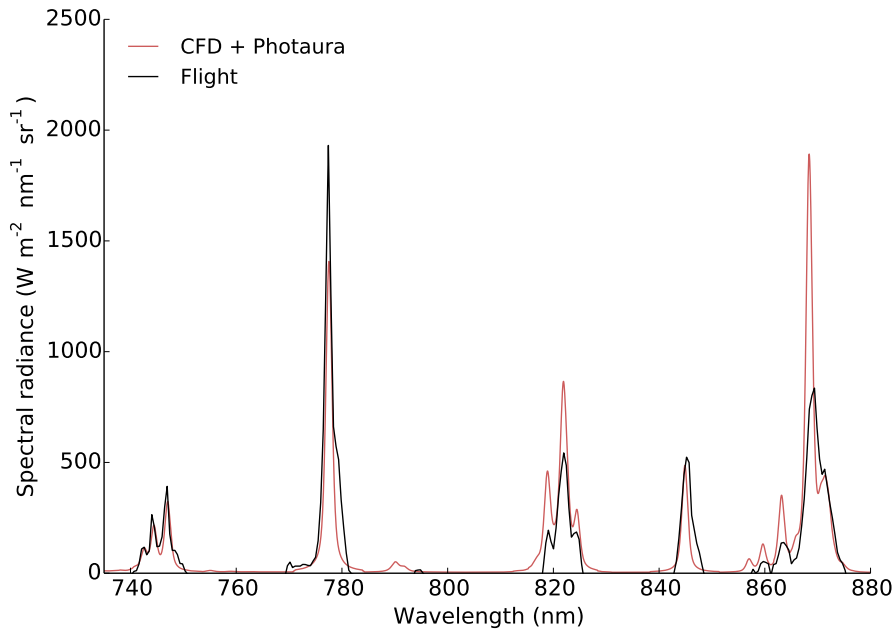
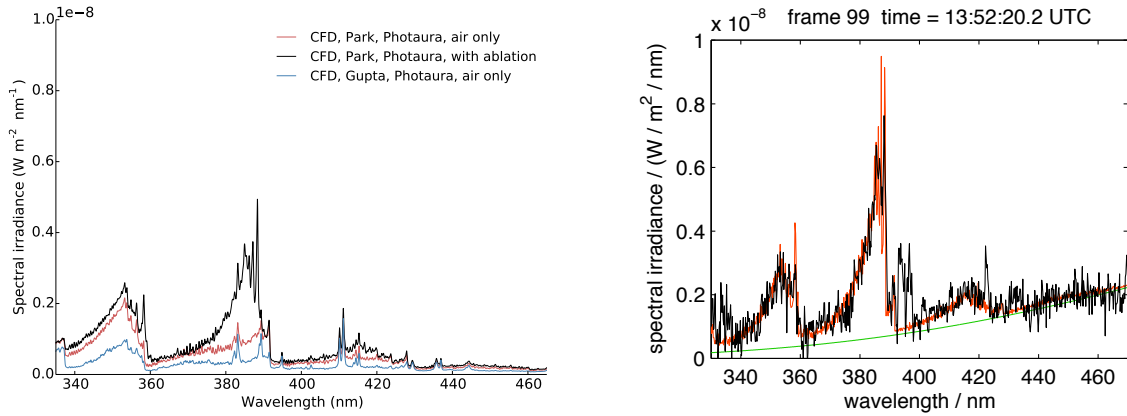


Figure 7.13: Hayabusa IR flight spectra against CFD spectra calculated and averaged over the whole vehicle.

7.7.2 Comparing CFD and flight

7.7.2.1 Hayabusa

Figure 7.13 plots the Hayabusa flight spectra from McIntyre *et al.* [4] against the CFD averaged spectra, using 100 horizontal lines of sight that are equally spaced in the vertical direction. The numerical spectra was broadened with a Voigt function with a FWHM of approximately 1.3 nm, to match the flight spectra as closely as possible. The best comparisons between the data are the nitrogen lines around 740 nm and the oxygen triplets at 777 nm and 844 nm. Several of the N lines around 820 nm, and 870 nm in particular, are overestimated in numerical modelling. The 868 nm N triplet looks to be overpredicted by the radiation data as the flight data, vertical line of sight experimental and numerical spectra, and other Hayabusa modelled spectra [35] indicate that the O 777 nm triplet should be the highest peak at the selected condition. It is promising, given the uncertainties in the flight data and the assumptions made in modelling; for example, using only a two-temperature model and a discrete number of lines-of-sight in the radiation calculation, that the spectra compare very well. This is a compliment to the modelling strategies and data, suggesting that for the Hayabusa trajectory point that is the focus of this work, simulations of the full scale Hayabusa vehicle return results that are very close to flight.



a) Full scale Hayabusa CFD and numerical spectra calculated in *Photaura* at selected trajectory point, 335–465 nm.

b) Full scale Hayabusa UV published results and flight data at selected trajectory point, 335–465 nm.

Figure 7.14: Hayabusa UV flight spectra against CFD spectra calculated and averaged over the whole vehicle. Flight data and published results using PARADE from Kraetzig, Loehle and Buttsworth [10].

Figure 7.14 compares the spectra from full scale Hayabusa CFD results and *Photaura* radiation calculations to the UV flight spectra and a previous PARADE calculation [10]. Spectra were calculated for an air only gas model with the Park and Gupta 11 species reaction schemes, and air with selected ablative species modelled by a mass flux boundary condition and the Park 20 species reaction scheme, both with FWHMs of about 0.33 nm. The added contributions in the air with ablation spectra are predominantly CN, especially in the band between 370 and 390 nm. The magnitudes of the CN peaks in this region are lower than recorded in flight, and the likely reason is the implementation of the boundary condition, which may need a different reaction rate or the inclusion of pyrolysis to completely model the Hayabusa TPS. N_2^+ appears to be the primary radiator in the band between 340 and 360 nm, and the addition of CN produced only a slight increase in peak magnitudes and emergence of a clear CN peak at about 358 nm. In general, this band compares very well between flight and the current *eilmer3* and *Photaura* calculations when using the Park reaction schemes, as flight is only slightly higher in magnitude. The N_2^+ bandhead at 391 nm, which was the focus of the expansion tube tests, is overlaid and nearly identical in the air only, and air with ablation spectra. The bandhead can be identified in the flight spectra by knowledge of its position in relation to the CN bandhead at about 389 nm from the current results, and is about 30 % higher the current calculated *Photaura* peak magnitudes. However, where the Gupta scheme brought the numerical

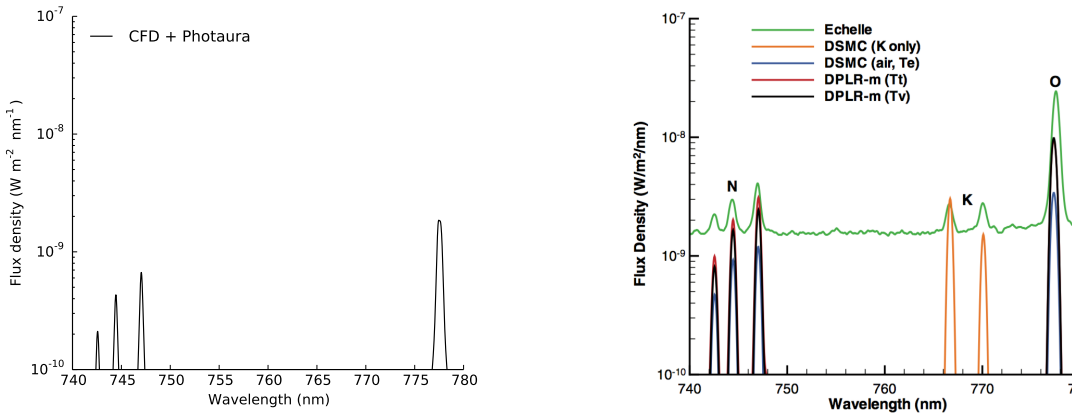
spectra closer to the experimental UV spectra, in the flight case it lowers most peak magnitudes and moves further away from the flight spectra. This is evidence of the different shock layer behaviour between flight and X2 experiments, and the potential for further modelling studies.

Wavelength range	730-750 nm	773-790 nm	810-830 nm	830-850 nm	855-880 nm
I, full scale CFD ($\text{W} \cdot \text{sr}^{-1}$)	206.6	373.5	514.1	149.5	836.4
I, ideal scaled CFD $\text{W} \cdot \text{sr}^{-1}$	17.76	31.05	44.13	11.76	71.73
I, X2 inflow scaled CFD ($\text{W} \cdot \text{sr}^{-1}$)	33.29	57.18	82.49	21.76	133.9
I, flight data ($\text{W} \cdot \text{sr}^{-1}$)	124.7	376.6	152.1	130.6	397.6
Ratio of flight data to full scale CFD	0.6	1.0	0.3	0.9	0.5
Ratio of flight data to ideal scaled CFD	7	12	3	11	6
Ratio of flight data to X2 scaled CFD	4	7	2	6	3
Ratio of full scale CFD to ideal scaled CFD	12	12	12	13	12
Ratio of full scale CFD to X2 scaled CFD	6	7	6	7	6
Ratio of X2 scaled CFD to ideal scaled CFD	2	2	2	2	2

Table 7.3: Final intensity values and ratios over selected wavelength ranges for Hayabusa CFD and flight data.

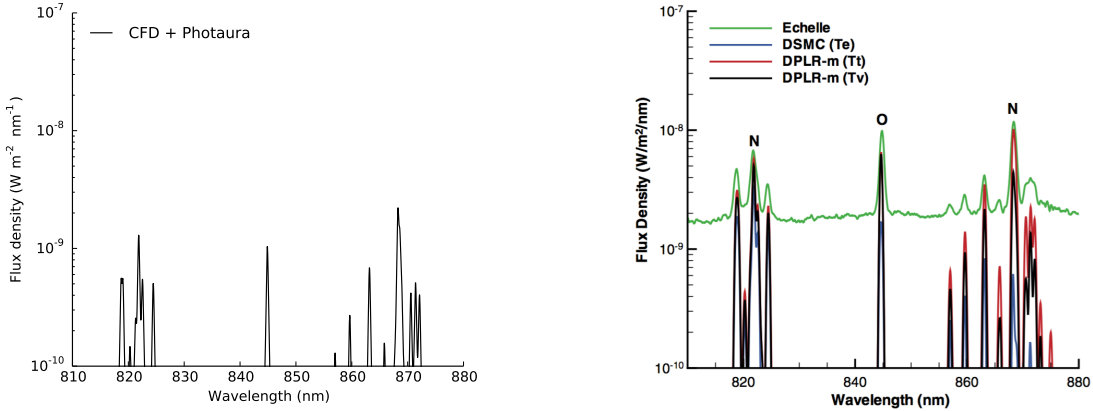
The emissivity at each radiating point was summed over lines of sight traced outwards and parallel with the stagnation line to produce an overall shock layer intensity, quoted in tabulated results as radiant intensity ($\text{W} \cdot \text{sr}^{-1}$). The overall radiant intensity for Hayabusa CFD at various scales and flight data are presented in Table 7.3. The best comparisons between full scale CFD and flight occur for the two atomic O triplets, at 777 nm and 844 nm, but the CFD overpredicts the three regions with N lines by around a factor of 2 compared to the flight data. This indicates that the radiation modelling of O more closely resembles flight for the selected condition than the modelling of N, which is complicated by integrating groups of lines rather than the stand-alone O triplets. The ratios of flight data, and flight CFD, to ideal and X2 scaled CFD are shown in Table 7.3 and based on the hypothesis, should be around 25, but most are about half of the target ratio, and some are nearly an order of magnitude less. The flight CFD to ideal scaled CFD ratio may differ from the target ratio because of the variation seen in the equilibrium region of the shock layer, especially in the equilibrium temperatures, and the fact that there is an equilibrium region at all. The higher radiant intensities/radiances from the X2 inflow scaled CFD are a direct result of the increased shock layer temperatures and inexact condition scaling in the facility simulation inflow. The magnitudes of atomic species are highest in the Hayabusa equilibrium region, and variance in those conditions

will drive different emission profiles and different overall values of radiant intensity or radiance. Differences at all scales could also be due to inaccuracies in the flight data. The consistency of the simulation ratios is good, but more work is necessary in refining the experimental and numerical measurements to understand why the target ratio is not reached.



a) Full scale Stardust CFD at 69 km flight trajectory point, 740-780 nm.

b) Full scale Stardust published results and flight data at 71 km trajectory point, 740-780 nm.



c) Full scale Stardust CFD at 69 km flight trajectory point, 810-880 nm.

d) Full scale Stardust published results and flight data at 71 km trajectory point, 810-880 nm.

Figure 7.15: Stardust IR flight spectra against CFD spectra calculated and averaged over the whole vehicle. Flight data and published results using DSMC and the DPLR CFD code from Boyd and Jenniskens [11].

7.7.2.2 Stardust

Boyd and Jenniskens [11] provided plots of their CFD and DSMC plus NEQAIR calculations against the Stardust flight spectra in the near IR region of interest, and these are reproduced here to compare

against the current results using *eilmer3* and *Photaura* in Figure 7.15. The *x*- and *y*-axes scales, including the logarithmic scale, have been preserved to enable direct comparison between plots, and the FWHM is approximately 0.33 nm. Although the two trajectory points are not the same, the Boyd and Jenniskens data should be lower for the 71 km point than the 69 km point, so it gives a good indication of how the current results are performing. The 740 to 780 nm region is shown in parts 7.15a and 7.15b, and the present result compares most closely to Boyd and Jenniskens' air DSMC result, with peak magnitudes about 50 % higher in the DSMC case. Parts 7.15c and 7.15d show that in the 810 to 880 nm region, the *eilmer3* result compares to the air DSMC result until the 868 nm N triplet. For that line and the subsequent N lines, the *eilmer3* more closely resembles the DPLR result using T_{ve} as the temperature for calculating spectra. The differences in eventual spectra can be explained by differences in the flowfield and/or radiation modelling. Most simply, the NEQAIR and *Photaura* radiation databases may have different emission and absorption data, causing the variations in IR spectra. On the flowfield side, the temperatures are such that ionisation of atomic species is becoming prominent, as discussed in Chapter 6. The temperature profiles that were calculated by *eilmer3* do not correspond to the Boyd and Jenniskens profiles [68], and the higher temperatures and high degree of nonequilibrium in the *eilmer3* flowfield could have caused more ionisation. Less atomic species present generate less atomic radiation, resulting in the lower peak magnitudes seen in Figure 7.15. Alternately or in combination with the influence of temperature, the reaction rates for electron-impact ionisation (atom to ion by impact with a free electron) differ, which would drive ionisation at different temperatures. Boyd and Jenniskens use $T_{tr}^{0.5}T_{ve}^{0.5}$ as the dissociation and ionisation rate-controlling temperature in CFD, another point of difference the the current simulations [68]. However, their DSMC simulations use $T_{tr}^{0.3}T_{ve}^{0.7}$, which is the same as the *eilmer3* calculations and could explain part of the similarity seen in Figure 7.15. It is interesting to note that all of the numerical spectra shown in Figure 7.15 underestimate the flight spectra, thus the question remains whether this is due to incorrect results from the simulations, or uncertainties impacting the flight data.

Table 7.4 summarises the radiant intensity over the entire radiating shock layer of Stardust in flight, and for CFD simulations at various scales, over the five discrete wavelength bands. The calculations were performed as outlined in Section 7.6.2 and opposite to the Hayabusa results in Table 7.3, the

Wavelength range	730-750 nm	773-790 nm	810-830 nm	830-850 nm	855-880 nm
I, full scale CFD ($\text{W} \cdot \text{sr}^{-1}$)	376.0	629.9	766.8	260.7	1208
I, ideal scaled CFD $\text{W} \cdot \text{sr}^{-1}$	10.34	16.99	24.11	6.671	38.60
I, X2 inflow scaled CFD ($\text{W} \cdot \text{sr}^{-1}$)	28.93	46.30	68.39	18.28	109.1
I, flight data ($\text{W} \cdot \text{sr}^{-1}$)	400.2	1186	1230	877.8	1635
Ratio of flight data to full scale CFD	1.1	1.9	1.6	3.4	1.4
Ratio of flight data to ideal scaled CFD	39	70	51	132	42
Ratio of flight data to X2 scaled CFD	7	26	18	48	15
Ratio of full scale CFD to ideal scaled CFD	36	37	32	39	31
Ratio of full scale CFD to X2 scaled CFD	13	14	11	14	11
Ratio of X2 scaled CFD to ideal scaled CFD	2.8	2.7	2.8	2.7	2.8

Table 7.4: Final intensity values and ratios over selected wavelength ranges for Stardust full scale CFD and flight data. All values are unfiltered (no transmission function applied to replicate experimental filter).

flight data is consistently larger than the full scale CFD. The closest comparisons are across the three N lines around 740 nm, where the full scale CFD value is 94 % of the flight value, and for the 855-880 nm group of N lines, where the full scale CFD value is 77 % of the flight value. The weakest comparisons occur for the two O triplets at 777 nm and 844 nm, and this could be due to earlier ionisation of O to O^+ in the reaction scheme than what truly occurred in flight. Overall, the fact that the full scale CFD consistently underpredicts flight could be an indication that the ionisation reactions of O and N are more prevalent than in the true flight shock layer. The X2 inflow scaled CFD results are in the range of double to triple the ideal scaled results, driven by overestimation of the extremely high speed, low density expansion tube condition in facility simulations. This condition was always going to prove difficult to simulate accurately for those reasons, and the comparison to the ideal illustrates the change needed through each part of the calculation to bring the intensities back to a meaningful result. The target ratio of flight data to ideal scaled CFD is 100 for Stardust, given the scale factor of 10 between the scaled model and the flight vehicle, and the calculated ratios are given in Table 7.4. Three ratios are within ± 50 % of the target ratio and the other two within ± 60 %; but, curiously, the two ratios furthest from the target value are for the two groups of N lines that had the closest comparison between full scale CFD and flight data. The change in flow condition when scaled could be affecting the number density of species and the rate of ionisation, especially density, as the scaled condition moves decisively away from the continuum borderline in the flight condition, and T_{ve} , which is the dominant temperature in ionisation reactions. If the behaviour of the

flow and consequent radiative emissions differs between scales, despite the overall nonequilibrium of the shock layer, there could be discrepancies between radiant intensity or radiance when examining particular species and transitions.

7.7.3 Comparing experiment and flight

7.7.3.1 Hayabusa

Wavelength range	730-750 nm	773-790 nm	810-830 nm	830-850 nm	855-880 nm
I, experiment ($\text{W} \cdot \text{sr}^{-1}$)	0.8342	3.467	3.943	1.002	4.477
I, flight data filtered ($\text{W} \cdot \text{sr}^{-1}$)	31.89	252.2	59.76	39.72	169.3
I, flight data unfiltered ($\text{W} \cdot \text{sr}^{-1}$)	124.7	376.6	152.1	130.6	397.6
Ratio of flight to experiment (all filtered)	38	73	15	40	38

Table 7.5: Final intensity values and ratios over selected wavelength ranges for Hayabusa X2 experimental data and flight data.

The intensity of the radiating shock layer enveloping the scaled Hayabusa model in X2 has been summed to give an overall value of radiant intensity for wavelength bands corresponding to the narrow band filters used, and these values are compared against the flight data in Table 7.5. The flight data has been presented as an unfiltered value in Table 7.3, but in order to compare with the filtered experimental data, the filter transmissivity must be applied to the flight spectra prior to integration. This is the same process as discussed in Section 5.4, when comparing integrated experimental spectra with experimental 2D images. The resulting I values are much smaller for experiment than for flight, even when filtered, but the ratios of filtered flight data to filtered experimental data provide the most interesting results to compare against the hypothesised ratio of 25, as calculated in Section 7.5. The experimental ratios have a lot more spread in the data than the CFD ratios in Table 7.3, due to the combination of uncertainties in the flight data and increased uncertainties in experimental results. Reasons for these uncertainties are outlined in Chapter 3 results, and include non-ideal shock speeds for the shot from which the measurement was taken, unknown conditions at the model location, and difficulties in inferring these conditions from conehead pressure measurements because they may appear smooth while fundamental flow variables (p , v etc.) are not. However, all of the ratios

in Table 7.3 are within a factor of 3 of the target ratio, and all except the 773-790 nm are around $\pm 50\%$ of the target ratio. Considering that both data sets could be subject to significant uncertainties, including from the application of a numerical Abel inversion method, these are very promising results.

7.7.3.2 Stardust

Wavelength range	730-750 nm	773-790 nm	810-830 nm	830-850 nm	855-880 nm
I, experiment ($\text{W} \cdot \text{sr}^{-1}$)	0.8414	5.583	8.470	1.340	17.53
I, flight data filtered ($\text{W} \cdot \text{sr}^{-1}$)	64.93	904.0	482.0	262.3	692.3
I, flight data unfiltered ($\text{W} \cdot \text{sr}^{-1}$)	400.2	1186	1230	877.8	1635
Ratio of flight to experiment (all filtered)	77	162	57	196	40

Table 7.6: Final intensity values and ratios over selected wavelength ranges for Stardust X2 experimental data and flight data.

The comparisons between radiant intensity and radiance summed over the Stardust flight vehicle and X2 experimental model are provided in Table 7.6. Once again, the radiant intensities have been calculated over five discrete wavelength bands corresponding to the filters used in the X2 experiments. The flight data is presented unfiltered and with the filter transmissivity applied, to enable like-for-like comparison with the experimental data as explained in Sections 5.4 and 7.7.3.1. The raw values tell part of the story but the critical comparison is in the ratio of flight data to experiment, which should be close to the hypothesised target ratio of 100. As with Hayabusa, there is more variance in the experimental and flight ratios than the CFD and flight ratios due to experimental and flight measurement uncertainties, but the ratios are near enough to the target value considering those uncertainties, perhaps with the exception of the O 844 nm value. As previously speculated, this could be due to different degrees of ionisation in the flow changing the amount of atomic species and the resulting atomic radiation, and between experiment and flight, that could come down to the different flow densities or incoming shock speeds. The ratios in Table 7.6 are within a factor of 2.5 of the target value, four ratios are within 60 % and two ratios are within 45 %. It is again promising that given the challenges of recording flight data and performing experiments at the edge of the X2 operating envelope, as well as using a numerical Abel inversion technique on the experimental data, the ratios resemble the target value.

7.8 Summary of Findings

A range of comparisons were performed between flight data, CFD and radiation modelling results, and X2 experimental results for both Hayabusa and Stardust, following the methodology and assumptions given at the beginning of this chapter. Spectra were calculated along particular lines of sight for comparison between CFD and flight, and CFD and experiment. The plasma emissivity across the axisymmetry half-plane extending from the stagnation line was plotted for Abel-inverted experimental images and each CFD simulation. Radiant intensity and radiance were calculated by summing line of sight integrated emissivity values across the entire radiating shock layer of full scale and scaled CFD models, and Abel-inverted experimental images, to compare against integrated flight spectra. When considering scaled experiments or simulations, an hypothesis was formulated to find the ratio with flight data or CFD based on energy in the flowfield and binary scaling, thus the final comparison was between the calculated and target ratios.

	Flight data	0.7 (1), $\sigma = 0.3$	40 (25), $\sigma = 21$	8 (25), $\sigma = 4$	4 (25), $\sigma = 2$
Flight data	-	-	-	-	-
Full scale CFD					
Experiment (X2)			-	0.2 (1), $\sigma = 0.1$	0.1 (1), $\sigma = 0$
Ideal scaled CFD				-	0.5 (1), $\sigma = 0$
X2 inflow scaled CFD					-
	Flight data	Full scale CFD	Experiment (X2)	Ideal scaled CFD	X2 inflow scaled CFD

Table 7.7: Qualitative and quantitative summary of the comparison quality between pairs of data sets for Hayabusa.

Table 7.7 provides a qualitative and quantitative summary of how well the data compares between two different methods, including flight, experiment and three different CFD simulations. The qualitative comparison is provided by the coloured boxes, where green is ‘good’, yellow is ‘satisfactory and needs improvement’, and red is ‘poor’. The qualitative data pairs are interpreted as the intersection of the rows and columns identified to the left of, and below, the data. The quantitative data has three important quantities, and each are the row data set divided by the column data set. Although there were five filters and a ratio for each filter in previous tables, the quoted ratio is the average of those five ratios for simpler representation in this summary table. The standard deviation is therefore calculated based on the deviation of the five filter band ratios to the mean. The value in brackets

is the target ratio of 25, when considering ratios between scales, and 1 when data sets are at the same scale, for example, flight data and full scale CFD. The quantitative values are a more defined representation of the performance of flight rebuilding or other comparisons, in terms of the difference to the target ratio and the variance of ratios in the data set. The flight to full scale CFD gives a strong agreement at 0.7 against the target of 1, and the experiment to flight comparison is the target ratio plus 60 %, which is sufficiently close. The full scale CFD and experiment ratio is slightly too high to be considered above satisfactory, as more work is needed to investigate overprediction of some spectral features in CFD. The ideal scaled CFD spectra overestimates the experimental spectra, but needs less improvement than the X2 scaled CFD, which is impacted by the facility simulations as well as scaling. Flight data and full scale CFD compares adequately with the ideal scaled CFD and 52 % less than the target ratio. However, the comparison is poor between flight data and full scale CFD, and X2 scaled CFD, as again it is too far away from the ideal scaled values and therefore the flight and full scale CFD values.

	Flight data	1.9 (1), $\sigma = 0.9$	106 (100), $\sigma = 69$	67 (100), $\sigma = 3$	23 (100), $\sigma = 16$
Flight data	-				
Full scale CFD		-	76 (100), $\sigma = 37$	35 (100), $\sigma = 3$	13 (100), $\sigma = 2$
Experiment (X2)			-	0.5 (1), $\sigma = 69$	0.2 (1), $\sigma = 0.1$
Ideal scaled CFD				-	0.4 (1), $\sigma = 0$
X2 inflow scaled CFD					-
	Flight data	Full scale CFD	Experiment (X2)	Ideal scaled CFD	X2 inflow scaled CFD

Table 7.8: Qualitative and quantitative summary of the comparison quality between pairs of data sets for Stardust.

The qualitative and quantitative summary of how well Stardust data pairs compare is presented in Table 7.8, and follows the same methodology as explained for Table 7.7. The experimental to flight data average ratio is within 6 % of the target ratio, and despite a large deviation in the constituent ratios, is a good result. The same outcomes are seen for all comparisons involving scaled CFD as for Hayabusa: the performance needs improvement, especially in the case of the X2 inflow scaled simulations. The comparisons between full scale CFD and flight data or experiment have been labelled satisfactory as the CFD is underpredicting where the results perhaps should be in reality, especially against the flight data. The closest numerical to experimental comparison involves the full scale CFD result, at 24 % less than the target ratio.

There are many potential reasons for differences or sources of uncertainties in the data sets, and therefore the comparisons between them. The small equilibrium region in the simulated Hayabusa shock layers could be affecting the application of binary scaling to the scaled models in experiment and simulation. The Stardust flight condition is nearing the non-continuum flow regime, and the X2 condition is pushing the operating envelope, leaving areas for inconsistencies in the numerical solutions. The X2 facility simulations and subsequent model shock layer calculations appear to be creating conditions that overestimate the ideal scaled conditions, which are also not scaling all properties perfectly, even though this is the expected outcome. Binary scaling is not working perfectly within the CFD simulations, which could be a consequence of the presence of an equilibrium region (known to impact the scaling performance) or by a translation of the data stemming from different relaxation behaviour and perhaps non-continuum effects in the full scale case. Ionisation reactions in particular appear to be affecting Stardust results, as the shock layer temperatures reach the point where atomic ionisation occurs and changes the composition of the flowfield. Radiation modelling data appears to be performing adequately, especially given the closeness of *Photaura* and PARADE results, but there are lines that appear to be overpredicted or underpredicted based on the radiation modelling only. The numerical Abel inversion method was applied to a noisy data set, and could benefit from higher resolution images and a more refined optical setup. This is the first time Abel inversions have been used quantitatively on X2 expansion tube data, and the first time that quantitative results have come from the 2D intensity mapping method for use with a numerical Abel inversion, so improvements can be made to capturing and processing the data. Experimental errors are hard to quantify beyond the condition parameters and their associated uncertainties for various methods as calculated in Chapter 3, but consistency between different optical measurements suggests that there are no systematic errors affecting the optical set-ups. Collection of flight data was not performed in this work but the nature of taking a measurement from hundreds of kilometres away, and imaging a moving spacecraft onto a handful of pixels to calculate emission spectra, means that the uncertainties are not only present, but most likely are significant. Attempting to further quantify any of these uncertainties is extremely difficult given the diverse data sets and complicated techniques employed.

Chapter 8

Conclusions

8.1 Addressing the Aim and Objectives

The aim of this thesis, to determine the identifiability and reproducibility of features from flight spectra in ground testing, through a three point comparison between flight, experimental and numerical data, was addressed through the completion of each objective. The Hayabusa and Stardust flight data was reviewed in Chapter 2 and trajectory points decided upon in Chapter 3. Chapter 3 progressed through the development and characterisation of the two X2 test conditions, producing analytical, experimental and numerical data to determine that the conditions were feasible. The experimental methodology, focusing on the optical imaging systems, was outlined in Chapter 4, and spectra and 2D imaging results for the Hayabusa and Stardust expansion tube tests were presented in Chapter 5. Chapter 6 moved to the CFD simulations of the full scale Hayabusa and Stardust vehicles at the selected trajectory points, and simulations of the scaled models at predicted and idealised test conditions. An ablating wall boundary condition was trialled with the full scale Hayabusa simulation, and radiation-flowfield coupling was assessed for both Stardust and Hayabusa. The radiation spectra calculations followed from the CFD results in Chapter 7, where the flight rebuilding with experimental and numerical data was described. The comparisons that were determined as the outcomes of the objectives in summarising Chapter 2 were presented and discussed in Chapter 7. Through making the comparisons between the array of flight, experimental and numerical data, the aim was achieved.

8.2 Major Findings

The major findings relate to the comparisons between flight, experimental and numerical data for Hayabusa and Stardust. Based on previous binary scaling studies, the hypothesis stated that along the same relative line of sight, radiation flux would be equivalent at different scales, and when summed over the entire forebody shock layer, the total radiation flux would differ by a factor of the length scale squared. In this case, the length scale refers to the ratio between characteristic lengths of the flight vehicle and scaled models. The comparisons adequately showed this hypothesis to be true, based on spectra and tabulated ratios of summed radiative intensity in Chapter 7.

For Hayabusa in the IR spectral region, flight and experiment generally compare well, and binary scaling appears to be quite effective in this case. The flight and full scale CFD spectra and radiation flux summed over the flowfield are very close to the target ratio of 1 for the O features, though there are greater differences for the grouped N features, due to numerical overprediction. The nonequilibrium flow region of the ideal scaled simulation was almost identical to the full scale case, but the modelling of reactions in the equilibrium region led to a higher equilibrium temperature, and therefore higher radiative emission. Therefore, the comparison between ideal scaled CFD radiation flux data and full scale CFD, experiment or flight radiation flux data was not as close as desired. The X2 inflow scaled case produced a worse comparison to the other data sets than the ideal scaled case due to the heated and imperfectly scaled inflow conditions, which led to a poorly simulated shock layer. The inadequate comparison to the ideal scaled data, especially, shows the improvements that are necessary in these simulations.

The Hayabusa UV flight data and full scale CFD compare fairly well in terms of N_2^+ , and the CN emissions are underpredicted in CFD but is a good first attempt with the new boundary condition. There are poor matches between experiment and CFD at all scales, which may be due to overprediction of the N_2^+ concentration and/or emissions in numerical modelling, but it was shown that the Gupta reaction scheme improves the comparison to experiment as compared to the Park reaction scheme. Since the flight to full scale CFD comparison is reasonable, the modelling may not capture the experimental conditions completely, and N_2^+ may act differently in the expansion tube than in

flight.

The focus of the Stardust comparisons was the IR region, and the results showed that flight and experiment compare well overall, despite larger deviations from the target ratio between flight and experimental results than seen for Hayabusa. Considering the proximity of the trajectory point to the non-continuum region and pushing the X2 operating envelope with the designed condition, this is a good result. Binary scaling appears to be effective in this case, likely due to the highly nonequilibrium flowfield as evidenced by numerical calculations. The flight spectra overestimates numerical spectra from full scale CFD, which is also seen in other published data. This could again be due to the high altitude factor, as well as overestimating ionisation in the CFD chemistry models, extrapolation of thermodynamic data sets beyond reasonable limits and resulting effects on radiation calculations. The ideal scaled simulations perform poorly because of a translation in shock layer properties and shock stand-off distance as compared to the full scale simulation, which needs further investigation. The X2 nozzle inflow scaled simulations perform poorly for the same reasons as the Hayabusa case.

Several findings that were not part of the three-point comparisons were also important outcomes of this research. Two new X2 conditions were designed to specifically suit the selected trajectory points and scales, but more generally to simulate Earth re-entry at approximately 10.4 and $12 \text{ km} \cdot \text{s}^{-1}$. There was general agreement between analytical, experimental and numerical methods and the conditions and uncertainties have been quantified for future use. Integrated 1D spectra and 2D imaging results compare well, proving the use of the 2D method in X2 shock layer measurements. Chemical composition of the inflow in X2 facility simulations does not appear to affect shock layer composition, agreeing with previous results. The thermodynamic parameters in the inflow do affect the resulting shock layer parameters, and concentrating on the scaled density while neglecting the temperature was likely detrimental to the scaled model results. However, concentrating on the temperature and not the density may have had a similar effect on the resulting shock layer. Radiation-flowfield coupling simulations were performed but did not significantly affect the Hayabusa or Stardust flowfields. Slight variations were visible in parameters such as temperature, which shows that the methodology and application are working and have the potential to produce interesting results for more strongly coupled conditions. The surface reaction mass flux boundary condition was a first

attempt at including mass flux in an aeroshell calculation in *eilmer3*, and the flowfield and radiation results were promising. The flight comparison was not perfect but useful, and improvements can be made to the nitridation reaction rates, and by including pyrolysis. Several radiation calculations were performed using both *Photaura* and *PARADE*, and they compared well, showing consistency between the two databases.

8.3 Future Work

This research produced comparisons between flight data, experimental data from X2 and CFD for the first time. Trying to enhance and improve these comparisons is the next step in fully understanding the extremely complex nature of superorbital re-entry shock layers, and many questions have been raised to be answered by further research. The facility simulations need further investigation, especially relating the flow exiting the nozzle to its impact on flow over a model. Developments would benefit greatly from more techniques to measure test flow properties in the expansion tube, rather than cone-head pressure only, as more parameters are needed to make comprehensive comparisons. Increasing the number of facility simulations performed to complement re-entry experiment campaigns would be beneficial to improving both the simulations and the flow measurement techniques. Radiation modelling, Abel inversions and other numerical methods including the flight rebuild strategy itself, should be checked and improved as new data or methods are available; for example, new atomic line data or an improved numerical Abel inversion algorithm. An investigation into spectral data sets in regions where flight or experimental radiation data differ appreciably from numerical results is important for the continued development of radiation calculations. Further testing in X2 of binary scaled conditions, especially where full nonequilibrium can be achieved, would be useful for future implementation and improvement of the flight rebuilding methodology. Testing binary scaled, enthalpy matched conditions and models with a heated wall and TPS-like materials would produce results closer to flight, and achieving a full scale experiment in X3 would be a great test for flight comparisons, and comparisons to scaled X2 experiments. More flight data would be extremely beneficial, and although it is difficult to obtain, there are several exciting missions, including Hayabusa 2, that would provide the perfect circumstances for future flight data collection and ground

testing. Ideally, the proven ability to recreate flight data in ground testing will be expanded upon to produce accurate pre-flight predictions of the re-entry environment, and the design methodology can be optimised through pre-flight ground testing. If the improvement in knowledge, design and prediction of the re-entry environment leads to optimisation of re-entry capsules, there will be an increase in the available payload weight and a concurrent increase in the capacity for successful missions, moving humankind one small step closer to safe and frequent space transportation.

References

- [1] P.N. Desai and G.D. Qualls. Stardust Entry Reconstruction. *Journal of Spacecraft and Rockets*, 47(5):736–740, 2010.
- [2] P. Jenniskens, P.F. Wercinski, J. Olejniczak, M. Wright, G. Raiche, D. Kontinos, P.N. Desai, R.E. Spalding, G. Sandquist, K .and Rossano, R.W. Russell, D.O. Revelle, D. Hladiuk, and A.R. Hildebrand. Surface heating from remote sensing of the hypervelocity entry of the NASA Genesis sample return capsule. *44th AIAA Aerospace Sciences Meeting*, pages 4451–4467, 2006.
- [3] J. Carpenter and G. Merkes. Hayabusa Re-entry Observed by Scientists Aboard DC-8, 2010.
- [4] T.J. McIntyre, R. Khan, T.N. Eichmann, and B. Upcroft. Visible and Near Infrared Spectroscopy of Hayabusa Re-entry using semi-autonomous tracking. *Journal of Spacecraft and Rockets*, 51(1):31–38, 2014.
- [5] D. Buttsworth, R. Morgan, and P. Jenniskens. Near Ultraviolet Emission Spectroscopy of the Hayabusa Re-entry. *Journal of Spacecraft and Rockets*, 50(6):1109–1120, 2013.
- [6] D.E. Gildfind. *Development of High Total Pressure Scramjet Flow Conditions using the X2 Expansion Tube*. Phd thesis, The University of Queensland, 2012.
- [7] R.J. Gollan. *The Computational Modelling of High-Temperature Gas Effects with Application to Hypersonic Flows*. Phd thesis, The University of Queensland, 2008.
- [8] G.A. Tirsky. Up-to-Date Gasdynamic Models of Hypersonic Aerodynamics and Heat Transfer with Real Gas Properties. *Annual Reviews in Fluid Mechanics*, 25:151–181, 1993.
- [9] C. Park, R. L. Jaffe, and H. Partridge. Chemical-Kinetic Parameters of Hyperbolic Earth Entry. *Journal of Thermophysics and Heat Transfer*, 15(1):76–90, 2001.
- [10] B. Kraetzig, S. Loehle, and D.R. Buttsworth. Evolution of Plasma Species and HeatShield Temperatures from Hayabusa Reentry Observation. *Journal of Spacecraft and Rockets*, 51(3):823–837, 2014.

- [11] I.D. Boyd and P. Jenniskens. Modeling of Stardust Entry at High Altitude, Part 2: Radiation Analysis. *Journal of Spacecraft and Rockets*, 47(6):901–909, 2010.
- [12] R.G. Morgan. Personal Communication, 2010.
- [13] D.F. Potter. *Modeling of radiating shock layers for atmospheric entry at Earth and Mars*. Phd thesis, The University of Queensland, 2011.
- [14] P.A. Gnoffo. Planetary-Entry Gas Dynamics. *Annual Reviews in Fluid Mechanics*, 31:459–494, 1999.
- [15] P. Jenniskens. Observations of the Stardust Sample Return Capsule Entry with a Slitless Echelle Spectrograph. *Journal of Spacecraft and Rockets*, 47(5):718–735, 2010.
- [16] C. Park. Stagnation-Point Radiation for Apollo 4. *Thermophysics and Heat Transfer*, 18(3):349–357, 2004.
- [17] B.R. Capra. *Aerothermodynamic Simulation of Subscale Models of the FIRE II and Titan Explorer Vehicles in Expansion Tubes*. Phd thesis, The University of Queensland, 2006.
- [18] D.B. Lee and W.D. Goodrich. The Aerothermodynamic Environment of the Apollo Command Module During Superorbital Entry. 1972.
- [19] C.O. Johnston. *Nonequilibrium Shock-Layer Radiative Heating for Earth and Titan Entry by Aerospace Engineering Titan Entry*. PhD thesis, Virginia Polytechnic Institute and State University, 2006.
- [20] R.M. Krek and R.J. Stalker. Experiments on Space Shuttle Orbiter models in a Free Piston Shock Tunnel. *The Aeronautical Journal of the Royal Aeronautical Society*, pages 249–259, August/September 1992.
- [21] D.M. Curry. Space Shuttle Orbiter Thermal Protection System Design and Flight Experience. In *First ESA/ESTEC Workshop on Thermal Protection Systems*, Noordwijk, The Netherlands, 1993.
- [22] W.R. Swift and R.M. Suggs. Genesis Reentry Observations and Data Analysis. Technical report, NASA, November 2005.

- [23] M.J. Taylor and P. Jenniskens. Near-Infrared Spectroscopy of Stardust Sample Return Capsule Entry: Detection of Carbon. *Journal of Spacecraft and Rockets*, 47(6):878–883, 2010.
- [24] M. Winter and K.A. Trumble. Spectroscopic Observation of the Stardust Re-Entry in the Near UV with SLIT: Deduction of Surface Temperatures and Plasma Radiation. Technical report, AIAA, 2010.
- [25] K.A. Trumble, I. Cozmuta, S. Sepka, P. Jenniskens, and M. Winter. Postflight Aerothermal Analysis of the Stardust Sample Return Capsule. *Journal of Spacecraft and Rockets*, 47(5):765–774, 2010.
- [26] S. Abe, K. Fujita, Y. Kakinami, O. Iiyama, H. Kurosaki, M.A. Shoemaker, Y. Shiba, M. Ueda, and M. Suzuki. Near-Ultraviolet and Visible Spectroscopy of Hayabusa Spacecraft. *Publications of the Astronomical Society of Japan*, 63(5):1011–1021, 2011.
- [27] T. Yamada, Y. Inatani, M. Honda, and K. Hirai. Development of thermal protection system of the MUSES-C/DASH reentry capsule. *Acta Astronautica*, 51(1-9):63–72, 2002.
- [28] H. Yano, T. Kubota, H. Miyamoto, T. Okada, D. Scheeres, Y. Takagi, K. Yoshida, M. Abe, S. Abe, A. Fujiwara, S. Hasegawa, T. Hashimoto, M. Ishiguro, M. Kato, J. Kawaguchi, T. Mukai, J. Saito, S. Sasaki, and M. Yoshikawa. Touchdown of the Hayabusa Spacecraft at the Muses Sea on Itokawa. *Science*, 312(June):4–7, 2005.
- [29] M. Abe, Y. Takagi, K. Kitazato, S. Abe, T. Hiroi, F. Vilas, B.E. Clark, P.A. Abell, S.M. Lederer, K.S. Jarvis, T. Nimura, Y. Ueda, and A. Fujiwara. Near-infrared Spectral Results of Asteroid Itokawa from the Hayabusa Spacecraft. *Science (New York, N.Y.)*, 312(5778):1334–1338, 2006.
- [30] A.M. Cassell, M.W. Winter, G.A. Allen, J.H. Grinstead, M.E. Antimisiaris, J. Albers, and P. Jenniskens. Hayabusa Re-Entry: Trajectory Analysis and Observation Mission Design. *AIAA Paper 2011-3330*, June 2011.
- [31] J. Borovička, S. Abe, L. Shrbený, P. Spurný, and P.A. Bland. Photographic Observations of the Hayabusa Re-entry. *Publications of the Astronomical Society of Japan*, 63(5), 2011.

- [32] K. Ohnishi, J. Watanabe, M. Sato, T. Ohkawa, and N. Ebizuka. Spectroscopic Observation of the Re-Entry Capsule of Hayabusa Spacecraft. *Publications of the Astronomical Society of Japan*, 63:987–993, 2011.
- [33] T.N. Eichmann. *Radiation Measurements in a Simulated Mars Atmosphere*. Phd thesis, The University of Queensland, 2012.
- [34] S. Loehle, A. Mezger, and H. Fulge. Measured surface temperatures of the Hayabusa capsule during re-entry determined from ground observation. *Acta Astronautica*, 84:134–140, September 2005 2013.
- [35] M. Winter, R. McDaniel, Y.K. Chen, Y. Liu, D. Saunders, and P. Jenniskens. Radiation Modeling for the Reentry of the Hayabusa Sample Return Capsule. In *50th AIAA Aerospace Sciences Meeting including the New Horizons Forum and Aerospace Exposition*, Nashville USA, 2012. AIAA.
- [36] J.B. Snively, M.J. Taylor, P. Jenniskens, M.W. Winter, M.J. Kozubal, R.F. Dantowitz, and J. Breitmeyer. Near-Infrared Spectroscopy of Hayabusa Sample Return Capsule Reentry. *Journal of Spacecraft and Rockets*, 51(2):1–6, 2014.
- [37] R. Khan. *Visible and Near IR Observation of the Hayabusa Re-entry: An Image-Based Visual Servoing Approach*. Mphil thesis, The University of Queensland, 2012.
- [38] C.M. James, D.E. Gildfind, R.G. Morgan, S.W. Lewis, E.J. Fahy, and T.J. McIntyre. On the Current Limits of Simulating Gas Giant Entry Flows in an Expansion Tube. *20th AIAA International Space Planes and Hypersonic Systems and Technologies Conference*, July 2015.
- [39] D.E. Gildfind, R.G. Morgan, and P.A. Jacobs. Expansion Tubes in Australia. In O. Igra and F. Seiler, editors, *Experimental Methods of Shock Wave Research*, pages 53–86. Springer International Publishing, 2016.
- [40] P.A. Jacobs and R.G. Morgan. Design, Operation and Testing in Expansion Tube Facilities for Super-Orbital Re-Entry. Technical report, Von Karman Institute for Fluid Dynamics, Brussels, Belgium, May 2013.

- [41] C.M. James, D.E. Gildfind, R.G. Morgan, P.A. Jacobs, and F. Zander. Designing and Simulating High Enthalpy Expansion Tube Conditions. In *Asia-Pacific International Symposium on Aerospace Technology*, Takamatsu, Japan, 2013.
- [42] R.L. Resler and D.E. Bloxsom. Very High Mach Number Flows by Unsteady Flow Principles, 1952.
- [43] R.L. Trimpli. A Preliminary Theoretical Study of the Expansion Tube, A New Device for Producing High-Enthalpy Short-Duration Hypersonic Gas Flows. Technical report, NASA Technical Report R-133, 1962.
- [44] C.G. Miller and J.J. Jones. Development and Performance of the NASA Langley Research Center Expansion Tube/Tunnel, a Hypersonic-Hypervelocity Real-gas Facility. In R.D. Archer and B.E. Milton, editors, *14th International Symposium on Shock Waves*, pages 363–373, Sydney, Australia, 1983.
- [45] A. Paull and R.J. Stalker. Experiments on an Expansion Tube with a Free Piston Driver. In *AIAA 15th Aerodynamic Testing Conference*, San Diego, USA, 1988. AIAA Paper 88-2018.
- [46] R.G. Morgan. A Review of the use of Expansion Tubes for creating Superorbital Flows. In *35th AIAA Aerospace Sciences Meeting and Exhibit*, Reno, USA, 1997. AIAA 97-0279.
- [47] C.J. Doolan and R.G. Morgan. A Two-Stage Free Piston Driver. *Shock Waves*, 9(4):239–249, 1999.
- [48] M.P. Scott, R.G. Morgan, and P.A. Jacobs. A New Single Stage Driver for the X2 Expansion Tube. In *43rd AIAA Aerospace Sciences Meeting and Exhibition*, Reno, USA, 2005. AIAA 2005-697.
- [49] M.P. Scott. *Development and Modelling of Expansion Tubes*. Phd thesis, The University of Queensland, 2006.
- [50] U.A. Sheikh. *Re-Entry Radiation Aerothermodynamics in the Vacuum Ultraviolet*. PhD thesis, The University of Queensland, 2014.

- [51] F. Zander, P.A. Jacobs, U.A. Sheikh, and R.G. Morgan. High speed imaging of spherical shock standoff in hypervelocity flows. In *18th Australasian Fluid Mechanics Conference*, Launceston, Australia, 2012.
- [52] U. Sheikh, S. Lewis, H. Wei, M. Ibrahim, R. Morgan, and T. McIntyre. Filtered Two-Dimensional Imaging in the X2 Expansion Tube. In *6th International Workshop on Radiation of High Temperature Gases in Atmospheric Entry*, St Andrews, Scotland, UK, November 2014.
- [53] E.J. Fahy, F. Zander, D.R. Buttsworth, and R.G. Morgan. Fast-Response Pyrometer Development for Expansion Tunnel Testing with Hot Carbon Models. In *18th Australasian Fluid Mechanics Conference*, Launceston, Australia, December 2012.
- [54] E.J. Fahy, D.R. Buttsworth, and R.G. Morgan. Scaled Earth Re-entry Experiments in the X2 Expansion Tube. In *7th Asia-Pacific International Symposium on Aerospace Technology*, Cairns, Australia, November 2015.
- [55] G. de Crombrugghe, D. Gildfind, F. Zander, T. McIntyre, and R. Morgan. Design of Test Flows to Investigate Binary Scaling in High Enthalpy CO₂N₂ Mixtures. *19th Australasian Fluid Mechanics Conference*, December 2014.
- [56] H. Porat. *Measurement of Radiative Heat Transfer in Simulated Titan and Mars Atmospheres in Expansion Tubes*. Phd thesis, The University of Queensland, 2015.
- [57] C. Jacobs. *Radiation in Low Density Hypervelocity Flows*. PhD thesis, The University of Queensland, 2011.
- [58] P. Toniato, D.E. Gildfind, P.A. Jacobs, and R.G. Morgan. Development of a new Mach 12 scramjet operating capability in the X3 expansion tube. In *7th Asia-Pacific International Symposium on Aerospace Technology*, Cairns, Australia, November 2015.
- [59] F. Zander. *High Temperature Testing of Carbon-Carbon Models in Hypersonic Impulse Facilities*. Phd thesis, The University of Queensland, 2013.
- [60] J.D. Anderson. *Hypersonic and High-Temperature Gas Dynamics*. AIAA Education Series, Reston, Virginia, USA, second edition, 2006.

- [61] W.E. Gibson. Dissociation Scaling for Nonequilibrium Blunt-Nose Flows. *Journal of the American Rocket Society*, 32(2), 1962.
- [62] D. Bose, E. Mccorkle, D. Bogdanoff, and G.A. Allen. Comparisons of Air Radiation Model with Shock Tube Measurements. In *47th AIAA Aerospace Sciences Meeting*, Orlando, USA, January 2009. AIAA.
- [63] D. Buttsworth, M. D'Souza, D. Potter, T. Eichmann, N. Mudford, M. McGilvray, T. McIntyre, P. Jacobs, and R. Morgan. Expansion Tunnel Radiation Experiments to Support Hayabusa Re-Entry Observations. In *48th AIAA Aerospace Sciences Meeting Including the New Horizons Forum and Aerospace Exposition*, Orlando, USA, January 2010. AIAA.
- [64] D. Buttsworth, P. Jacobs, D. Potter, N. Mudford, M. D'Souza, T. Eichmann, P. Jenninskens, T. McIntyre, M. Jokic, C. Jacobs, B. Upcroft, R. Khan, H. Porat, A. Neely, and S. Loehle. Super-orbital Re-entry in Australia Laboratory Measurement, Simulation and Flight Observation. In *28th International Symposium on Shock Waves*, Manchester, UK, July 2011.
- [65] R.J. Gollan and P.A. Jacobs. About the formulation, verification and validation of the hypersonic flow solver Eilmer. *International Journal for Numerical Methods in Fluids*, 73(1):19–57, September 2013.
- [66] P.A. Jacobs, R.J. Gollan, and D.F. Potter. The Eilmer3 Code: User Guide and Example Book 2014 Edition, 2014.
- [67] C. Park. Review of chemical-kinetic problems of future NASA missions. I - Earth entries. *Journal of Thermophysics and Heat Transfer*, 7(3):385–398, jan 1993.
- [68] I.D. Boyd, K.A. Trumble, and M.J. Wright. Modeling of Stardust Entry at High Altitude, Part 1: Flowfield Analysis. *Journal of Spacecraft and Rockets*, 47(5), 2010.
- [69] A. Martin, E.D. Farbar, and I.D. Boyd. Numerical modeling of the CN spectral emission of the Stardust re-entry vehicle. In *42nd AIAA Thermophysics Conference*. AIAA 2011-3125, June 2011.

- [70] Y. Liu, D. Prabhu, K.A. Trumble, D. Saunders, and P. Jenniskens. Radiation Modeling For the Reentry of the Stardust Sample Return Capsule. *Journal of Spacecraft and Rockets*, 47(5):741–752, 2010.
- [71] R.N. Gupta. Aerothermodynamic Analysis of Stardust Sample Return Capsule With Coupled Radiation and Ablation. In *37th Aerospace Sciences Meeting*, Reno, USA, 1999. AIAA 99-0227.
- [72] D. Olynick, Y.K. Chen, and M.E. Tauber. Aerothermodynamics of the Stardust Sample Return Capsule. *Journal of Spacecraft and Rockets*, 36(3):442–462, 1999.
- [73] C.I Park. Calculation of Stagnation-Point Heating Rates Associated with Stardust Vehicle. *Journal of Spacecraft and Rockets*, 44(1):24–32, 2007.
- [74] T. Suzuki, K. Fujita, T. Yamada, Y. Inatani, and N. Ishii. Postflight Thermal Protection System Analysis of Hayabusa Reentry Capsule. *Journal of Spacecraft and Rockets*, 51(1):96–105, 2014.
- [75] H. Kihara, N. Hirata, and K. Abe. A Study of Thermal Response and Flow Field Coupling Simulation around Hayabusa Capsule Loaded with Light-Weight Ablator. *Open Journal of Fluid Dynamics*, 3:100–107, 2013.
- [76] T. Suzuki, M. Furudate, and K. Sawada. Unified Calculation of Hypersonic Flowfield for a Reentry Vehicle. *Journal of Thermophysics and Heat Transfer*, 16(1):94–100, 2002.
- [77] S. Loehle, A. Brandis, T. Hermann, and J. Peter. Numerical Investigation of the Re-entry Flight of Hayabusa and Comparison to Flight and Ground Testing Data. In *43rd AIAA Thermophysics Conference*, New Orleans, USA, June 2012.
- [78] D.F. Potter, R.J. Gollan, T.N. Eichmann, T.J. McIntyre, R.G. Morgan, and P.A. Jacobs. Simulation of CO₂-N₂ Expansion Tunnel Flows for the Study of Radiating Shock Layers. In *46th AIAA Aerospace Sciences Meeting and Exhibit*, Reno, USA, 2008. AIAA 2008-1280.
- [79] B. Kraetzig. *Hayabusa radiation data analysis and ground testing investigation*. Master’s thesis, IRS Stuttgart, 2013.

- [80] P.A. Jacobs. Shock Tube Modelling with L1d, 1998.
- [81] V. Wheatley, H.S. Chiu, P.a. Jacobs, M.N. Macrossan, D.J. Mee, and R.G. Morgan. Rarefied, superorbital flows in an expansion tube. *International Journal of Numerical Methods for Heat & Fluid Flow*, 14(4):512–537, 2004.
- [82] S. Gordon and B.J. McBride. Computer Program for Calculation of Complex Chemical Equilibrium Compositions and Analysis. Technical report, NASA Reference Publication 1311, Cleveland, Ohio, 1994.
- [83] M. McGilvray. *Scramjet Testing at High Enthalpies in Expansion Tube Facilities*. PhD thesis, The University of Queensland, 2008.
- [84] M.N. Macrossan. Hypervelocity Flow of Dissociating Nitrogen Downstream of a Blunt Nose. *Journal of Fluid Mechanics*, 217:167–202, 1990.
- [85] J.W. Slater. Examining Spatial (Grid) Convergence, available <http://www.grc.nasa.gov/WWW/wind/valid/tutorial/spatconv.html>, last accessed 25/1/2016, 2008.
- [86] S.W. Lewis, R.G. Morgan, T.J. McIntyre, C.R. Alba, and R.B. Greendyke. Comparison of Carbon Ablative Shock-Layer Radiation with High Surface Temperatures. In *45th AIAA Thermophysics Conference*, Dallas, USA, June 2015. AIAA.
- [87] S.W. Lewis, R.G. Morgan, T.J. McIntyre, C.R. Alba, and R.B. Greendyke. Expansion Tunnel Experiments of Earth Re-entry Flow with Surface Ablation. *Journal of Spacecraft and Rockets*, 2016.
- [88] N. Banerji, P. Leyland, and R. Morgan. Expansion Tube Ablation Testing in Venus Entry Conditions. In *46th AIAA Thermophysics Conference*, Washington D.C., USA, June 2016. AIAA.
- [89] R.A. Serway, C.J. Moses, and C.A. Moyer. *Modern Physics*. Brooks/Cole - Thomson Learning, Belmont, USA, 3rd edition edition, 2005.
- [90] NIST Atomic Spectra Database, Version 5.0.

- [91] C. Park. The Limits of Two-Temperature Model. In *48th AIAA Aerospace Sciences Meeting Including the New Horizons Forum and Aerospace Exposition*, Orlando, USA, January 2010. AIAA 2010-911.
- [92] P.J. Roache, K. Ghia, and F. White. Editorial Policy Statement on the Control of Numerical Accuracy. *ASME Journal of Fluids Engineering*, 108(1), 1986.
- [93] R.N. Gupta, J.M. Yos, R.A. Thompson, and K.-P. Lee. A Review of Reaction Rates and Thermodynamic and Transport Properties for an 11-Species Air Model for Chemical and Thermal Nonequilibrium Calculations to 30000 K. Technical report, NASA RP-1232, 1990.
- [94] G.E. Palmer and M.J. Wright. Comparison of Methods to Compute High-Temperature Gas Viscosity. *Journal of Thermophysics and Heat Transfer*, 17(2):232–239, 2003.
- [95] R.C. Millikan and D.R. White. Systematics of Vibrational Relaxation. *The Journal of Chemical Physics*, 39(12):3209–3213, 1963.
- [96] J. Appleton and K. Bray. The Conservation Equations for a Nonequilibrium Plasma. *Journal of Fluid Mechanics*, 20(4):659–674, 1964.
- [97] M. Lino da Silva, V. Guerra, and J. Loureiro. Two-Temperature Models for Nitrogen Dissociation. *Chemical Physics*, 342(1-3):275–287, 2007.
- [98] P.A. Jacobs, R.J. Gollan, A.J. Denman, B.T. O’Flaherty, D.F. Potter, P.J. Petrie-Repar, and I.A. Johnston. Eilmer’s Theory Book: Basic Models for Gas Dynamics and Thermochemistry, 2012.
- [99] K. Sutton and P.A. Gnoffo. Multi-Component Diffusion with Application To Computational Aerothermodynamics. In *7th AIAA / ASME Joint Thermophysics and Heat Transfer Conference*, Albuquerque, USA, 1998. AIAA 98-2575.
- [100] J. D. Ramshaw and C. H. Chang. Computational fluid dynamics modeling of multicomponent thermal plasmas. *Plasma Chemistry and Plasma Processing*, 12(3):299–325, September 1992.
- [101] E.J. Fahy, N. Banerji, V. Marguet, J. Mora-Monteros, D. Potter, F. Zander, P. Leyland, and R.G. Morgan. Ground to Flight Investigations of Hayabusa with Ablation Effects. In *ESA Thermal*

- Protection Systems and Hot Structures Workshop*, Noordwijk, The Netherlands, April 2013.
European Space Agency.
- [102] G. Palmer, G. Allen, C. Tang, and J. Brown. Coupled Fluids-Radiation Analysis of a High-Mass Mars Entry Vehicle. *AIAA Paper 2011-3495*, June 2011.
- [103] R. Goulard. The Coupling of Radiation and Convection in Detached Shock Layers. *Journal of Quantitative Spectroscopy and Radiative Transfer*, 1:249–257, 1961.
- [104] M.W. Winter, B. Pfeiffer, M. Fertig, M. Auweter-Kurtz, and A.J. Smith. Recent Status of the Plasma Radiation Database PARADE. In *AIAA Thermophysics Conference*, Portland, Oregon, USA, 2004. AIAA.
- [105] J. Mora-Monteros, E.J. Fahy, N. Banerji, N. Joiner, G. Duffa, and P. Leyland. Rebuilding Thermal Response and Ablation Radiation Coupling for Superorbital Return. In *8th European Symposium on Aerothermodynamics for Space Vehicles*, Lisbon, Portugal, 2015. ESA.
- [106] J. Mora-Monteros, P. Leyland, G. Hannema, U.A. Sheikh, E.J. Fahy, R.G. Morgan, and T.J. McIntyre. Analysis and Rebuilding of Experiments on a Heated Graphite Model in X2 Expansion Tube. In *46th AIAA Thermophysics Conference*, Washington D.C., USA, June 2016. AIAA.
- [107] B.A. Cruden, R. Martinez, J.H. Grinstead, and J. Olejniczak. Simultaneous Vacuum Ultraviolet through Near IR Absolute Radiation Measurement with Spatiotemporal Resolution in an Electric Arc Shock Tube. In *41st AIAA Thermophysics Conference*, San Antonio, Texas, USA, June 2009.
- [108] C.J. Dasch. One-dimensional tomography: a comparison of Abel, onion-peeling, and filtered backprojection methods. *Applied Optics*, 31:1146–1152, 1992.
- [109] H. Fulge, A. Knapp, C. Eichhorn, R. Wernitz, S. Loehle, S. Fasoulas, and G. Herdrich. Improved Abel Inversion Method for Analysis of Spectral and Photo-Optical Data of Magnetic Influenced Plasma Flows. In AIAA, editor, *42nd AIAA Plasmadynamics and Lasers Conference*, Honolulu, USA, June 2011.

- [110] A. Sainz, A. Diaz, D. Casas, M. Pineda, F. Cubillo, and M. D. Calzada. Abel inversion applied to a small set of emission data from a microwave plasma. *Applied Spectroscopy*, 60(3):229–236, 2006.
- [111] J. Glasser, J. Chapelle, and J.C. Boettner. Abel inversion applied to plasma spectroscopy: a new interactive method. *Applied optics*, 17(23):3750–3754, 1978.
- [112] R. Alvarez, A. Rodero, and M. C. Quintero. An Abel inversion method for radially resolved measurements in the axial injection torch. *Spectrochimica Acta - Part B Atomic Spectroscopy*, 57(11):1665–1680, 2002.

Appendices

Appendix A

Facility simulation grid resolution

The radial variation of flow properties at the model location are shown in Figure A.1. Temperature and x -velocity are almost identical for each grid resolution across the radial dimension, and there is about a 3 % change in pressure and density near the centreline between different grids.

The pressure histories at the AT6 transducer location and nozzle exit, and grid sensitivity for various parameters, are presented in Figure A.2. The least squares fit for pressure and density is not as close as for temperature and x -velocity, and further investigation may be necessary. The pressure histories remain similar for each grid resolution as the test gas passes, and differ in the pressure rises that follow the test gas but do not impact upon it.

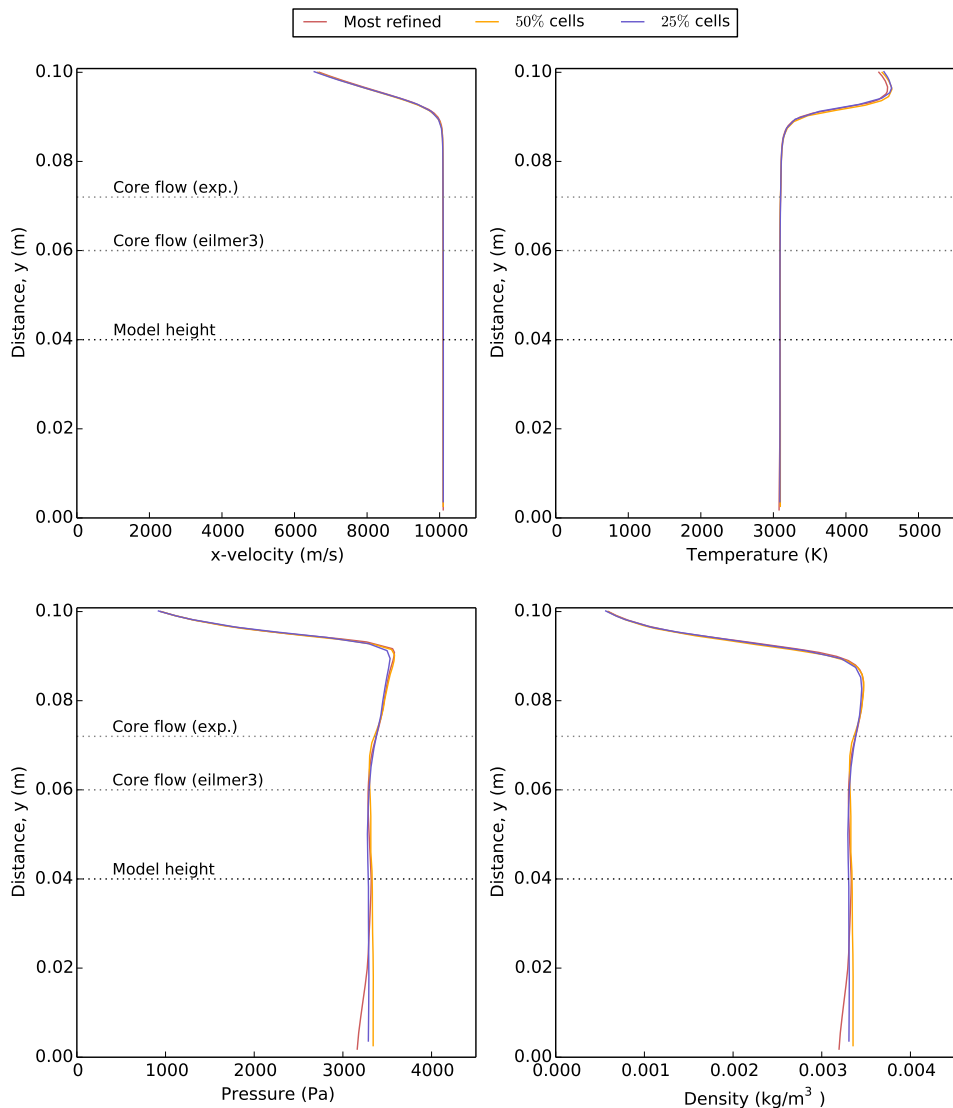


Figure A.1: Radial variation of selected flow properties at the model location and at 50 % of the test time, across three different grid spacings.

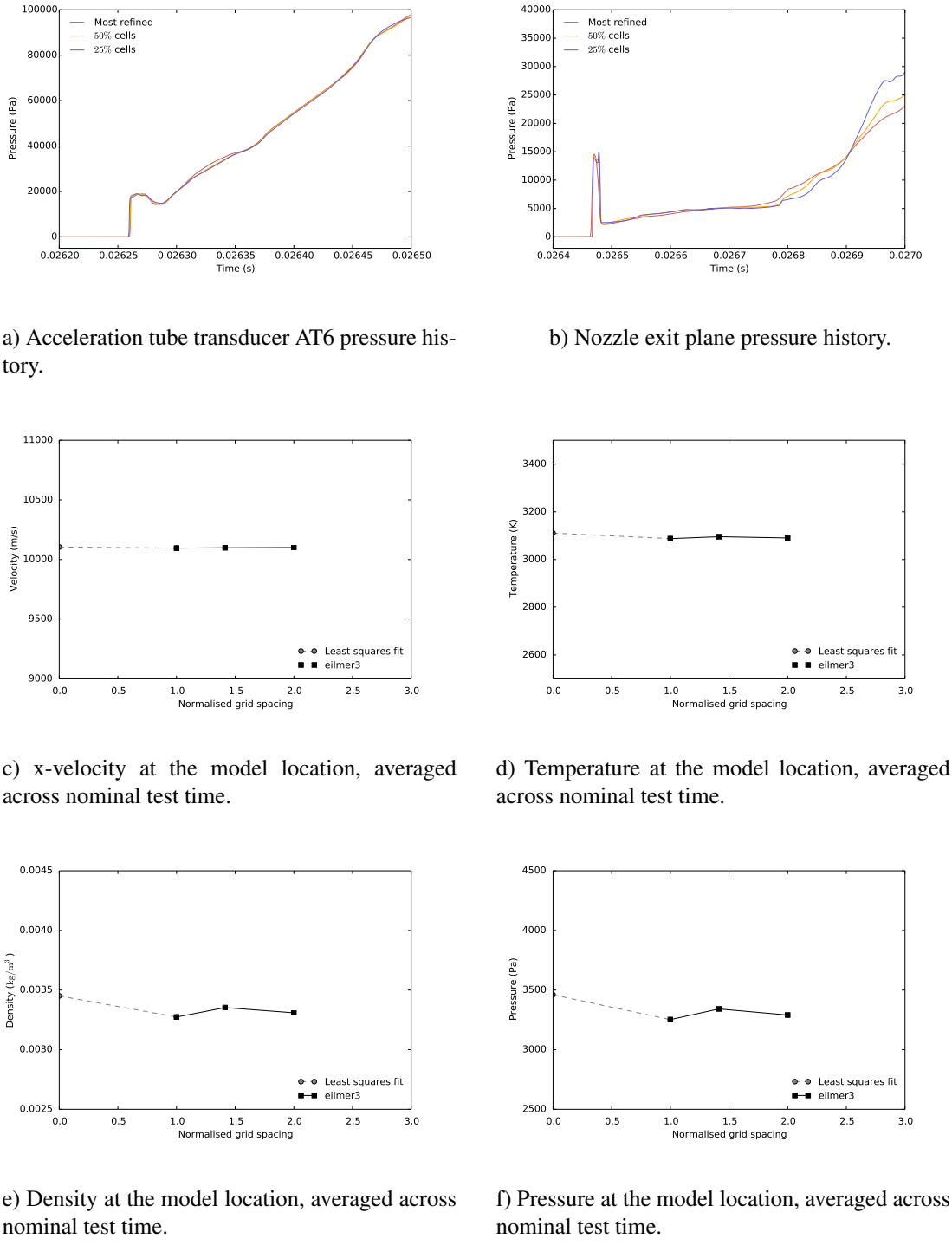


Figure A.2: Comparisons of various flow parameters across three different grid spacings.

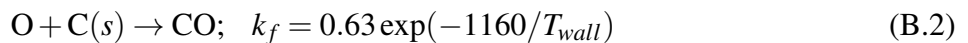
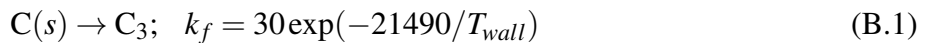
Appendix B

Implementation of Ablation Boundary Condition in *eilmer3*

The underlying equations and structure implemented in a simple ablating boundary condition for *eilmer3* aeroshell simulations is presented. This is based heavily on Park, Jaffe and Partridge [9], so the reader is directed there for all equations and further discussion of the boundary condition.

B.1 Surface reactions

The reactions for sublimation, oxidation and nitridation of surface carbon are defined in the following three equations, respectively. The reaction rates are provided and follow the Arrhenius equation, with the wall temperature T_{wall} as the reaction temperature. Currently, T_{wall} is held constant at the converged radiative equilibrium wall value but ideally, T_{wall} would also be dynamic in this part of the simulation. The reaction rate for the nitridation reaction is quoted by Park to be anywhere between 0 and 1, but the decision was made to keep it small for the initial calculations.





B.2 Structure of *eilmer3* boundary condition

The reaction rates quoted above are calculated using the wall temperature, and the reaction velocities are calculated per participating species with the relevant reaction rate. Here, k_B is the Boltzmann constant and m_s is the species molecular mass.

$$v_{reac,s} = k_f \sqrt{\frac{k_B T_{wall}}{2\pi m_s}} \quad (\text{B.4})$$

The molecular mass is selected based on the flowfield species participating in the nitridation and oxidation reactions (N and O), and C₃ as the only participant in the sublimation reaction. The species mass fluxes are then calculated in kg · m⁻² · s⁻¹, using the current density and species mass fraction at the wall. Depletion of flowfield species O and N is assigned a negative sign, as the mass flow is out of the domain.

$$\dot{m}_{c,s} = -\rho v_{reac,s} f_s \quad (\text{B.5})$$

Addition of ablative species CN and CO is assigned a positive sign, as the mass flow is into the domain.

$$\dot{m}_{c,s} = +\rho v_{reac,s} f_s \quad (\text{B.6})$$

The equilibrium composition of C₃ is required to determine C₃ mass flux, as a way to describe the reaction of solid graphite. The equilibrium mass fraction is calculated by the following equation.

$$f_{eq,C_3} = \frac{1.90 \times 10^9 \times M_{C_3} \exp(-59410/T_{wall})}{\rho T_{wall}} \quad (\text{B.7})$$

Then, the mass flux for C₃ can be described by the difference between the equilibrium C₃ composition

and the composition at the current timestep.

$$\dot{m}_{c,C_3} = +\rho v_{reac,s} (f_{eq,C_3} - f_{C_3}) \quad (\text{B.8})$$

The species mass fluxes, and the total mass flux generated by summing the species components, are sent back to the main equations for inclusion in the flux vectors at the wall.

Appendix C

Radiation-Flowfield Coupling for Hayabusa

A radiation-flowfield coupled calculation for Stardust was presented in Chapter 7, and a calculation was also performed for Hayabusa despite expecting very little effect from radiation, as indicated by the Goulard number of 0.008. The radiation source term was updated every one body length of flow (about 1.9×10^{-5} s) and 1000 rays per cell were used for the monte-carlo ray tracing calculations, at a spectral resolution of 30 points per nm. The first radiation calculation was performed on a converged flowfield solution and five iterations were performed, with the final time recorded as five body lengths after the commencement of the radiation-flowfield coupled calculation. The vibrational-electron-electronic temperature T_{ve} at the beginning and end of the radiation-flowfield coupled calculation is plotted along the stagnation line in Figure C.1, and there is very little change due to the inclusion of radiation.

The divergence of the radiative heat flux along the stagnation line is also included in Figure C.2. The general trends are that negative values are emission, through the majority of the shock layer, and positive values are absorption, which occurs prior to the shock and in the boundary layer. There are some issues with grid resolution and the number of rays, as seen by the discrete sections of the curve, but both parameters were sufficient to show the lack of coupling between radiation and flowfield at this Hayabusa trajectory point.

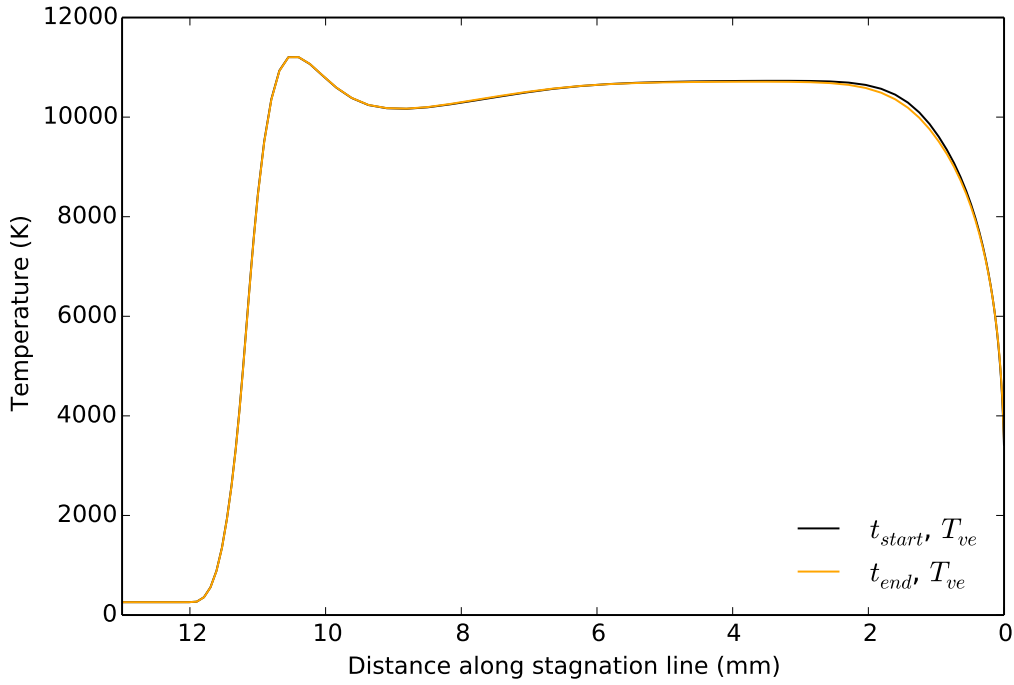


Figure C.1: T_{ve} along the stagnation line at the beginning and end of the Hayabusa radiation-flowfield coupled calculation, with a radiation source term update every 1 body-length of flow.

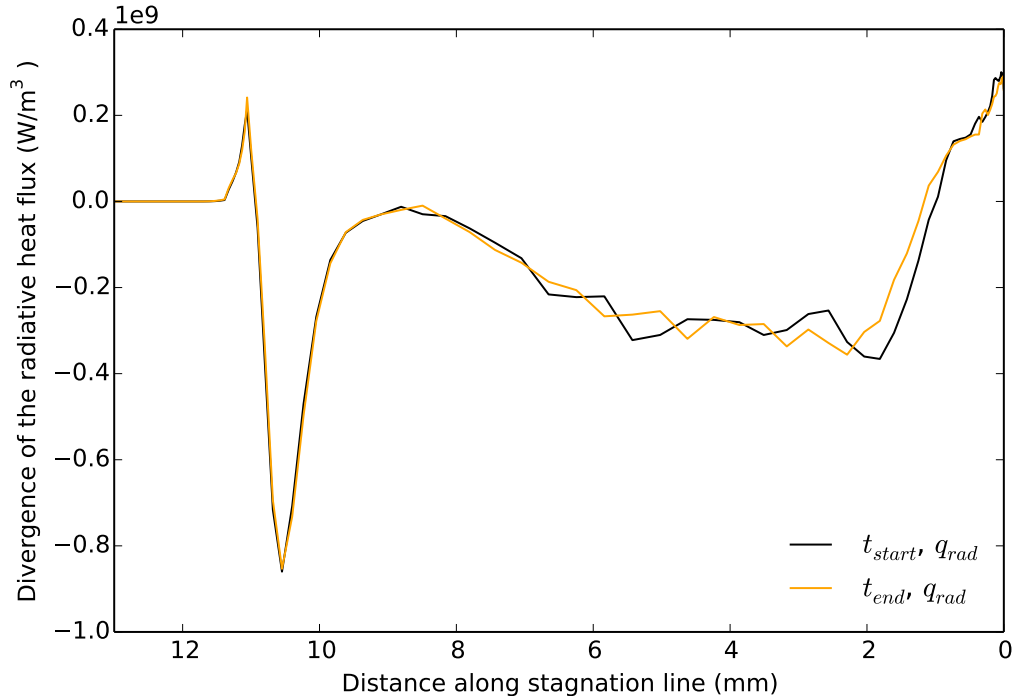


Figure C.2: Divergence of the radiative heat flux along the stagnation line at the beginning and end of the Hayabusa radiation-flowfield coupled calculation.

Appendix D

Flow visualisation

Specific results were required within the main text from each simulation or experiment, for example flow data at the model location, aeroshell simulation stagnation line profiles and flow properties and spectra along specific lines of sight. However, visualising the flow from simulations or recorded in high-speed videos is useful for understanding the flow through the facility and around the model.

D.1 Facility simulations

The flow through X2 from the inflow location at the tertiary diaphragm plane, to the exit plane placed sufficiently downstream of the model location, is visualised through the evolution of the velocity in Figures D.1 and D.2. Figures involve the Hayabusa condition only. Figure D.1 gives an understanding of the entire *eilmer3* simulation domain at 100 μ s before the middle of the test time. Figure D.2 focuses on the nozzle and test section, and shows the shock front moving into the test section and steadyng, once the flow features directly behind the shock front have passed. The wall does not cause noticeable reduction of the core flow size during the test time, and there is a well-defined boundary profile, even if it cannot be visualised adequately at this resolution and magnification.

D.2 Aeroshell simulations

The axisymmetric aeroshell CFD simulations performed in *eilmer3* can be visualised across the entire domain through various flow parameters. Figure D.3 shows T_{tr} , T_{ve} , the magnitude of the velocity

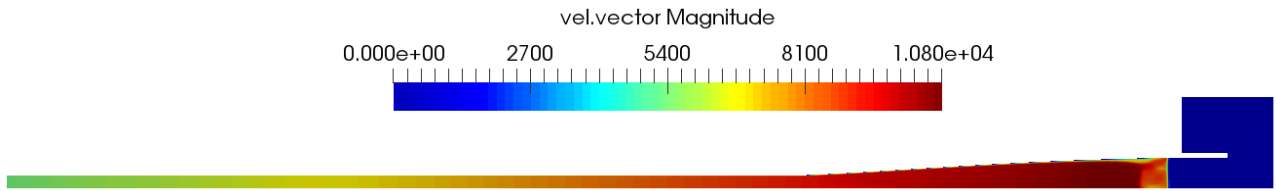


Figure D.1: Velocity ($\text{m} \cdot \text{s}^{-1}$) of flow through entire *eilmer3 X2* simulation domain, at $100 \mu\text{s}$ before middle of test time.

vector, and p for the full scale Hayabusa domain. Figure D.4 presents the same flow parameters for the full scale Stardust domain. The enormous increase in T and p across the shock front is evident, as is the substantial decrease in v , towards zero at the stagnation point. The shock layers increase in v , and drop in p and T further towards the shoulder and outflow boundary, and an expansion fan is visible around the Stardust shoulder.

D.3 Experimental campaign high speed video

High speed videos were recorded with the Shimadzu HPV-1 camera during most shots, to visualise the flow evolution and features around the Hayabusa and Stardust models. Figure D.5 shows bow shock establishment, steady flow and increasing brightness due to incoming unsteadiness for the Hayabusa model. Figure D.6 for Stardust was recorded at a different frame rate, delay and contrast, and the shock establishment was not recorded. The video frames do show the steady test time, the beginning of unsteady flow and brighter expansion around the shoulder, and increasing unsteadiness and brightness in the visual and near IR spectral region, which the camera records. The high speed recordings can assist in determining the test time, required delay for the spectrometer, and shock stand-off distance.

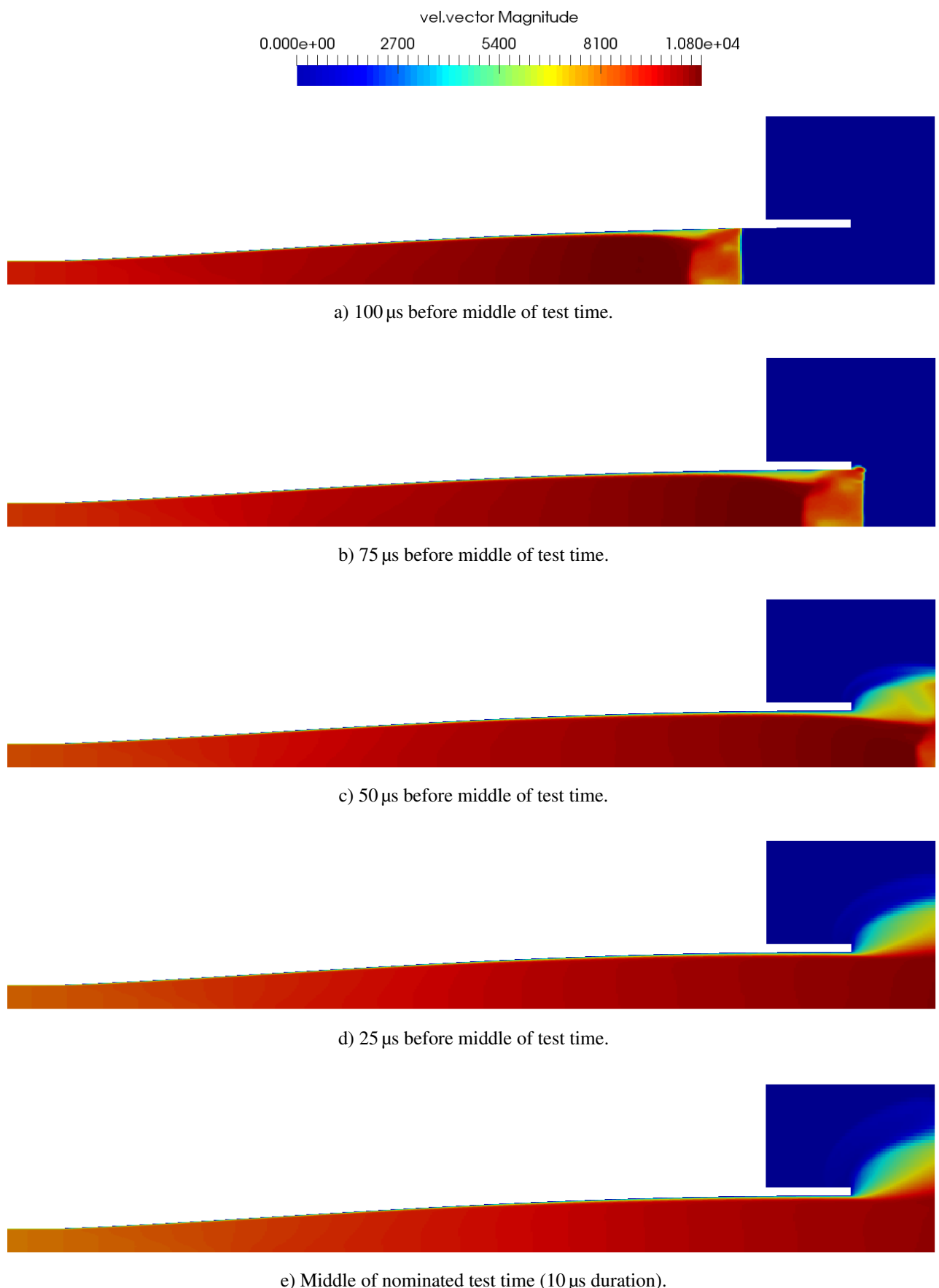


Figure D.2: Evolution through the X2 nozzle and test section of the magnitude of the velocity vector ($\text{m} \cdot \text{s}^{-1}$) leading up to, and including, the test time.

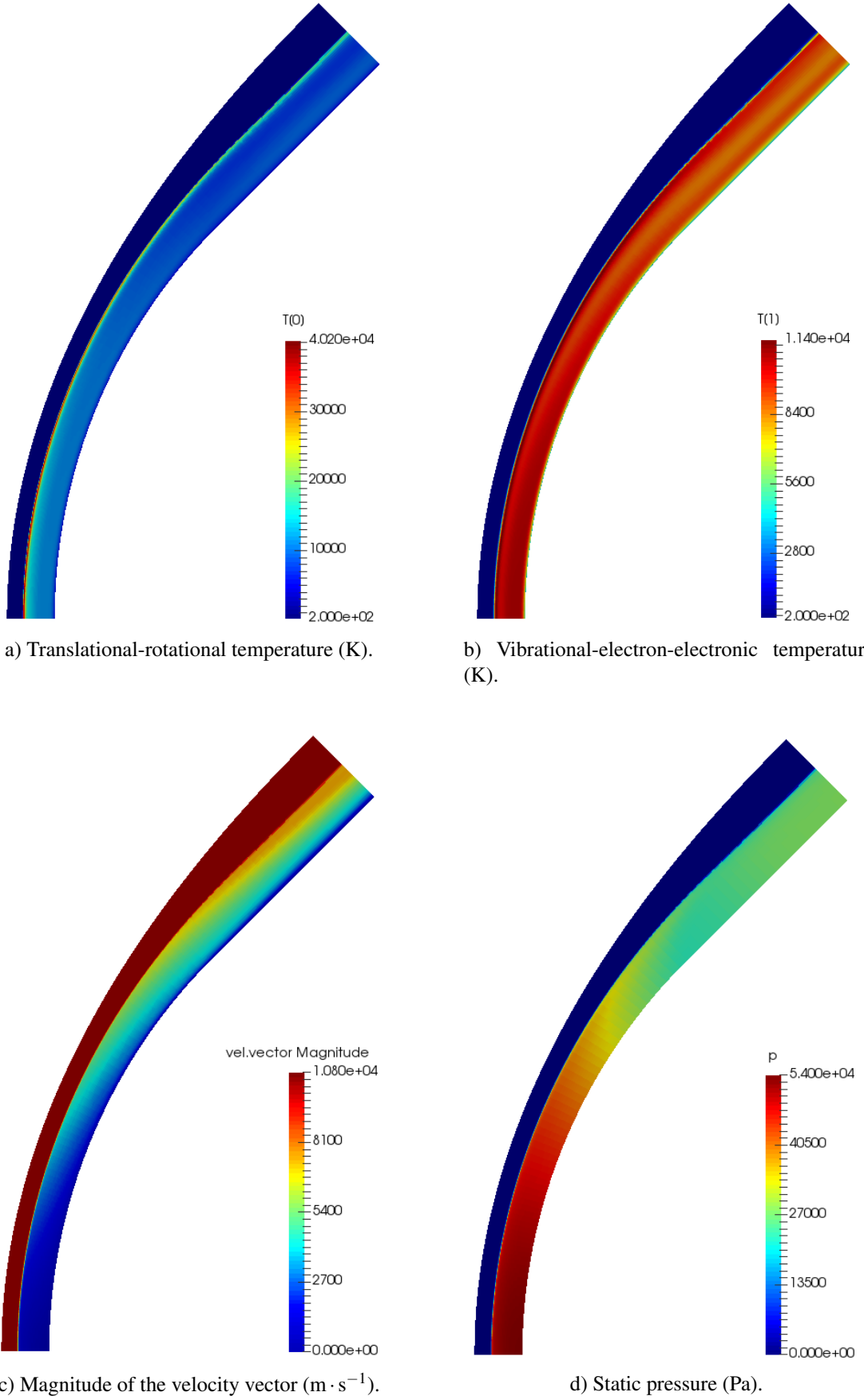


Figure D.3: Featured flow parameters for converged full scale Hayabusa solution.

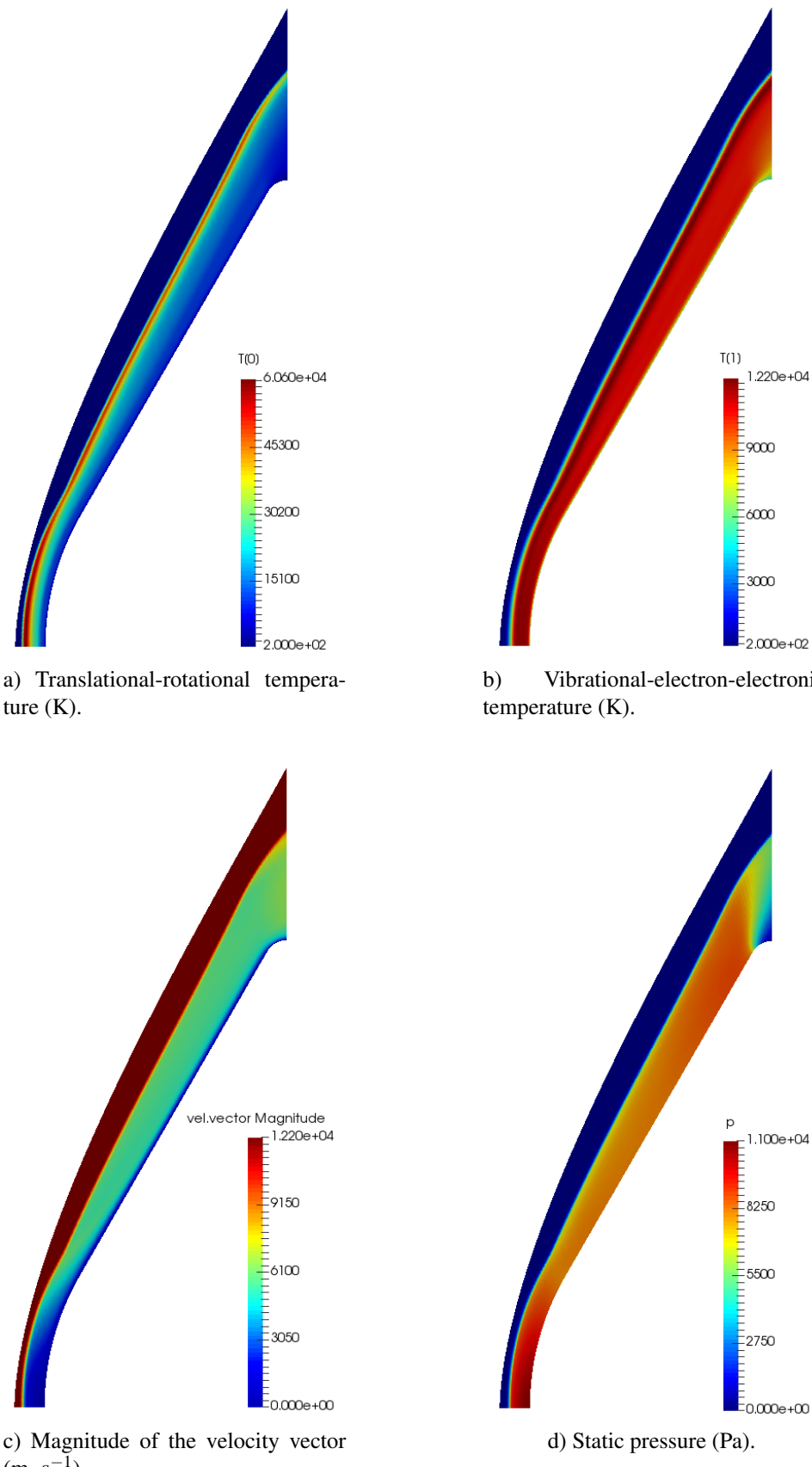
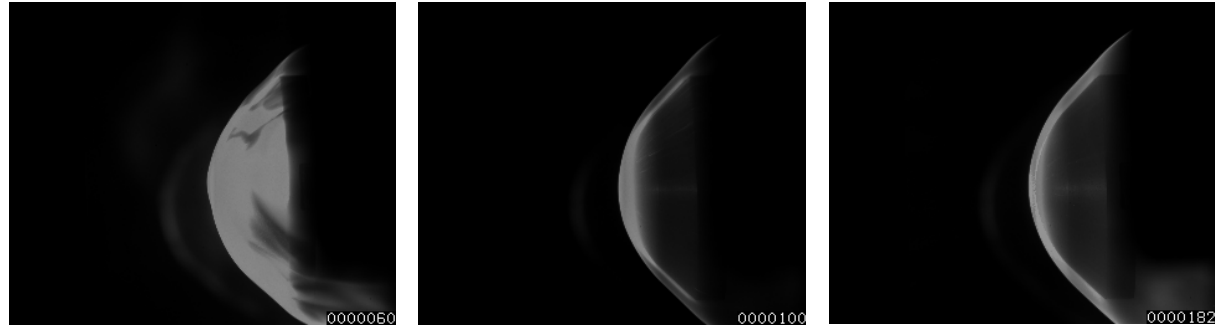
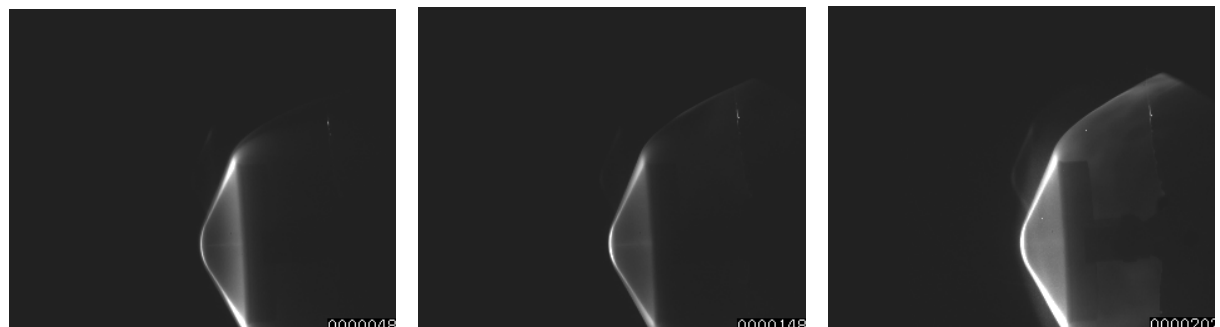


Figure D.4: Featured flow parameters for converged full scale Stardust solution.



a) Shock arrival and bow shock establishment.
b) Steady flow time.
c) Unsteadiness due to noise from driver, and driver gas arrival.

Figure D.5: Hayabusa high speed video frames, shot x2s2317.



a) Steady flow time.
b) Visible continuation of shock past corner, beginning of unsteadiness.
c) Unsteadiness due to noise from driver, and driver gas arrival.

Figure D.6: Stardust high speed video frames, shot x2s2817.